Palacký University Olomouc

Faculty of Science

Department of Zoology and Laboratory of Ornithology

Innovative Adaptations of Mesozoic Diapsids

Revealed through Synchrotron Microtomography

Studium inovativních adaptací druhohorních zástupců skupiny Diapsida pomocí synchrotronové mikrotomografie

Ph.D. Thesis

Dennis Franciscus Adrianus Eduardus Voeten

Supervisors: Prof. Ing. Stanislav Bureš, CSc.

Dr. Paul Tafforeau

Dr. Sophie Sanchez

Olomouc 2018

I declare that this thesis is my original work and has not been submitted for the purpose of obtaining the same or any other academic degree earlier or at another institution. My contribution to each of the publications underlying this work is expressed through the authorship order of the referred publications.

07.02.2018 ……

Dennis F.A.E. Voeten

Dedication I proudly dedicate this work to my loving parents, Ludo and Marja Voeten, who have unconditionally supported me in pursuing my passion for science and discovery from an early age onwards. My father has enthusiastically shared a growing interest in geology and paleontology with me, which has inspired me towards developing my ambitions irrespective of practical hindrances. My mother is the most kind-hearted and loving organism that evolution has brought forward and has always encouraged me to walk the paths that I dreamt of taking. Thank you both for everything, I love you very much.

Bibliographic identification

Author:	Dennis F.A.E. Voeten
Title:	Innovative adaptations of Mesozoic diapsids revealed through synchrotron microtomography
Type of thesis:	Ph.D. thesis
Institute:	Department of Zoology and Laboratory of Ornithology, Palacký University (Olomouc, Czech Republic)
Supervisors:	Prof. Ing. Stanislav Bureš, CSc.
	Dr. Paul Tafforeau
	Dr. Sophie Sanchez
Study program:	P1527 Biology
Study field:	Zoology
Year:	2018
Number of pages:	207 (including seven appendices)
Language:	English

Bibliografická identifikace

Jméno a příjmení autora:	Dennis F.A.E. Voeten
Název práce:	Studium inovativních adaptací druhohorních zástupců skupiny Diapsida pomocí synchrotronové mikrotomografie
Typ práce:	Doktorská disertační práce
Pracoviště:	Katedra zoologie a ornitologická laboratoř PřF UP v Olomouci
Vedoucí práce:	Prof. Ing. Stanislav Bureš, CSc.
	Dr. Paul Tafforeau
	Dr. Sophie Sanchez
Studijní program:	P1527 Biologie
Studijní obor:	Zoologie
Rok obhajoby práce:	2018
Počet stran:	207 (včetně sedmi příloh)
Jazyk:	anglický

Abstract and keywords

The fossil record provides an informative yet incomplete overview of the history of life on Earth. Evolution is a gradual process that operates at varying rates, and particular biological adaptations may appear suddenly in the fossil record. Explaining the origin and nature of such adaptations relies on understanding the lifestyles and life histories of key taxa that conservatively recorded their ecomorphological affinities. Appreciation of the corresponding anatomical expressions requires complete and three-dimensional visualization of the considered traits. Where traditional paleontological methods relied on destructive exposure of fossils and superficial morphological assessment, computed tomography has made a lasting entry in vertebrate paleontology fueled by its non-destructive nature and increasingly improving spatial resolution. Synchrotron microtomography is the apex of virtual paleontology and offers flexible solutions for optimizing reliable data acquisition in a wide variety of applications. Synchrotron microtomographic data of a skull of the Triassic shallow marine reptile *Nothosaurus marchicus* (245 Mya) revealed the presence of numerous adaptations attesting to its secondarily marine lifestyle and demonstrated that it occupied a piscivorous niche that relied on visual ambush predation. These adaptations illustrate the successful radiation and diversification of Sauropterygia in the aftermath of the largest mass extinction (252 Mya) that life on Earth experienced and demonstrate that biotic recovery of shallow marine ecosystems was unexpectedly fast-paced. Synchrotron microtomographic data on the wing bones of the iconic and potentially free-flying avialan *Archaeopteryx* (150 Mya) disclosed important architectural agreements with corresponding elements in modern flying birds, particularly in primarily ground-foraging groups that incidentally use escape flight. *Archaeopteryx* also accommodates an unexpectedly well-developed vascular mesh in its long bones that advocates better metabolic performance than believed, consistent with the demands of active flight. Since *Archaeopteryx* was incapable of executing the modern avian flight stroke, further studies will need to elucidate on the fashion of volancy that *Archaeopteryx* employed. The rapidly expanding opportunities that synchrotron microtomography provides will continue to play an important role in vertebrate paleontology.

Keywords: synchrotron microtomography, Sauropterygia, *Nothosaurus*, endocranium, *Archaeopteryx*, Avialiae, Archosauria, biomechanics, vertebrate flight, virtual histology

Abstraktní a klíčová slova

Fosilní záznam poskytuje poučný, avšak nekompletní přehled historie života na Zemi. Přestože je evoluce postupný proces probíhající na několika úrovních, některé biologické adaptace se mohou ve fosilním záznamu objevit poměrně náhle. Vysvětlení původu takovýchto adaptací závisí na našem porozumění života a zvyků zástupců jednotlivých taxonů, které konzervativně zaznamenávají své ekomorfologické znaky. Porozumění takovýchto anatomických projevů vyžaduje kompletní trojrozměrné zobrazení uvažovaných znaků. Tam, kde tradiční paleontologické metody závisely na vystavení fosilií destruktivnímu vnějšímu morfologickému hodnocení, tam počítačová tomografie učinila krok vpřed tím, že je nedestruktivní a umožňuje pracovat s větším rozlišením. Synchrotronová mikrotomografie je pak vrcholem virtuální paleontologie a nabízí flexibilní řešení pro optimalizaci získávání spolehlivých dat v návaznosti na širokou škálu aplikací. Synchrotronová mikrotomografická data lebky plaza *Nothosaurus marchicus* vyskytujícího se v mělkých mořích triasu odhalila přítomnost početných adaptací dokazujících jeho sekundární přizpůsobení se mořskému životu. Demonstrují také, že zaujal ekologickou niku piscivorních živočichů, kteří spoléhají na vizuální orientaci při lovu kořisti ze zálohy. Tyto adaptace ilustrují úspěšnou radiaci a diverzifikaci zástupců skupiny Sauropterygia po největším masovém vymírání, které se na Zemi odehrálo, a ukazují, že obnova bioty mělkých moří byla neobvykle rychlá. Dále data získaná pomocí synchrotronové mikrotomografie kostí křídel ikonického a potenciálně létajícího druhu *Archaeopteryx* odhalila důležité schody v architektuře kostí s moderními létajícími ptáky a to především s těmi, kteří se pohybují na zemi a létají jen příležitostně při útěku před predátorem. *Archaeopteryx* měl také nečekaně dobře vyvinutý cévní systém dlouhých kostí, což hovoří pro dobrou metabolickou výměnu potřebnou pro aktivní let. Avšak protože víme, že A*rchaeopteryx* nebyl schopen úderu křídly podobně jako dnešní moderní ptáci, je zapotřebí dalšího výzkumu, který by objasnil přesný způsob, jakým létal. Rapidně se rozvíjející synchrotronová mikrotomografie by proto mohla hrát důležitou roli nejen obecně v paleontologii obratlovců, ale zejména ve studiu *Archeopteryxe*.

Klíčová slova: synchrotronová mikrotomografie, Sauropterygia, *Nothosaurus*, endokranium, *Archaeopteryx*, Avialiae, Archosauria, biomechanika, let u obratlovců, virtualní histologie

Table of contents

Preface

Vertebrate paleontology seeks to reveal, reconstruct, and study the physiologies and lifestyles of extinct animals characterized by the possession of a backbone. This field of research centers around the vertebrate fossil record: the cumulative body of preserved and recovered material that informs on vertebrate life in the past. Information was traditionally extracted from paleontological samples through manual or mechanical freeing of body fossils to allow for subsequent depiction, analysis, and comparison with extinct and extant taxa. The Digital Revolution opened up a plethora of new opportunities for paleontological research. These range from digital measurement techniques to the compilation of comprehensive databases and from facilitating the development of intricate new tools for data analysis to the rapid communication and attractive presentation of novel findings.

Substantial advances in the development of digital computers in the middle of the twentieth century inadvertently sparked a revolution in tomographic imaging. Tomography employs penetrating waves to visualize the internal compositions of (usually) opaque structures that were initially presented as two-dimensional images that map the internal makeup along a single line-of-sight. The availability of digital tomographic imagery enabled the creation of tomographic reconstruction algorithms capable of revealing the true, three-dimensional nature and extent of internal or obscured phenomena from multiple radiographs obtained of the same sample at different angles. An important advantage of using computed tomography in paleontology, sometimes colloquially referred to as “virtual paleontology”, is that data acquisition is essentially non-destructive. This quality allows tomography to unlock material for scientific study that is considered too valuable to be subjected to invasive sampling methods such as excessive mechanical preparation or physical cross sectioning. Since tomographic data are stored as easily accessible digital image stacks, the records containing the three-dimensional information become available for study independent from the physical material itself and are, in theory, rapidly sharable among researchers. Synchrotron microtomography accounts for the most advanced and detailed tomographic approach available today and permitted the high-resolution non-destructive study of paleontological specimens described in this work.

The Mesozoic Era saw the dawn and extinction of some of the most iconic fossil taxa known to paleontology today. We will focus on two completely different Mesozoic taxa crucially sharing

one important quality: they are among the first representatives of their clade to evolve novel ecomorphologies that would ultimately prove highly successful and became the most recognizable trait to characterize their respective high-order clades.

Sauropterygia originated in the aftermath of the Permian-Triassic mass extinction event and rapidly invaded various predatory niches in Early Triassic shallow marine habitats. Basal (non-plesiosaurian) sauropterygians went extinct towards the end of the Triassic after giving rise to the highly successful plesiosaurs that continued to dominate pelagic environments until their demise in the Cretaceous-Paleogene extinction. Sauropterygia is considered a model clade for successful secondarily aquatic adaptation and has accordingly received broad attention from those aiming to identify morphological and physiological modifications that accompany the transition from terrestrial to marine lifestyles in amniotes. In collaboration with an international team of scientists, I created a virtual cranial endocast of an early eusauropterygian species, *Nothosaurus marchicus*, to reveal important adaptations that enabled aquatic life early in sauropterygian evolution. Since the referred endocast represents the oldest sauropterygian endocast visualized to date, it does not only inform strictly on the condition of the genus *Nothosaurus* but also provides a broader insight into the developmental principles that contributed to the successful invasion of marine niches by early Sauropterygia.

Flight is a highly complex form of locomotion that counterintuitively constitutes the most efficient vertebrate locomotory strategy per distance covered. Avian flight has intrigued scientists for millennia and remains yet to be fully understood. Birds are the only dinosaurs that managed to evade extinction and their volancy ensured an endured successful radiation recognizable until this very day, as birds represent the single most speciose clade of vertebrates in the world around us. The earliest taxon to possibly have been capable of dinosaurian powered feathered flight is the enigmatic genus *Archaeopteryx* from the Late Jurassic of Bavaria in southeastern Germany. This fossil creature has been the main focus of research towards understanding locomotory developments that took place in the evolutionary continuum between non-avian theropods and flying birds. A vital and persisting question with reference to *Archaeopteryx* revolves around its volant capacities: were its feathered wings used for passive gliding, for active flapping flight, or for purposes not pertaining to volancy at all? We have answered this question through comparison of the geometry of its anterior limb bones, visualized

through synchrotron microtomography, with those of a broadly sampled set of archosaurs spanning a wide range of locomotory strategies. It was shown that the structural architecture of the wing bones in *Archaeopteryx* recorded important agreements with those of modern birds that use occasional flapping flight, such as pheasants, and allowed us to conclude that *Archeopteryx* was indeed an active flyer. Nevertheless, because the pectoral girdle and wing morphology of *Archaeopteryx* are not compatible with the execution of a modern avian wing-beat cycle, we infer that it must have employed a more primitive mode of active flight that was probably closer to the range of anterior limb motion reconstructed for small maniraptoran dinosaurs. The findings imply that dinosaurian active volancy must have originated before the Latest Jurassic. The dorsoventral flight stroke adopted by modern birds probably appeared only during the Early Cretaceous at the root of Ornithothoraces, which encompasses the extinct enantiornithes as well as the euornithes that include all modern birds and their extinct kin.

Synchrotron microtomography was not only capable of capturing the full cross-sectional geometry of the bones of *Archaeopteryx* but also offered a first insight into the vascular patterns contained within its long bone cortex. Particular properties of intracortical vascularization can be quantified and adopted as informative proxies towards resolving physiological, ontogenetic, and biomechanical conditions that characterize various aspects of the life of a vertebrate individual. Established insights in such conditions furthermore allow for informed extrapolation during consideration of the phylogenetic relations that exist between different specimens. A proposal for recommended research into the existing data set with a focus on further contextualization of the identity of *Archaeopteryx* and its status as the oldest known ambassador of dinosaurian flight are presented in an outlook towards future research endeavors in which synchrotron microtomography will continue to play an instrumental role.

Chapter 1: General introduction

1.1 Thesis outline

This thesis comprises six chapters and includes two chapters that consist of the published accounts forming the core of the presented research.

Chapter 1 offers a brief introduction into radiography and tomography and summarizes the applications and benefits of synchrotron microtomography for paleontological research. The focal taxa that were studied using synchrotron microtomography are introduced and placed in the evolutionary context of the innovative adaptations they represent.

Chapter 2 considers several topical challenges, solutions, and opportunities for paleontological tomography with synchrotron radiation, builds on the novel research presented in Chapters 4 and 5, and evaluates its implications for the ecomorphology of the focal taxa considered. In addition, the significance of the findings is discussed in light of secondarily aquatic adaptation in marine reptiles and the origin of dinosaurian flight.

Chapter 3 presents the main conclusions of the paleontological studies undertaken and offers a perspective on future opportunities for synchrotron microtomography in paleontological research.

Chapter 4 is formed by the published article *Synchrotron microtomography of a* Nothosaurus marchicus *skull informs on nothosaurian physiology and neurosensory adaptations in early Sauropterygia* (*PloS One*).

Chapter 5 is formed by the manuscript *Wing bone geometry reveals active flight in* Archaeopteryx (currently in press with *Nature Communications*).

Chapter 6 represents a stand-alone section describing the relevance, methods, and perspectives of a future study into the nature and orientation of intracortical vascularization in the long bones of *Archaeopteryx*.

1.2 X-ray radiography, tomography, and synchrotron microtomography

1.2.1 Principles of radiography

Towards the end of the 19th century, Wilhelm Röntgen discovered X-ray radiation (Röntgen 1896) through a radiographic accident. Röntgen found that radiation produced by an electron-discharge tube excited a fluorescent screen and caused it to give off visible light. He subsequently observed that lead placed between the X-ray source and the fluorescent screen blocked the X-rays, but also noticed that the bones inside his hand had the same effect whereas the flesh did so to a markedly smaller degree, thereby revealing his manual skeleton (Frankel 1996). After this discovery, Röntgen recorded the now famous first radiograph of his wife's finger bones, while she was still wearing her wedding ring, on photographic film (Jakubek 2007). Radiography relies on the capacity of certain types of radiation to penetrate and traverse a diverse array of materials and visually opaque objects (e.g. Eisenberg 1992; Kak et al. 2001; Hsieh 2015). Differential attenuation within the sample subsequently transmits information on internal properties of the sample to a data recorder that makes it available for evaluation. For example, a potentially non-transparent heterogeneous sample placed between an X-ray source and an X-ray detector setup will project onto the detector a two-dimensional distribution field of X-ray transmission by cumulatively superimposing the absorption of individual features within the three-dimensional sample along the direction in which the radiation traveled. The resulting radiograph maps the relative distribution of media with different X-ray absorbent properties, also known as the radiodensity shadow, and when captured on film can inform on particular obscured phenomena in fossils that remain (partially) encased in their host matrix (Stürmer 1963; see also *Archaeopteryx* radiographs in Wellnhofer 2008).

1.2.2 Computed tomography provides three-dimensional data

The principles of radiography exploited through digital recording techniques allowed for computed tomography (CT) to make its appearance in the beginning of the 1970s. Computed tomography combines multiple X-ray measurements into a single, three-dimensional reconstruction of the sample of interest by employing the concept of the inverse Radon transform (Radon 1917) that translates density data of a three-dimensional object into its projections in the

form of sinograms. The inverse process used in tomographic image reconstruction transforms projection data into a reconstruction of the object, although the various solutions to this inverse problem (e.g. Deans 2007) are non-exact and demand substantial computing power. A virtual, three-dimensional, and representative X-ray attenuation model of obscured phenomena, such as fossilized remains inside a rock matrix or even cavities within a bone encased in rock, can only be extracted from volumes reconstructed through a multitude of projections (Brooks et al. 1975; Herman 2009). Sequential recording of a sufficient amount of radiographs over at least half a revolution of the sample within the field of view of the detector setup (180° plus the beam divergence angle for fan beam or conical beam tomography) creates a set of radiographs containing sufficient information to reconstruct the distribution of these media in three dimensions (Radon 1917). Alternative CT acquisition setups may achieve the same results through a tomographic gantry that is rotated around the sample, or by multiple detectors or sources arranged around the sample. Reconstruction of two-dimensional digital radiographs into a three-dimensional volume can be achieved by application of, for example, the commonly used analytic reconstruction algorithm known as filtered back projection that was initially developed for the reconstruction of radio-astronomical data (Bracewell et al. 1967; Brooks et al. 1975). Where original photographic radiographs visualized the presence of more absorbent media within the sample as darker X-ray shades, this differential absorption is nowadays typically expressed in a grey level gradient scaled inversely to transmission so that areas absorbing more radiation will appear lighter on the ultimate image. In medical tomography, individual voxels in the reconstructed 3D volumes are assigned radiodensity values through the standardized Hounsfield unit scale (Brooks 1977) that was named after the inventor of the computerized axial tomography scanner (Hounsfield 1973). In most other tomographic applications, the grey level scale communicates the linear attenuation coefficient of the media present in the sample.

1.2.3 The advantages of synchrotron microtomographic imaging techniques

Today, synchrotron micro-computed tomography represents the preeminent tomographic opportunity for the virtual imaging of paleontological samples. Several properties inherent to a third-generation synchrotron source (Kunz 2001) ensure higher data quality than achievable with conventional X-ray sources and facilitate the application of technical imaging methods that cannot be used with traditional tomographic setups. For example, the high flux of a synchrotron

source enables the application of monochromators to narrow the energetic bandwidth of the beam passing through the sample and onto the scintillator-detector array, which largely eliminates the artifacts of beam hardening that conventional setups suffer from (Tafforeau et al. 2006). Nowadays, synchrotron beam configurations with broader bandwidths (referred to as pink beams) are increasingly adopted for tomographic visualization as they do not invoke significant beam hardening effects but do offer the benefits of using a stronger beam with higher quality and stability. Besides traditional absorption-based approaches, the partial spatial beam coherence of synchrotron radiation enables propagation-based phase-contrast imaging techniques that provide improved resolution and contrast of the boundaries between different media in a sample through edge enhancement and phase retrieval solutions (Cloetens et al. 1996; Paganin et al. 2002; Tafforeau et al. 2006; Lak et al. 2008). In addition, the energy of synchrotron light (although often lower than typical laboratory or linear accelerator sources) enables penetration of relatively thick and dense samples (Horowitz et al. 1972; Raven et al. 1996) and permits short acquisition times (Bordas et al. 1980). The synchrotron at the ESRF is unique in that some of its beamlines are capable of delivering a relatively large beam with comparably high coherence and energy. Such properties ensure the efficient delivery of exception image contrast up to significant magnifications and for comparably large samples (Sanchez et al. 2013a).

Towards filtered back projection, the parallel-beam geometry of synchrotron light ensures a more reliable reconstruction of tomographic data than a cone-beam configuration allows for, as the lateral beam cone creates missing angles that invoke substantial artifacts in the ultimate reconstruction (Peters 2002). During complete data acquisition in a tomographic setup involving a CCD-based detector, a stack of n sinograms is created where n is equal to the number of vertical sensor lines in the detector. For absorption-based tomography, each sinogram captures the changing attenuation distribution across angular rotation of the sample in the setup for each horizontal sensor line in the detector and thereby records all information required to reconstruct a single virtual slice of the sample. Prior to back projection, the projection data is subjected to a high-pass filter in the Fourier domain to prevent diffuse blurring of the objects in the reconstructed sample. Subsequent back projection mathematically projects the radiodensity distribution for all recorded angular steps back across the center of the virtual environment. These back-projected sinograms will cumulatively converge on a slice stack that is oriented orthogonally to all individual projections and describes the attenuation distribution within a

virtual right cylinder with a diameter and height equal to the width and height of the original projections, respectively (e.g. Peters 2002; Deans 2007). If a sufficiently large amount of projections (i.e. radiographs of the rotating sample) was recorded, the reconstructed data present the three-dimensional linear attenuation coefficient distribution within the sample at adequate detail to confidently recognize and describe the nature and geometry of obscured media. Multiple scans that have sufficient overlap may be stitched together to obtain a single expanded digital volume.

A reconstructed three-dimensional tomographic volume is compiled out of a slide stack that describes the volume in consecutive slides along the original rotation axis of the sample in the tomographic setup during data acquisition. Designated software loads and interpolates such image stacks dynamically and allows the contained data to be appreciated in any orientation in a three-dimensional environment. Regions of interest (ROIs), typically defined by medium and morphology, may be extracted manually or automatically and can be expressed and studied both qualitatively and quantitatively. These regions identify and visualize discrete subvolumes within the sample and may be exported to virtual surface polygons for particular applications. After creation, ROIs become immediately available for dimensional or volumetric measurements and representations.

1.2.4 Computed tomography in paleontology

Computed tomography in general and synchrotron micro-computed tomography in particular have revolutionized paleontological research. The anatomy of some fossil taxa is now better characterized than those of their living counterparts (Cunningham et al. 2014). Even the visualization and reconstruction of delicate organs through fossilized soft-tissue structures has entered the realm of possibilities (e.g. Pradel et al. 2009; Perreau et al. 2011; Eriksson et al. 2012; Trinajstic et al. 2013; Maldanis et al. 2016; Qvarnström et al. 2017; Lautenschlager 2017). Most importantly, the present theoretical maximum resolution of synchrotron microtomography rivals that of optical microscopy (Sanchez et al. 2012). Combined with the non-destructive nature of data acquisition, providing that the radiation dose is well controlled, this implies that valuable material unavailable for invasive sampling becomes accessible for assessment of its internal structures and the retained integrity of a visualized specimen ensures complete

reproducibility of the study. Three-dimensional data at sufficient spatial resolutions allows for continuous assessment of internal structures throughout a sample, whereas physical cross sectioning, even when done sequentially, may not capture particular properties of interest (e.g. Stein et al. 2014). Physical sectioning to reveal osteohistological structures involves the consumption of most of a sample during the creation of a microscopic thin section and any continuity beyond the final prepared sample is lost forever. Conversely, material sampled with computed tomography is visualized throughout and remains completely available for later opportunities, for example when improvements in tomographic acquisition techniques warrant a re-evaluation of the sample at a later stage. Finally, tomographic data sets can be duplicated at will, shared virtually instantaneous or accessed remotely, and allow for multiple parties to appreciate and work with the data simultaneously (Rahman et al. 2012). It should be noted that optical microscopy still retains certain unique benefits over tomographic imaging. Although material is always lost during preparation of physical thin sections, the sections themselves have a certain thickness that, with optical confocal microscopy, allows for a three-dimensional exploration of microstructural properties within the sample using depth of field. Certain properties, such as those expressed in color or crystal orientation, cannot be evaluated with tomography and revealing them therefore requires optical solutions. Finally, a physical slide can be continuously assessed at any desired magnification whereas the close relation between resolution and field of view in tomographic data implies that high-resolution scans typically cover only a limited volume of the sample. Stitching individual smaller scans into one large volume is possible but results in increasingly large data sets that require adequate storage solutions and appropriately equipped workstations for data processing and evaluation.

The presented tomographic principles, advantages, and applications motivate and underlie the data acquisition pipeline that enabled the studies presented here. Synchrotron microtomography conducted at the European Synchrotron Radiation Facility (ESRF) unlocked information that would presently not be accessible without the unique opportunities enabled by non-destructive three-dimensional imaging at the spatial resolutions that the ESRF has to offer (Weitkamp et al. 2010a, 2010b; Sanchez et al. 2013a).

1.3 Sauropterygia: Secondarily marine adaptation and specialization

1.3.1 Early Triassic biotic recovery in newly formed habitats

The Permian-Triassic extinction event (circa 252 Mya) represents the largest mass extinction in the history of life on Earth. This biotic crisis, which affected over 90% of latest Permian marine species and circa 70% of terrestrial vertebrate families (Erwin 1994), defines the transition between the Paleozoic and Mesozoic eras. It profoundly influenced the evolutionary course of the taxa that managed to evade extinction, as the ecological void left after the catastrophe provided new opportunities for invasion into and occupation of then-vacant niches (Erwin 2007). Biotic recovery after the Permian-Triassic extinction event was traditionally assumed to have been protracted, stepwise, and slow paced (summarized in Tong et al. 2007 and Cheng et al. 2012). However, recent appreciation of Early Triassic taxonomic diversity and body size variation throughout marine vertebrate guilds has revealed a quicker and more gradual pattern of recovery (Scheyer et al. 2014) that warrants re-evaluation of the pacing of Early Triassic faunal reestablishment.

The Permo-Triassic transition approximately coincided with the onset of crustal extension that would ultimately culminate in the break-up of the supercontinent Pangea into Laurasia and Gondwana during Jurassic times (Ziegler 1982). In present-day Europe, this tectonic chapter initiated with the development of the network of grabens and troughs of the Central European Basin System (CEBS; Ziegler 1982). This intracratonic basin system spans large portions of western and central Europe and experienced progressive subsidence to form an important depocenter (Aigner 1985; see Fig. 1 in Palermo et al. 2012 for paleogeography). The Germanic Basin (synonymous with the Triassic episode of CEBS development) recorded the characteristic tripartite lithostratigraphic succession of the Triassic Germanic facies province that encompasses the continental Buntsandstein unit (partially Permian in age), the marine Muschelkalk sequence, and regressively marine, lacustrine and fluvial Keuper deposits (Aigner 1985; Szulc 1999). These three distinct lithostratigraphic units inspired the designation of the aptly named Triassic period by Von Alberti (1834) and are now united in the Germanic Trias Supergroup (Bachmann et al. 1999; Stollhofen et al. 2008). A relative sea level rise in the early Anisian provided an open communication between the Tethys and the intracratonic basins in central and subsequently

western Europa (Kozur 1974; Aigner 1985). This Muschelkalk transgression invaded the subsided domains of the continental interior from east to west, which resulted in a diachronous transition from the continental Buntsandstein deposits to shallow marine Muschelkalk strata throughout Europe (McCann 2008) and confuses absolute dating of local deposits and the faunal remains preserved within. Late Paleozoic biomes were broadly restricted to the vast continental expanses of Pangea and the surrounding deep oceans. A more diversified paleogeography including the shallow marine environments that originated from progressive continental flooding in Early Triassic times (Ziegler 1982) provided attractive new habitats for several vertebrate lineages during the biotic recovery after the Permian-Triassic mass extinction event.

1.3.2 The origin of Sauropterygia and the earliest chapter of sauropterygian evolution

Sauropterygia is a clade of secondarily marine reptiles encompassing the exclusively Triassic non-plesiosaurian (stem-group sensu Rieppel 2000) Sauropterygia and the Late Triassic to end-Cretaceous plesiosaurs (crown-group Sauropterygia sensu Rieppel 2000; see also Callaway et al. 1997). Non-plesiosaurian Sauropterygia are believed to have been restricted to nearshore habitats and shallow epicontinental seas (Rieppel 1999) whereas plesiosaurs were highly pelagic and likely had a trans-oceanic distribution (Benson 2012). The origin of Sauropterygia remains debated (Rieppel 2000). Recent studies propose it represents a sauropsid lineage that branched off before the divergence between lepidosauromorphs and archosauromorphs (e.g. Neenan et al. 2013), although the paucity of recognized unequivocal synapomorphies has hampered conclusive phylogenetic placement (consider e.g. Lee 2013). The earliest sauropterygian fossils date from the Olenekian of Europe and China (Rieppel 2000, Ji et al. 2013). This broad geographic disparity indicates that the true origin of Sauropterygia must have substantially preceded its presently known stratigraphic range to allow for the dispersal observed in their earliest known members and implies the presence of unrecognized ghost lineages. Most described early sauropterygian assemblages already exhibit a rich ecological diversity (Rieppel 2000), reinforcing the notion that important aspects of the earliest evolutionary history of Sauropterygia have thus far remained unrecognized. The fossil record of non-plesiosaurian sauropterygians is known to still be crucially incomplete (Rieppel 1997), and the relatively poor fossil preservation

potential of continental deposits and limited availability of representative fossiliferous shallow marine archives complicates the reconstruction of sauropterygian origins.

1.3.3 Disparate ecologies for non-plesiosaurian Sauropterygia indicate successful radiation

The evolutionary history of non-plesiosaurian Sauropterygia (Fig. 1.1) reflects its secondarily aquatic origins, as phylogenetically incrementally younger and more derived groups describe a morphofunctional gradient towards increasingly more open-marine lifestyles (Rieppel 2000, Neenan et al. 2017). Although Neenan et al. (2013) recovered a different topology than Rieppel (2000), their placement of Pachypleurosauria considerably more crownward than Plesiosauria is challenging to reconcile with the substantially earlier appearance of pachypleurosaurs in the fossil record (Rieppel 1999; Liu et al. 2014; Wintrich et al. 2017). The topology retrieved from the analysis by Wintrich et al. (2017) that was aimed particularly at resolving early plesiosaurian relations and only included six non-plesiosaurian sauropterygians did return pachypleurosaurs to a more basal position but placed them in a shared divergence with Nothosauroidea (Wintrich et al. 2017). Rieppel (2000) also considered this relation between pachypleurosaurs and nothosaurs and we here follow his evaluation to tentatively retain and discuss the original topology by Rieppel (1999, 2000) that was also adopted in the time-calibrated phylogeny optimized for non-plesiosaurian Sauropterygia by Neenan et al. (2017). The most basal group, the Placodontia, predated on sessile prey and has been interpreted to forage through “bottom walking” (Neenan et al. 2017). The second sauropterygian divergence is represented by the pachypleurosaurs, which encompass mostly small-bodied forms with a generalized morphology (Rieppel 2000) that exercised anguilliform swimming (Klein et al. 2015). All other sauropterygians are included in Eusauropterygia (Rieppel 2000). At least some members of Nothosauroidea within Eusauropterygia (Rieppel 2000) share the employment of paraxial aquatic locomotion (Krahl et al. 2013; Klein et al. 2015) with the most derived sauropterygians, the Pistosauroidea (Storrs, 1993), although this has been interpreted to represent a convergence rather than a primitive trait for Eusauropterygia (Krahl et al. 2013). Nevertheless, the plesiomorphic presence of interlocking pectoral and pelvic girdle elements forming rigid anchor points for appendicular musculature in this clade (e.g. Rieppel 2000, Fig. 7) provides some support for a transition of anguilliform (undulatory) to early paraxial (limbed) locomotion at the root of Eusauropterygia. Within

Nothosauroidea, a propulsive bias on the anterior limb is evident (Krahl et al. 2013), with the locomotory strategies of the sister genera *Nothosaurus* and *Lariosaurus* slightly differing in that *Lariosaurus* exhibits manual hyperphalangy (Rieppel 2000) consistent with more pelagic foraging. *Nothosaurus* and *Lariosaurus* are nevertheless known to have been preserved in the same deposits (e.g. Klein et al. 2016), but this may very well represent a thanatocoenotic association (i.e. an allopatric post-mortem association; see also Klein et al. 2015). Pistosauroidea includes the most pelagic of non-plesiosaurian sauropterygians, although some of its earliest representatives are encountered alongside nearshore early sauropterygian groups as well (e.g. Sander et al. 2014, Voeten et al. 2015), and the plesiosaurs that evaded the end-Triassic extinctions through their highly pelagic ecomorphology enabling oceanic dispersal (Benson et al. 2012; Wintrich et al. 2017).

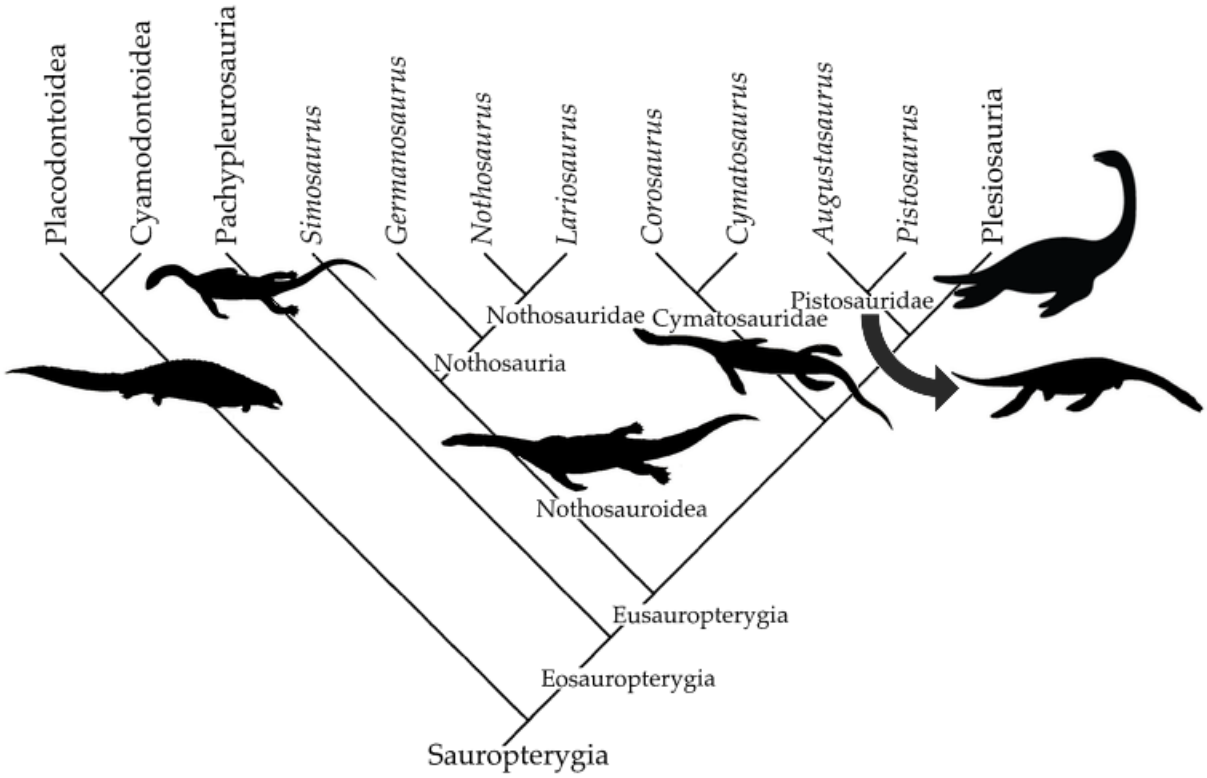

Figure 1.1 Schematic phylogeny of non-plesiosaurian Sauropterygia (modified after Rieppel 2000, but also consider Neenan et al. 2013, 2017; Wintrich et al. 2017; see 1.3.3 for discussion).

1.3.4 *Nothosaurus* as a model taxon for early sauropterygian diversification

Several species within the genus *Nothosaurus* are recognized in latest Early to Late Triassic European, North African, and Chinese assemblages (e.g. Rieppel 2000; Qing-Hua 2006; Liu et al. 2014; but also consider Klein et al. 2016). The genus exhibits an elongated yet dorsoventrally flattened skull that is characterized by the presence of large supratemporal fenestrae (Rieppel 2000) and a dentition forming a "trapping basket" with large, needle-like to conical, interlocking premaxillary and anterior mandibular fangs, and numerous smaller maxillary and dentary teeth (Rieppel 2002; Shang 2007 and references therein). *Nothosaurus marchicus* (Fig. 1.2) is an agile, likely piscivorous form that is the most common of early *Nothosaurus* species (Rieppel 2000).

Figure 1.2 Cranium of *Nothosaurus marchicus* (TW480000375; Museum TwentseWelle, Enschede, The Netherlands) described in Chapter 4.

The ecological vacancy that remained after the Permian-Triassic extinction event and the coeval appearance of novel shallow marine habitats appear to have sparked the successful initial

radiation and facilitated the subsequent diversification and niche segregation of non-plesiosaurian sauropterygians. Their rapid occupation of nearly all tetrapodal predatory niches in these nearshore habitats establishes the non-plesiosaurian Sauropterygia as a model clade for a successful invasion of the aquatic realm followed by immediate subsequent specialization towards more pelagic lifestyles. *Nothosaurus* represents a crucial taxon for understanding these evolutionary developments for four reasons:

Firstly, the genus is already present in some of the earliest sauropterygian assemblages of Anisian age (Liu et al. 2014; Voeten et al. 2015). This ensures sufficient insight into its most basal conditions, including those that may inform on the secondarily marine nature of Sauropterygia.

Secondly, the first chapter of nothosaurian evolution is characterized by a highly plesiomorphic suite of morphological conditions in *Nothosaurus marchicus* (Rieppel 2000; Albers et al. 2003; Albers 2011). *Nothosaurus marchicus* is the only widespread *Nothosaurus* species recognized before the Pelsonian (Liu et al. 2014), which propones a certain degree of monospecific opportunistic colonization. Later members of the genus are often sympatic and typically exhibit more disparate apomorphic morphologies (Rieppel 2000) indicative of substantial intrageneric specialization. This contrast between *Nothosaurus marchicus* and congeneric post-Bithynian forms aids identification of the anatomical developments that accompany intrageneric niche segregation.

Thirdly, the morphology of *Nothosaurus* is sufficiently documented through its relative abundance in the fossil record (e.g. Rieppel 2000; Oosterink et al. 2003; Liu et al. 2014) to allow for a confident reconstruction of its ecomorphology.

Fourthly, primitive paraxial aquatic locomotion in nothosaurs represents an unambiguous secondarily marine adaptation that prefaced the locomotory strategy of ocean-cruising plesiosaurs. Associated adaptations in *Nothosaurus* that may be homologous with those in plesiosaurs (i.e. were present at the root of Eusauropterygia, but also consider the discussion on eusauropterygian paraxial locomotion in 1.3.3) have the potential to illuminate on the establishment of conditions that allowed plesiosaurs to conquer and thrive in oceanic environments until their extinction in the Cretaceous-Paleogene event.

1.4 *Archaeopteryx* and the origin of dinosaurian flight

1.4.1 The iconic *Archaeopteryx* and the dinosaurian nature of birds

Since the second century A.D., the region surrounding the picturesque town of Solnhofen in Bavarian Germany has acted as an important supplier for the Solnhofen Plattenkalk that has been used in the construction of buildings, stonemasonry, and later also in lithography. The homogeneity and straight bedding planes (Barthel et al. 1990) have rendered this Tithonian (latest Late Jurassic) limestone the agent of choice for transferring images drawn on stone to paper. Although inclusions in the rock can render a slab valueless for lithographic purposes, an imperfect slab of lithographic limestone from Solnhofen is not necessarily worthless. The value of some fossilized remains originally captured in the forming limestone far exceeds those of the most expensive lithographs. The most famous and precious fossils from these deposits (in the broader sense; see Rauhut et al. 2018) are the remains of the oldest avialan potentially capable of powered flight known to date: the Urvogel *Archaeopteryx*.

Archaeopteryx has been considered a symbol of evolution ever since it was first discovered in the middle of the nineteenth century (Wellnhofer 2008) and played a pivotal role in the realization that birds are dinosaurs. Inspired by his friend Charles Darwin in the 1860s, Thomas Huxley was among the first to recognize the skeletal blueprint of birds as essentially "reptilian" in nature, with dinosaurs presenting an intermediate anatomy between earlier reptiles and birds (Switek 2010). In the 1970s, this work was revisited and expanded upon by John Ostrom, who studied the Haarlem "*Archaeopteryx*" (Ostrom 1970) and noticed profound morphological agreements with the dromaeosaur *Deinonychus* that he described one year earlier (Ostrom et al. 1969a; Ostrom 1969b). Although the referred specimen of "*Archaeopteryx*" is now identified as an anchiornid in its own genus (*Ostromia*; Foth et al. 2017), the proposed characters linking *Deinonychus* to birds are also recognized in unambiguous *Archaeopteryx* specimens (Wellnhofer 2008). For example, the semilunate carpal bone of *Deinonychus* (Ostrom 1969b) that allows for planar extension and flexion of the hand is also present in *Archaeopteryx* (Wellnhofer 2008) and is homologous with the trochlea carpalis of the avian compound carpometacarpus that enables manual supination during wing folding in birds (Sullivan et al. 2010).

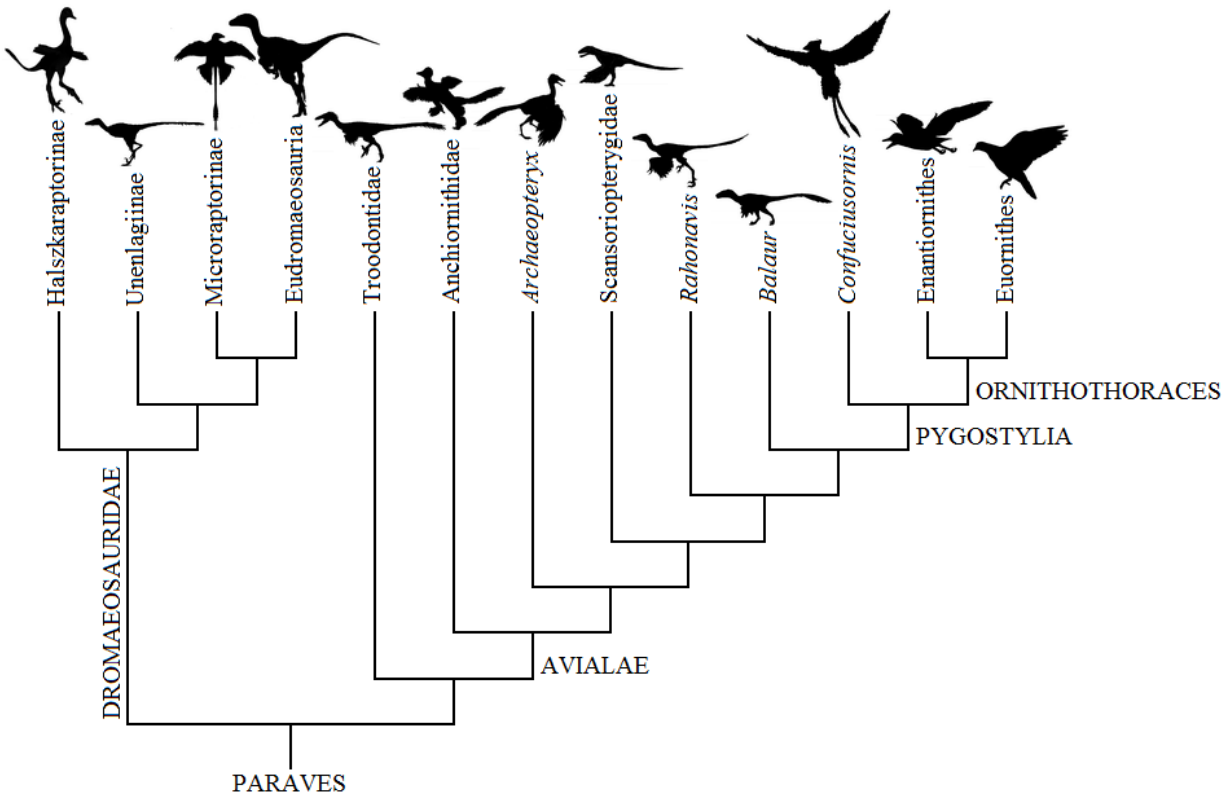

Figure 1.3 Simplified paravian phylogeny (after Cau et al. 2017), silhouettes not to scale.

1.4.2 Definition of Aves and competing theories for the origin of dinosaurian flight

The concept of what constitutes a bird is far from straightforward, and multiple definitions exist (Gauthier et al. 2001). In the late 20th century, Aves was defined as the common ancestor of *Archaeopteryx* and the house sparrow *Passer domesticus*, and all its descendants (Padian et al. 1997). Nowadays, Aves is restricted to the clade bracketed by modern birds (Gauthier et al. 2001). The larger group that encompasses Aves and all extinct forms closer to birds than to *Deinonychus* is accommodated in Avialiae (e.g. Senter 2007). Although *Archaeopteryx* is not positioned on the evolutionary pathway leading towards modern birds but rather represents an early phylogenetic divergence from that lineage (e.g. Thulborn 1984; Cau et al. 2017: Appendix I, Fig. 1.3), its former status as the oldest known bird still resonates in recent contextual reports

(Lee et al. 2011; Horner 2012; Godefroit et al. 2013; Manning et al. 2013; Ksepka 2014; Brusatte et al. 2015; Chiappe et al. 2016). The anatomy of *Archaeopteryx* combining features of both non-avian pennaraptorans and birds offers important information towards reconstructing the origin of Aves and has been central in the long-standing debate whether dinosaurian flight originated as passive gliding or as powered flapping flight (summarized in Wellnhofer 2008). The gliding or arboreal model for the origin of dinosaurian volancy describes how aerial locomotion appeared in scansorial (arboreal) forms where anterior limbs adapted to allow for controlled gliding from a perch down (typically envisioned as the branch of a tree), either to a lower perch or to ground level. In this model for the early chapters of dinosaurian flight, obligate gliding gradually evolved into powered flight. The opposing cursorial theory relies on a model where principally ground-based forms initially acquired airfoils to support terrestrial habits related to hunting or fleeing from predators, such as leaping or high-velocity stabilization, which subsequently also permitted progressively longer aerial excursions (Wellnhofer 2008). A crucial contrast between these dichotomous hypotheses is that the arboreal model allows early aerial avialans to have adopted a relatively simple mode of gliding descent whereas the cursorial model requires a much more demanding and complex mode of active, powered aerial ascent to have been available quite early on.

The recently resolved maniraptoran phylogeny by Cau et al. (2017: tree provided in Appendix I, Fig. 1.3) recovers Paraves as the most inclusive clade containing both Dromaeosauridae and Avialiae, including modern birds. Anchiornithidae now represents the most basal clade within Avialiae, followed by *Archaeopteryx*. Notably, Scansoriopterygidae was retrieved within Avialiae on one branch more inclusive than *Archaeopteryx* towards Pygostylia. Nevertheless, the phylogenetic placement of anchiornithids and scansoriopterygids remains debated.

1.4.3 The origin of feathers

Dinosaurian flight, including avian volancy, is virtually synonymous with feathered flight. Unsurprisingly, the development of feathered flight was intimately dependent on the evolution of feathers and feathery integuments, which is briefly summarized here for context (see 2.3.2 for discussion on its relevance for *Archaeopteryx*). The origin of feathers significantly predates the origins of archosaurian flight in general (Dalla Vecchia 2013) and dinosaurian flight in particular

(Wellnhofer 2008). Genetic data suggest that the structural protein constituting dinosaurian feathers, "feather-keratin"; a form of beta-keratin (Alibardi et al. 2006), is homologous with the beta-keratin of crocodilian scutes and pterosaurian pycnofibres (Alibardi et al. 2006; Lowe et al. 2014; Wu et al. 2017). The oldest conclusive recognitions of dinosaurian feathers and feather-like integuments were established for Late Jurassic feathered theropods (Liu et al. 2012 and references therein) and in the roughly contemporary primitive ornithischian *Tianyulong* (Zheng et al. 2009; Liu et al. 2012) from China. If these structures are indeed mutually homologous with modern bird feathers (consider Zheng et al. 2009 and references therein), they must represent a synapomorphy for the group encompassing both ornithischians and saurischians, which pushes their origin back to at least the Triassic (Gauthier et al. 1989). Even the recently reported (yet controversial; Langer et al. 2017) reappraisal of dinosaurian interrelations (Barron et al. 2017) recognizes a Triassic origin for both Ornithischia and Theropoda (Barron et al. 2017), the only groups in which such integument is observed, and thereby places the oldest non-molecular evidence for feathers before the Jurassic as well. Since all reported potentially parachuting, gliding, or flying dinosaurs appear from the Jurassic onwards, as the concept of Triassic "birds" has proven untenable (Wellnhofer 2008), it is clear that feathers evolved in a non-volant context. It has furthermore been defended that proposed Middle Triassic dinosaurian protofeathers cannot be conclusively interpreted as such (Lingham-Soliar 2010), which specifically hints to the Late Triassic as the stage for the origin of dinosaurian plumage.

1.4.4 An overview of earlier interpretations of volancy in *Archaeopteryx*

Although the convincingly "avian" appearance of its feathered wings (Elzanowski 2002 and references therein; Wellnhofer 2008) proposes that *Archaeopteryx* was capable of complex flight, certain aspects of its skeletal morphology and reconstructed myology appear to contradict this conclusion (Wellnhofer 2008). The ability and modes of aerial locomotion permitted in fossil taxa can generally only be assessed on osteomorphological characters. Most paravian lineages were clearly incapable of flight despite the substantial suite of physical traits they share with volant avialans, some of which have been proposed to indicate a secondary loss of aerial locomotion (Paul 1988; Olshevsky 1994; Czerkas et al. 2002; Paul 2002; Feduccia et al. 2015; Cau et al. 2015; but also consider Padian et al. 2005). Mesozoic pygostylians and pterosaurs, on the other hand, exhibit a degree of morphological adaptation that is only warranted by a lifestyle

dependent on the ability to fly freely (Zhou et al. 2001; Padian 1991). The mosaic of traits and often intermediate nature of *Archaeopteryx*' adaptations on the perceived morphological continuum between obligatory terrestrial archosaurs and flying birds has proven challenging to interpret.

Assessment of flight capability and reconstruction of flight mode in Mesozoic avialans in general and of *Archaeopteryx* in particular has been attempted through studying pectoral, furcular and sternal morphology (Olson 1979; Senter 2006; Baier et al. 2007; Close et al. 2012; Zheng et al. 2014; Foth et al. 2014), wing and wing element morphology (Vazquez 1992; Burgers et al. 1999), proportions (Wang et al. 2011; Wang et al. 2015) and biomechanical tolerance (Heptonstall 1970), feather morphology and arrangement (Speakman et al. 1994; Nudds et al. 2010; Wang et al. 2011; Carney et al. 2012; Longrich et al. 2012; Manning et al. 2013; Nudds 2014, Feo et al. 2015; Wang et al. 2015), inference of cognitive, vestibulary, and sensory specialization (Alonso et al. 2004; Balanoff et al. 2013; Benson et al. 2017), analog modeling (Meseguer et al. 2012; Evangelista et al. 2014a, 2014b) and digital modeling (Chatterjee et al. 2003; Longrich 2006; Allen et al. 2013; Carney 2016). Conclusions on the inferred aerial capabilities and flight mode of *Archaeopteryx* range from insignificant (e.g. limited control during pouncing or swooping; Garner et al. 1999) and primitive gliding (e.g. Senter 2006) to powered (free) flight (e.g. Carney 2016). Specific intermediate modes have also been proposed, such as running over water (Videler 2000, 2005; but also consider Ma et al. 2002), "flap-assisted gliding" or "flutter-gliding" (Long et al. 2003), obligatory wind-assisted flight (Thulborn 2003) and wing-in-ground effect flying (Easley 1999; Burgers et al. 1999; O'Farrell et al. 2002). The presence of pennaceous feathers preserved on the hind limbs in several specimens of *Archaeopteryx* (e.g. Foth et al. 2014) lends some support for a (reduced) tetrapteryx aerofoil distribution that may have aided its flight strategy (Longrich 2006). Theories involving morphological functions for the pectoral wing of *Archaeopteryx* or a closely related taxon other than producing aerial lift and/or thrust involve display (Xu et al. 2009), insect "netting" (Ostrom 1974, but later abandoned; Ostrom 1979), improved agility during cursorial locomotion (Caple et al. 1983; Peterson 1985), "stability flapping" during prey subduction (Fraser 2014), forming a wing "canopy" over shallow water to attract prey (Thulborn et al. 1985), and even wing-propelled diving (Jäger 1978; Ebel 1996).

Compared to modern birds, the capability of powered flight in *Archaeopteryx* is generally considered poor at best. Execution of the modern avian flight stroke involves an ossified, keeled sternum, humeral abduction over the dorsum, and a pectoral "pully" arrangement in which the tendon of the supracoracoideal muscle loops over the triosseal articulation between coracoid, scapula, and humerus, to allow for anchoring of the upstroke musculature to the sternal keel. All these conditions are lacking in *Archaeopteryx* (Zheng et al. 2014; Poore et al. 1997; Senter 2006; Olson et al. 1979; Mayr 2017; compare Fig. 6.8 and 6.9 in Wellnhofer 2008). The loss of the fourth trochanter on the femur does, however, reflect a forward shift of the center of balance (Wellnhofer 2008), which may indicate the presence of enlarged flight musculature. Several studies suggest that *Archaeopteryx* flew in a substantially different fashion than any modern bird (Wang et al. 2011; Close et al. 2012; Wang et al. 2015). The more primitive modes of controlled descent, such as parachuting, are not obligatory employed by present-day birds, which prevents a direct comparison with modern homologs. Gliding and soaring actually reflect relatively derived flight strategies in extant avians (Rayner 1999), whereas "burst"-flying represents the flight mode adopted by birds that fly rarely and/or poorly (Ruben 1991; Marden 1994; Dial 2003; Close et al. 2012). Specifically such a "burst"-flying strategy has been ascribed to *Archaeopteryx* by supposing a reptilian metabolic physiology (Ruben 1991: range of circa 20 m to 1.5 km; Easley 1999), whereas Marden (1994) arrived at a marginal powered take-off ability for *Archaeopteryx* by assuming the maximum (anaerobically generated) power available in avian muscle tissue. Later studies have found that the maximum relative anaerobic power output in the flight muscles of "burst"-flying quails can match that of reptilians for a very limited period of time to specifically permit a fleeing strategy where a short, vigorous flight is followed by a sustained running escape (Askew et al. 2001, 2002).

1.4.5 Chinese gliding paravians

Discoveries of spectacular Late Jurassic and Early Cretaceous Chinese paravians over the last decades have greatly improved our understanding of early dinosaurian flight (Chiappe et al. 2016). Notable taxa include the elaborately feathered but non-volant microraptorine genus *Caihong* (Hu et al. 2018) and possibly arboreal and gliding scansoriopterygids, of which *Yi* is interpreted to have employed a patagious membrane rather than feathered airfoils (Xu et al. 2015). China also yielded feathered gliding microraptorians that coupled conventional (anterior)

wings with hindwings to enable tetrapteryx gliding (Alexander et al. 2010; Dyke et al. 2013). Volant microraptorians may have predominantly glided between trees (Xu et al. 2003), as their hindlimb plumage would have hampered terrestrial locomotion (Alexander et al. 2010). Birds ultimately evolved from obligatory terrestrial bipeds and particular components of their flight apparatus appear to have arisen in a terrestrial context (Padian et al. 1998). This means that, for now, *Archaeopteryx* remains as the most suitable taxon for investigating the earliest modes of dinosaurian powered flight in relation to modern avian volancy.

1.4.6 Introduction to wing bone biomechanics

Avian wings constitute efficient, highly adjustable airfoils that are morphologically unique to birds (Pennyquick 2008). Biomechanically, the wing skeleton as a whole can be considered as a beam supported on one side (e.g. Cubo et al. 1998; Pennyquick 2008). Furthermore, wing elements themselves act as individual beams that are loaded according to their position in the wing, the nature and tolerance of the joints providing articulation with adjacent bones and associated tendons and tissues, and the magnitude and distribution of the wing load. This setup principally subjects the wing skeleton to bending and torsional forces (De Margerie et al. 2005; Pennyquick 2008). The geometry of a long bone in cross-section is influenced by evolutionary selection on the interplay between strength and weight (Currey et al. 1985; De Margerie 2005; Currey 2012) and the effects of biomechanical loading regimes on morphology and (micro-) structure experienced during life (Biewener et al. 1993; but also consider Meers 2002). In addition, this parameter is susceptible to the influence of phylogenetic heritage and physiological and metabolic demands (Cubo et al. 2008). Various correlations between avian flight mode and transverse wing element geometry have been described through parameters that quantify the (relative) amount and geometry of bone material present in (mid-diaphyseal) cross sections of long bones, mechanical parameters, collagen fiber orientation, and bone tissue arrangement (De Margerie et al. 2005; Habib et al. 2008; Simons et al. 2011). Although a biomechanical approach to studying wing bones of *Archaeopteryx* was pioneered by Heptonstall (1970), non-destructive imaging techniques (Tafforeau et al. 2006; Sanchez et al. 2012) now permit a more detailed reconstruction of the parameters involved.

In the study presented in Chapter 5, we reconstruct and describe the full cross-sectional geometry of *Archaeopteryx* wing bones (humerus and ulna sampled at circa mid-diaphysis; Fig. 1.4) and

compare this quantified information with homologous parameters in a variety of archosaurs, both from literature and through newly obtained data. We aim to test the application of both new and known relations between cross-sectional humeral and ulnar characters and locomotion in extant groups, taking into account body mass variation, in order to assess their relevance for studying potentially volant extinct archosaurs in general and for resolving the volancy of *Archaeopteryx* in particular.

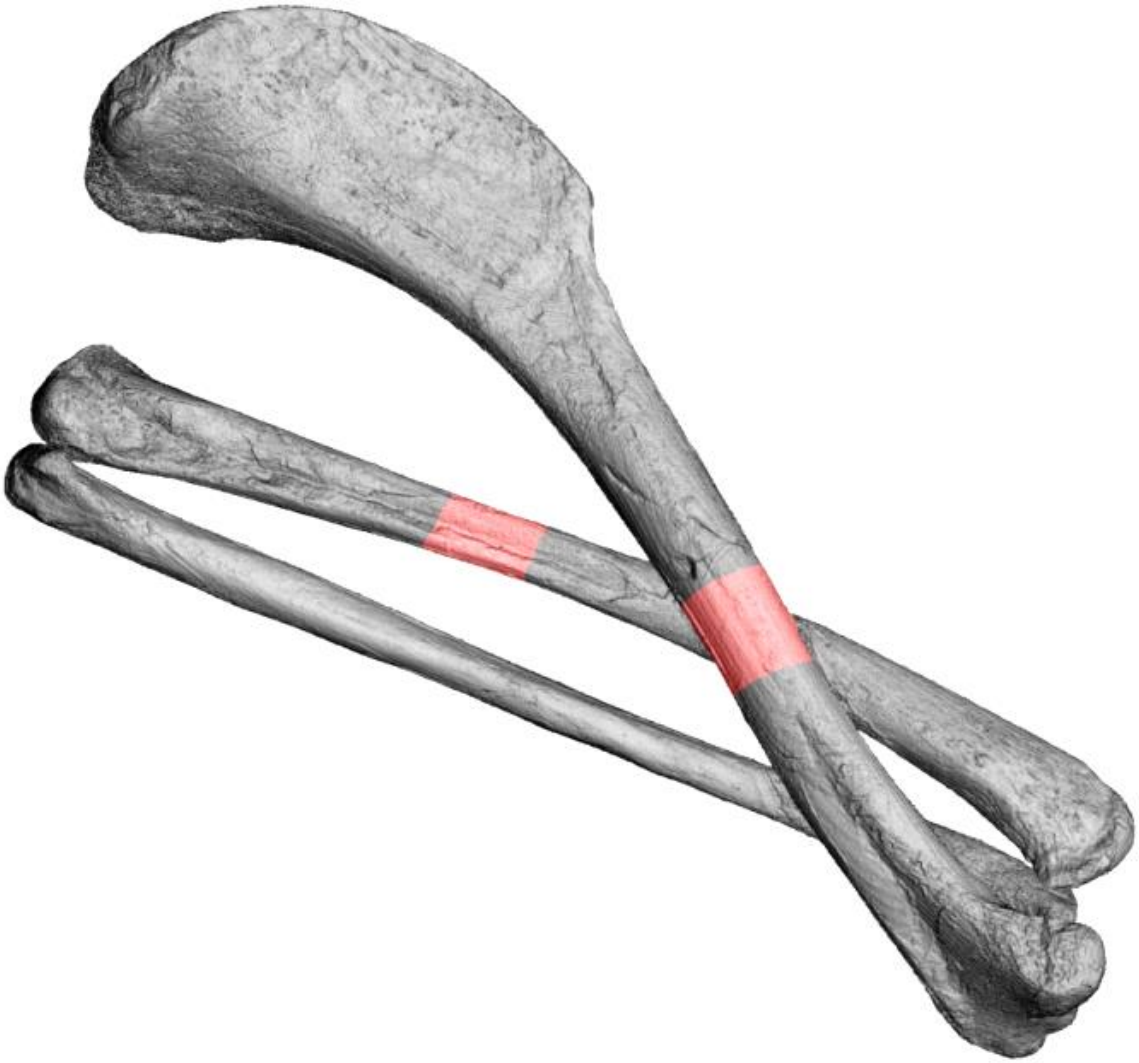

Figure 1.4 Surface rendering of humerus, ulna, and radius of *Archaeopteryx* (BMMS-BK1a; but consider Rauhut et al. 2018) with circa mid-diaphyseal virtual sample locations indicated in red.

Chapter 2: General discussion

2.1 Synchrotron microtomography of paleontological samples: challenges, solutions, and opportunities

2.1.1 The fossil-rock interface and fossils in large slabs

Computed tomography is an established and widely appreciated method for visualizing and studying paleontological material. However, particular properties of lithified fossil remains, especially those filled with or still encased in the host rock, make virtual extraction of their original geometry and reliable anatomical reconstructions far from straightforward.

Fossilization of the Mesozoic skeletal remains described in Chapters 4 and 5 occurred through petrification and involved both replacement and permineralization (Donovan 1991; Wellnhofer 2008). Replacement implies that original biogenic material is largely substituted by minerals precipitating out of solution from percolating groundwater while the biogenic matter dissolves or decays whereas permineralization involves deposition of minerals in pores and cavities (Donnovan 1991).

Sauropterygian body fossils from the Anisian Vossenveld Formation have conservatively preserved their three-dimensional geometry and exhibit a striking dark-brown color that sharply contrasts the light grey micritic limestones they are embedded in (Oosterink et al. 2003). Nevertheless, uncorrected tomographic data on this material showed a low initial contrast between cranial bones and sediment (see also Tafforeau et al. 2006). Furthermore, although skeletal material from the Vossenveld Formation is generally free of distortion by secondarily forming crystals (Oosterink et al. 2003), the occurrence of pyrite in close association with fossils (permineralization) and even complete replacement with pyrite are occasionally observed.

During the taphonomical history of *Archaeopteryx* body fossils, biogenic hydroxylapatite that originally made up the osseous mineral lattice was replaced with calcite (calcium carbonate: $CaCO_3$; Wellnhofer 2008). Furthermore, natural cavities within or around the skeleton, such as

the medullary cavity of long bones, accommodated the post-depositional formation of calcite crystals that now often line the interior of such voids (Wellnhofer 2008; see also Fig. 2.1-a). Since the surrounding limestone matrix consists of consolidated micritic and sparitic clasts of the same mineral (Barthel et al. 1990), the fossils and matrix are chemically (almost) indistinguishable and therefore share a very similar absorption signature when subjected to X-ray tomography (Tafforeau et al. 2006; Wellnhofer 2008). In reconstructed volumes, most recognized differences between skeletal elements and the surrounding matrix originate from the differential structure, porosity, and compactness (and therefore density) between fossil bone and limestone. Finally, tomographic reconstruction algorithms generally favor source data from samples with a broadly equidimensional geometry to ensure roughly homogenous X-ray absorption during data acquisition (e.g. Carlson et al. 2011; Sanchez et al. 2013; Fernandez 2013). The planar geometry of the often large yet thin limestone slabs that carry *Archaeopteryx* fossils (Wellnhofer 2008) induces substantial variation in the thickness of the sample in the path of the beam over half a revolution of the sample stage. The resulting strong attenuation in plate orientations aligning with the beam path leaves a weak recorded signal that may be close to the noise of the detector upon recording (Cau et al. 2017). This creates a number of missing angles that reconstruction algorithms cannot reliably correct and thereby represents a source of undesirable artifacts. A related phenomenon occurs at the same plate orientation in accumulation mode (see 2.1.3) in bones that slightly rise from the surface of the slab (Fig. 2.1-b). This non-linear effect arises from several sources, including beam hardening, phase contrast, local beam reflection on the surface, and diffusion of visible light in the scintillator. A complex interplay of these phenomena generates a perceived “overexposure” of elements protruding just above the plate in the reconstructed volumes, thereby violating the internal structural and compositional homogeneity such elements may be expected to exhibit (Chapter 5; Cau et al. 2017).

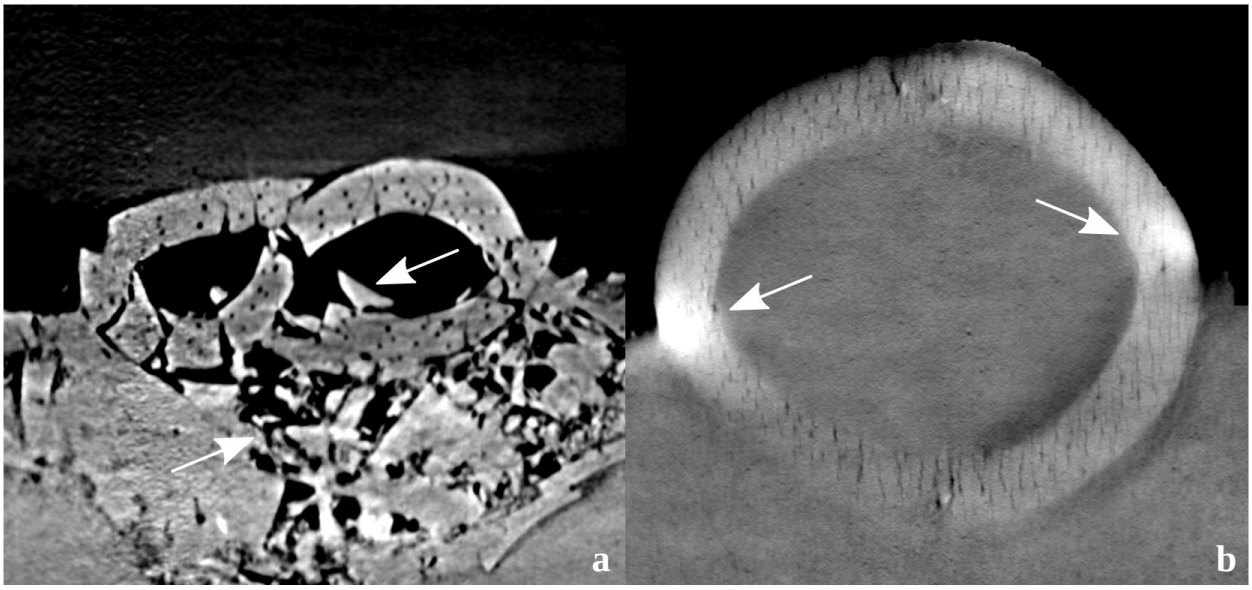

Figure 2.1 Virtual cross sections of *Archaeopteryx* wing bones. **a.** Left ulna of fifth specimen, arrows indicate secondarily formed calcite crystals in and around the osseous element. **b.** Right humerus of seventh specimen, arrows indicate the described non-linear effects occurring in cortical bone at the surface of the lithic slab. Elements not depicted to scale.

2.1.2 Visualization of a *Nothosaurus marchicus* cranium

Low contrast between skeletal fossils and sediment not only frustrates visual appreciation of targeted morphological details but also prevents automated region-based volume segmentation methods, such as region growing, from correctly identifying the medium of interest or adhering to the referred contrast throughout the considered volume. Tomographic data of *Nothosaurus marchicus* (Chapter 4) were gathered through propagation phase-contrast synchrotron radiation micro-computed tomography (PPC-SR μCT) with a propagation distance of 13 m to obtain optimal contrast in the reconstructed volumes but initially provided insufficient contrast still. Various solutions for automated contrast improvement of an entire image stack exist, for example through a designated MATLAB (MathWorks, Natick, USA) script or by employing a macro that sequentially applies a chosen succession of (proprietary) operations in graphical editing software (e.g. Adobe Photoshop, Adobe Systems, San Jose, USA) to the image stack. In the virtual tomographic data of *Nothosaurus marchicus*, a recoding of the original data set based on local texture complexity (see also Cau et al. 2017) sufficiently resolved low-contrast features

of interest to facilitate virtual extraction of the cranium (Fig. 2.2) and permit the description provided in Chapter 4.

Figure 2.2 Surface rendering of *Nothosaurus marchicus* cranium (TW480000375; Figure 1.2).

2.1.3 Visualization of *Archaeopteryx* elements

High-resolution imaging of fossils preserved in and on lithic slabs is a recognized challenge (Houssaye et al. 2011; Bonnin et al. 2014; see also 2.1.1). Homogenization of transmission through anisotropic samples with the attenuation protocol that incorporates additional physical components in the data acquisition setup (Carlson et al. 2011; Sanchez et al. 2013; Fernandez et al. 2013) provides improved data quality but is demanding and, in the case of delicate fossils, potentially damaging to the specimens studied (as discussed in Cau et al. 2017). A newly developed protocol, the accumulation mode, cannot match the ultimate contrast delivered by the attenuation protocol but does solve the problem of the weak recorded signal and prevents unnecessary manipulation of fossils (Cau et al. 2017). In accumulation mode, the intrinsic limitation of the detector's dynamic range is overcome by improved sampling of the X-ray signal through progressive summing of multiple images obtained during data acquisition into a single image (Chapter 5; Cau et al. 2017). The final images enjoy amplified contrast, which translates into improved contrast of the reconstructed volumes, but this approach also introduces "overexposed" artifacts along the surface of fossil-bearing slabs (Chapter 5; Cau et al. 2017; see also 2.1.1). Nevertheless, the accumulation mode is to be preferred over the attenuation protocol when the complex physical setup associated with the attenuation protocol could potentially inflict damage to the specimen (Chapter 5; Cau et al. 2017). Because the fifth and seventh specimen of *Archaeopteryx* reside in particularly large limestone slabs (Wellnhofer 2008), they could only be reliably imaged with PPC-SR μCT in accumulation mode for the purpose of the study presented in Chapter 5.

2.1.4 Additional solutions

PPC-SR μCT principally exploits phase shifts in an originally partially coherent synchrotron beam that occur during transmission through a heterogeneous sample. These phase shifts arise through refraction within the sample and, when recorded at multiple angles, inform on the location, extent, and nature of obscured phenomena within. The parallel geometry of a synchrotron beam enables placement of the detector at a considerable distance from the sample without invoking undesirable magnification effects or risking partial diversion of the signal beyond the detector and allows for the X-ray interference pattern containing detailed information

on the sample to develop and be recorded (Tafforeau et al. 2006). PPC-SR μCT produces three-dimensional data with phase-contrast-resolved edge detection superimposed on absorption contrast (Tafforeau et al. 2006). Phase-contrast edge detection at multiple propagation distances allows for a holotomographic approach towards quantifying the properties of the media within the sample themselves rather than merely their refractive relations (e.g. Pradel et al. 2009) but requires intervention in the setup during the experiment. At the ESRF, the complex associated setup and demanding data processing has led to a departure from holotomography in favor of single-distance phase retrieval solutions for imaging fossils. Quantitative reconstruction of phase-contrast data obtained at a single propagation distance is challenging (Häggmark et al. 2017), but can be achieved through a phase-retrieval protocol based on assumption of homogeneity, for example with a (modified; Sanchez et al. 2012) version of the algorithm developed by Paganin et al. (2002). The central phase-retrieval parameter is the delta/beta ratio that assumes and describes a linear relationship between the refractive index decrement (δ; delta) and the absorption index (β; beta) for particular materials (Hesse et al. 2014) to be applied accordingly during phase retrieval. Although adoption of the optimal delta/beta ratio during reconstruction ensures the appropriately homogenous assignment of suitable grey values truthfully reflecting properties inherent to the media present in the sample, particular small details within these media (relative to data resolution) may be blurred as well. It was found that heuristic manual adjustment of the delta/beta ratio before phase retrieval to values considered too low for appropriately characterizing the observed media may in particular cases provide improved resolution of such features. Although this approach can inform on particular aspects that may be poorly resolvable with conventional delta/beta assignments, the data set as a whole typically exhibits over-emphasized edge contrast and thereby often becomes unsuitable for region-based automatic segmentation solutions.

In tomographic data, artifactual grey-level anomalies may be present as low-frequency gradients within a medium with an assumed homogenous composition (Cau et al. 2017). Such gradients misrepresent the true nature of the medium under consideration and frustrate segmentation and rendering efforts. However, application of an appropriately configured selective high-pass filter can sufficiently correct for these artifacts (Cau et al. 2017). Notably, the contrast in the data on the seventh specimen of *Archaeopteryx* used in the study described in Chapter 5 (see also 2.1.1

and 2.1.3) was substantially improved following a similar approach involving a median and a blurring filter.

Inclusions of metallic oxides are often saturated in tomographic imagery adjusted for optimal contrast (Vidal et al. 2005) between fossil bone and sediment (Cau et al. 2017). These artifacts commonly invade the surrounding material, thereby potentially obscuring phenomena of interest. Grey values representing the considered artifacts may be normalized with respect to the fossil bone and sediment to enable proper contrast adjustment during data assessment (Cau et al. 2017). Furthermore, application of a selective high-pass filter can also reduce the dominant expression of metallic inclusions in the data set (Cau et al. 2017).

2.1.5. Forensic paleontology

Extinct life speaks to the imagination of many, and especially articulated remains of iconic vertebrates are popular among paleontological researchers and non-academic enthusiasts alike. This often instills a substantial inherent value to such material, which has provided a stimulus for the forgery of paleontological specimens throughout human history (Corbacho et al. 2012). Today, particularly the "low-income countries" with a rich fossil heritage, such as China and Morocco, are known to produce relatively high-quality forged fossils (Milner et al. 2001; Mateus et al. 2008; Stone 2010) since the time-consuming manufacture of convincing forgeries represents a lucrative source of income. Such fraudulent fossils may deceive and misinform those wishing to study novel material. Although all material studied and described herein proved genuine, tomographic imaging techniques provide unique and particularly appropriate tools for evaluating the integrity of fossils (Rowe et al. 2001; Rowe et al. 2015; Cau et al. 2017).

Counterfeit fossil material can be either completely fabricated or partially modified, which includes both excessive and chimeric restoration. The internal structure of completely manufactured material will strikingly disagree with that of authentic reference specimens. In sufficiently resolved tomographic data, the lack of osseous microstructures and well-understood microanatomical details can offer clear evidence to that effect. In partially restored or "improved" fossils, genuine elements or parts thereof are distinguishable from manipulated regions through similar indicators (e.g. Cau et al. 2017). Although the surface of such samples may appear homogenous and continuous, insight into their internal composition can demonstrate

the presence of allochthonous substances such as glue, filler, (metallic) reinforcements, or either arranged or ground up fragments of locally sourced rock. Arrangement of originally separate fragments may be revealed through the inconsistent or non-continuous expression of host-rock geological properties, which include bed thickness, sedimentary structure, and structural or tectonic deformation. Laminated fossiliferous layers often split through a fossil, which results in two largely mirrored slabs. Unilaterally lacking elements are sometimes supplemented using the counter slab of preserved elements to achieve a more "complete" specimen (e.g. Rowe et al. 2016). Chimeric composites may be more difficult to recognize as such, since they are created out of individual (although often fragmentary) fossil specimens that are genuine in their own right. Although most aforementioned indicators for doctoring should be evaluated, the confident recognition of a chimera could require additional lines of evidence. A closer tomographic study of the presented biological anatomy focusing on the internal consistency of morphological conditions indicative for phylogeny, ontogeny, gender, and provenance should bring to light any irregularities that may not be evident at first glance (e.g. Cau et al. 2017).

Finally, in particular cases the virtual nature of tomographic data sets offers several opportunities for reconstructing material that may have been lost during discovery, preparation, or damage. Fossils recovered from the lithographic limestones in Solnhofen are often preserved on two slabs, with the "main slab" typically composed of the layer that formed around the remains during burial, and the "counter slab" representing the seabed on which the body came to rest before burial (Barthel et al. 1990; Wellnhofer 2008). When tomographic data on both corresponding slabs are available, virtual retrofitting of the two volumes will reveal all sediment and fossil material that was lost from the original fossilized assembly before discovery, during recovery, preparation, or manipulation (such as casting), or as a result of other damaging practices. The superficial morphology of fragments not preserved on either of the slabs but represented by a sufficiently well-preserved natural mold can be virtually reconstructed and subsequently studied or provide a reference for restoration of the considered element.

2.2 New implications for early sauropterygian physiology and ecomorphology in the context of Triassic biotic recovery

2.2.1 A refined paleoecology for *Nothosaurus marchicus*

In the study presented in Chapter 4, we identified numerous adaptations in the cranium of *Nothosaurus marchicus* that increase our understanding of the physiology of this taxon. The endocast that originally accommodated the brain (e.g. Witmer et al. 2008) exhibits a remarkably straight and thereby somewhat tubular geometry indicating that the ancestral braincase architecture had already adapted to allow for the development of large temporal musculature to ensure rapid and powerful mandibular closure. The large pineal foramen continues ventrally into a broad connection with the braincase endocast and indicates the presence of a well-developed pineal complex during life. Although functional interpretation of this condition is challenging, we explore several possible explanations pertaining to thermoregulatory strategies. Through independently sourced paleogeographical data (Rieppel 2000) and paleotemperature proxies (Korte et al. 2005), we were able to infer a probable ectothermic metabolic regime for *Nothosaurus*, which contrasts elevated metabolic rates proposed for more crownward sauropterygians (Krahl et al. 2013; Wintrich et al. 2017). Since the main olfactory system, aimed at perceiving and evaluating aerial cues, does not function in aquatic environments (Schwenk 2008), and osseous indicators for chemosensory organs aimed at resolving fluid-stage stimuli were found to be unpaired and reduced, we concluded that the olfactory system as a whole did not substantially contribute to spatial awareness. In addition, the virtually unpaired vomeronasal morphology did not allow for tropotaxis (i.e. foraging guided by gradient evaluation through bilaterally paired receptors sensitive to, in this example, chemical stimuli). Anatomical indications for acoustic senses are absent or underdeveloped. Large, predominantly dorsally oriented orbits and potentially resolved optic lobes on the endocast do suggest substantial visual acuity, although the intracranial configuration also appears to only have allowed for relatively marginal ocular mobility. A mechanoreceptive intrarostral plexus contributed to proximal and tactile sensing (e.g. Barker et al. 2017). We identified the intracranial voids that accommodated the lateral nasal glands, which we interpret to have served as salt glands in *Nothosaurus*.

Nothosaurus marchicus exhibits a cranial morphology that incorporates a specialized, needle-like and anteriorly recurved dentition forming a "trapping basket" (1.3.4; Rieppel 2002; Shang 2007). Furthermore, Chinese ichnofossils of nothosaurian affinity (Nothosauridae; Zhang et al. 2014: either *Nothosaurus* or *Lariosaurus*; Rieppel 2000) have revealed sea floor foraging for nothosaurs (Zhang et al. 2014). These insights allowed us to reconstruct the paleoecological niche for *Nothosaurus marchicus* as a shallow marine piscivorous visual ambush predator with a life position near the seabed.

2.2.2 Mosaic developmental heterochrony in sauropterygian cranial evolution

Heterochrony has been described as "the evolution of ontogeny" (Mabee 1991) and describes various modes of differential developmental pacing that result in delayed or advanced expression of certain physical traits (Gould 1977). Important to our case is the distinction between paedomorphosis, expressed in traits appearing ontogenetically younger than homologous conditions of an ancestral taxon, and peramorphosis, which describes a more mature expression of a trait relative to its ancestral condition; both at the same ontogenetic stage. Although the studied cranium of *Nothosaurus marchicus* superficially appears adult through the well-ossified cranial sutures, we found that important elements contributing to the endosseous labyrinth had not (yet) ossified. Notably, postcranial paedomorphosis is widely recognized in Mesozoic marine reptiles (e.g. Lehman 1959) but cranial paedomorphosis has only received limited attention. Cranial paedomorphosis has furthermore been observed in other nothosaurs, but also in plesiosaurs (Chapter 4 and references therein). Such a paedomorphic development is sharply contrasted by the large and massively developed eosauropterygian pterygoid, which may represent a peramorphic development (Chapter 4).

Although the identification of a mosaic of heterochronic traits in the skull of *Nothosaurus* may aid in the recognition of developmental pathways governing the establishment of sauropterygian cranial adaptations, it also has important implications for phylogenetic studies. Alpha taxonomy of non-plesiosaurian Sauropterygia in general and for *Nothosaurus* in particular largely relies on cranial characters, for which complete ossification of the cranial roof is often considered indicative of the adult condition (Rieppel 2000). Our study suggests that variable heterochrony may explain disparate observations traditionally considered phylogenetically informative as

ontogenetic in origin rather than truly taxonomical, and warrants caution when identifying a cranium as mature based on scarce developmental indicators.

2.2.3 *Nothosaurus* and Triassic biotic recovery

The Permian-Triassic mass extinction accounted for the demise of countless taxa but the ecological void that remained also opened the door for other groups that would ultimately grow to dominate Mesozoic ecosystems. Sauropterygia is a poster child for successful environmental colonization, as it is completely unknown from Paleozoic deposits (Rieppel 2000) but made a spectacular and lasting entry during the Early Triassic. The earliest broadly sampled Triassic shallow marine deposits in continental Europe and China, dating to circa five million years after the mass extinction, already yield a large diversity of representatives (Rieppel 2000; see 1.3.1 and 1.3.2). This indicates that Sauropterygia achieved dominance in most of the higher trophic niches in circum-Tethyan shallow marine environments within five million years after its first recognized occurrence.

Nothosaurus marchicus (see also 1.3.4) is the oldest recognized member of its genus, as corroborated by its suite of plesiomorphic characters (Albers et al. 2003; Albers et al. 2011). Our study has revealed that *Nothosaurus marchicus* did not adhere to a generalized opportunistic ecology but exhibits particular adaptations beyond those relating to its secondarily marine lifestyle. Its cranial anatomy is niche-adapted and the diversity of broadly similar yet phylogenetically disparate sympatric taxa in the Vossenveld Formation (e.g. Oosterink et al. 2003; Klein et al. 2009; Sander et al. 2014; Voeten et al. 2015; Klein et al. 2016) suggests that a rich trophic hierarchy was already established. This may indicate that the ecosystem had reached carrying capacity (Monte-Luna et al. 2004), which would imply that a well-developed and stable ecological web in shallow marine habitats was already achieved by then. In light of the post-Permian-Triassic recovery, recognition of established niche heterogeneity in an early sauropterygian ecosystem (Rieppel et al. 1996; Oosterink et al. 2003; Rieppel 2000) provides strong supportive evidence that post-extinction recovery following the Permian-Triassic event had indeed proceeded rapidly (Scheyer et al. 2014), at least in circum-Tethyan shallow marine environments.

2.3 The flight of *Archaeopteryx* and early bird-line volancy

2.3.1 Overview and context of novel insights

Avian aerial locomotion relies on various morphological attributes unique in the modern animal kingdom. Feathered flight, that is volancy achieved through highly modified limbs featuring asymmetrical flight feathers, exploits a wide range of flight kinematics and aerodynamic opportunities (e.g. Longrich et al. 2012) that probably determined the evolutionary success of birds (e.g. Sanz et al. 2002). It is now increasingly clear that many of the adaptations underlying avian aerial dexterity arose in non-avian dinosaurs for purposes unrelated to flight but were subsequently exapted towards enabling or improving the dinosaurian conquest of the aerial realm (Gould et al. 1982; Beyrand et al. submitted). Because exaptation implies that certain characters were already present before the novel application of focus was adopted, the presence of such characters alone does not conclusively resolve their function.

In the study discussed in Chapter 5, we found that particular conditions resolvable from two-dimensional circa mid-diaphyseal cross-sections virtually extracted from the humerus and ulna of three *Archaeopteryx* specimens recorded the influence of active volancy. These involve the remarkably avian-like thin bone cortices uniquely present in volant archosaurs (see also Cubo et al. 2000) and the low relative torsional resistance that characterizes the wing bones of modern flying birds employing flapping flight (Simons et al. 2011). Notably, evaluation of additional parameters in the wing bones of modern birds has also demonstrated that particular adaptations not or unreliably resolvable in tomographic data propose additional refined responses to torsional forces (De Margerie et al. 2005), which will require further investigation. We also demonstrated that earlier research likely underestimated the metabolic performance of *Archaeopteryx* and thereby provide contextual arguments consistent with a physiology that facilitated the elevated energetic regime typically associated with active volancy (Chapter 5; see also Pouech 2008). Our study is unique in that other reports evaluating the volancy of *Archaeopteryx* usually present aspects explained to demonstrate whether or not a certain physiological aspect could have allowed for particular locomotory strategies in this taxon (see Elzanowski 2002 and Wellnhofer 2008 for reviews). We report that the newly presented parameters witnessed load adaptation to flight rather than potentially permitted volancy, and are most consistent with active flight.

Where well-understood passively gliding limbed amniotes, such as the flying lizard *Draco* and flying squirrels, converged exclusively on the application of membranous patagia along the lateral body line as gliding surfaces, the actively movable anterior limbs of winged maniraptorans inherently provide power for and control over airfoil mobility. Furthermore, feathered (or incidentally partially patagial; Xu et al. 2015) four-winged avialans interpreted to have potentially adopted gliding modes of aerial locomotion (i.e. Scansoriopterygidae and Microraptoria; see 2.3.2) exhibit wing planforms with combined low aspect ratios relative to the airfoils of *Archaeopteryx* and modern flying birds. Although the anterior wings of *Microraptor* exhibit an "avian" aspect ratio of 7.4 (calculated as wingspan^2/planform area), its reconstructed complete tetrapteryx aspect ratio of 3.7 is much closer to those of other gliding animals (Alexander et al. 2010) than to those of avialan powered flyers with a strong bias on the anterior winged limbs. *Archaeopteryx* exhibits a wing aspect ratio of circa 7 (Yalden 1971) and falls well within the range of modern birds (contextualized by Fowler et al. 2011). The fundamentally tetrapteryx wing configuration of dinosaurs with envisioned gliding locomotion inherently moves the lifting surfaces closer to the center of mass, as in modern amniote gliding configurations, and may even have adversely affected the functional range of motion of a hypothetical propulsive anterior wing through interference with the posterior wing. In light of the adaptations resolved from archaeopterygian wing bone geometry, such observations support the conclusion that *Archaeopteryx* employed an active mode of feathered flight (Norberg 1990; Chapter 5). This outcome renders *Archaeopteryx* the oldest presently known dinosaur to have advanced beyond passive forms of aerial locomotion and implies that dinosaurian powered flight originated before the Solnhofen Limestone was deposited in the Late Jurassic (Chapter 5). In order to appreciate the implications of our findings, it is important to understand the context in which they are to be placed.

2.3.2 The evolution of feathers, and *Archaeopteryx* as a feathered flyer

Studies into the functional origin of feathers, excluding flight as a satisfactory explanation (see 1.4.3), focus on their role in thermal insulation and in display (Sumida et al. 2000). Both purposes have been proposed to explain the presence of plumage in non-volant dinosaurs (e.g. Van der Reest et al. 2016; Ruxton et al. 2017). An important implication of the hypothesis presenting plumage as primarily an insulation agent is that it suggests an endothermic

metabolism or even homeothermia for feathered non-avian dinosaurs, although such conclusions must be considered with care (Ruben 2000; Xu et al. 2009a). Furthermore, insulation agents are most effective when they occur in a continuous coat or dense pelt rather than as the isolated patches or integumentary elements that some dinosaurs exhibit (Xu et al. 2009b). *Archaeopteryx* appears to have featured a continuous body plumage (Foth et al. 2014) intuitively consistent with the thermal insulation demand of an endothermic organism (Elzanowski 2002), with substantial cortical vascularization (Chapter 5) and indications for an avian-like breathing apparatus (Christiansen et al. 2000, but also consider Elzanowski 2002) supporting such a speculation. Although the hypothesis that some non-avian dinosaurs enjoyed insulating plumage may provide tentative insight into the corresponding metabolic regime, it does not inform on the poorly understood origin of feathers itself, as such a function may represent an exaptation in its own right (Persons et al. 2015).

An original display function has been specifically attributed to pennate feathers (e.g. Foth et al. 2014), partially through the recognition that their planar geometry in non-avian dinosaurs provided a suitable canvas for exhibiting the morphological patterns and coloration that modern birds involve in communication, for example during courtship (Li et al. 2010; Koschowitz et al. 2014; Li et al. 2014; Petaya et al. 2017; Hu et al. 2018). Pennaceous feathers precede inferred volancy in the dinosaurian fossil record (Clarke 2013). Bilaterally asymmetrical remiges associated with an aerodynamic function (Feo et al. 2015) may have originated at least two times independently within Paraves, importantly uncoupling the advent of (gliding) volancy in *Microraptor* (Xu et al. 2003) from (active) volancy in the more inclusive avialan clade (Senter et al. 2012; Foth. 2014; Cau et al. 2017: Appendix I, Fig. 1.3). The inferred scansorial and arboreal scansoriopterygids that exhibit morphologies consistent with gliding locomotion (Zhang et al. 2002) were recently recovered within the most inclusive clade containing both *Archaeopteryx* and Aves (Cau et al. 2017), although no conclusive consensus has been reached (consider e.g. Lefèvre et al. 2014; Lefèvre et al. 2017). Nevertheless, *Archaeopteryx* and active volancy now appear to reside at the root of a continuous volant avialan lineage morphofunctionally culminating in modern avian flight. The phylogenetic and temporal decoupling of paravian gliding and avialan active flight also implies that paravian passive gliding does not necessarily represent the functional precursor of avialan active volancy, as suggested by some (e.g. Benson et al. 2012). Avialan volancy may have evolved in a cursorial ancestor through exaptation of

terrestrial aerodynamic functions (e.g. Peterson 1985) to aid in escape, foraging, or predatory behavior. Finally, if the elaborate pennaceous plumage of Pennaraptora is interpreted to reflect a strong selection on display, and aerodynamic plumage arose multiple times in the group, then avialan active volancy itself may be hypothesized to have arisen as an active expression of display. Nevertheless, like proposed explanations for the origin of plumage itself, such inferences must remain to be considered speculative for now.

2.3.3 A cursorial *Archaeopteryx* and its significance for the origin of dinosaurian active flight

Birds are mainly associated with their capacity of flight, yet most of them are also very capable terrestrial bipeds (Lee et al. 1997, Casinos et al. 2001); a trait that reflects their origins in obligate ground-living cursorial dinosaurs (e.g. Qiang et al. 1998). Besides possessing feathers, birds are also unique in combining two well-developed locomotory strategies through three uncoupled locomotory modules (wing module, hind limb module, and tail module; Gatesy et al. 1997; Hunter 1998). *Archaeopteryx* has been argued to represent the first recognized theropod exhibiting the three distinct locomotory modules also characterizing modern birds (Gatesy 2002).

Some argue that birds should primarily be considered as terrestrial or land-dwelling animals (e.g. Urf 2004), as the majority of avian species have adaptations clearly reflecting their intimate dependence on the terrestrial realm (Remsen et al. 1990). In fact, most members of two of the most basal groups of true birds (sensu Gauthier et al. 2001), Palaeognatae and galliform Galloanserae (Prum et al. 2015), are habitually terrestrial and are non-volant or only fly occasionally. Multiple adaptations in the skeletal morphology and body posture of *Archaeopteryx* (Wellnhofer 2008) reflect its terrestrial affinity (Ruben 1991) and provide “a remarkable congruence of evidence” for a paleoecological role as a “ground forager in open spaces” (Elzanowski 2002). Notably, this latter interpretation was also expanded to conclusively include escape climbing, as Elzanowski considers *Archaeopteryx* incapable of ground take-off (Elzanowski 2002; but also consider Burgers et al. 1999). However, the proportionally long neck and limbs of *Archaeopteryx* contradict an arboreal lifestyle (Peterson 1985). An independent study across a comprehensive set of morphological characters significantly retrieved *Archaeopteryx* within the cluster of extant terrestrial mammals and ground-based birds (Dececchi et al. 2012).

The proportions within the leg of *Archaeopteryx* exhibit good agreement with those of the escape running and incidentally flying Galliformes and Tinamiformes (Balda et al. 1985; Elzanowski 2000). The wing aspect ratio of *Archaeopteryx* is also remarkably close to those of birds foraging in open spaces (Shipman 1999) and agrees with those of escape flyers (Van den Hout 2009); a niche shared with, for example, modern-day pheasants. *Archaeopteryx*, as a volant yet predominantly ambling or cursorial forager, presents the oldest known dinosaurian taxon to occupy this ecological niche shared with most basal Neornithes, as scansoriopterygids (but also the younger microraptorines) are often considered scansorial and arboreal rather than terrestrial (Zhang et al. 2002; Sullivan et al. 2012; but also consider Dececchi et al. 2016).

Circumstantial evidence on the habitat of *Archaeopteryx* reconstructed from remains of terrestrial flora that accompany its fossils in the same deposits (Barthel et al. 1990) proposes that *Archaeopteryx* inhabited a landscape that notably lacked a particular abundance of large trees but may have resembled modern-day open shrubland. Volant paleognaths (i.e. tinamous) and galliforms inhabiting such habitats exclusively employ a "short flight" strategy in which short yet broad wings used in energetic bursts allow for brief aerial excursions followed by a running escape (Viscor et al. 1987). Despite the substantially more advanced flight apparatus of even the most primitive volant Neornithes (see 2.3.4; consider also Wellnhofer 2008), the broadly similar general morphology and proportions of the wings and hind limbs in *Archaeopteryx* used in partially open shrubland do suggest corresponding ecological niches and lifestyles. The influence of an associated "short flight" mode has now also been recovered from the cross-sectional geometry of the humerus and ulna of *Archaeopteryx* (Chapter 5) and adds to the growing body of indications for incidental yet active volancy in this taxon. Besides escape flight, occasional bouts of vigorous aerial locomotion may also have aided in crossing barriers or ambush predation.

The establishment of active volancy in *Archaeopteryx* does not satisfactorily resolve the question whether the first dinosaur to have developed aerial locomotion was a passive glider or an active flyer. As discussed, the apparently independent achievement of various modes of aerial locomotion recognized in multiple Paravian groups (Appendix I, Fig. 1.3) may be explained by multiple truly independent origins of "experimental" dinosaurian volancy. However, the relatively broad phylogenetic distribution of winged dinosaurs may also reflect an origin in a yet unidentified single shared ancestral volant form at the root of Paraves that gave rise to a lineage

in which a secondary return to non-volant lifestyles occurred multiple times (e.g. Chatterjee 2015 and references therein; see also 1.4.4). Such a hypothesis theoretically leaves open the consideration of a conceptual ancestral "*Tetrapteryx*" (see Wellnhofer 2008 for review), which would represent a gliding form ancestral to dinosaurian powered volancy that phylogenetically resides deeper than presently recognized volant dinosaurs (but also consider Caple et al. 1983). Nevertheless, this concept is regarded controversial and not supported by the present phylogenetic solution for Paraves (Appendix I, Fig. 1.3).

Scansoriopterygidae, of uncertain locomotory affinity but potentially gliding, now resides within the group rooted in the common ancestor of *Archaeopteryx* and modern birds, which is incompatible with the older age of the scansoriopterygian material in the fossil record relative to *Archaeopteryx* (Zhang et al. 2008; Chiappe et al. 2016). Phylogenetic uncertainty regarding Scansoriopterygidae (see 1.4.2 and 2.3.2) complicates unambiguous inferences on the significance of its potentially gliding ecology for reconstructing the avialan precursors of avian flight. Alternative phylogenies (e.g. Lefèvre et al. 2017) placed Scansoriopterygidae at the root of Paraves, which sharply disagrees with the updated phylogeny (Cau et al. 2017: Appendix I, Fig. 1.3) and would render their potential volancy an independent third chapter of dinosaurian flight. The Late Cretaceous flightless genus *Balaur* is presently nested crownward from both *Archaeopteryx* and Scansoriopterygidae (Cau et al. 2017), which implies it may have been secondarily flightless (Cau et al. 2015). This would be reinforced by the probable active volancy of *Rahonavis* with *Archaeopteryx*-like terrestrial adaptations in the pelvis and posterior limb (Forster et al. 1998; Chiappe 2007) recovered more primitive than *Balaur* but crownward from *Archaeopteryx* (Cau et al. 2017), thereby further confusing the recognition of shared locomotory affinities at the root of avialan volancy. Until the phylogenetic models for Paraves converge, parsimony dictates that the capacity of active, forewing-powered flight is the primitive condition for the more inclusive yet now revised group previously referred to as Aves (Avialiae between *Archaeopteryx* and *Passer domesticus*) that often remains colloquially referred to as such.

2.3.4 An illustrated hypothesis for the flight of *Archaeopteryx*

Irrespective of the newly recognized expressions of active flight in *Archaeopteryx*, the modern avian flight stroke is achieved through several pectoral adaptations that, based on presently available material, had not yet evolved in the Late Jurassic (see 1.4.4; Chapter 5). The lack of

such adaptations in *Archaeopteryx* (compare Fig. 6.8 and 6.9 in Wellnhofer 2008) would have prevented it from achieving ample supradorsal humeral abduction. It also lacked converged up- and downstroke musculature on a keeled sternum through which the modern avian flight apparatus alternates the power stroke with a sufficiently vigorous recovery stroke (Chapter 5). The angle between the scapula and coracoid is acute in modern volant birds but obtuse in non-volant ratites (circa 160°) and pennaraptorans (Carpenter 2005). Since the pectoral girdle of *Archaeopteryx* was not firmly connected to the axial skeleton through conservative osseous articulations (Jenkins 1993), the exact orientation and range of motion of the pectoral girdle during life remain incompletely understood (but also consider Carney 2016; Rauhut et al. 2018). However, the relation between scapula and coracoid presented by some specimens proposes an angle of 100-110° (Rauhut et al. 2018) that approaches but not lies within the range of this spatial relation in modern birds. Nevertheless, various studies have proposed that *Archaeopteryx* was capable of volancy in a fashion differing substantially from that of modern birds (e.g. Longrich et al. 2012; Close et al. 2012). For future consideration, I here propose a conceptual model for the flight of *Archaeopteryx* respecting its intermediate pectoral morphology between those of non-volant maniraptorans and volant avialans (Ostrom 1976; Gishlick 2001).

The pectoral girdle of *Archaeopteryx* includes large coracoids (Wellnhofer 2008; Mayr 2017; Rauhut et al. 2018) and a robust, flattened, and broadly braced furcula that lacks or exhibits only incipient hypocleidial communication with the sternum (Wellnhofer 2008; Rauhut et al. 2018). The generalized pectoral reconstruction provided by Wellnhofer (2008; but also consider the note on the scapulocoracoidal angle by Rauhut et al. 2018) exhibits posterior rotation of the shoulder girdle relative to the primitive maniraptoran condition. This positioned the furcula more dorsally (more dorsally even than in the reconstruction by Wellnhofer; Rauhut et al. 2018) and elevated the passage for the *Musculus pectoralis profundus* relative to the glenoid. Action of the *M. pectoralis profundus*, assisted by the *coracobrachialis-deltoideus* muscle complex originating from anterodorsal aspects of (respectively) the coracoid and scapula, permitted an anterodorsally oriented humeral excursion through combined protraction and abduction. Supported by the robust furcula, this morphological analog to the posterodorsally oriented upstroke of modern birds may have permitted an anterodorsally-posteroventrally oriented flight stroke cycle that was morphologically closer to the "grabbing" motion of obligatory terrestrial maniraptorans (Gishlick 2001; Senter 2006) with humeral abduction not substantially extending over the dorsum. In this

model (see Figs. 2.3 and 2.4), an anteriorly directed upstroke generating lift through anterior acceleration of the wing airfoil alternates with a posteriorly oriented downstroke of the ventrally tilted wing generating lift and thrust in the direction of travel.

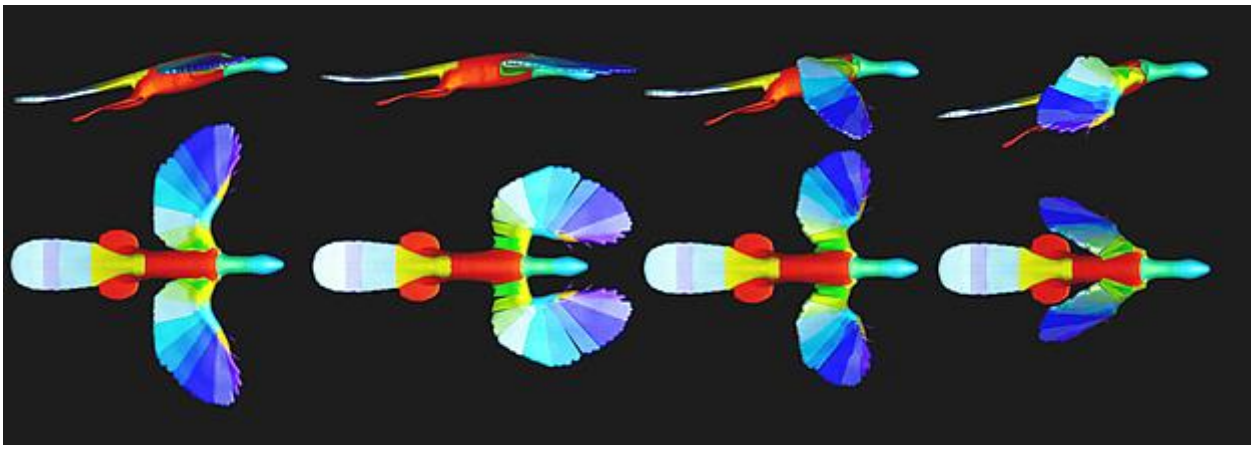

Figure 2.3 Schematic visualization of the conceptual flight model for *Archaeopteryx*.

Recovering from maximum downstroke, the *M. pectoralis profundus* that effectuates the supracoracoideal pully of modern birds would have accomplished combined anterodorsal protraction and abduction, which is intermediate between its homologous action in non-avian maniraptorans and in modern birds (Mayr 2017). Musculature originating from the thoracic and/or gastral baskets (Zheng et al. 2014; Chiappe et al. 2016) would have enabled a posteroventral "downstroke" through initial internal humeral rotation resulting in a downward tilt of the leading wing edge, followed by powerful humeral retraction and abduction through flight musculature originating from the lateral and ventral trunk. This down- and rearwards stroke generates lift and thrust in the direction of travel. External humeral rotation reinstated the airfoil and braced the wing for the successive upstroke.

In my model, the *M. pectoralis profundus* contributes to an aerodynamically active upstroke, morphologically intermediate between maniraptoran grasping and the modern avian upstroke, for which the main muscle mass is located largely anterior to the shoulder girdle. Flight musculature responsible for the propulsive downstroke originated ventral and posterior to the glenoid. Crucially, spatial separation of up- and downstroke myology into discrete furculocoracoidal and ventral thoracoabdominal domains, respectively, elevates the requirement for extensive sternal

ossification, as this musculature does not converge on the sternum. In addition, plumage on the pelvic limb (Longrich et al. 2006; Foth et al. 2014) and particularly on the tail (Peters et al. 1985; Foth et al. 2014) could have provided additional lift and promoted longitudinal stability (Gatesy et al. 1996). Although both up- and downstroke of the winged limbs contribute to generating lift, a running start was likely required to achieve take-off velocity (see Burgers et al. 1999). Selective pressure towards static take-off may have contributed to the development of the dorsoventral wing stroke cycle on the lineage towards modern birds where the origins of both up- and downstroke musculature converged in the anteroventral thoracic domain and gave rise to a pronounced sternal keel. *Archaeopteryx* required a running start to take wing and the proposed mode of active lift and thrust generation only appear to support the brief and energetically demanding aerial excursions of present-day short-range flyers rather than sustained flight.

My hypothetical and qualitative flight model aims to illustrate that reconstructions of the volancy of *Archaeopteryx* need not restrict themselves to identifying the agreements or differences that exist between the modern flight apparatus and those of extinct avialans for the sole purpose of investigating whether or not the modern avian flight stroke was permitted in *Archaeopteryx*. It is clear that it was not, although this does not necessarily preclude the capacity of active flight through alternative configurations. In that light, more analog and digital modeling of reliable reconstructions (e.g. those suggested by Carney 2016) may provide sufficient leads for resolving the fashion in which *Archaeopteryx* achieved active flight, which in turn will provide additional insight into the very origins of the advanced volancy that fueled the dynasty of more derived volant avialans and, ultimately, modern birds.

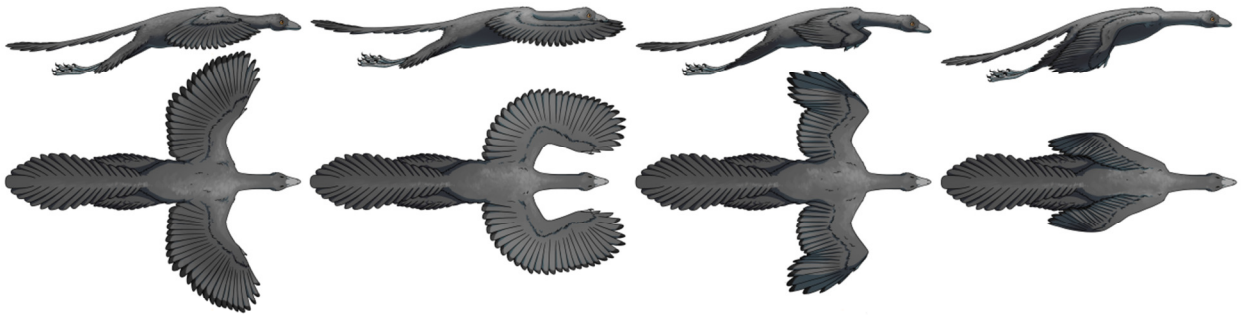

Figure 2.4 Artist's rendering of the conceptual flight model for *Archaeopteryx* (credit: Jana Růžičková).

Chapter 3: General conclusion and outlook

The work presented in this thesis revolves around two core topics. Firstly, it describes the present state of synchrotron tomographic techniques and evaluates their benefits and pitfalls towards paleontological investigations. Secondly, novel research on unique ecological adaptations in two different clades of Mesozoic diapsids, enabled by synchrotron tomography, is presented and discussed.

Synchrotron microtomography offers exceptional opportunities for paleontological research. More traditional approaches to computed tomography already unite the benefits of non-destructive data acquisition and complete three-dimensional visualization of obscured phenomena, but often still lack the capacity to realize sufficient magnification, resolution, and contrast to enable detailed appreciation of the complete internal anatomy of lithic paleontological samples. Synchrotron microtomography has unique properties that ensure superior data quality. Numerous configurations can be realized to allow for great flexibility in optimizing tomographic parameters for particular applications. A wide range of reconstruction and post-processing algorithms aid in processing, correcting, and improving obtained data for optimal results. Continuous development and refinement of tomographic setups and associated protocols will open up exciting new avenues towards larger sample sizes, improved contrast, and higher magnifications. The ESRF is presently developing the designated tomographic beamline BM18 that will allow for rapid imaging of substantially larger samples at multiscale hierarchical resolutions in a partially automated setup optimized for phase-contrast approaches (Chenevier et al. 2018). Nevertheless, synchrotron microtomography already represents a superior alternative to invasive paleontological investigations today and is to be preferred over destructive sampling for rare, exceptionally preserved, or otherwise valuable material.

Synchrotron tomography provided important new insights into the cranial anatomy of the early Middle Triassic sauropterygian species *Nothosaurus marchicus*. Novel cranial conditions were identified, characterized, and interpreted towards refining its paleoecological niche as a shallow marine piscivorous visual ambush predator. These findings furthermore inform on the

secondarily aquatic adaptations of Sauropterygia and provide supportive evidence for rapid diversification during the recovery after the Permian-Triassic mass extinction event. The recognition of variable heterochronic expression in cranial development warrants caution when adopting sauropterygian cranial characters for phylogenetic exploration. Future studies focusing on comparative material sampled at equally high resolutions will provide additional information on the diverse niches that early sauropterygians occupied and will further contextualize the ecological flexibility of the clade during its early evolutionary history.

Access to the iconic material of the oldest potentially free-flying avialan *Archaeopteryx* was unlocked through the non-destructive quality of synchrotron microtomography. Study of its wing bones revealed a closer architectural affinity with those of actively flying birds than previously understood and allowed for the interpretation of *Archaeopteryx* as a powered flyer. Novel conclusions on its metabolic regime correct earlier studies and proved more consistent with the active lifestyle associated with the capacity of active volancy. Nevertheless, other aspects of this enigmatic taxon's mosaic anatomy remain challenging to explain in a locomotory context and require further investigation. *Archaeopteryx* seems to represent one of many experimental modes of Mesozoic avialan volancy that may very well have originated independently but ultimately went extinct, with the important exception of the modern avian flight stroke. Improved understanding of the anatomy of *Archaeopteryx* and discoveries of new material will progressively resolve the fashion in which avialans achieved flight.

Future research into the broader taxa studied here is being developed. One particular approach aims to visualize and quantify the vascular mesh within the long bones of various specimens of *Archaeopteryx* and those of archosaurian reference groups through synchrotron microtomography. Vascular orientation reflects important biomechanical adaptations in bone but is also influenced by phylogeny, ontogeny, and metabolism. Disentangling these influences in *Archaeopteryx* through comparative material may help to further contextualize the findings of the research presented here and would contribute to our understanding of the biology and life history of this intriguing fossil creature.

Chapter 4: Synchrotron microtomography of a *Nothosaurus marchicus* skull informs on nothosaurian physiology and neurosensory adaptations in early Sauropterygia

Reference: **Voeten, D. F. A. E.**, T. Reich, R. Araújo, and T. M. Scheyer. Synchrotron microtomography of a Nothosaurus marchicus skull informs on nothosaurian physiology and neurosensory adaptations in early Sauropterygia. *PloS One* 13, no. 1 (2018): e0188509.

Abstract Nothosaurs form a subclade of the secondarily marine Sauropterygia that was well represented in late Early to early Late Triassic marine ecosystems. Here we present and discuss the internal skull anatomy of the small piscivorous nothosaur *Nothosaurus marchicus* from coastal to shallow marine Lower Muschelkalk deposits (Anisian) of Winterswijk, The Netherlands, which represents the oldest sauropterygian endocast visualized to date. The cranial endocast is only partially encapsulated by ossified braincase elements. Cranial flattening and lateral constriction by hypertrophied temporal musculature grant the brain a straight, tubular geometry that lacks particularly well-developed cerebral lobes but does potentially involve distinguishable optic lobes, suggesting vision may have represented an important sense during life. Despite large orbit size, the circuitous muscular pathway linking the basisphenoidal and orbital regions indicates poor oculomotor performance. This suggests a rather fixed ocular orientation, although eye placement and neck maneuverability could have enabled binocular if not stereoscopic vision. The proportionally large dorsal projection of the braincase endocast towards the well-developed pineal foramen advocates substantial dependence on the corresponding pineal system *in vivo*. Structures corroborating keen olfactory or acoustic senses were not identified. The likely atrophied vomeronasal organ argues against the presence of a forked tongue in *Nothosaurus*, and the relative positioning of external and internal nares contrasts respiratory configurations proposed for pistosauroid sauropterygians. The antorbital domain furthermore accommodates a putative rostral sensory plexus and pronounced lateral nasal glands that were likely exapted as salt glands. Previously proposed nothosaurian 'foramina eustachii' arose from architectural constraints on braincase development rather than representing

functional foramina. Several modifications to brain shape and accessory organs were achieved through heterochronic development of the cranium, particularly in the braincase. In summary, the cranium of *Nothosaurus marchicus* reflects important physiological and neurosensory adaptations that enabled the group's explosive invasion of shallow marine habitats in the late Early Triassic.

PLOS ONE

RESEARCH ARTICLE

Synchrotron microtomography of a *Nothosaurus marchicus* skull informs on nothosaurian physiology and neurosensory adaptations in early Sauropterygia

Dennis F. A. E. Voeten[1,2]*, Tobias Reich[3], Ricardo Araújo[4,5,6], Torsten M. Scheyer[3]

1 European Synchrotron Radiation Facility, Grenoble, France, **2** Department of Zoology and Laboratory of Ornithology, Palacký University, Olomouc, Czech Republic, **3** University of Zurich, Palaeontological Institute and Museum, Zurich, Switzerland, **4** Institute for Plasma Research and Nuclear Fusion, Technical University of Lisbon, Lisbon, Portugal, **5** Museum für Naturkunde, Leibniz-Institut für Evolutions- und Biodiversitätsforschung, Berlin, Germany, **6** Institute of Evolutionary Sciences, University of Montpellier 2, Montpellier, France

* dennis.voeten01@upol.cz

OPEN ACCESS

Citation: Voeten DFAE, Reich T, Araújo R, Scheyer TM (2018) Synchrotron microtomography of a *Nothosaurus marchicus* skull informs on nothosaurian physiology and neurosensory adaptations in early Sauropterygia. PLoS ONE 13 (1): e0188509. https://doi.org/10.1371/journal.pone.0188509

Editor: William Oki Wong, Indiana University Bloomington, UNITED STATES

Received: June 21, 2017

Accepted: November 8, 2017

Published: January 3, 2018

Data Availability Statement: The two tomographic volumes presented and described herein are made publicly accessible as .tiff stacks through the ESRF Paleontological Database (paleo.esrf.eu).

Funding: This study was partly funded by the Swiss National Science Foundation (www.snf.ch) through SNF grant Nos. 31003A_149506 & 173173 to TMS and by the Fundação para a Ciência e Tecnologia (www.fct.pt) through fellowship SFRH/BPD/96205/2013 to RA. The

Abstract

Nothosaurs form a subclade of the secondarily marine Sauropterygia that was well represented in late Early to early Late Triassic marine ecosystems. Here we present and discuss the internal skull anatomy of the small piscivorous nothosaur *Nothosaurus marchicus* from coastal to shallow marine Lower Muschelkalk deposits (Anisian) of Winterswijk, The Netherlands, which represents the oldest sauropterygian endocast visualized to date. The cranial endocast is only partially encapsulated by ossified braincase elements. Cranial flattening and lateral constriction by hypertrophied temporal musculature grant the brain a straight, tubular geometry that lacks particularly well-developed cerebral lobes but does potentially involve distinguishable optic lobes, suggesting vision may have represented an important sense during life. Despite large orbit size, the circuitous muscular pathway linking the basisphenoidal and orbital regions indicates poor oculomotor performance. This suggests a rather fixed ocular orientation, although eye placement and neck manoeuvrability could have enabled binocular if not stereoscopic vision. The proportionally large dorsal projection of the braincase endocast towards the well-developed pineal foramen advocates substantial dependence on the corresponding pineal system *in vivo*. Structures corroborating keen olfactory or acoustic senses were not identified. The likely atrophied vomeronasal organ argues against the presence of a forked tongue in *Nothosaurus*, and the relative positioning of external and internal nares contrasts respiratory configurations proposed for pistosauroid sauropterygians. The antorbital domain furthermore accommodates a putative rostral sensory plexus and pronounced lateral nasal glands that were likely exapted as salt glands. Previously proposed nothosaurian 'foramina eustachii' arose from architectural constraints on braincase development rather than representing functional foramina. Several modifications to brain shape and accessory organs were achieved through heterochronic development of the cranium, particularly the braincase. In summary, the cranium of *Nothosaurus*

funders had no role in study design, data collection and analysis, decision to publish, or preparation of the manuscript.

Competing interests: The authors have declared that no competing interests exist.

marchicus reflects important physiological and neurosensory adaptations that enabled the group's explosive invasion of shallow marine habitats in the late Early Triassic.

Introduction

The Permian-Triassic (P-T) mass extinction profoundly influenced the evolutionary history of most taxa that survived the P-T event [1, 2]. Sauropterygia are a particularly successful group of secondarily marine sauropsids of which the oldest recognized fossils date back to the Spathian sub-stage of the Olenekian [3, 4], about 5 million years after the P-T mass extinction [1]. These initially small- to medium-bodied predators exhibited rapid dispersal in the newly formed epicontinental Muschelkalk Sea and along the shallow marine margins of the Tethyan realm [5] in a highly competitive arena shared with a diverse variety of other secondarily marine reptile taxa [1]. Lower Muschelkalk deposits have yielded a suite of related but morphologically distinct families [6], which demonstrates that the Sauropterygia were already established in close to all the higher trophic levels of the food chain by then [1, 7]. Following this initial radiation, several sauropterygian taxa display intrageneric niche partitioning and speciation that proceeded up to the extinction of the non-plesiosaurian sauropterygians in the Rhaetian [8]. The earliest sauropterygians recognized to date already exhibit significant aquatic specializations, such as skeletal paedomorphosis and propodial simplification and shortening [9, 10], as early as the Olenekian. The explosive radiation that followed their still enigmatic origin make Sauropterygia a model clade for successful ecological adaptation to a vacated environment that likely reflects the influence of a rapid and nearly uninterrupted aquatic adaptation and trophic optimization.

Even the oldest Lower Muschelkalk deposits of the Germanic Basin, among which is the Anisian Vossenveld Formation that crops out in the Winterswijkse Steengroeve quarry complex in the east of the Netherlands [11], already exhibit a highly diversified sauropterygian assemblage. *Nothosaurus marchicus* is among the largest recognized sauropterygian species in these deposits, smaller only than some generally rare placodonts [6, 12, 13] and undescribed Eosauropterygia known only from isolated and non-diagnostic postcranial material [6, 12, 14]. The cranial morphology of *Nothosaurus marchicus* exhibits profound dorsoventral flattening, wide orbits, large and strongly elongated temporal fenestrae, and a dentition with protruding needle-like fangs [6]. The corresponding postcranium represents that of an agile paraxial swimmer [15–17] with a propulsive bias on the anterior limbs [18]. Such observations are consistent with reconstructions of *Nothosaurus marchicus* as a piscivorous marine predator. Recent reports on the morphology and bone histology of *Nothosaurus* have improved our understanding of its secondary aquatic adaptations as well as early sauropterygian diversification in general [16, 19], but the corresponding adaptations of the neurosensory system have received only limited attention.

The modern research field of paleoneurology owes its inception to Tilly Edinger nearly 100 years ago [20]. Her first publication provided the description of a lithic endocast of *Nothosaurus mirabilis* that was obtained by sacrificing the osseous braincase [21]. The most recent endocranial exploration and associated description of several neurosensory and vascular structures of *Nothosaurus* was conducted by detailed examination of a braincase that was freed from the surrounding and enclosed matrix through acid preparation [22]. The advent of computed tomography has enabled new opportunities for paleoneurological research since the non-destructive nature of data collection permits the study of material deemed too valuable

for invasive sampling [23–25]. Ongoing developments in synchrotron microtomography and particularly advances in Propagation Phase-Contrast Synchrotron X-Ray Microtomography (PPC-SRμCT) now permit virtual dissection at resolutions that are comparable to those of traditional physical sampling methods [25, 26].

The crucially different physical demands of aquatic habitats with respect to terrestrial environments are reflected in the sensory configuration of organisms that are secondarily adapted to an aquatic niche [27–29]. Studies to the sensory systems of extinct aquatic tetrapods have identified important adaptations in a variety of aquatic taxa, such as the miniaturization of the vestibular system and severe atrophy of the olfactory system in cetaceans [30, 31], and a profound reliance on vision in ichthyosaurs [32]. Recent years have seen an acceleration in the study of sensory systems in Mesozoic marine reptiles that is partially fueled by the increasing availability of non-destructive three-dimensional investigation methods. Computed tomography has revealed the morphology of the cranial endocast and endosseous labyrinth across a diverse array of taxonomic groups that had remained concealed before. Such structures are now increasingly better understood in mosasaurs [33], ichthyosaurs [34], placodonts [35], metriorhynchid crocodyliforms [36, 37], and phytosaurs [38, 39]. The neuroanatomy of early sauropterygians, however, has received only limited attention thus far [21, 22, 35, 40].

Here, we report on a description of the endocranial morphology of *Nothosaurus marchicus* based on high-resolution data acquired through PPC-SRμCT that represents the first digital visualization of a eusauropterygian cranial endocast as well as the oldest virtual sauropterygian endocast retrieved to date. This information permits an assessment of the sensory cues that *Nothosaurus* relied on during life and illustrates the adaptations that accompany the early specialization of Sauropterygia five million years after the P-T mass extinction event.

Material and methods

TW480000375 (Fig 1) is housed in the collections of Museum TwentseWelle in Enschede, The Netherlands, and represents a complete cranium that has conservatively preserved its three-dimensional morphology [12, 41, 42]. Synspecific crania from this locality are known to range in length up to circa 130 mm [43]. TW480000375 has a condylobasal skull length of 101 mm and its well-ossified cranial sutures suggest that this individual had reached skeletal maturity [44]. TW480000375 was retrieved from Layer 9 (after [45]) of the Vossenveld Formation at the Winterswijkse Steengroeve locality (Winterswijk, The Netherlands). Ventral and medial aspects of the cranium remain obscured by a matrix that consists of a fine-grained micritic limestone.

Institutional abbreviations

PGIMUH, Palaeontological and Geological Institute and Museum (now Museum für Geowissenschaften), University of Heidelberg, Germany; SMNS, Staatliches Museum für Naturkunde, Stuttgart, Germany; TW, Museum TwentseWelle Enschede, The Netherlands.

Data accessibility

The two tomographic volumes presented and described herein are made publicly accessible as. tiff stacks through the ESRF Paleontological Database (paleo.esrf.eu).

Visualization

TW480000375 was visualized using PPC-SRμCT conducted at beamline ID19 of the European Synchrotron Radiation Facility in Grenoble (France) to obtain sufficient contrast between the osseous cranium and the endocranial cavities and surrounding limestone matrix. Scanning

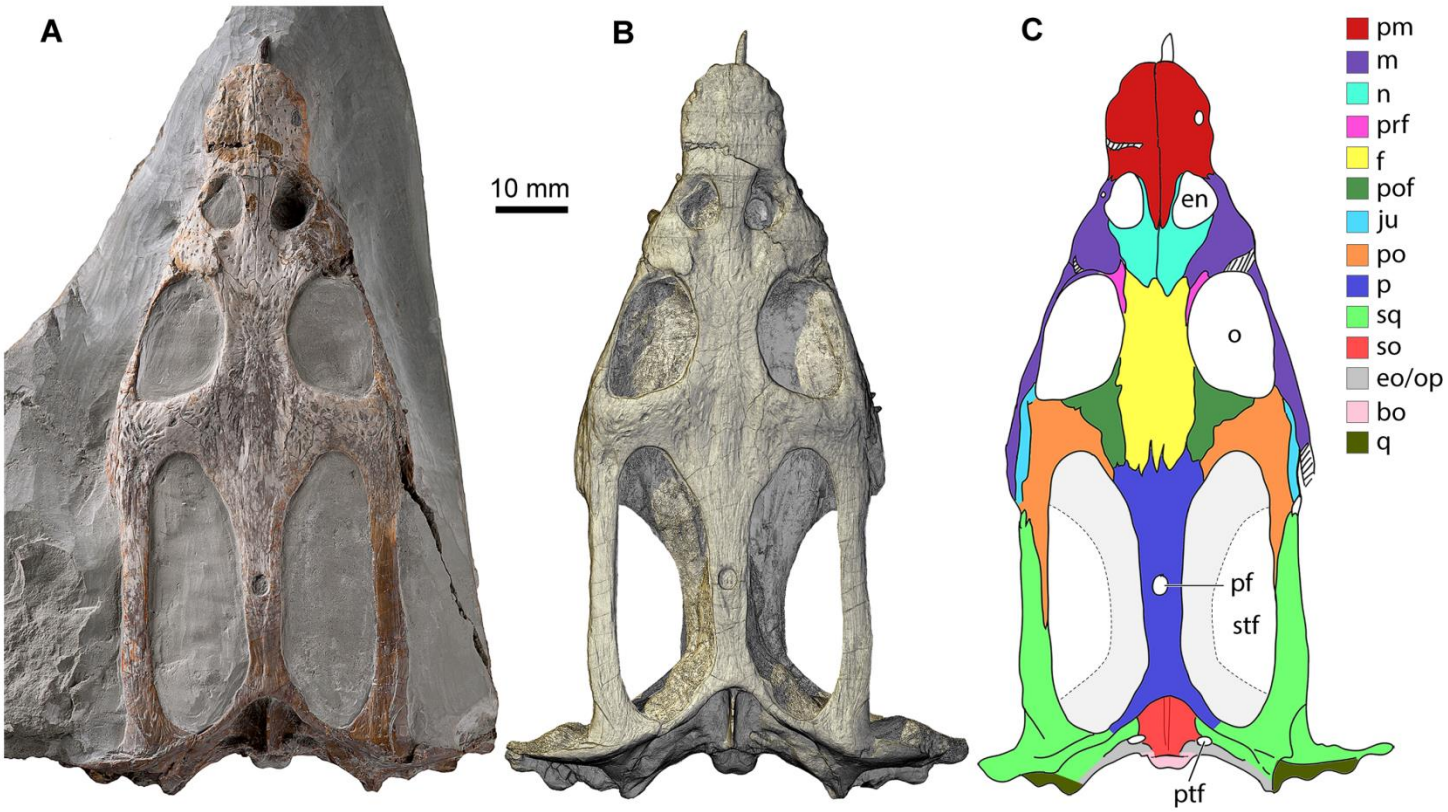

Fig 1. The cranium of *Nothosaurus marchicus* (TW480000375) from the Lower Muschelkalk (Anisian) of Winterswijk, The Netherlands, in dorsal view. A. Original cranium in matrix. **B.** Digital surface rendering. **C.** Interpretative line drawing with visible cranial bones color coded. Note that the outlines of the ventrally situated pterygoids have been indicated in light grey, bordered by a stippled line. Abbreviations: bo, basioccipital; en, external naris; eo/op, excoccipital/opisthotic; f, frontal; ju, jugal; m, maxilla; n, nasal; o, orbit; p, parietal; pf, pineal foramen; pm, premaxilla; po, postorbital; pof, postfrontal; prf, prefrontal; ptf, posttemporal foramen; q, quadrate; so, supraoccipital; sq, squamosal; stf, supratemporal fenestra.

https://doi.org/10.1371/journal.pone.0188509.g001

data with isotropic voxel sizes of 12.82 and 28.2 μm were acquired in polychromatic mode with 13 m of propagation and at energy levels of 148 and 132 KeV, respectively. Three-dimensional volume reconstruction was conducted through filtered back projection following a phase retrieval protocol that relies on a homogeneity assumption by using a modified version [26] of the Paganin algorithm [46]. We assessed the original tomographic reconstruction as well as a recoded version of the three-dimensional data based on local texture complexity to reveal low-contrast features.

The volumes obtained through reconstruction of the PPC-SR μCT data were segmented in VGStudio MAX 2.2 (Volume Graphics, Heidelberg, Germany) to create a virtual endocast of TW480000375 (Fig 2). The cranial endocast (Fig 3) and most of the additional morphological features reported here were extracted from the data set with a 12.82 μm voxel size (e.g. Fig 4), whereas the lateralmost domains in the posterior cranium were resolved from scan data with a 28.2 μm voxel size. The cranial endocast and additional endocranial features were rendered in VGStudio MAX 2.2 and exported at high resolution. Digital imagery and figure plates were subsequently assembled using Adobe Creative Suite 6.

Delimitation and identification of cranial voids

Cranial topography informs on the nature and extent of the associated soft tissue anatomy and thus provides a valuable tool in defining and identifying certain intracranial domains. Since

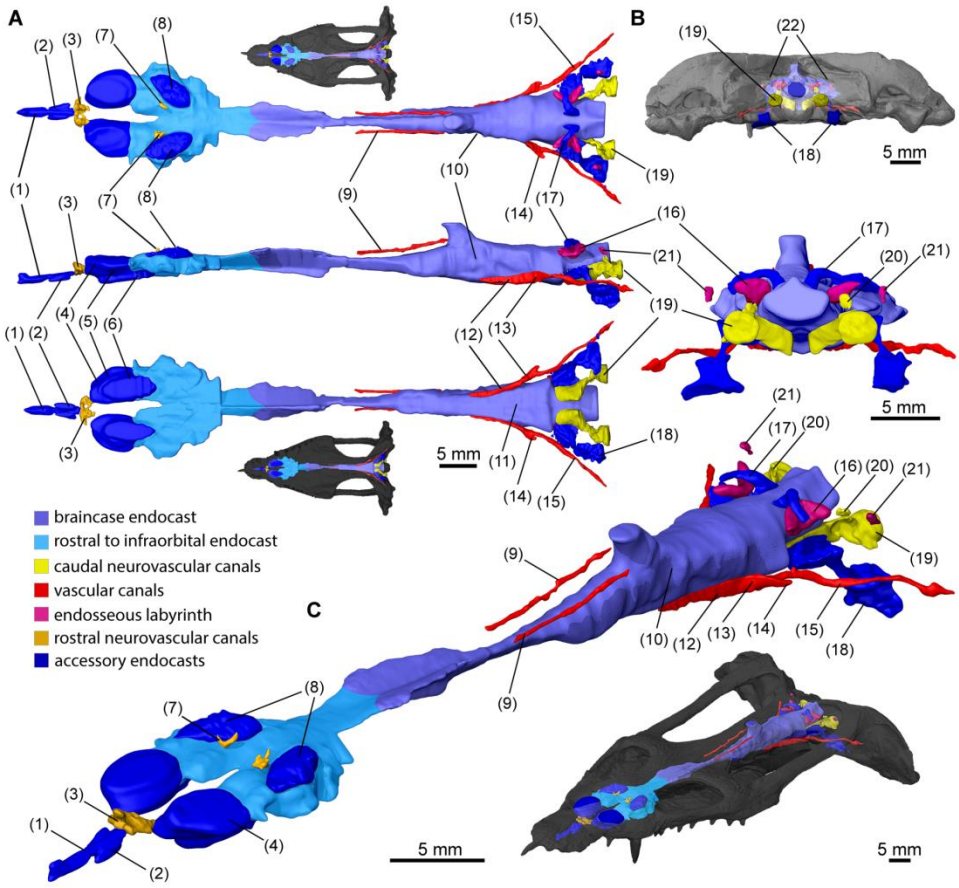

Fig 2. Surface renderings of cranial endocast and casts of additional endocranial voids in *Nothosaurus marchicus* (TW480000375). Different structures are color coded, integer regions excluding brain subdivisions are labeled as the structures they correlated with *in vivo*. **A.** Cranial endocast and other endocranial voids in dorsal (top), lateral (middle), and ventral (bottom) view. **B.** Cranial endocast and other endocranial voids in occipital view. **C.** Cranial endocast and other endocranial voids in angled anterodorsal view. Dorsal, ventral, occipital and anterodorsal views associated with endocast projections in cranial model. (1) premaxillary lumen; (2) vomeropremaxillary passages; (3) rostral nervous passage; (4) nasal vestibules; (5) cava nasi; (6) nasopharyngeal duct; (7) branching dorsal apertures of nasal cavity; (8) salt glands; (9) infraparietal canals; (10) endocast of cava epipterica; (11) pituitary domain; (12) interpretated location of bifurcation into sphenopalatine artery and internal carotid arch irrigating pituitary domain; (13)? cerebral branch of internal carotid artery; (14)? stapedial artery; (15) internal carotid artery; (16) apex of crus communis; (17) middle cerebral vein or paratympanic sinus; (18) interosseous casts of paracondylar interstices; (19) interosseous casts of the foramina associated with glossopharyngeal, vagoaccessory and hypoglossal cranial nerves; (20) root of hypoglossal nerve XII; (21) posterior sections of posterior semicircular canals; (22) posttemporal foramina.

https://doi.org/10.1371/journal.pone.0188509.g002

the braincase of *Nothosaurus* is well documented, we briefly recall the generic cranial osteology of *Nothosaurus* from literature [6, 22].

The ventral braincase of *Nothosaurus* is completely closed through the massive, paired pterygoids that share an interdigitated median suture and extend from the level of the central orbits back to the ventrolateral occiput. The basioccipital forms the ventromedial occiput where it defines the ventral margin of the foramen magnum and forms the occipital condyle. It is laterally flanked by the opisthotics in occipital view and dorsolaterally meets the exoccipitals that form the lateral margins of the foramen magnum. The foramen magnum is dorsally delimited by the supraoccipital that ascends anterodorsally up to the skull roof and supports a pronounced supraoccipital crest. From its posterior opening, the cranio-quadrate passage

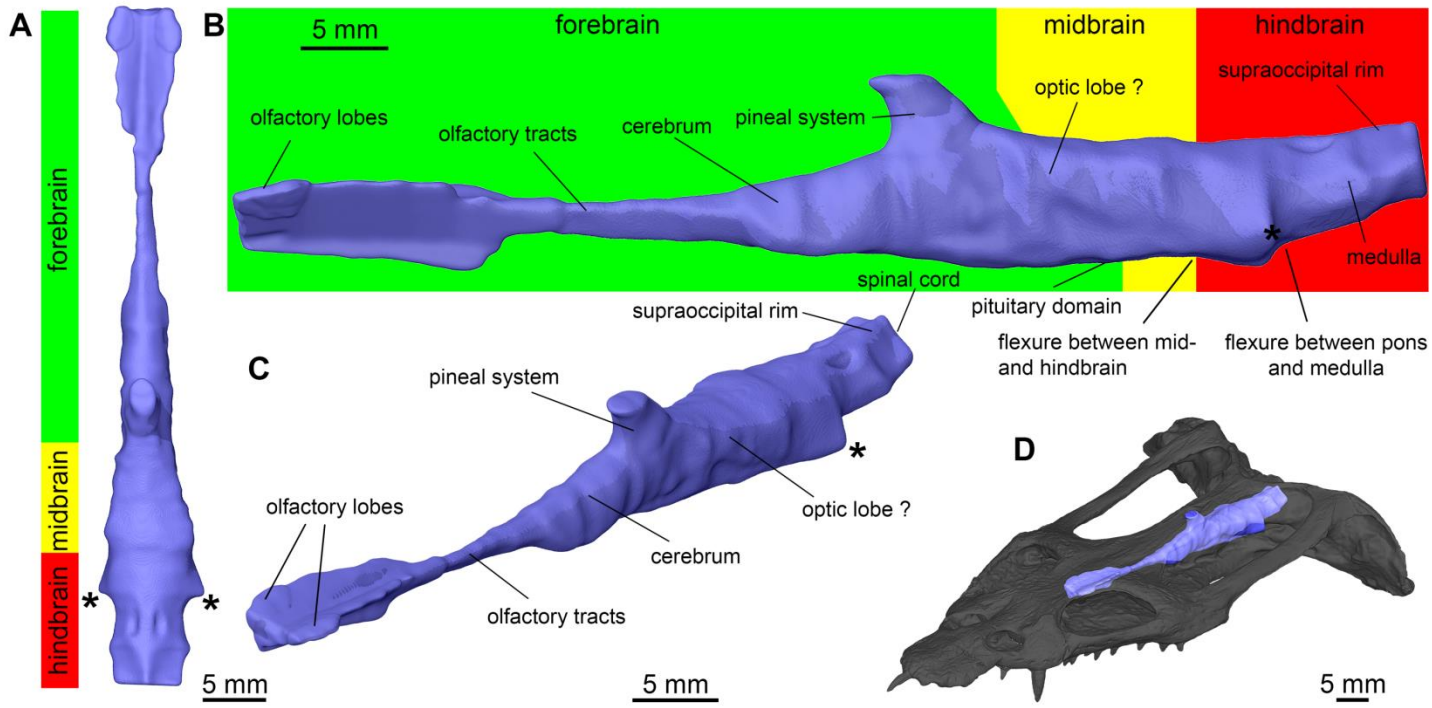

Fig 3. Surface rendering of the cranial endocast of *Nothosaurus marchicus* (TW480000375). Brain division and identified domains are indicated. Cranial endocast in dorsal (**A**), left lateral (**B**), and angled anterodorsal (**C**) views. **D.** Reconstructed cranial endocast projected into cranial model. Asterisks (*) indicate bilaterally positioned and transversely oriented boundaries where large hollows diverge from the central endocast.

https://doi.org/10.1371/journal.pone.0188509.g003

leads straight through to its anterior opening and simultaneously opens up into a medial recess between the dorsal pterygoid, ventral squamosal, and posterior prootic. Together with the opisthotic, the prootic also contributes to the otic capsule that remains medially unossified. The median basicranial floor is posteriorly formed by the dorsal surface of the basioccipital, which proceeds anteriorly onto the basisphenoid where it supports a low dorsum sellae that borders a shallow sella turcica. More anteriorly, the paired epipterygoids rise from the dorsal pterygoids up to the parietal to define laterally enclosed cava epipterica. Here, the medial pterygoids warp up to form a low ridge separating the left from the right cavum epiptericum. The roof of the braincase is largely formed by the parietal that forms a slender, anteroposteriorly elongated element appearing hourglass-shaped in dorsal view. The parietal extends along the elongated temporal fenestrae and accommodates a well-defined median pineal foramen that is placed somewhat posteriorly. Anteriorly, the pterygoid meets the frontal in a deeply interdigitating suture at a level that roughly corresponds with the anterior margin of the temporal fenestrae. The frontal extends roughly between the level of the anterior margin of the temporal fenestrae up to nearly the anterior margin of the orbits.

In *Nothosaurus*, important medial and lateral walls that bordered endocranial voids *in vivo* have not ossified [21, 22, 47], which locally prevents accurate reconstruction of such cavity boundaries during segmentation. However, a conservative approach to reconstructing the endocranium was used in these areas to link the dorsally and ventrally well-constrained parts.

Although the adult braincase of most lizards, turtles, and *Sphenodon* is not fully ossified (e.g. [48]), in archosauriforms, arguably the best studied reptilian group thus far, the brain and other intracranial structures are usually well encapsulated and thus delimited by ossified braincase elements (e.g. [37, 48–52]).

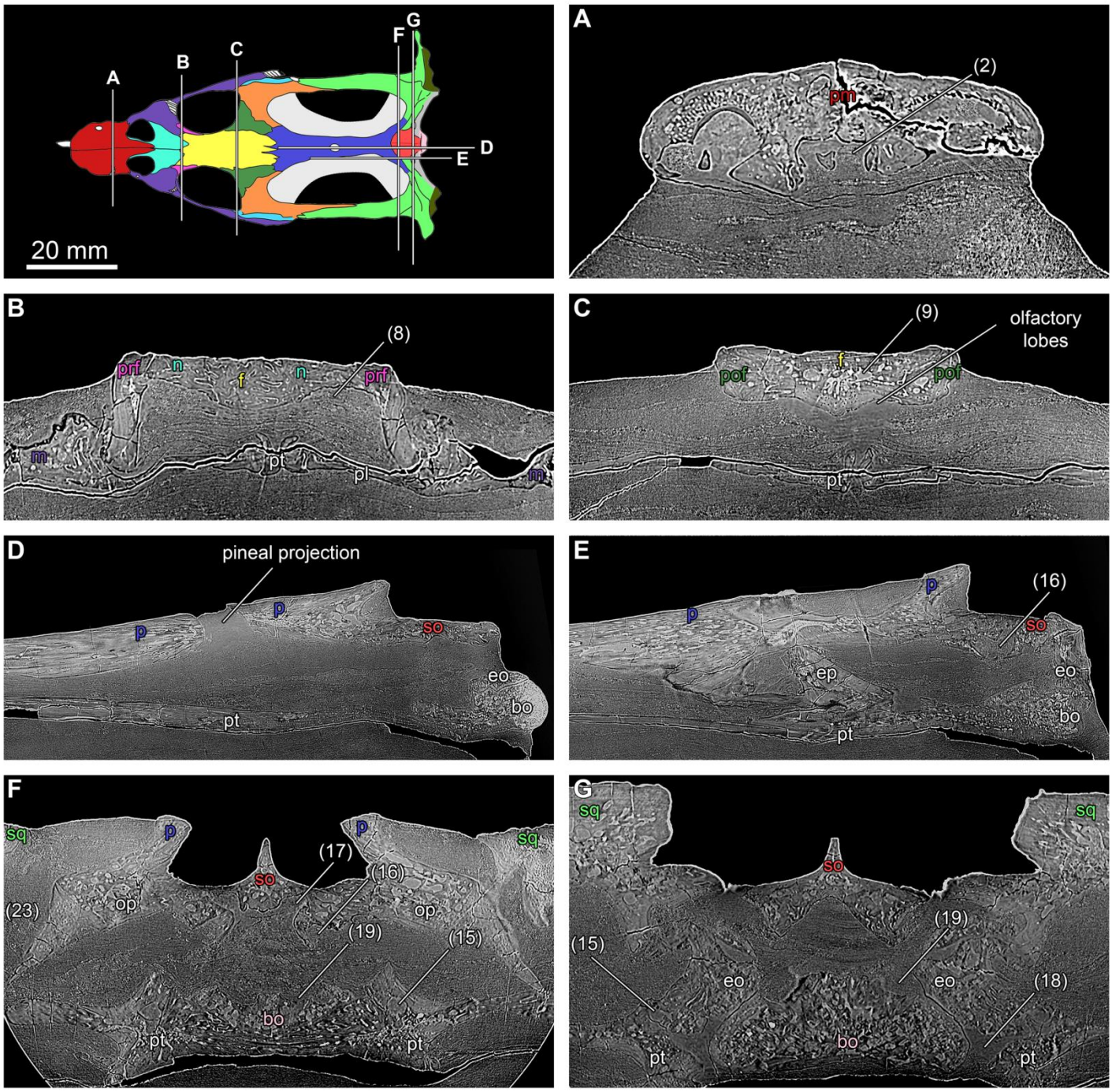

Fig 4. Individual slice data (A-G) through the cranium of *Nothosaurus marchicus* (TW480000375). Positions of the transverse (**A-C, F, G**) and longitudinal (**D, E**) sections shown in cranial surface model (see Fig 1C). Voids labeled following numbering in Fig 2. Images in A-G not to scale. Abbreviations: bo, basioccipital; eo, exoccipital; ep, epipterygoid; f, frontal; n, nasal; op, opisthotic; p, parietal; pl, palatine; pm, premaxilla; pof, postfrontal; prf, prefrontal; pt, pterygoid; so, supraoccipital; sq, squamosal.

https://doi.org/10.1371/journal.pone.0188509.g004

Particularly in most of the anterior parietal and frontal domain of the endocranial vault, we chose to delimit the lateral extent of the endocast along anteroposteriorly trending bone ridges extending dorsally from the pterygoids that may have supported delimiting but non-ossified

structures or tissues during life. In the endocranial portions where no well-defined ridges were apparent, we adopted the ventralmost extent of the cranial roof elements and the dorsalmost extent of the cranial floor as lateral delimitations (e.g. around the frontoparietal suture). In such domains, mainly dorsal and locally ventral aspects of the endocast remain informative. Two bilaterally positioned and transversely oriented boundaries were placed where large hollows diverged from the central endocast (indicated with asterisks in Fig 3). The interpretation of soft-tissue structures is based on anatomical comparison with the cranial neurosensory systems of selected extant sauropsids, such as lepidosaurs, turtles and crocodylians, which collectively form a broad phylogenetic bracket [53] for sauropterygians.

Contrary to mammals and birds, the internal geometry of the reptilian braincase does not conservatively reflect the external geometry of the brain itself [48]. However, the close association between the dural venous sinuses and the underlying brain does allow for particular information on brain structures, such as position and relative size, to be transmitted to the internal surface of the braincase [39, 54]. Furthermore, the particularly constricted nature of the brain in *Nothosaurus* (see Discussion) ensures a more conservatively defined brain shape to be reflected in the cranial endocast than would be the case for taxa with a less constrained braincase. The location of a geometric feature on the cranial endocast allows for its identification through comparison with the phylogenetic bracket. Since the mass, and thus size, of a neural tissue is proportionally correlated with the amount of information processed during execution of the corresponding function [55], relative size comparison allows for a consideration of the importance of this function during life.

Results

Osteological aspects

Sella turcica. A dorsally projected indentation of the ventral endocast slightly anterior to the level of the pineal foramen (endocast impression: feature 11 in Fig 2) results from the contact between the basioccipital and the basisphenoid forming an incipient yet poorly preserved sella turcica on the basioccipital [22]. In TW480000375, the sella turcica is not anteriorly delimited by an anterior clinoid process but continues smoothly onto the parasphenoid. Its limited preservation does not allow for a detailed assessment of this important braincase structure, nor of the perforations known to irrigate it with blood or innervate it, as was demonstrated for the placodont sauropterygian *Placodus gigas* [35]. Well-defined projections of the hypophysis or pituitary lobes are absent on the ventral aspect of the endocast. Such an undifferentiated hypophysis also characterizes the cranial endocast of crocodylians and turtles [56–60]. The complex division of the "cavité hypophysaire" that was described by Gorce [61] cannot be recognized in TW480000375, likely due to the damage sustained in this domain. Nevertheless, the generic configuration of the sella turcica in *Nothosaurus* has been described in detail (e.g. [22]). A pituitary fossa was initially considered absent [47]. However, when it was eventually identified, its morphology was explained to have potentially accommodated an underdeveloped hypophysis relative to those of *Sphenodon* and lizards [56], where the hypophysis occupies a deep recess. In *Sphenodon*, *Varanus* and *Lacerta*, the lateral periphery of the sella turcica around the crista trabecularis serves as the origin for important oculomotor musculature, notably the *m. bursalis* and the retractor bulbi group [62]. The ocular muscle configuration of Crocodylia is similar to that of *Sphenodon* [63]. Furthermore, a low dorsum sellae and shallow sella turcica have been correlated with a reduction of the eyes and ocular muscles in reptiles ([64] and references therein). *Nothosaurus* exhibits a low dorsum sellae that is positioned quite posteriorly and well behind the intertemporal constriction of the braincase (see also Fig 10 in [22]). Ocular muscles attaching to the basisphenoidal region must thus have

reached a considerable distance to reach the eyes (further even than the "extremely long" optic nerves [21]), including the passage of the laterally constricted section of the braincase in between the temporal fenestrae. Where considerable relative orbital size in *Nothosaurus marchicus* may indicate substantial visual acuity, this indirect pathway for ocular musculature also suggests restricted oculomotor dexterity and thus a relatively fixed ocular orientation in the cranium. However, the positioning of the orbits and relatively elongated neck in *Nothosaurus* could have granted partial binocular overlap and sufficient cervical agility (possibly even head saccades, as birds [65]) to compensate for poor intracranial ocular mobility. In other words, the constrained ocular musculature was probably compensated for by cervical mobility and a refined vestibulocollic reflex. Basal members of the genus appear to exhibit a relatively larger orbital size associated with shorter temporal fenestrae than more advanced forms that exhibit significant relative cranial elongation (e.g. [6]).

Cava epipterica. In the cerebral domain immediately posterior to the pineal foramen, the central to ventral aspects of the cranial endocast are laterally constricted and consequentially well defined (endocast impression: feature 10 in Fig 2) through the presence of the medially bulging epipterygoids. The ventrolateral margins of this domain are formed by distinct, anteroposteriorly trending ventral sulci that gradually even out onto the pterygoidal cranial floor anteriorly. More posteriorly, these sulci give rise to paired semitubular passages (feature 12 in Fig 2) that posterolaterally depart from the ventrolateralmost margins of this endocast domain at a small angle. The epipterygoids form the lateral walls of the cava epipterica; enclosed, paired cerebral compartments that are roofed by the palatines, floored by the pterygoids, and separated by a cartilaginous median septum *in vivo* [22]. Although the straight braincase endocast of TW480000375 exhibits a nearly flat ventral margin that prevents recognition of the transition from the forebrain to the inconspicuously expressed midbrain through a distinct flexure, the cava epipterica provides a more general indication for the position of this transition.

"Foramen eustachii" of Koken (1893). The basioccipital forms the occipital condyle and the ventral margin of the foramen magnum. It meets the exoccipitals dorsolaterally along a smooth suture and shares an irregular and locally strongly interdigitating suture with the paired pterygoids ventrally. More anteriorly up to the level of the epipterygoids, the basioccipital-pterygoidal contact is deeply depressed. It continues anteriorly along the unossified lateral walls of the braincase where it gives rise to a paired, dorsally open trough (interosseous casts: feature 18 in Fig 2). More anteriorly still, these troughs pass ventral to the otic domain and join the cranial endocast at the level of the basisphenoid. Posteriorly, these troughs develop into the large, posteroventrally widening occipital gaps that result from the natural separation between the lateral basioccipital tuber and the pterygoids. These occipital corridors flanking the basioccipital have been argued to represent the passages of the eustachian tube in *Nothosaurus* [47], but have also been interpreted to (partly) accommodate the internal carotid arteries [22]. Furthermore, their variable configuration in *Nothosaurus* has been argued to indicate closure of these passages at a late ontogenetic stage [22]. In TW480000375, the trajectory of these "eustachian foramina" does not involve the internal carotids, nor does it link the pharynx with a potential middle ear cavity, as is the case for a true eustachian passage [66]. In addition, the depressed basioccipital-pterygoidal suture that distally forms the lateral troughs does not correspond to a conventional cerebral compartment but represents a dorsally unossified recess of the basicranium with an unknown function.

Occipital foramina associated with the glossopharyngeal, vagoaccessory and hypoglossal cranial nerves. Paired ventral troughs depart from the posteroventral braincase endocast and initially trend posterolaterally (interosseous casts: feature 19 in Fig 2). They originate as depressions of the dorsal basioccipitals and continue posteriorly between the medial margin of the opisthotics and the lateral borders of the exoccipitals. Posterior to a mediolateral

constriction, these passages depart the cranium through a pair of occipital openings that flank the foramen magnum. These occipital openings are largely defined by the exoccipitals and are only laterally bordered by the opisthotics. Additionally, minute paired conical canals with a subequal diameter of 0.5–0.6 mm branch off near the posterior boundary of cranial endocast at the level of the foramen magnum (feature 20 in Fig 2). These canals project ventrolaterally where they pierce the exoccipital and join the recess of the aforementioned occipital foramina (Fig 4F and 4G). The occipital foramina between the exoccipitals and opisthotics have been explained to be homologous to the jugular foramina (metotic foramina) of extant amniotes that accommodate the pathways of the glossopharyngeal and vagoaccessory nerves [22]. Cranial nerves (CN) IX and X typically branch off closely together [56, 67] and depart the cranium through the jugular foramina in tandem with CN XI [22, 47]. The paired perforation of the exoccipital more posteriorly to the medial endocast accommodated the root of hypoglossal nerve XII that joined cranial nerves IX-XI slightly anterior to their collective cranial departure through the jugular foramina.

Posttemporal foramina. In TW480000375, an inconspicuous but paired perforation of the occiput resides in the sutural junction of the ventral supraoccipital, dorsolateral exoccipital and medial expansion of the opisthotic (feature 22 in Fig 2). Dorsolaterally to the foramen magnum, these concealed apertures are partially obscured by the lateral projections of the exoccipitals, rendering them nearly invisible in posterior view. They do not proceed into well-defined osseous canals anteriorly but access the non-ossified and therefore poorly resolved otic domain. Small posttemporal foramina have been identified in *Nothosaurus mirabilis* crania from the Early Ladinian of Germany and it has been proposed that reduced to obliterated posttemporal foramina are synapomorphic for Nothosauridae [22]. Their topographical position agrees with the proportionally even smaller occipital perforations recognized in TW480000375. Well-developed posttemporal fenestrae have been reported for *Placodus*, but were placed more laterally in the occiput and are delimited by the squamosal, parietal, opisthotic and possibly the pterygoid (Fig 2B in [68]). Notably, that contribution does depict potential occipital perforations of much smaller size at topographical locations that corresponds to those of the posttemporal fenestrae in *Nothosaurus* ([22]; Fig 2B in [68]). Although the posttemporal fenestrae in *Nothosaurus* are substantially smaller, they appear to be homologous to the wide apertures found in some plesiosaurs [69]. In crocodylians, the posttemporal fenestrae are small and covered over with cartilage during life [70]. The posttemporal foramina of most squamates are large vacuities, but they are completely absent in scincids [71]. No major vessel passes through the posttemporal fenestrae of extant diapsids [70, 72]. In TW480000375, they appear to communicate with the weakly defined void at or near the region that accommodated the otic capsule in TW480000375. Despite the external expression of the posttemporal openings in TW480000375, their internal morphology is inconsistent with an innervation function in *Nothosaurus*.

Cranial endocast

Brain macrostructure. Overall, the osseous braincase of *Nothosaurus marchicus* is dorsoventrally constricted by the strongly flattened cranial architecture and laterally by the extremely large temporal fenestrae and associated temporal domain that accommodated the hypertrophied jaw adductor muscle complex [22]. The cranial endocast of TW480000375 consequentially takes the shape of a straight, anteriorly tapering cone, the dorsal margin of which trends anteroposteriorly (Fig 3). Its ventral margin is slightly tilted in an anterodorsal-posteroventral direction. Various additional morphological features can be resolved on the cranial

endocast, which will be described and interpreted through osseous landmarks and following comparison with extant and extinct taxa.

Forebrain–olfactory lobes. The portion of the cranial endocast delimited by the frontal dorsally and posterior vomers and pterygoids ventrally exhibits a longitudinal, V-shaped dorsal cleft resulting from a ventrally projecting sagittal ridge on the frontal. Near the posterior orbits and lateral to the V-shaped sagittal trough, two shallow but clearly paired and distinctly ovoid recesses in the ventral frontal mark the location of the olfactory lobes (Fig 3). Slightly further posterior, a sagittal ridge dorsally terminating in a minor bifurcation rises from the interdigitating suture between the paired pterygoids. This osseous ridge extends from the midpoint between the central orbits up to the frontoparietal suture and causes a confined yet pronounced medial cleft on the ventral endocast. The subtle anteroposteriorly extending bifurcating rim carried by the sagittal upwarp of the interpteryoidal suture defines the support for a cartilaginous interorbital septum (see Fig 4C), as is expected for a tropibasic cranium [22]. During life, this septum carried the planum supraseptale; a cartilaginous trough-shaped structure occurring ventral to the frontal that forms the ventral envelope for the olfactory tracts and bulbs [21, 73–75]. The positions of the two shallow but resolvable recesses in the ventral frontal (see Fig 4C), possibly also referred to by Edinger ("between the orbits") [21], correspond to those of the osteological correlates of the olfactory lobes in mosasaurs [76], *Varanus* [77], rhynchosaurs [78], archosaurs such as phytosaurs [73], ichthyosaurs [34], and potentially in elasmosaurid plesiosaurs [79]. This provides sufficient support for a confident recognition of the location of the olfactory lobes in TW480000375.

Forebrain–olfactory tracts. A medial connection extends posteriorly between the interorbital domain and the cerebral portion of the endocast (Fig 3). Since its lateral to ventrolateral margins represents artificial truncations, it only informs on the dorsal geometry of the corresponding endocranial domain. As such, it describes a gradual dorsal inflexion of the anteroposterior endocast axis at the transition from a laterally and lateroventrally poorly defined element with an incised to flattened dorsal osseous delimitation of its anterior and central domains to a more overarched and better-defined transition to the cerebral domain posteriorly. The olfactory lobes and distal part of the olfactory tracts are bilaterally divided by a sagittal ventral projection of the interfrontal suture. Posteriorly, this ventrally protruding ridge shallows until it progressively disappears, after which the passage accommodating the olfactory tracts continues posteriorly as a dorsally undivided passage [21].

Forebrain–cerebrum. Moving posteriorly along the confined olfactory tracts, a gradual yet conspicuous lateral divergence of the osseous walls resulting in a pronounced bilateral bulging of the endocranial void marks the anterior margin of the cerebral domain (Fig 3). The dorsal, lateral, and particularly the ventrolateral osseous margins delimiting this median void resolve bilaterally symmetrical yet faint bulges that seems to have accommodated discrete soft-tissue structures *in vivo*. The braincase appears to be constricted (e.g. [47]) by physiological constraints, which most likely resulted in a strongly sequential division of cerebral domains (see Discussion). Coupled with the presence of additional, non-cerebral tissues in the braincase vault [49], this complicates the delimitation of integer brain domains. The cerebral hemispheres, however, are readily discernible in dorsal and ventral view as a bilateral set of faint lateral bulges following the gradual widening of the olfactory tracts [21].

Forebrain–pineal organ. On the cranial endocast, the pineal system is expressed as an elliptic cone that is apically truncated at the pineal foramen (Fig 3). Consequentially, the pineal foramen ventrally opens up into the cranial endocast through this large, diverging and initially posteroventrally oriented passage that has an ellipsoid cross-section in the anterolateral plane. The anterior and lateral margins of this passage are subtly concave whereas its posterior margin is straight and oriented posteroventrally. More ventrally, the posterior margin of the

passage exhibits an apparent deflection towards a more posteriorly trending dorsal boundary that occurs near the major body of the endocast. The walls of the pineal passage progressively diverge ventrally to meet the cranial endocast, on which it is set dorsally, in a gradual and flush manner. A well-developed, true pineal foramen in *Nothosaurus* conclusively reflects the presence of a photoreceptive pineal organ [80], also referred to as anterior parietal organ [81], which resembles the lateral eye to a remarkable degree [82]. The relatively large size of the pineal foramen and volume of the corresponding endocranial parietal passage compared to other taxa ([80]; this study) suggests a substantial reliance on the pineal complex during life for *Nothosaurus* and *Placodus* [35]. However, these voids also accommodated supportive and/or additional tissues that prevent a detailed reconstruction of the original size and morphology of the receptor system during life (e.g. [80]). Nevertheless, the relatively thick-walled parietal enclosure in TW480000375 strongly suggests that the large dorsal aperture of its pineal foramen conservatively reflects the actual size of the pineal eye, which in turn indicates a strong photoreceptive capability [80]. Although the posterior parietals of more derived *Nothosaurus* species often exhibit a pronounced lateral constriction inflicted by the enlarged temporal fenestrae, the relative size of the pineal foramen remains unchanged [83], which reinforces the conclusion of a significant dependence on the associated photosensor.

Midbrain and hindbrain. The posterior portion of the cranial endocast behind the cava epipterica (endocast impression: feature 10 in Fig 2) gradually widens laterally and slightly expands dorsoventrally. This expansion extends up to the level of the parietal-supraoccipital suture dorsally and extends beyond the pterygoids ventrally up to the basisphenoid-basioccipital suture. The portion of the endocast corresponding to the midbrain exhibits a subtle, apparently bilateral swelling on its dorsolateral aspect (Fig 3) that results from corresponding depressions on the ventral parietals, resembles the optic lobes identified in an ichthyosaur [34] with regard to location and orientation, and may thus represent a homologous structure in *Nothosaurus*. Although morphologically unpronounced, they do occupy one of the broadest cephalic domains, which would be consistent with a certain degree of visual acuity. Nevertheless, although extant crocodylians feature optic systems adapted for their respective niches [84], their optic lobes are poorly delimited due to the locally particularly thick dural envelope [56, 85, 86]. In crocodylians, bulges observed in this region typically reflect a portion of the venous blood system [87]. Furthermore, the lateral boundary of this endocranial domain is not continuously ossified and cannot be accurately identified throughout. These factors warrant caution when interpreting the referred features in *Nothosaurus*. At the level of the posteriormost part of the parietals, the endocast laterally communicates with paired voids that are formed by the descending flanges of the opisthotics and are excluded from the braincase endocast (Fig 4F—23). However, the referred lateral expansions in the posterior braincase endocast (asterisks in Fig 3) follow topographical contours of the ventral parietals slightly beyond the original delimitation of the brain into these voids. They thus result from artificial truncation and do not reflect the local lateral morphology of the cerebral envelope. The anterior hindbrain exhibits only a non-informative lateral expression in the domain where the floccular lobes may be expected to have resided, if present. This is comparable to the condition of extant lepidosaurian and crocodylian reptiles, which also share a small (yet distinct) flocculus [88], and disagrees with the well-developed floccular expression of birds, many other dinosaurs, and pterosaurs [89]. The floccular complex has an important role in visual stabilization and may potentially aid the reconstruction of habitual activity patterns (see Discussion, but see also [90]). Although the transition from the midbrain to the hindbrain is poorly resolved, the transition from the pons to the medulla oblongata within the hindbrain is discernable through a faint flexure and marked by dorsal and ventral "steps" in the endocast that result from a constriction associated with the parietal-supraoccipital suture (Fig 3). However, since the

aforementioned artificial truncations contribute particularly to ventrolateral aspects of these "steps", the appearance of this transition is artefactually pronounced in the endocast presented here. Between the parietal-supraoccipital constriction and the foramen magnum, the medulla oblongata tapers posteriorly, is dorsally confined by the supraoccipital and ventrally by the basioccipital, and carries a pronounced dorsal sagittal rim that extends under the (dorsal) supraoccipital crest (Fig 3).

Sensory structures

Vomeropremaxillary foramina and premaxillary lumen. Two slit-like passages perforate the palate at the level of the vomeropremaxillary suture and close to the sagittal midline of the skull (feature 2 in Fig 2) to anterodorsally access a medially located lumen (feature 1 in Fig 2). This elliptic-cylindrical cavity resides completely within the premaxilla and measures circa 1.25 mm in anteroposterior diameter, 0.75 mm in width, and circa 1.30 mm in dorsoventral height. The posterodorsal margin of the lumen bifurcates into a paired and generally posteriorly trending tubular passage that can be traced up to the internarial domain (feature 3 in Fig 2). The lumen and posterior tubules connect to smaller peripheral passages that originate in surrounding rostral hollows, such as the alveoli, and at irregular grooves at the dorsal surface of the premaxillae (not depicted). An unpaired "foramen incisivum" has been previously reported for the eusauropterygian genera *Simosaurus*, *Nothosaurus*, *Cymatosaurus* and *Pistosaurus* ([91]; [7] and references therein). Conversely, a paired vomeropremaxillary foramen, such as present in TW480000375, has also been depicted in other specimens of *Nothosaurus marchicus* (Fig 11 in [42]; Figs 39 and 61 in [83]; Fig 60 in [6]; Fig 1B in [41]), as well as in *Simosaurus* (Fig 91C in [92]). Assuming this discrepancy does not represent ontogenetic disparity or a preservational, preparatory and/or visualization artefact, it illustrates that both paired and unpaired vomeropremaxillary foramina may occur within one eusauropterygian genus and thereby suggests that the contrast between singular and paired vomeropremaxillary foramina is less conservatively distributed among nothosaurian genera than presently understood. The vomeronasal fenestrae of squamates typically reside in the vomeromaxillary suture [93], whereas the antrochoanal palatal foramina of Eosauropterygia perforate the vomeropremaxillary suture. The latter condition partially agrees with that of the anterior choanae accommodating the vomeronasal ducts in *Sphenodon*, which separate the premaxillae from the anterolateral vomers [93].

We interpret that the sauropterygian antrochoanal foramina, which may be either paired or unpaired within a single genus or be absent altogether, are conservatively located in the vomeropremaxillary suture. Such foramina in plesiosaurs, when present, have been proposed to represent vomeronasal fenestrae that communicated with the Jacobson's or vomeronasal organ [94] that appears to be plesiomorphic for Tetrapoda. Notably, the large unpaired premaxillary foramina of crocodylians exist completely within the interpremaxillary suture [92] and do not house a functional vomeronasal organ, rendering them heterologous to the palatal foramina discussed here, contra [95]. Whereas an ichthian vomeronasal system may exist in some form [96], possibly including a hybrid olfactory and vomeronasal epithelium [67], a distinct vomeronasal chemoreceptor accommodated in a nasal diverticulum makes its first appearance in non-amniote tetrapods [97–99]. Although turtles enjoy chemoreception through a vomeronasal epithelium located in the nasal cavity [100], a discrete vomeronasal system separated from the nasal cavity is commonly present in many amniotes, such as in synapsids [98] and squamates [93, 101, 102]. The tubular Jacobson's organs of the rhynchocephalian *Sphenodon* communicate with the oral cavity through the anterior choanae [103]. They reside on the vomer and remain separated from the osseous nasal cavity only by the septomaxillae and

cartilaginous elements [104]. Within extant Archosauria, discrete extra-nasal vomeronasal organs do form in the embryonic crocodylian rostrum but subsequently disappear during early development while accessory olfactory lobes never form [105]. Nevertheless, the main olfactory epithelium in the nasal cavity of *Alligator* does incorporate solitary chemosensory cells [106]. Birds lack accessory olfactory lobes and vomeronasal nerves [107], and both zebra finch and chicken genomes have been demonstrated to lack genes encoding vomeronasal receptors altogether [108].

A discrete adult amniote vomeronasal system consistently comprises three osteologically discriminable components. Those are: 1) dorsoventrally trending ducts that originate at recesses in the dorsal oral cavity, 2) a pair of lumina that typically remains separated from the more dorsolaterally residing nasal cavities, and 3) posteriorly trending vomeronasal (terminal) nerves that ultimately penetrate the cribriform plate to terminate in the accessory olfactory lobes [98, 100, 102, 109]. In TW480000375, the anteriormost palatal foramina were found to independently connect to a single, small and discrete endosseous semi-cylindrical chamber positioned anteroventrally to the narial passage. The endosseous morphology of the vomeronasal organ in *Varanus exanthematicus* [93, 110] demonstrates that the bilateral separation of its vomeronasal lumina, which are positioned directly dorsal to the vomeronasal fenestrae (Panels A-C in S1 Fig; [110]), is largely achieved through a median internasal septum [111, 112] and most ventrally through a membranous wall (see also Fig 1 in [77]). Although the vomeronasal organs in the rostrum of *Sphenodon punctatus* [93, 113] are less constrained, the corresponding topography of the narial chamber floor exhibits clear bilateral separation ([104]; Panels D-F in S1 Fig; [113]).

The single median lumen in TW480000375 lacks any morphological indication for a median partition during life. It communicates peripherally with a premaxillary infrastructure arguably homologous to the rostral canal system resolved in an Upper Jurassic pliosaur [114] and at least superficially resembling those encountered in crocodylians and some theropod dinosaurs [115]. Those structures were tentatively interpreted to represent the peripheral neurovascular plexus of a dermal sensor innervated by the trigeminal nerve [114] and may very well have facilitated a corresponding function in *Nothosaurus*. Notably, a superficially similar maxillary infrastructure was interpreted to accommodate nutritive canals in a second Upper Jurassic pliosaur [116]. Although the vomeropremaxillary domain in TW480000375 has been demonstrated to crucially deviate from the conventional tetrapodal vomeronasal architecture, the bilateral nature of the vomeropremaxillary fenestrae, ducts, and associated posterior innervation in TW480000375 lends some support for an origin through median fusion of a bilateral system. The elongated yet slender rostral morphology of nothosaurs supports a deeply rooted dentition to form a piscivorous "trapping basket" [83, 117] that may conceivably have prevented the accommodation of extensive intraosseous systems and could justify an adaptive modification of the vomeronasal system.

Bony labyrinth. The dorsalmost portion of the endosseous labyrinth, represented by the dorsal apex of the crus communis and the medialmost aspects of the diverging posterior and anterior semicircular canals, are preserved in TW480000375 at the dorsolateral margins of the braincase endocast posterior to the osseous constriction that defines the transition to the posteriormost braincase endocast domain (feature 16 in Fig 2). These bifurcating tubular projections arise from a descending flange of the supraoccipital lateral to the braincase endocast and the nuchal ridge. Lateral to their origin on the braincase endocast, these voids anteroposteriorly expand into a bifurcation before their abrupt lateral truncation against matrix infilling. However, if the general curvature of the posterior branches of the bifurcations is continued through the opisthotics, additional tubular sections can be discerned along this trajectory (feature 21 in Fig 2). Except for these minor tubular sections of the posterior semicircular canals,

no other portions of the semicircular canals, the lagenae, and the vestibules could be reconstructed due to the absence of ossified correlates. The proximodorsal portion of the endosseous labyrinth is abruptly truncated at the level of the original sutures between (probably the epiotic contributions to) the supraoccipitals and the prootics, suggesting that both prootics were either lost or completely unossified. The anterior portion of the posterior semicircular canal and the posterior portion of the anterior semicircular canal are ellipsoidal in cross-section and measure ~0.66 mm along their major axis and ~0.45 mm along their minor axis, which renders them quite robust with respect to the size of the cranium. Furthermore, the spatial relation between the dorsal divergence of the anterior and posterior semicircular canal and the posteriormost expression of the posterior semicircular canal in the opisthotics demonstrates an anteroposterior expansion of the vestibular apparatus with respect to its dorsoventral height. This condition was also described for *Placodus* [35] and has been associated with an adaptation to an aquatic lifestyle [38, 118]. The discontinuously resolved endosseous labyrinth prevents the reconstruction of the "alert position" (see [51] for discussion).

Respiration and osmoregulation

Uppermost respiratory tract. The somewhat posteroventrally tilted external nares continue posteromedially into the nasal cavity that extends between the paired nasals and the vomers. The posterior portion of the nasal cavity constricts dorsally while ventrally opening up into the oral cavity through the internal nares (choanae). These are situated behind the external nares at the junction of the vomers, maxillae and palatines, and appear to be tilted somewhat posteroventrally with respect to the palate. Slightly anterior to the posterodorsal constriction of each narial passage, the nasal is perforated by a minute and dorsally branching aperture (feature 7 in Fig 2). The dorsally bulging chambers that continue immediately ventral and posterior the external nares represent nasal vestibules (feature 4 in Fig 2) and, more posteriorly, the cava nasi (feature 5 in Fig 2). Towards the internal nares, the narial passage slightly constricts into the nasopharyngeal duct (feature 6 in Fig 2). The geometry of the narial passage between the external and the internal nares offers reduced airway resistance, which is selected upon in the narial respiratory tracts in numerous marine tetrapods [119]. We conclude that this complex represents the air passage during nasal respiration. The maxilla and vomer share a well-developed suture that separates the vomeropremaxillary foramen from the internal naris, which represents the neochoanate condition (sensu [120]) for sauropsids [93].

Salt glands. The lateral and ventrolateral margins of the central antorbital void are mainly defined by the paired pterygoids. Around the anterior margin of the orbits, the inconspicuous prefrontals contribute to the lateral delimitation of the medial endocranial cavity. Posterolateral to the narial passages and internal choanae, and dorsomedially and dorsolaterally confined by respectively the lateral nasals and the medial maxillae, the cast of the nasal cavities reflects the presence of two pronounced and anterolaterally—posteromedially trending oblate, bilaterally paired, and partially constrained ellipsoid recesses that align with the anteromedial margin of the orbits (feature 8 in Fig 2). They correspond with voids that are in open communication with the posterolateral narial passages but remain excluded from the posteroventral narial passages and internal nares by a low bony ridge. All extant marine diapsids require extrarenal mechanisms for salt excretion, which are universally derived from cephalic glands (e.g. [121]). This advocates the presence of cephalic salt glands in *Nothosaurus marchicus*. The developmental affinity of cephalic salt glands is variable between groups and ranges from orbital glands in sea turtles to exclusively lateral nasal glands in lizards and (accessory) sublingual glands in sea snakes, to orbital, lingual and nasal glands in crocodylians [121–127]. It has been argued that nasally derived salt glands constitute the primitive diapsid condition that arose

through selection on maintaining ionic balance in particularly arid terrestrial habitats at the end of the Paleozoic [128]. The lacertid genus *Acanthodactylus* exhibits a "typical" squamate nasal architecture in which the nasal glands that reside in conchal spaces lateral to the cava nasa act as functional salt glands [126]. Fluid secreted by the lateral nasal glands passes into the nasal cavity through a secretory pore, collects in the vestibules, and is subsequently expelled by "sneezing" or allowed to dry out [126]. The paranasal recesses identified in TW480000375 are positioned posterolateral to the nasal cavity rather than purely lateral, but exhibit a similar communication with the nasal cavity as *Acanthodactylus*, which supports the inference that the paranasal recesses likely accommodated lateral nasal glands in TW480000375. The antorbital recesses in TW480000375 share their geometry, orientation and topographical position of the referred paranasal sinuses ventral to the nasomaxillary suture with the paired antorbital protuberant structures described in the marine fossil crocodylomorph *Geosaurus araucanensis* and in various other marine reptiles (e.g. [128] and references therein). Those antorbital structures have been explained to have accommodated hypertrophied nasal salt glands [128]. Such salt glands have furthermore been preliminarily reported in the Late Cretaceous polycotylid plesiosaur *Pahasapasaurus haasi* [129, 130] at a homologous location, although a detailed description has thus far been lacking. Their shared location under the medial maxillary suture posterior to the premaxillae and shared oblate spheroid geometry (indicated as "nc" in Fig 4 of [130]) corroborate the presence of homologously developed salt glands in TW480000375.

Vascularization

Infraparietal canals. Pronounced anteroposteriorly trending paired tubules were encountered in the fused parietals (feature 9 in Fig 2). Each parietal contains a posteroventral perforation near its anterior margin that gives rise to a posteriorly trending tubular channel. These channels gradually verge out into the secondary tubular mesh around the pineal foramen. The dorsal head vein (vena capitis dorsalis; vcd) enters the cranial endocast posterior to the pineal foramen in *Sphenodon* [131] and is associated with the dorsal sagittal sinus in squamates [59, 72]. In the dicynodont *Niassodon mfumukasi*, the pineal foramen perforates the medial aspect of the frontoparietal suture [101], comparable to the condition of *Sphenodon* [132], whereas it occupies a medial position in the posterior part of the compound parietal in TW480000375. This disparity in osseous configuration may have originated to accommodate the extreme elongation of the nothosaurian temporal domain [83]. Slightly posterior to the frontoparietal suture in *Niassodon mfumukasi*, the local trajectories of the bilateral branches of the vcd were resolved as posteromedially trending dorsal ridges that appear to discharge the frontal anterolaterally to the pineal foramen [133]. Intrafrontal veins supplying these endocranial intervals of the vcd were not described, but may be expected to be present anterior to the pineal foramen. The aforementioned tubules in TW480000375 were encountered at a corresponding location relative to the pineal foramen in, albeit in the parietal rather than in the frontal, and verge out before actually reaching the level of the pineal foramen. As such, these intraparietal tubules in TW480000375 would roughly continue into the inferred endocranial course for the vcd of *Niassodon mfumukasi* if the endocasts were superimposed. This lends support for the interpretation that the intraparietal pathways of TW480000375 accommodated the branches of the vcd discharging the vasculature of the dorsal cranium.

Internal carotid branches. Paired longitudinal cylindrical passages enter the cranium from the direction of the neck through occipital foramina distinctly lateral to the foramen magnum. They subsequently penetrate the pterygoid and ultimately merge with the braincase endocast near the cava epipterica. In their trajectories, these canals gradually arc from an anteromedial course near their occipital origin to an anterior course close to their contact with the

braincase endocast. A posterolateral bifurcation branches off at the level of the anterior squamosal suture with the parietal. This marks the posteromedial arrival of a second duct that lacks an osseous enclosure posteriorly to its penetration of the pterygoid. The internal carotid arteries are among the major cranial vessels in squamates [72] and crocodylians [134, 135]. The common carotid arteries depart from the dorsal branch of the aortic arch and bifurcate into an external and an internal carotid ramus before reaching the skull [72, 134, 135]. The internal carotid ramus gives rise to the cerebral carotid where the stapedial artery branches off [72, 134, 135]. After the departure of the stapedial artery, the cerebral carotid advances through the carotid canal where it eventually reaches the sella turcica. It continues anteriorly as the sphenopalatine artery [72, 134, 135]. More anteriorly still, the sphenopalatine artery runs through the vidian canal that also carries the palatine branch of the facial nerve [22, 71, 72, 136].

Most of the endocranial path of the internal carotid artery and its branches could be resolved in TW480000375, where they were found to broadly resemble the condition of *Nothosaurus mirabilis* [22]. The internal carotid penetrates the pterygoidal flange and remains entirely enclosed by bone during its lateral bypass of the hindbrain behind the cavum epiptericum in the carotid canal (feature 15 in Fig 2) and remains entirely excluded from the paracondylar interstices (feature 18 in Fig 2; see Discussion). The important connection to the sella turcica is not preserved in TW480000375, but the sphenopalatine artery that branches off simultaneously with the arch irrigating the pituitary gland must be located where the vidian canal shallows at the cavum epiptericum (feature 12 in Fig 2). Here, the corresponding artery passes onto the dorsal surface of the pterygoid [72] as it enters the basicranium at the level of the midbrain. This has previously been considered a derived condition in Nothosauroidea [22].

The encountered bifurcation may represent the departure of the stapedial artery (feature 14 in Fig 2) from the internal carotid, which would also imply that the internal carotid continues into the cerebral branch of the internal carotid (feature 13 of Fig 2) at this level. This interpretation is supported by the observations that the internal carotid artery bifurcates into the cerebral branch and the stapedial artery in the posteriormost region of the cranium in both *Iguana* [72] and *Alligator* [134]. In those taxa, the cerebral branch proceeds anteriorly to cross the sella turcica and irrigate the pituitary gland, which is partially reflected in the course of the cerebral branch in TW480000375. This is also consistent with nothosaurian material from Tunisia where the ventrolateral arrival of large carotid canals at the pituitary fossa was recorded [61]. The poorly resolved short branch of the referred bifurcation is directed posterolaterally in TW480000375, which is where the otic capsule resides. In both *Iguana* and *Alligator*, the stapedial artery proceeds dorsally towards the otic domain after its departure from the internal carotid [72, 134], where it irrigates the middle ear [100, 118]. Alternatively, this bifurcation could represent the arrival of a vein or nerve at the pterygoidal canal on its course towards the postcranium independent from the internal carotid but sharing the trans-pterygoidal osseous passage. In iguanids, both the internal jugular vein and the vagus nerve traverse the posterior cervical domain in close association with the internal carotid artery [72, 75].

Middle cerebral vein or paratympanic sinus. In the posteriormost segment of the braincase endocast, a bilateral pair of curved canals departs from the posterodorsal aspect of the endocranial cavity into the supraoccipitals while curving downwards and inflecting ventrolaterally into the otic capsule (feature 17 of Fig 2). These tubules arise at the suture shared by the supraoccipital and the prootic and overarch the dorsolateral bifurcation of the crus communis into the anterior and posterior semicircular canal (feature 16 of Fig 2) before opening up into the void of the otic domain ventrally. Based on comparison with extant crocodylians, the position and geometry of these passages suggest they either accommodated the middle cerebral vein [135] or allowed for communication between the paratympanic air sinus system and the

paired auditory system by overarching the brain [57]. A similar structure has recently been described in a highly secondarily-adapted crocodylomorph as the dorsal dural venous sinus [36] and was recognized as unnamed cavity in a related marine crocodylomorph taxon [37]. In squamates however, this region is formed by the dorsal longitudinal sinus or the parietal sinus [72], which would be expected to have corresponded with a clear osteological correlate. These foramina are unlikely to have accommodated cranial nerves, as they arise from a dorsal region of the endocast.

Discussion

Comparison with earlier work by Tilly Edinger

A wealth of morphological features of the cranial endocast and the otic system of *Nothosaurus mirabilis*, the type species of *Nothosaurus*, was previously identified [21]. This cranial endocast led Tilly Edinger to recognize, for example, an enlarged pineal organ, a continuously thick medulla oblongata, an olfactory complex without hemispherical swelling, an elongated olfactory tract, and three well-developed cranial nerves; the trigeminal (V), the statoacoustic (VIII, internal opening shared with the facial nerve VII), and the vagus nerve (X, opening shared with IX). However, Edinger later recognized that her initial interpretation [21] did include several errors [137]. The unossified nature of the otic region in our specimen leads us to consider that the statoacoustic and facial nerves reported [21] were actually artefacts of the endocast. In the otic domain, she further noted the presence of the external auditory meatus leading to the middle and inner ear, the position and extent of the endocasts of the vestibular system on the lateral walls of the braincase endocast (e.g. the saccule imprints in the prootic and the utricle), as well as the horizontal semicircular canal. The other semicircular canals were reportedly damaged during preparation. The pattern of cranial ossification in nothosaurs, which will be discussed in the following section in light of heterochronic trends, argues that finer structures, such as the utricle and saccule, may also represent artefacts of the endocast. Notably, we found no trace of the horizontal semicircular canal in our specimen, which also appears to be absent in other congeneric specimens (e.g. PGIMUH K3881 and SMNS 16363, TR pers. obs.).

Osteological aspects

Braincase heterochrony. The absence of (ossified) prootics suggests that TW480000375 had not yet reached skeletal maturity, which is inconsistent with the observation that the external cranial sutures appear well ossified. Prolonged or truncated physical and osteohistological maturation is a well-known trend in organisms secondarily adapted to an aquatic lifestyle [6, 9, 17, 92, 138–144]. This predominantly affects the postcranium in secondarily-adapted Mesozoic marine reptiles [9], but the specimen described here exhibits important cranial paedomorphism as well. Skeletal paedomorphosis in secondarily-adapted aquatic taxa is a common trait [144–146]. It typically results in decreased ossification during bone development, as with the extremely deferred prootic ossification in *Nothosaurus*, but it occasionally leads to deletion of cranial elements altogether [147, 148].

In TW480000375, the prootic is absent and only the occipital portion of the opisthotic is preserved. In the generalized developmental ossification sequence across reptiles, elements of the otic capsule are among the last to ossify [149, 150]. This is a common trait shared with synapsids [151], thus emphasizing the conservative nature of this pattern. The delayed, reduced or lacking ossification of components of the otic capsule is not an isolated preservational issue, as it was also observed in other nothosaurid specimens (e.g. [47, 148]; PGIMUH K3881, SMNS 16363; TR pers. obs.), as well as in plesiosaurs [139, 148]. We interpret this selective delay in ossification to result from paedomorphosis [152] through which the development of the bones

forming the otic capsule was considerably delayed relative to the ancestral state of basal neodiapsids, whose osseous otic capsule is conspicuously ossified (e.g. [153, 154]).

In nothosaurids, the delayed development of bones forming and supporting parts of the braincase and the otic capsule is reflected in the absence of various structures that are commonly preserved surrounding the brain in other taxa. For example, placodonts exhibit an osteologically matured braincase that permits the extraction of several well-defined cranial nerve passages and the osseous labyrinth [35], which is also the case for the Late Cretaceous plesiosaur *Libonectes morgani* [155]. Because the lateralmost braincase walls can only be interpolated in *Nothosaurus*, definition of the topology of most cranial nerves, the vestibular organ, and several brain structures is rendered impossible. The eosauropterygian pterygoid, on the other hand, is exceptionally large [9, 156–158] and remarkably well ossified [159]. It typically extends posteriorly from the preorbital region towards its contribution to the occiput where it supports the basicranial axis bones ventrally. Although the pterygoid is one of the first bones to ossify in reptiles [149, 150], the pronounced development of the eosauropterygian pterygoid relative to the ancestral state, conversely to the condition of the otic capsule, might be the result of peramorphosis [152]. Although the postcranial anatomy of eusauropterygians appears to predominantly reflect a paedomorphic trend, the cranial anatomy seems to exhibit a mosaic of heterochronic effects. This may have important implications for phylogenetic coding, as ossification of the external cranial elements is typically considered a reliable indicator for skeletal maturity in *Nothosaurus* where alpha taxonomy is predominantly founded on cranial characters (e.g. [16, 83, 160, 161]).

"Foramina eustachii" of Koken (1893). The ontogenetic plasticity [22], relatively large size, posteroventrally oriented occipital eruption, and absence of main vascular passages or potentially homologous foramina in other diapsids indicate that "foramina eustachii" probably represent taxon-specific and ontogeny-dependent morphological expressions of the junction between the basioccipital and the pterygoids rather than functional cranial foramina. Therefore, the geometry of these paracondylar interstices appears to be an architectural byproduct of the unique cranial construction of nothosauroids. Because these occipital gaps do not represent cranial foramina in the strict sense of the term, we suggest avoiding the interpretative term "eustachian foramina" and instead propose to adopt the descriptive term "paracondylar interstices" when referring to these phenomena,.

Cranial endocast

Endocast macrostructure. The specialized cranial condition in *Nothosaurus* that combines dorsoventral flattening with strong lateral constriction of the braincase by the temporal fenestrae is associated with an extremely elongated linear brain morphology that exhibits an overall sequential zonation of the brain along its anteroposterior axis, including a strongly extended olfactory tract [21, 47, 56]. Although the hindbrain is broader than the forebrain, which represents the conventional reptilian condition, the forebrain and hindbrain reside at the same dorsoventral level in the unusually straight and strongly anteroposteriorly orientated cranial endocast. A generally corresponding but less pronounced linear endocranial morphology has been reported for other marine reptiles, including the closely-related placodont *Placodus gigas* [35] and a lower Jurassic ichthyosaur [34]. A similar reconstructed brain morphology of thalattosuchians [36] was recently proposed to result from the large, laterally placed orbits [85], which would have provided comparable constraints on cerebral morphology as the temporal fenestra in *Nothosaurus marchicus*.

The total volume of the endocranial cavity, excluding the poorly defined olfactory tract and olfactory lobes, amounts to circa 810 mm^3. In reptiles, the brain itself does not fill the

endocranial cavity, which in fact mirrors the external surface of the dural envelope [49]. Therefore, the brain of crocodiles and certain dinosaurs is believed to occupy only circa 50–60% of the endocranial cavity [55, 162, 163]. The relation between condylobasal skull length and full body length in *Nothosaurus marchicus*, not corrected for ontogenetic allometry, was recently described [14], and yields a reconstructed body length of circa 650 mm for TW480000375. Assuming TW480000375 exhibited a body length to body mass ratio comparable with that of *Varanus keithhornei*, its total body mass would have been circa 270 g [164]. Similarly, comparison with a juvenile alligator (610 mm [165]) yields a reconstructed body mass of 306 g for TW480000375. A corresponding brain mass (assuming a brain density of 1.036 g/cm^3 [89]) between 0.4 (circa 50% of the braincase vault) and maximally 0.8 g (nearly 100% of the braincase vault) corresponds with a reptilian encephalization quotient (REQ; [166]) between 0.15 and 0.35. This places *Nothosaurus marchicus* within the typical range of the relation between body weight and brain weight followed by extant reptilian taxa [167].

The complex division of the brain in cerebral compartments is particularly challenging to recognize in extinct forms due to the presence of additional structures (e.g. meningeal layers) in the endocranial vault during life that usually do not preserve during fossilization [49, 56, 168]. Identification of discrete cerebral domains in fossils represented by exclusively osseous remains can only be successfully achieved through recognition and conservative application of well-understood osteological correlates of such soft-tissue structures in the cranium. For example, in the elongated brain of *Nothosaurus* with an associated sequential brain zonation, this implies that the suture between the prootic and the opisthotic, which ventrally terminates in the fenestra vestibuli, accounts for the anteriormost possible extent of the medulla oblongata, as the prootic represents an indisputable posterolateral delimitation of the cerebral domain, corroborated by a faint flexure. Particularly for taxa exhibiting a sequential zonation of the brain, the developmentally conservative relations between osseous markers and associated soft-tissue structures, such as those between the vestibular system and the cerebellum [169], are to be respected when delimiting and identifying individual brain compartments.

Pineal organ. Both the pineal eye and the associated pineal gland (also termed posterior parietal organ or epiphysis), which is retained as a neuroendocrine gland in numerous vertebrates lacking the pineal eye [170, 171]; see also [172]) have photosensitive capabilities [81], possibly because they represent the bilateral remnants of an originally paired structure [82, 173]. Together, these organs comprise the pineal complex [174] that, in modern lizards, influences behavior, body temperature regulation and reproductive synchrony on circadian to annual timescales through sensory stimulation of the endocrine pineal system that, for example, regulates thyroid activation [82, 170, 174–177]. Notably, contribution of the pineal eye to spatial orientation by means of a "time-compensated sun compass" when negotiating a water maze [178] and to the expression of aggressive display through an interaction between pineal endocrinal cues and thermoregulation [179] have also been documented. Finally, parietal foramen size in mosasaurs has been suggested to correlate positively with diving depth, but a hypothesized positive correlation with latitude could not be substantiated [180].

In most modern lizards, however, the size of the pineal organ strongly correlates with latitude and diurnality [181, 182], and the pineal eye may be absent altogether in equatorial species ([183] and references therein). A particular role for the pineal organ in "fine-tuning" thermoregulation in ectotherms was described and it was hypothesized that the reduction and loss of the pineal eye in Eucynodontia reflects the transition from exo- and mesothermia to endothermia [184]. Although plesiosaurs have been proposed to be homeothermic and capable of maintaining a body temperature substantially higher than that of ambient waters [185], a pineal foramen is variably present [155], and a somewhat enlarged pineal foramen was recognized in a Cretaceous plesiosaur recovered from a high paleo-latitude [186]. Pistosaurs exhibit

a cortical microstructure in their long bones indicative for high growth rate and high metabolic rate [18, 138] but also retain a well-developed pineal foramen (e.g. [6]). This suggests that, in Sauropterygia, an elevated metabolic rate does not preclude the presence of a well-developed pineal foramen, as was also noted for Eucynodontia [183]. Also, the pineal organ has been described as an adaptation to terrestriality [186], which is at odds with the large size of the pineal foramen in nothosaurs.

Nothosaurus exhibits a cortical microstructure that indicates a moderately low growth rate [138] and suggests a comparably low metabolic rate [18, 138]. The conclusion that *Nothosaurus marchicus* relied substantially on the pineal organ (see also [80]) is consistent with an exo- to marginally mesothermic thermoregulatory strategy inferred from osteohistological proxies. *Nothosaurus* has thus far only been reported from warm epicontinental seas [138] at tropical and subtropical paleolatitudes (Western and Central Europe, Israel, Tunisia, Saudi Arabia and South China; [6]), suggesting a distribution governed by isotherms. Exothermic sea snakes, notably lacking a photoreceptor in their pineal organ [82, 177], are incapable of elevating their body temperature substantially above the ambient water temperature, even when floating at the surface. They are therefore restricted within specific surface isotherms of circa 18–20˚ C [187–189]. Furthermore, most sea snakes and all sea kraits are bottom foragers that rapidly equilibrate to the lower temperatures at depths up to 100 m [189]. Although *Pelamis platurus* can stand a water temperature of 5˚ for about an hour of time and can tolerate circa 11˚ C for about 36 hours, substantially longer periods endured at even 17˚ C are lethal [188]. Paleotemperature proxies applied to stacked Triassic marine deposits across Europe, including Lower Muschelkalk deposits from Germany, have recovered a paleotemperature range between circa 18–32˚ C [190]. This demonstrates that a thermoregulatory strategy similar to that of modern sea snakes (e.g. [191]) appears to have been available to *Nothosaurus* without the necessity for a photosensitive pineal organ. This, in turn, suggests that an alternative or contributing accessory function may have provided the pineal organ with a functional advantage that warranted its proportionally large size in several non-pistosauroid sauropterygians. Interestingly, the pineal organ is also known to perform a neurosecretory function governing melatonin secretion and distribution [192]. Melatonin is responsible for regulating skin pigmentation, locomotion, somnia and reproduction [193]. Melatonin controls the activity of melanophores and thereby melanin concentrations in tissues [194, 195]. Furthermore, it has been observed that the admission of pineal gland extracts to various tetrapods causes lightening of skin color [196–199]. Countershading, or Thayer's Law, describes a mode of camouflage in which an animal's coloration is darker on the upper side and lighter on the underside of the body. This pattern is found in many species of mammals, reptiles, birds, fish, and insects, both predators and prey, and has occurred in marine reptiles at least since the Cretaceous period [200]. In marine environments, countershading appears to offer camouflage particularly for mid-level dwellers towards both deeper and shallower vantage points in the water column. In a shallow marine exotherm foraging at the sea floor over a light substrate, such as *Nothosaurus marchicus*, skin coloration is intuitively subjected to the conflicting demands of promoting heat absorption while afloat at the surface (conventional countershading) and ensuring sufficient camouflage while sojourning at the sea bottom. Involvement of the remarkably large pineal foramen and potentially enlarged pineal gland could offer a functional solution for this dilemma in *Nothosaurus*. Such a hypothesis, although speculative, proposes the consideration of a mode of adaptive skin pigmentation (metachrosis) through pigment translocation that adjusts skin tone on seasonal, diurnal or even sub-diurnal timescales towards optimally balancing thermoregulation and crypsis

Floccular complex. Relative size of the floccular complex has been argued to proportionally reflect the requirement for image stabilization during rapid, agile locomotion in

archosaurs through the vestibulocular and vestibulocollic reflexes [89], which grant a steady gaze during, for example, optical guidance while pursuing prey. This claim was recently challenged in a study assessing the relation between the size of the floccular fossa and ecology and behaviour across mammals and birds [90]. No floccular complex was recognized in TW480000375, although poor ossification of the prootic prevents reconstruction of this domain with absolute certainty. However, a floccular expression is also lacking in the endocast of the strongly ossified braincase of *Placodus gigas* [35]. Irrespective of the absolute predictive capabilities of relative floccular size and the contribution of other cerebellar regions to visual stabilization, the virtual absence of a floccular expression in the endocast of TW480000375 may be expected to correlate with reduced processing capacity and corresponding decreased performance [55], and may be linked with reduced oculomotor performance. This is intuitively more consistent with ambush predation than with endured, agile, high-speed pursuit of prey. Aquatic ambush predation guided by visual cues characterizes crocodylians (e.g. [84] and references therein), whereas vision also represents a crucial sense in short-distance ambush predation by various aquatic snakes and sea kraits [201, 202].

Sensory systems

Chemoperception. While the vomeronasal organ is present in many tetrapods, only selected squamates possess a deeply cleft or forked tongue of which the tips individually communicate (either directly or indirectly through sublingual plicae [203]) with paired palatal fenestra that lead to the paired lumen accommodating sensory epithelium [101, 204]. Such an arrangement enables tropotaxis: the immediate perception of directional gradients in the concentration of certain chemical compounds after tongue flicking, which permits sampling and directional comprehension of chemical prey cues prior to attack [101, 204]. Other squamates, including ambush-hunting iguanian lizards, but also the rhynchocephalian *Sphenodon*, have a less or non-bifurcated tongue that does not permit true tropotaxis but can aid in mediating chemosensory evaluation of prey during capture by lingual pretensions or after oral contact is established [204], which does not rely on perception of a directional component. Among squamates that engage in tongue flicking, actively hunting taxa tongue-flick regularly throughout their forage, whereas ambush hunting taxa only tongue-flick when moving between ambush sites [205].

Although *N. marchicus* possess paired vomeropremaxillary foramina that appear homologous to the vomeronasal fenestrae of extant tetrapods, these are spaced closely together and continue dorsally into a single, shared lumen. This pattern is most consistent with the absence of a forked tongue in *Nothosaurus* and, consequently, the inability of a "squamate" mode of chemical gradient detection by means of tropotaxis. Retention of chemosensory capability in *Nothosaurus*, however, cannot be ruled out. Non-directional applications of chemoperception, such as the evaluation of potential prey, do not rely on spatial separation of sampling locations. Furthermore, in a nectic marine predator, the capability of sequentially sampling ambient water currents rather than obtaining instantaneous directional information should be sufficient to engage in tracking biochemical gradients using klinotaxis. Notably, klinotaxis represents the plesiomorphic mode of spatial chemoperception for lepidosaurs [205].

Vomeronasal chemoreception has been suggested to contribute to the array of sensory perceptions available to Sauropterygia [94]. We have observed that sauropterygian foramina incisiva occur as either one single or as two paired vomeropremaxillary foramina (e.g. [7]). Furthermore, the paired vomeropremaxillary foramina of TW480000375 communicate with a single, medially positioned lumen. The endorostral morphology of TW480000375 thereby departs from the conventional architecture of vomeronasal chemoreceptors in tetrapods but

may have originated through median fusion of an initially bilaterally developed chemosensor under the morphological and ecological constraints imposed by the specialized rostral morphology of nothosaurs. It is well established that secondarily marine amniotes exhibit a reduced or even completely lost vomeronasal organ [206, 207], although a functional tropotactic vomeronasal system has been argued to have been present in mosasaurs [208]. The unique reduced endorostral morphology of TW480000375 reflects that of an atrophied vomeronasal organ with respect to those typically present in ground-dwelling tetrapods. Such an atrophied vomeronasal organ does not preclude the presence of an eusauropterygian rostral sensory system such as that proposed to enable mechano- or electrosensory perception in a pliosaur [114]. Notably, these two systems are not intrinsically linked, as chemoperception by the vomeronasal organ is achieved through innervation by the vomeronasal nerves connecting to the accessory olfactory lobes [209], whereas mechanoelectric perception is typically enabled through the facial nerve of the trigeminal nerve [210].

Olfaction. The limited osseous expression of the olfactory lobes on the ventral frontal prevents a confident reconstruction of their size and of the inferred neurosensory dependence on olfaction during life. Although the main olfactory system of extant marine reptiles performs poorly or not at all during submersion [100], and accommodation space for nasal olfactory epithelium may have been restricted through the presence of well-developed salt glands in *Nothosaurus* (this contribution), poorly defined osseous expressions of the olfactory lobes cannot be construed to conclusively support reduced olfactory performance. However, olfaction was evidently inhibited and will not have contributed considerably to successful subaqueous foraging. This pattern is convergent with many other secondarily aquatic tetrapods (e.g. [31, 211, 212]).

Respiration and osmoregulation

Nasal cavity. A previous study argued against a primarily respiratory function for the narial passage in Eusauropterygia in general and for Nothosauria in particular [116]. Exclusive nasal respiration is inconsistent with an oral morphology supporting relatively irregularly protruding fangs that would likely have prevented a watertight seal of the oral cavity (see also [213]), for example during surfacing with a partially submerged cranium. However, in absence of a secondary palate [116], we conclude that the narial passage between the external and the internal nares did provide an air passage accessory to oral respiration, providing the choanae were not continuously covered with a palatal tissue. Size reduction of the internal nares from pistosauroids to Plesiosauria has been reported [7, 156], and the resulting size discrepancy between the external and the internal nares in plesiosaurs has been deemed a critical obstruction during respiration [119]. More importantly, the referred evolutionary trajectory is also accompanied by a gradual rearrangement of the internal nares to a location anterior to the external nares (e.g. [94, 213]), which has been proposed to coincide with the development of a functional secondary palate [116, 119]. However, more basal sauropterygian taxa exhibit the more conventional choanal placement posterior to the external nares (e.g. *Nothosaurus*) or approximately at the same level (e.g. pachypleurosaurs [214]), which is consistent with a more traditional respiratory function in these groups.

Chelonioidea accommodate a designated and strongly domed olfactory chamber (the "upper chamber" of [98]) in their nasal architecture. It has been speculated that an air bubble trapped in this dome during submersion receives volatile chemicals from water pulsed through the sinuses, which permits olfactory access to waterborne chemicals in marine turtles [100]. Compared to the more strongly domed compartments in sea turtles, the dorsoventrally

flattened cranium of *Nothosaurus* only houses shallow nasal chambers in which air retention during cranial tilting or in turbulence appears highly unlikely.

Salt excretion. The "upper" olfactory chambers of marine Cryptodira share their topographical location and geometry with the recesses housing the postulated salt glands in *Nothosaurus marchicus* (consider the morphology of the "nasal cavity" of *Plesiochelys etalloni*; [59]). This suggests that the cryptodiran "upper olfactory chambers" and the nothosaurian antorbital recesses could represent homologous cranial voids in which glandular tissue may have exaptively replaced olfactory epithelium towards accommodating the increased need for salt excretion in the secondarily marine Sauropterygia. In extant diapsids, the secreted hypertonic solution is discharged into the nasal cavity and secreted through the nostrils [128]. In *Nothosaurus marchicus*, the postulated salt glands are contained within the posterior nasal domain and appear to remain partially separated from the narial airway by non-ossified septa, as indicated by bony ridges that supported such structures *in vivo*. Glandular discharge of hypertonic fluid likely proceeded into the cava nasa, where this solution could subsequently be expelled through the external nares, possibly aided by partial nasal respiration (as in some modern lizards [126]). Furthermore, choanal expulsion of saline discharge has been proposed specifically for Pistosauria [116]. However, since analogous modes of choanal discharge do not exist in modern taxa, phylogenetic support for this secondary mode of saline fluid emission is lacking. Additional discrete antorbital fenestra or neomorphic preorbital fenestra, such as present in *Geosaurus* and there suggested to potentially contribute to salt excretion [128], are absent in *Nothosaurus*. Lacrimal salt excretion as in sea turtles [123] appears highly unlikely for *Nothosaurus*, since sufficient interorbital accommodation space and the corresponding large interorbital foramen [214] that support lacrimal salt glands larger than the brain in sea turtles [215, 216] are absent in TW480000375.

An inferred hydrodynamically optimized "ram jet" configuration of the plesiosaurian narial passage has been proposed to benefit a speculative subaqueous operation of the main olfactory system or a vomeronasal chemosensor [213]. The main olfactory system probably does not function during submersion in extant non-chelonian reptiles [100] and we inferred that the chamber ancestrally lined with olfactory epithelium was likely at least partially occupied by the salt glands in *Nothosaurus*, which suggests a shared diminished dependence on the main olfactory system in plesiosaurs. Although the presence of hydrodynamically aided olfaction is therefore unsupported, the described forced flushing mechanism in plesiosaurs would be consistent with drainage of the hypertonic solution through the external nares rather than into the oral cavity.

Implications for lifestyle

Nothosaurus marchicus is among the most common reptilian components of the faunal assemblage preserved in the coastal to shallow marine deposits of the Vossenveld Formation [12, 45]. The abundance of *Nothosaurus marchicus* relative to the comparably common but smaller-bodied pachypleurosaur *Anarosaurus heterodontus* in the paleohabitat [12, 217] would not have supported a sustainable predator-prey relationship. Furthermore, *Nothosaurus marchicus* exhibits a dental morphology unsuitable for subduing or manipulating proportionally large or particularly hard-shelled prey. Its needle-like teeth and large, recurved rostral fangs are most consistent with a principally piscivorous diet [218, 219]. *Nothosaurus* remains are mostly recovered as isolated skeletal elements interpreted to have washed up and accumulated on the tidal flats post-mortem, implying these bones form a thanatocoenosis of taxa that may not all have been preserved in the habitat occupied *in vivo* [16]. However, the degree of articulation or association of some individuals and the integrity of most material recovered [12, 16] is inconsistent with prolonged post-mortem exposure and indicates a certain

proximity to the original habitats. The locally negligible gradient of the basin floor [220] therefore illustrates that *Nothosaurus marchicus* must have inhabited a shallow marine habitat, which is also corroborated by its pachyostotic ribs and limb bones [18, 19]. Such an environment should have enabled *N. marchicus* to traverse the entire water column to reach breathable air with ease. Notably, the combination of hyperostotic bones and piscivory in the basal cetacean *Remingtonocetus* has been argued to indicate ambush predation from a perch on the sea bottom, as rapid pursuit was deemed unlikely [221].

In the absence of indications for a pronounced development of the vomeronasal, olfactory or acoustic senses and pending the investigation of the presence and nature of integumentary mechanosensory organs in the rostrum of early sauropterygians, vision remains as the prime contactless sensory faculty. *Nothosaurus marchicus* features proportionally large orbits (~20% of total skull length), and optic lobes were potentially resolved on its endocast. It should be noted, however, that orbit size itself has been found to not absolutely correlate with eye size when phylogenetic effects are corrected for [222]. Furthermore, although no nothosauroids preserve sclerotic rings [6], various plesiosaurian specimens [69, 223–225] and European pachypleurosaurs [6] that collectively bracket *Nothosaurus* phylogenetically possess scleral rings with a relatively small internal diameter. Ichthyosaurs possessed large eyes and scleral rings with large apertures resulting in small f-numbers, which reflect adaptations to low-light environments [32, 226]. This discrepancy in scleral ring aperture between sauropterygians and ichthyosaurs may therefore also be explained by the pelagic nature and inferred deep-diving behavior of ichthyosaurs [200] that contrasts the shallow marine environments inhabited by *Nothosaurus marchicus*. Its orbital placement in the wedge-shaped cranium orients the eyes dorsally and somewhat anterolaterally, thus providing an inferred corresponding field of view with possible (partial) stereopsis. Crocodylians share this general ocular configuration and habitually engage in ambush predation, aided by their relatively low profile [227]. Modern marine predators carrying upward-directed eyes, such as particular crustaceans, typically inhabit the lower parts of the water column and use their vision to detect moving prey against the gloom above [65].

Dikoposichnus luopingensis is an ichnospecies reported from the Anisian of China [15] and interpreted to represent a foraging track of nothosaurid affinity. It reveals a foraging strategy that relied on punting locomotion over the seafloor envisioned to flush out crustaceans and fish that were subsequently snatched through sideway darting of the head [15]. Sojourning at or near the seafloor would have provided *Nothosaurus marchicus* with shelter against larger predators (e.g. [14]) while simultaneously enabling detection of potential overhead prey that could be ambushed and seized. As such, even the oldest known species of *Nothosaurus* already appears well adapted to a piscivorous ambush hunting strategy with an emphasized reliance on visual contrast. The intricate suite of adaptations to a marine lifestyle of late Early Triassic to early Middle Triassic sauropterygians in general and *Nothosaurus marchicus* in particular imply a profound specialization to a secondarily marine lifestyle that occurred in the first few million years after the P-T mass extinction event. Despite the more plesiomorphic appearance of Triassic sauropterygians, numerous aquatic adaptations that prefaced the prosperity of highly pelagic plesiosaurs during the Jurassic and Cretaceous were already present in the earliest such forms recognized to date.

Conclusions

Although *Nothosaurus marchicus* from the Vossenveld Formation of Winterswijk is among the oldest representatives of the genus, its cranial architecture and corresponding endocranial neurosensory configuration involve a broad variety of cranial adaptations that may have

underlain the explosive invasion of shallow marine habitats by Triassic eosauropterygians during the biotic recovery after the P-T event. Perhaps the most striking aspect of the *Nothosaurus* endocast is its simplified, straight brain morphology lacking particularly prominent cerebral portions, except for the epiphysis. Its anteroposteriorly elongated yet dorsoventrally flattened cranium with a particularly enlarged temporal musculature [22] imposed important constraints on the arrangement of neural and sensory organs and resulted in a remarkably straight brain shape. Despite these spatial limitations, TW480000375 accommodated a well-developed pineal photosensor and epiphysis, which suggests an important reliance on the corresponding pineal system *in vivo* and leads us to hypothesize may have been involved in a dynamic mode of skin tone regulation. Furthermore, vision must have presented one of the dominant distant senses, as suggested by the relatively large orbits, the potentially resolved optic lobes, and the lack of indications for other particularly well-developed remote sensory systems. The antorbital architecture of TW480000375 likely accommodated an atrophied vomeronasal organ and a rostral sensory organ, as well as well-developed salt glands, the latter two of which appear to have been retained in a Jurassic pliosaur and a Cretaceous polycotylid plesiosaur and as such may represent the plesiomorphic condition for Eusauropterygia. Specific adaptations in brain shape and certain modifications of associated organs, such as the anteroposterior elongation of the vestibular apparatus, were accommodated by heterochronic development of the cranium in general and of the braincase in particular. This differential expression of heterochronic effects warrants caution during the assessment of ontogenetic stages from cranial ossification patterns alone.

Nothosaurus marchicus appears to have occupied a largely piscivorous niche in shallow marine environments where a life position near the sea floor provided sufficient access to food sources through visual ambush predation, arguably some protection against apex predators, and ample access to breathable air at the surface. The spatial distribution of *Nothosaurus* between the reconstructed 18˚ C isotherms suggests an exothermic to possibly mesothermic thermoregulatory strategy, contrary to some Jurassic and Cretaceous pistosauroid sauropterygians.

Supporting information

S1 Fig. Vomeronasal structure in extant squamates. A-C. Virtual surface model of *Varanus exanthematicus* cranium in dorsal (A), ventral (B), and angled lateral (C) view. D-F. Virtual surface model of *Sphenodon punctatus* skull in dorsal (D), ventral (E), and angled lateral (F) view; anterior mandible excluded to reveal anterior palate in ventral view. The paired vomeronasal organ is labeled in red in both partially transparent crania. CT data sets of *Varanus exanthematicus* and *Sphenodon punctatus* were consulted on December 12 2016 through DigiMorph.org (Digimorph, 2004; The University of Texas High-Resolution X-ray CT Facility UTCT, and NSF grants IIS-0208675 and EF-0334961).
(TIF)

Acknowledgments

G. Diepenbroek discovered, prepared and generously donated TW480000375 to a public repository. We thank all members of the Muschelkalk Workgroup and Sibelco Europe MineralsPlus Winterswijk, which operates the Winterswijkse Steengroeve, and its manager Gerard ten Dolle for discussions and their relentless support of research to the Vossenveld Formation. D. Nieweg (TwentseWelle, Enschede, The Netherlands) is acknowledged for trusting us with the material in his care. HW van Dorssen kindly provided photographic material of

TW480000375. We are grateful to S. Voeten, F. Willekens and V. Beyrand for their vital assistance in specimen logistics. P. Tafforeau and V. Fernandez (European Synchrotron Radiation Facility, Grenoble, France) have made invaluable efforts in enabling and performing data acquisition and processing, and familiarized the first author with 3D visualization software. F. Spoor (University College London, London, United Kingdom) offered valuable advice towards resolving the portions of the endosseous labyrinth preserved in the studied specimen. S. Bureš (Palacký University, Olomouc, Czech Republic) arranged and provided access to facilities that were imperative for conducting the presented research. The suggestions proposed by A. Paulina-Carabajal, F. Knoll, and an anonymous reviewer, as well as the comments of editor W. Wong greatly improved the quality of the presented work. This study was partly funded by SNF grant Nos. 31003A_149506 & 173173 to TMS and through Fundação para a Ciência e Tecnologia fellowship SFRH/BPD/96205/2013 to RA. Data acquisition was performed during in-house beamtime at the ID19 Beamline of the ESRF.

Author Contributions

Conceptualization: Dennis F. A. E. Voeten, Tobias Reich.

Data curation: Dennis F. A. E. Voeten.

Formal analysis: Dennis F. A. E. Voeten, Tobias Reich, Ricardo Araújo.

Funding acquisition: Torsten M. Scheyer.

Investigation: Dennis F. A. E. Voeten, Tobias Reich, Ricardo Araújo.

Methodology: Dennis F. A. E. Voeten, Tobias Reich, Ricardo Araújo.

Project administration: Dennis F. A. E. Voeten, Tobias Reich.

Resources: Dennis F. A. E. Voeten, Torsten M. Scheyer.

Supervision: Dennis F. A. E. Voeten, Torsten M. Scheyer.

Validation: Dennis F. A. E. Voeten, Tobias Reich, Ricardo Araújo, Torsten M. Scheyer.

Visualization: Dennis F. A. E. Voeten, Tobias Reich.

Writing – original draft: Dennis F. A. E. Voeten, Tobias Reich, Ricardo Araújo.

Writing – review & editing: Dennis F. A. E. Voeten, Tobias Reich, Ricardo Araújo, Torsten M. Scheyer.

References

1. Scheyer TM, Romano C, Jenks J, Bucher H. Early Triassic marine biotic recovery: the predators' perspective. PLOS ONE. 2014; 9(3): e88987 https://doi.org/10.1371/journal.pone.0088987 PMID: 24647136
2. Sepkoski JJ. A factor analytic description of the Phanerozoic marine fossil record. Paleobiology. 1981; 7(1):36–53.
3. Jiang D-Y, Motani R, Tintori A, Rieppel O, Chen G-B, Huang J-D, et al. The Early Triassic eosauropterygian *Majiashanosaurus discocoracoidis*, gen. et sp. nov. (Reptilia, Sauropterygia), from Chaohu, Anhui Province, People's Republic of China. J Vertebr Paleontol. 2014; 34(5):1044–52 https://doi.org/10.80/02724634.2014.846264
4. Lucas SG, editor. The Triassic Timescale: Geol Soc Lond, Spec Publ, No. 334; 2010.
5. Rieppel O. Osteology of *Simosaurus gaillardoti* and the relationships of stem-group Sauropterygia. Fieldiana (Geol), New Series. 1994; 28:1–85.
6. Rieppel O. Sauropterygia I—Placodontia, Pachypleurosauria, Nothosauroidea, Pistosauroidea. Handbuch der Paläoherpetologie. 2000;Part 12A:1–134 [http://www.pfeil-verlag.de/07pala/d2_78.html].

7. Rieppel O, Sander PM, Storrs GW. The skull of the pistosaur *Augustasaurus* from the Middle Triassic of northwestern Nevada. J Vertebr Paleontol. 2002; 22(3):577–92.
8. Neenan JM, Scheyer TM. New specimen of *Psephoderma alpinum* (Sauropterygia, Placodontia) from the Late Triassic of Schesaplana Mountain, Graubünden, Switzerland. Swiss J Geosci. 2014; 107(2–3):349–57 https://doi.org/10.1007/s00015-014-0173-9
9. Rieppel O. *Helveticosaurus zollingeri* Peyer (Reptilia, Diapsida) skeletal paedomorphosis, functional anatomy and systematic affinities. Palaeontographica, Abt A. 1989; 208:123–52.
10. Sues H-D. The postcranial skeleton of *Pistosaurus* and the interrelationships of the Sauropterygia (Diapsida). Zool J Linn Soc. 1987; 90(2):109–31.
11. Hagdorn H, Simon T. Vossenveld-Formation. In: LithoLex [Online-Datenbank; Lithostratigraphisches Lexikon der Deutschen Stratigraphischen Kommission]. Hannover: BGR. Last updated 02.08.2010 [cited 19.06.2017]. Available from: https://litholex.bgr.de/gesamt_ausgabe_neu.php?id=45. 2010.
12. Oosterink HW, Berkelder W, de Jong C, Lankamp J, Winkelhorst H. Sauriërs uit de Onder-Muschelkalk van Winterswijk. Tilburg: Nederlandse Geologische Vereniging (Staringia 11, Grondboor & Hamer 57, 1a); 2003. 144 p.
13. Klein N, Scheyer TM. A new placodont sauropterygian from the Middle Triassic of the Netherlands. Acta Palaeontol Pol. 2014; 59(4):887–902 https://doi.org/10.4202/app.2012.0147
14. Voeten DFAE, Sander PM, Klein N. Skeletal material from larger Eusauropterygia (Reptilia: Eosauropterygia) with nothosaurian and cymatosaurian affinities from the Lower Muschelkalk of Winterswijk, The Netherlands. Pal Z. 2015; 89(4):943–60 https://doi.org/10.1007/s12542-014-0250-4
15. Zhang Q, Wen W, Hu S, Benton MJ, Zhou C, Xie T, et al. Nothosaur foraging tracks from the Middle Triassic of southwestern China. Nat Commun. 2014; 5:3973 https://doi.org/10.1038/ncomms4973 PMID: 24917514
16. Klein N, Voeten DFAE, Lankamp J, Bleeker R, Sichelschmidt OJ, Liebrand M, et al. Postcranial material of *Nothosaurus marchicus* from the Lower Muschelkalk (Anisian) of Winterswijk, The Netherlands, with remarks on swimming styles and taphonomy. Pal Z. 2015; 89(4):961–81 https://doi.org/10.1007/s12542-015-0273-5
17. Araújo R, Correia F. Soft-tissue anatomy of the plesiosaur pectoral girdle inferred from basal Eosauropterygia taxa and the extant phylogenetic bracket. Palaeontologia Electronica. 2015; 18.1.8A: 1–32 [palaeo-electronica.org/content/2015/1062-plesiosaur-pectoral-myology].
18. Krahl A, Klein N, Sander PM. Evolutionary implications of the divergent long bone histologies of *Nothosaurus* and *Pistosaurus* (Sauropterygia, Triassic). BMC Evol Biol. 2013; 13:1–23 https://doi.org/10.1186/1471-2148-13-123
19. Klein N, Sander PM, Krahl A, Scheyer TM, Houssaye A. Diverse aquatic adaptations in *Nothosaurus* spp. (Sauropterygia)—inferences from humeral histology and microanatomy. PLOS ONE. 2016; 11(7):e0158448 https://doi.org/10.1371/journal.pone.0158448 PMID: 27391607
20. Buchholtz EA, Seyfarth EA. The gospel of the fossil brain: Tilly Edinger and the science of paleoneurology. Brain Res Bull. 1999; 48(4):351–61 https://doi.org/10.1016/S0361-9230(98)00174-9 PMID: 10357066
21. Edinger T. Über *Nothosaurus*. I. Ein Steinkern der Schädelhöhle. Senckenbergiana. 1921; 3(5/6):121–9.
22. Rieppel O. The braincases of *Simosaurus* and *Nothosaurus*: monophyly of the Nothosauridae (Reptilia: Sauropterygia). J Vertebr Paleontol. 1994; 14(1):9–23.
23. Knoll F. La boîte crânienne d'un théropode (Saurischia) du Jurassique des Vaches Noires: ostéologie et paléoneurologie. Montpellier: Université des Sciences et Techniques du Languedoc. 1997;22 p. + 15 pl.
24. Knoll F, Buffetaut E, Bülow M. A theropod braincase from the Jurassic of the Vaches Noires cliffs (Normandy, France): osteology and palaeoneurology. Bull Soc géol Fr. 1999; 170(1):103–9.
25. Tafforeau P, Boistel R, Boller E, Bravin A, Brunet M, Chaimanee Y, et al. Applications of X-ray synchrotron microtomography for non-destructive 3D studies of paleontological specimens. Appl Phys A Mater Sci Proc. 2006; 83:195–202 https://doi.org/10.1007/s00339-006-3507-2
26. Sanchez S, Ahlberg PE, Trinajstic KM, Mirone A, Tafforeau P. Three-dimensional synchrotron virtual paleohistology: a new insight into the world of fossil bone microstructures. Microsc Microanal. 2012; 18:1095–105 https://doi.org/10.1017/S1431927612001079 PMID: 23026256
27. Walls GL. The Vertebrate Eye and its Adaptive Radiation. New york: Hafner Publishing Company; 1963. 785 p.
28. Atema J, Fay RR, Popper AN, Tavolga WN, editors. Sensory Biology of Aquatic Animals. New York: Springer-Verlag; 1988.

29. Thewissen JGM, Nummela S, editors. Sensory Evolution on the Threshold. Adaptations in Secondarily Aquatic Vertebrates [ISBN 978-0-520-25278-3]. Berkeley: University of California Press; 2008.
30. Spoor F, Thewissen JGM. Comparative and functional anatomy of balance in aquatic mammals. In: Thewissen JGM, Nummela S, editors. Sensory Evolution on the Threshold Adaptations in Secondarily Aquatic Vertebrates [ISBN 978-0-520-25278-3]. Berkeley: University of California Press; 2008. p. 257–84.
31. Kishida T, Thewissen JGM, Hayakawa T, Imai H, Agata K. Aquatic adaptation and the evolution of smell and taste in whales. Zool Lett. 2015; 1:9 https://doi.org/10.1186/s40851-014-0002-z PMID: 26605054
32. Motani R, Rothschild BM, Wahl W Jr. Large eyeballs in diving ichthyosaurs. Nature. 1999; 402:747 https://doi.org/10.1038/45435
33. Cuthbertson R, Maddin HC, Holmes R, Anderson JS. The braincase and endosseous labyrinth of *Plioplatecarpus peckensis* (Mosasauridae, Plioplatecarpinae), with functional implications for locomotor behaviour. Anat Rec. 2015: 298(9):1597–611 https://doi.org/10.1002/ar.23180 PMID: 26052684
34. Marek RD, Moon BC, Williams M, Benton MJ. The skull and endocranium of a Lower Jurassic ichthyosaur based on digital reconstructions. Palaeontology. 2015; 58(4):723–42 https://doi.org/10.1111/pala.12174
35. Neenan JM, Scheyer TM. The braincase and inner ear of *Placodus gigas* (Sauropterygia, Placodontia)—a new reconstruction based on micro-computed tomographic data. J Vertebr Paleontol. 2012; 32 (6):1350–7 https://doi.org/10.080/02724634.2012.695241
36. Brusatte SL, Muir A, Young MT, Walsh S, Steel L, Witmer LM. The braincase and neurosensory anatomy of an Early Jurassic marine crocodylomorph: implications for crocodylian sinus evolution and sensory transitions. Anat Rec. 2016; 299:1511–30 https://doi.org/10.002/ar.23462
37. Fernández MS, Paulina-Carabajal A, Gasparini Z, Chong-Díaz G. A metriorhynchid crocodyliform braincase from northern Chile. J Vertebr Paleontol. 2011; 31(2):369–77 https://doi.org/10.1080/02724634.2011.550361
38. Lautenschlager S, Butler RJ. Neural and endocranial anatomy of Triassic phytosaurian reptiles and convergence with fossil and modern crocodylians. PeerJ. 2016; 4:e2251 https://doi.org/10.7717/peerj.2251 PMID: 27547557
39. Holloway WL, Claeson KM, O'Keefe FR. A virtual phytosaur endocast and its implications for sensory system evolution in archosaurs. J Vertebr Paleontol. 2013; 33(4):848–57 https://doi.org/10.1080/02724634.2013.747532
40. Nosotti S, Rieppel O. The braincase of *Placodus* Agassiz, 1833 (Reptilia, Placodontia). Mem Soc Ital Sci Nat Mus Civ Stor Nat Milano. 2002; 31(1):3–18.
41. Albers PCH. New *Nothosaurus* skulls from the Lower Muschelkalk of the western Lower Saxony Basin (Winterswijk, The Netherlands) shed new light on the status of *Nothosaurus winterswijkensis*. Netherlands J Geosci / Geol Mijnbouw. 2011; 90(1):15–22.
42. Oosterink HW, Diepenbroek GH. Nieuwe vondsten uit de Winterswijkse Trias. Grondboor en Hamer. 1990; 44(6): 150–4
43. Albers PCH. A new specimen of *Nothosaurus marchicus* with features that relate the taxon to *Nothosaurus winterswijkensis*. PalArch Papers (Vertebrate Palaeontology) [wwwPalArchnl]. 2005; 3(1):1–7.
44. Bailleul AM, Horner JR. Comparative histology of some craniofacial sutures and skull-base synchondroses in non-avian dinosaurs and their extant phylogenetic bracket. J Anat. 2016; 229(2):252–85 https://doi.org/10.1111/joa.12471 PMID: 27111332
45. Oosterink HW. Winterswijk, Geologie Deel II. De Trias-periode (geologie, mineralen en fossielen). Wetenschappelijke Mededelingen van de Koninklijke Nederlandse Natuurhistorische Vereniging. 1986; 178.
46. Paganin D, Mayo SC, Gureyev TE, Miller PR, Wilkins SW. Simultaneous phase and amplitude extraction from a single defocused image of a homogeneous object. Journal of Microscopy. 2002; 206 (1):33–40 https://doi.org/10.1046/j.365-2818.002.01010.x
47. Koken E. Beiträge zur Kenntnis der Gattung *Nothosaurus*. Z dt geol Ges. 1893; 45:337–77.
48. Bellairs Ad'A. The anterior brain-case and interorbital septum of Sauropsida, with a consideration of the origin of snakes. Zool J Linn Soc. 1949; 41(281):482–512.
49. Witmer LM, Ridgely RC, Dufeau DL, Semones MC. Using CT to peer into the past: 3D visualization of the brain and ear regions of birds, crocodiles, and nonavian dinosaurs. In: Endo H, Frey R, editors. Anatomical Imaging Towards a New Morphology [ISBN: 978-4-431-76932-3; 105 pp]. Tokyo: Springer; 2008. p. 67–87.
50. Witmer LM, Ridgely RC. Structure of the brain cavity and inner ear of the centrosaurine ceratopsid *Pachyrhinosaurus* based on CT scanning and 3D visualization. In: Currie PJ, editor. A New Horned

Dinosaur From an Upper Cretaceous Bone Bed in Alberta. Ottawa: National Research Council Research Press; 2008. p. 117–44.

51. Witmer LM, Ridgely RC. New insights into the brain, braincase, and ear region of tyrannosaurs (Dinosauria, Theropoda), with implications for sensory organization and behavior. Anat Rec. 2009; 292 (9):1266–96 https://doi.org/10.002/ar.20983

52. Witmer LM, Ridgely RC. The paranasal air sinuses of predatory and armored dinosaurs (Archosauria: Theropoda and Ankylosauria) and their contribution to cephalic structure. Anat Rec. 2008; 291:1362–88 https://doi.org/10.002/ar.20794

53. Witmer LM. The Extant Phylogenetic Bracket and the importance of reconstructing soft tissues in fossils. In: Thompson JJ, editor. Functional Morphology in Vertebrate Paleontology. Cambridge: Cambridge University Press; 1995. p. 19–33.

54. Kley NJ, Sertich JJW, Turner AH, Krause DW, O'Conner PM, Georgi JA. Craniofacial morphology of *Simosuchus clarki* (Crocodyliformes: Notosuchia) from the Late Cretaceous of Madagascar. J Vertebr Paleontol. 2010; 30(sp1):13–98 https://doi.org/10.1080/02724634.2010.532674

55. Jerison HJ. Evolution of the Brain and Intelligence. New York: Academic Press; 1973.

56. Hopson JA. Paleoneurology. In: Gans C, Northcutt RG, Ulinski P, editors. Biology of the Reptilia Vol 9 —Neurology A. London: Academic Press; 1979. p. 39–146.

57. Dufeau DL, Witmer LM. Ontogeny of the middle-ear air-sinus system in *Alligator mississippiensis* (Archosauria: Crocodylia). PLOS ONE. 2015; 10(9): e0137060 https://doi.org/10.1371/journal.pone.0137060 PMID: 26398659

58. Paulina-Carabajal A, Sterli J, Georgi J, Poropat SF, Kear BP. Comparative neuroanatomy of extinct horned turtles (Meiolaniidae) and extant terrestrial turtles (Testudinidae), with comments on the palaeobiological implications of selected endocranial features. Zool J Linn Soc. 2017:1–21 https://doi.org/10.1093/zoolinnean/zlw024

59. Paulina-Carabajal A, Sterli J, Müller J, Hilger A. Neuroanatomy of the marine Jurassic turtle *Plesiochelys etalloni* (Testudinata, Plesiochelyidae). PLOS ONE. 2013; 8(7): e69264 https://doi.org/10.1371/journal.pone.0069264 PMID: 23844257

60. Mautner A-K, Latimer AE, Fritz U, Scheyer TM. An updated description of the osteology of the pancake tortoise *Malacochersus tornieri* (Testudines: Testudinidae) with special focus on intraspecific variation. J Morphol. 2017; 278(3):321–33 https://doi.org/10.1002/jmor.20640 PMID: 28121010

61. Gorce F. Étude de quelques vertébrés du Muschelkalk du Djebel Rehach (Sud tunisien). Mém Soc Géol France (N. S.). 1960; 88, B:1–33.

62. Säve-Söderbergh G. On the fossa hypophyseos and the attachment of the retractor bulbi group in *Sphenodon*, *Varanus*, and *Lacerta*. Ark Zool. 1946; 38:1–24.

63. Wedin B. The origin and development of the extrinsic ocular muscles in the alligator. J Morphol. 1953; 92(2):303–35 https://doi.org/10.1002/jmor.1050920205

64. Hanken J, Hall BK, editors. The Skull: Volume 2, Patterns of Structural and Systematic Diversity. Chicago: University of Chicago Press; 1993.

65. Land MF, Nilsson D-E. Animal Eyes. Oxford: Oxford University Press; 2002. 244 p.

66. Hetherington T. Comparative anatomy and function of hearing in aquatic amphibians, reptiles, and birds. In: Thewissen JGM, Nummela S, editors. Sensory Evolution on the Threshold Adaptations in Secondarily Aquatic Vertebrates [ISBN 978-0-520-25278-3]. Berkeley: University of California Press; 2008. p. 183–209.

67. Dendy A. The intracranial vascular system of *Sphenodon*. Phil Trans R Soc Lond B, Containing Papers of a Biological Character. 1909; 200(548):403–26.

68. Sues H-D. On the skull of *Placodus gigas* and the relationships of the Placodontia. J Vertebr Paleontol. 1987; 7(2):138–44 [http://www.jstor.org/stable/4523133].

69. Ketchum HF, Benson RBJ. Global interrelationships of Plesiosauria (Reptilia, Sauropterygia) and the pivotal role of taxon sampling in determining the outcome of phylogenetic analyses. Biol Rev. 2010; 85 (2):361–92 https://doi.org/10.1111/j.1469-185X.2009.00107.x PMID: 20002391

70. Iordansky NN. The skull of the Crocodylia. In: Gans C, Parsons TS, editors. Biology of the Reptilia Volume 4—Morphology D. London: Academic Press; 1973. p. 201–62.

71. Evans SE. The skull of lizards and tuatara. In: Gans C, Gaunt AS, editors. Biology of the Reptilia Volume 20 Morphology H The Skull of Lepidosauria. Ithaca, New York: SSAR; 2008. p. 1–348.

72. Porter WR, Witmer LM. Vascular patterns in iguanas and other squamates: blood vessels and sites of thermal exchange. PLOS ONE. 2015; 10(10):e0139215 doi: 10.1371/journal.pone.0139215. PMID: 26466378

73. Ali F, Zelenitsky DK, Therrien F, Weishampel DB. Homology of the "ethmoid complex" of tyrannosaurids and its implications for the reconstruction of the olfactory apparatus of non-avian theropods. J Vertebr Paleontol. 2008; 28(1):123–33 https://doi.org/10.1671/0272-4634(2008)28[123:HOTECO]2.0.CO;2

74. Paluh DJ, Sheil CA. Anatomy of the fully formed chondrocranium of *Emydura subglobosa* (Chelidae): a pleurodiran turtle. J Morphol. 2013; 274:1–10. https://doi.org/10.1002/jmor.20070 PMID: 22972700

75. Oelrich TM. The anatomy of the head of *Ctenosaura pectinata* (Iguanidae). Mus Zool, Univ Michigan, Misc Publ. 1956;No. 94:9–122.

76. Konishi T, Caldwell MW. New material of the mosasaur *Plioplatecarpus nichollsae* Cuthbertson et al., 2007, clarifies problematic features of the holotype specimen. J Vertebr Paleontol. 2009; 29(2):417–36 https://doi.org/10.1671/039.029.0225

77. Dakrory AI. Innervation of the olfactory apparatus of *Varanus niloticus* (Squamata–Lacertilia-Varanidae). J Am Sci. 2011; 7(9):118–25.

78. Sales MAF, Schultz CL. Paleoneurology of *Teyumbaita sulcognathus* (Diapsida: Archosauromorpha) and the sense of smell in rhynchosaurs. Palaeontologia Electronica. 2014; 17, Issue 1; 15A; 10p [palaeo-electronica.org/content/2014/705-olfaction-in-rhynchosaurs].

79. Sato T. *Terminonatator ponteixensis*, a new elasmosaur (Reptilia; Sauropterygia) from the Upper Cretaceous of Saskatchewan. Jo J Vertebr Paleontol. 2003; 23(1):89–103 https://doi.org/10.1671/0272-4634(2003)23[89:TPANES]2.0.CO;2

80. Edinger T. The size of parietal foramen and organ in reptiles. A rectification. Bull Mus Comp Zool. 1955; 114(1):1–34.

81. Crumly CR. The "parietal" foramen in turtles. J Herpetol. 1982; 16(3):317–20.

82. Hamasaki DI, Eder DJ. Adaptive radiation of the pineal system. In: Crescitelli F, editor. Handbook of Sensory Physiology Volume VII/5 The Visual System in Vertebrates. Berlin: Springer; 1977. p. 497–548.

83. Rieppel O, Wild R. A revision of the genus *Nothosaurus* (Reptilia: Sauropterygia) from the Germanic Triassic, with comments on the status of *Conchiosaurus clavatus*. Fieldiana (Geol), New Series. 1996; No. 34:1–82.

84. Nagloo N, Collin SP, Hemmi JM, Hart NS. Spatial resolving power and spectral sensitivity of the saltwater crocodile, *Crocodylus porosus*, and the freshwater crocodile, *Crocodylus johnstoni*. J Exp Biol. 2016; 219:1394–404 https://doi.org/10.1242/jeb.135673 PMID: 27208035

85. Pierce SE, Williams M, Benson RBJ. Virtual reconstruction of the endocranial anatomy of the early Jurassic marine crocodylomorph *Pelagosaurus typus* (Thalattosuchia). PeerJ. 2017; 5:e3225 https://doi.org/10.7717/peerj.3225 PMID: 28462034

86. Jirak D. Janacek J. Volume of the crocodilian brain and endocast during ontogeny. PLOS ONE 2017; 12(6): e0178491 https://doi.org/10.1371/journal.pone.0178491 PMID: 28614349

87. Rogers SW. *Allosaurus*, crocodiles, and birds: evolutionary clues from spiral computed tomography of an endocast. Anat Rec. 1999; 257:162–73. PMID: 10597341

88. Nieuwenhuys R, Ten Donkelaar HJ, Nicholson C, editors. The Central Nervous System of Vertebrates. Volume 3. Berlin: Springer; 1998.

89. Witmer LM, Chatterjee S, Franzosa J, Rowe T. Neuroanatomy of flying reptiles and implications for flight, posture and behaviour. Nature. 2003; 425:950–3. https://doi.org/10.1038/nature02048 PMID: 14586467

90. Ferreira-Cardoso S, Araújo R, Martins NE, Martins GG, Walsh S, Martins RMS, et al. Floccular fossa size is not a reliable proxy of ecology and behaviour in vertebrates. Nat Sci Rep. 2017; 7:2005 https://doi.org/10.1038/s41598-017-01981-0 PMID: 28515458

91. Hv Meyer. Die Saurier des Muschelkalks mit Rücksicht auf die Saurier aus Buntem Sandstein und Keuper. Zur Fauna der Vorwelt, zweite Abtheilung, VIII+ 167 pages. Frankfurt: Heinrich Keller; 1847–1855.

92. Romer AS. Osteology of the Reptiles. Chicago: University of Chicago Press; 1956. 772 p.

93. Rieppel O, Gauthier J, Maisano J. Comparative morphology of the dermal palate in squamate reptiles, with comments on phylogenetic implications. Zool J Linn Soc. 2008; 152(1):131–52.

94. Carpenter K. Comparative cranial anatomy of two North American Cretaceous plesiosaurs. In: Callaway JM, Nicholls EL, editors. Ancient Marine Reptiles. San Diego, California: Academic Press; 1997. p. 191–216.

95. Chatterjee S, Small BJ. New plesiosaurs from the Upper Cretaceous of Antarctica. Geol Soc Lond, Spec Publ. 1989;No 47:197–215.

96. Ubeda-Bañon I, Pro-Sistiaga P, Mohedano-Moriano A, Saiz-Sanchez D, de la Rosa-Prieto C, Gutierrez-Castellanos N, et al. Cladistic analysis of olfactory and vomeronasal systems. Front Neuroanat. 2011; 5:3 https://doi.org/10.3389/fnana.2011.00003 PMID: 21290004

97. Reiss JO, Eisthen HL. Comparative anatomy and physiology of chemical senses in amphibians. In: Thewissen JGM, Nummela S, editors. Sensory Evolution on the Threshold Adaptations in Secondarily Aquatic Vertebrates [ISBN 978-0-520-25278-3]. Berkeley: University of California Press; 2008. p. 43–63.

98. Taniguchi K, Taniguchi K. Phylogenic studies on the olfactory system in vertebrates. J Vet Med Sci. 2014; 76(6):781–8 https://doi.org/10.1292/jvms.13-0650 PMID: 24531771

99. Dawley EM, Bass AH. Chemical access to the vomeronasal organs of a plethodontid salamander. J Morphol. 1989; 200(2):163–74 https://doi.org/10.1002/jmor.1052000206

100. Schwenk K. Comparative anatomy and physiology of chemical senses in nonavian aquatic reptiles. In: Thewissen JGM, Nummela S, editors. Sensory Evolution on the Threshold Adaptations in Secondarily Aquatic Vertebrates [ISBN 978-0-520-25278-3]. Berkeley: University of California Press; 2008. p. 65–81.

101. Schwenk K. Why snakes have forked tongues. Science. 1994; 263(5153):1573–7. https://doi.org/10.1126/science.263.5153.1573 PMID: 17744784

102. Schwenk K. Of tongues and noses: chemoreception in lizards and snakes. Trends Ecol Evol. 1995; 10:7–12. PMID: 21236937

103. Pratt CW. The morphology of the ethmoidal region of *Sphenodon* and lizards. Proc Zool Soc Lond. 1948; 118(1):171–201 https://doi.org/10.1111/j.096-3642.1948.tb00372.x

104. Broom R. On the Organ of Jacobson in *Sphenodon*. Zool J Linn Soc. 1906; 29(194):414–20.

105. Parsons TS. Nasal anatomy and the phylogeny of reptiles. Evolution. 1959; 13(2):175–87.

106. Hansen A. Olfactory and solitary chemosensory cells: two different chemosensory systems in the nasal cavity of the American alligator, *Alligator mississippiensis*. BMC Neurosci. 2007; 8:64 https://doi.org/10.1186/1471-2202-8-64 PMID: 17683564

107. Wenzel BM. The olfactory and related systems in birds. Ann NY Acad Sci. 1987; 519:137–49.

108. Warren WC, Clayton DF, Ellegren H, Arnold AP, Hillier LW, Künstner A, et al. The genome of a song bird. Nature. 2010; 464:757–62 https://doi.org/10.1038/nature08819 PMID: 20360741

109. Halpern M. The organization and function of the vomeronasal system. Annu Rev Neurosci. 1987; 10:325–62 https://doi.org/10.1146/annurev.ne.10.030187.001545 PMID: 3032065

110. The Deep Scaly Project, 2006, "Varanus exanthematicus" (On-line), Digital Morphology. Accessed June 27, 2017 at http://digimorph.org/specimens/Varanus_exanthematicus/.

111. Bahl KN. Skull of *Varanus* monitor (Linn.). Rec Indian Mus. 1937; 39:133–74.

112. Russell DA. Systematics and morphology of American mosasaurs. Peabody Mus Nat Hist Bull. 1967; No. 23:1–241.

113. Maisano J. "Sphenodon punctatus, Tuatara" (On-line), Digital Morphology. Accessed June 27, 2017 at http://digimorph.org/specimens/Sphenodon_punctatus/adult/.

114. Foffa D, Sassoon J, Cuff AR, Mavrogordato MN, Benton MJ. Complex rostral neurovascular system in a giant pliosaur. Naturwissenschaften. 2014; 101(5):453–6 https://doi.org/10.1007/s00114-014-1173-3 PMID: 24756202

115. Hone DWE, Holtz TR Jr. A century of spinosaurs - a review and revision of the Spinosauridae with comments on their ecology. Acta Geol Sin (English Edition). 2017; 91:1120–1132.

116. Buchy M-C, Frey E, Salisbury SW. The internal cranial anatomy of the Plesiosauria (Reptilia, Sauropterygia): evidence for a functional secondary palate. Lethaia. 2006; 39:289–303.

117. Rieppel O. Feeding mechanics in Triassic stem-group sauropterygians: the anatomy of a successful invasion of Mesozoic seas. Zool J Linn Soc. 2002; 135(1):33–63.

118. Georgi JA, Sipla JS. Comparative and functional anatomy of balance in aquatic reptiles and birds. In: Thewissen JGM, Nummela S, editors. Sensory Evolution on the Threshold Adaptations in Secondarily Aquatic Vertebrates [ISBN 978-0-520-25278-3]. Berkeley: University of California Press; 2008. p. 233–56.

119. Schumacher BA, Carpenter K, Everhart MJ. A new Cretaceous pliosaurid (Reptilia, Plesiosauria) from the Carlile Shale (middle Turonian) of Russell County, Kansas. J Vertebr Paleontol. 2013; 33(3):613–28 https://doi.org/10.1080/02724634.2013.722576

120. Lakjer T. Studien über die Gaumenregion bei Sauriern im Vergleich mit Anamniern und primitiven Sauropsiden. Zool Jahrb, Abt Anat Ontog Tiere. 1927; 49:57–356.

121. Schmidt-Nielsen K, Fange R. Salt glands in marine reptiles. Nature. 1958; 182:782–5 https://doi.org/10.1038/182783a0

122. Cramp RL, Meyer EA, Sparks N, Franklin CE. Functional and morphological plasticity of crocodile (*Crocodylus porosus*) salt glands. J Exp Biol. 2008; 211(9):1482–9 https://doi.org/10.242/jeb.015636

123. Dunson WA. Salt glands in reptiles. In: Gans C, Dawson WR, editors. Biology of the Reptilia Volume 5 Physiology A. London: Academic Press; 1976. p. 413–45.

124. Dunson WA, Packer RK, Dunson MK. Sea snakes: an unusual salt gland under the tongue. Science. 1971; 173(3995):437–41 https://doi.org/10.1126/science.173.3995.437 PMID: 17770448

125. Peaker M, Linzell JL. Salt glands in birds and reptiles. Monogr Physiol Soc. 1975;No. 32:1–297.

126. Duvdevani I. The anatomy and histology of the nasal cavities and the nasal salt gland in four species of fringed-toed lizards, *Acanthodactylus* (Lacertidae). J Morphol. 1972; 137(3):353–63 https://doi.org/10.1002/jmor.1051370306

127. Hazard LC. Sodium and potassium secretion by iguana salt glands: acclimation or adaptation? In: Alberts AC, Carter RL, Hayes WK, Martins EP, editors. Iguanas: Biology and Conservation. Berkeley: University of California Press; 2004. p. 84–96.

128. Babonis LS, Brischoux F. Perspectives on the convergent evolution of tetrapod salt glands. Integr Comp Biol. 2012; 52(2):245–56 https://doi.org/10.1093/icb/ics073 PMID: 22586069

129. Martin J, Fernández M. Salt glands identified in a Late Cretaceous polycotylid plesiosaur. J Vertebr Paleontol, SVP Program and Abstracts Book, 2009. 2009:143A.

130. Schumacher BA. A new polycotylid plesiosaur (Reptilia; Sauropterygia) from the Greenhorn Limestone (Upper Cretaceous; lower upper Cenomanian), Black Hills, South Dakota. Geol Soc AM Spec Pap. 2007;No. 427:133–46.

131. O'Donoghue CH. The blood vascular system of the tuatara, *Sphenodon punctatus*. Phil Trans R Soc Lond B. 1921; 210:175–252 https://doi.org/10.1098/rstb.921.0006

132. Rieppel O. The skull in a hatchling of *Sphenodon punctatus*. Journal of Herpetology. 1992; 26(1):80–84.

133. Castanhinha R, Araújo R, Júnior LC, Angielczyk KD, Martins GG, Martins RMS, et al. Bringing dicynodonts back to life: paleobiology and anatomy of a new emydopoid genus from the upper Permian of Mozambique. PLOS ONE. 2013; 8(12): e80974 https://doi.org/10.1371/journal.pone.0080974 PMID: 24324653

134. Porter WR, Sedlmayr JC, Witmer LM. Vascular patterns in the heads of crocodilians: blood vessels and sites of thermal exchange. J Anat. 2016; 229(6):800–24 https://doi.org/10.1111/joa.12539 PMID: 27677246

135. Sedlmayr JC. Anatomy, evolution, and functional significance of cephalic vasculature in Archosauria. PhD Thesis. Ohio: University of Ohio; 2002.

136. Rieppel O, Zaher H. The braincases of mosasaurs and *Varanus*, and the relationships of snakes. Zool J Linn Soc. 2000; 129:489–514.

137. Edinger T. Paleoneurology 1804–1966: an annotated bibliography. Adv Anat Embryol Cell Biol 1975; 49: 1–258.

138. Klein N. Long bone histology of Sauropterygia from the Lower Muschelkalk of the Germanic Basin provides unexpected implications for phylogeny. PLOS ONE. 2010; 5(7): e11613 https://doi.org/10.1371/journal.pone.0011613 PMID: 20657768

139. O'Keefe FR. Neoteny and the plesiomorphic condition of the plesiosaur basicranium. In: Carrano MT, Gaudin TJ, Blob RW, Wible JR, editors. Amniote Paleobiology. Chicago, Il.: University of Chicago Press; 2006. p. 391–409.

140. Carroll RL, Gaskill P. The nothosaur *Pachypleurosaurus* and the origin of plesiosaurs. Phil Trans R Soc Lond B. 1985; 309(1139):343–93.

141. Vd Buffrénil, Mazin J-M. Bone histology of the ichthyosaurs: comparative data and functional interpretation. Paleobiology. 1990; 16(4):435–47 [http://www.jstor.org/stable/2400968].

142. Galatius A. Paedomorphosis in two small species of toothed whales (Odontoceti): how and why? Biol J Linn Soc. 2010; 99(2):278–95 https://doi.org/10.1111/j.095-8312.2009.01357.x

143. Fordyce RE, Barnes LG. The evolutionary history of whales and dolphins. Annu Rev Earth Planet Sci. 1994; 22:419–55.

144. Ricqlès Ad. Quelques remarques paléo-histologiques sur le problème de la néoténie chez les stégocéphales. In: Centre National de la Recherche Scientifique Problèmes actuels en Paléontologie–Evolution des Vertébrés Paris [Colloque International CNRS, 4–9 juin 1973]; 1975. p. 351–363.

145. Dechaseaux C. Lepospondyli. In: Piveteau J, editor. Traite de Paleontologie Vol 5. Paris: Masson et Cie; 1955. p. 275–305.

146. Lehman J-P. L'évolution des vertébrés inférieurs: quelques problèmes. Paris: Monographies Dunod; 1959.

147. Britz R, Conway KW, Rüber L. Spectacular morphological novelty in a miniature cyprinid fish, *Danionella dracula* n. sp. Proc R Soc Lond B. 2009; 276(1665):2179–86 https://doi.org/10.1098/rspb.2009.0141 PMID: 19324738

148. Koken E, Linder H. Osteologische Notizen über *Muraenosaurus*. N Jb Min, Geol Paläontol. 1913; 1:101–15.

149. Rieppel O. Studies in skeleton formation in reptiles. I. Studies on skeleton formation in reptiles. I. The postembryonic development of the skeleton in *Cyrtodactylus pubisulcus* (Reptilia: Gekkonidae). J Zool. 1992; 227(1):87–100.

150. Rieppel O. Studies on skeleton formation in reptiles. V. Patterns of ossification in the skeleton of *Alligator mississippiensis* Daudin (Reptilia, Crocodylia). Zool J Linn Soc. 1993; 109:301–25.

151. Koyabu D, Werneburg I, Morimoto N, Zollikofer CPE, Forasiepi AM, Endo H, et al. Mammalian skull heterochrony reveals modular evolution and a link between cranial development and brain size. Nat Commun. 2014; 5:3625 https://doi.org/10.1038/ncomms4625 PMID: 24704703

152. McNamara KJ. A guide to the nomenclature of heterochrony. J Paleontol. 1986; 60(1):4–13.

153. Gardner NM, Holliday CM, O'Keefe FR. The braincase of *Youngina capensis* (Reptilia, Dipsida): new insights from high-resolution CT scanning of the holotype. Palaeontologia Electronica. 2010;Vol. 13, Issue 3; 19A:16p; http://palaeo-electronica.org/2010_3/217/index.html.

154. Sobral G, Sues H-D, Müller J. Anatomy of the enigmatic reptile *Elachistosuchus huenei* Janensch, 1949 (Reptilia: Diapsida) from the Upper Triassic of Germany and its relevance for the origin of Sauria. PLOS ONE. 2015; 10(9):e0135114 doi: 10.1371/journal.pone.0135114. PMID: 26352985

155. Allemand R, Bardet N, Houssaye A, Vincent P. Virtual reexamination of a plesiosaurian specimen (Reptilia, Plesiosauria) from the Late Cretaceous (Turonian) of Goulmima, Morocco, using computed tomography. J Vertebr Paleontol. 2017;e1325894 https://doi.org/10.1080/02724634.2017.1325894

156. Sato T, Cheng Y-N, Wu X-C, Li C. Osteology of *Yunguisaurus* Cheng et al., 2006 (Reptilia; Sauropterygia), a Triassic pistosauroid from China. Paleontol Res. 2010; 14(3):179–95 https://doi.org/10.2517/1342-8144-14.3.179

157. Albers PCH, Rieppel O. A new species of the sauropterygian genus *Nothosaurus* from the Lower Muschelkalk of Winterswijk, The Netherlands. J Paleontol. 2003; 77(4):738–44.

158. Smith AS. Anatomy and systematics of the Rhomaleosauridae (Sauropterygia: Plesiosauria). Dublin, Ireland: University College Dublin; 2007.

159. Müller J, Sterli J, Anquetin J. Carotid circulation in amniotes and its implications for turtle relationships. N Jb Geol Palaeont Abh. 2011; 261(3):289–97 https://doi.org/10.1127/0077-7749/2011/0157

160. Klein N, Albers PCH. A new species of the sauropsid reptile *Nothosaurus* from the Lower Muschelkalk of the western Germanic Basin, Winterswijk, The Netherlands. Acta Palaeontol Pol. 2009; 54(4):589–98 https://doi.org/10.4202/app.2008.0083

161. Liu J, Hu S-x, Rieppel O, Jiang D-y, Benton MJ, Kelley NP, et al. A gigantic nothosaur (Reptilia: Sauropterygia) from the Middle Triassic of SW China and its implication for the Triassic biotic recovery. Nat Sci Rep. 2014; 4: 7142 https://doi.org/10.1038/srep07142 PMID: 25429609

162. Hopson JA. Relative brain size and behaviour in archosaurian reptiles. Annu Rev Ecol Syst. 1977; 8:429–48.

163. Lauters P, Vercauteren M, Bolotsky YL, Godefroit P. Cranial endocast of the lambeosaurine hadrosaurid *Amurosaurus riabinini* from the Amur Region, Russia. PLOS ONE. 2013; 8(11): e78899 https://doi.org/10.1371/journal.pone.0078899 PMID: 24236064

164. Pianka ER, King D, King RA. Varanoid Lizards of the World. Bloomington: Indiana University Press; 2004.

165. Masser MP. Alligator production: breeding and egg incubation. Southern Regional Aquaculture Center, Publication. 1993;No. 231:1–7.

166. Hurlburt G. Relative brain size in recent and fossil amniotes: Determination and interpretation [Unpublished PhD thesis], Toronto: University of Toronto; 1996. 250 p.

167. Northcutt RG. Variation in reptilian brains and cognition. Brain Behav Evol. 2013; 82(1):45–54 https://doi.org/10.1159/000351996 PMID: 23979455

168. Rogers SW. Reconstructing the behaviors of extinct species: an excursion into comparative paleoneurology. Am J Med Genet. 2005; 134A(4):349–56 https://doi.org/10.1002/ajmg.a.30538 PMID: 15759265

169. Butler AB, Hodos W. Comparative Vertebrate Neuroanatomy: Evolution and Adaptation. Second Edition. Hoboken, New Jersey: Wiley-Interscience; 2005. 715 p.

170. Quay WB. The parietal eye-pineal complex. In: Gans C, Northcutt RG, Ulinski P, editors. Biology of the Reptilia Volume 9 Neurology A. London: Academic Press; 1979. p. 245–406.

171. Gaffney ES. Comparative cranial morphology of Recent and fossil turtles. AMNH Bull. 1979; 164 (2):67–376.

172. Emerling CA. Archelosaurian color vision, parietal eye loss, and the crocodylian nocturnal bottleneck. Mol Biol Evol. 2016; 34(3):666–76 https://doi.org/10.1093/molbev/msw265 PMID: 27940498

173. Dodt E. The parietal eye (pineal and parietal organs) of lower vertebrates. In: Jung R, editor. Visual Centers in the Brain Handbook of Sensory Physiology Volume VII /3 Central Processing of Visual Information Part B Berlin https://doi.org/10.1007/978-3-642-65495-4_4]: Springer; 1973. p. 113–40.

174. Tosini G. The pineal complex of reptiles: physiological and behavioral roles. Ethol Ecol Evol. 1997; 9 (4):313–33 https://doi.org/10.1080/08927014.1997.9522875

175. Ralph CL, Firth BT, Gern WA, Owens DW. The pineal complex and thermoregulation. Biol Rev. 1979; 54(1):41–72 https://doi.org/10.1111/j.469-185X.979.tb00867.x PMID: 375995

176. Eakin RM. The Thrid Eye. Berkeley: University of California Press [ISBN: 0-520-02413-3]; 1973.

177. Ekström P, Meissl H. Evolution of photosensory pineal organs in new light: the fate of neuroendocrine photoreceptors. Phil Trans R Soc B. 2003; 358(1438):1679–700 https://doi.org/10.1098/rstb.2003.1303 PMID: 14561326

178. Foà A, Basaglia F, Beltrami G, Carnacina M, Moretto E, Bertolucci C. Orientation of lizards in a Morris water-maze: roles of the sun compass and the parietal eye. J Exp Biol. 2009; 212:2918–24 https://doi.org/10.1242/jeb.032987 PMID: 19717673

179. Phillips JA, Howes KA. The pineal complex, aggressive behavior and thermoregulation in curly-tailed lizards, *Leiocephalus carinatus*. Physiol Behav. 1988; 42(1):103–8 https://doi.org/10.1016/0031-9384(88)90268-5 PMID: 3387471

180. Connolly A, Martin LD, Hasiotis S. The paleobiogeographical effects of the parietal foramen in mosasaurs. Program and Abstracts of the 4th Triennial International Mosasaur Meeting, Dallas, Texas, May 20–25,2013: 13–14.

181. Gundy GC, Ralph CL, Wurst GZ. Parietal eyes in lizards: zoogeographical correlates. Science. 1975; 190(4215):671–3 https://doi.org/10.1126/science.1237930 PMID: 1237930

182. Ralph CL. The pineal gland and geographical distribution of animals. Int J Biometeorol. 1975; 19 (4):289–303 https://doi.org/10.1007/BF01451040 PMID: 1232070

183. Benoit J, Abdala F, Manger PR, Rubidge BS. The sixth sense in mammalian forerunners: Variability of the parietal foramen and the evolution of the pineal eye in South African Permo-Triassic eutheriodont therapsids. Acta Palaeontol Pol. 2016; 61(4):777–89 https://doi.org/10.4202/app.00219.2015

184. Bernard A, Lécuyer C, Vincent P, Amiot R, Bardet N, Buffetaut E, et al. Regulation of body temperature by some Mesozoic marine reptiles. Science. 2010; 328(5984):1379–82 https://doi.org/10.1126/science.1187443 PMID: 20538946

185. Kear BP, Schroeder NI, Lee MSY. An archaic crested plesiosaur in opal from the Lower Cretaceous high-latitude deposits of Australia. Biol Lett. 2006; 2(4):615–9 https://doi.org/10.1098/rsbl.2006.0504 PMID: 17148303

186. Muntz WRA. Reptile sensory systems and the electromagnetic spectrum. In: Ali MA, editor. Sensory Ecology: Review and Perspectives New York: Plenum Press; 1978. p. 197–216 https://doi.org/10.1007/978-1-4684-3363-0_9

187. Graham JB. Aquatic respiration in the sea snake *Pelamis platurus*. Resp Physiol. 1974; 21(1):1–7 https://doi.org/10.1016/0034-5687(74)90002-4

188. Graham JB, Rubinoff I, Hecht MK. Temperature physiology of the sea snake *Pelamis platurus*: an index of its colonization potential in the Atlantic Ocean. PNAS. 1971; 68(6):1360–3. PMID: 16591934

189. Heatwole H, Grech A, Monahan JF, King S, Marsh H. Thermal biology of sea snakes and sea kraits. Integrative and Comp Biol. 2012; 52(2):257–73 https://doi.org/10.1093/icb/ics080 PMID: 22669175

190. Korte C, Kozur HW, Veizer J. δ 13 C and δ 18 O values of Triassic brachiopods and carbonate rocks as proxies for coeval seawater and palaeotemperature. Paleogeogr Paleoclimatol Paleoecol. 2005; 226(3):287–306 https://doi.org/10.1016/j.palaeo.2005.05.018

191. Saint Girons H. Thermoregulation in reptiles with special reference to the tuatara and its ecophysiology. Tuatara. 1980; 24(2):59–80.

192. Falcón J. Cellular circadian clocks in the pineal. Prog Neurobiol. 1999; 58(2):121–62 https://doi.org/10.1016/S0301-082(98)00078-1 PMID: 10338357

193. Zachmann A, Falcon J, Knijff SCM, Bolliet V, Ali MA. Effects of photoperiod and temperature on rhythmic melatonin secretion from the pineal organ of the white sucker (*Catostomus commersoni*) in vitro.

Gen Comp Endocrinol. 1992; 86(1):26–33 https://doi.org/10.1016/0016-6480(92)90122-Z PMID: 1505727

194. Kv Frisch. Das Parietalorgan der Fische als funktionierendes Organ. Ges Morphol Physiol München, Sitzungsber. 1911; 27:16–8.

195. Korf W, Schomerus C, Stehle JH. The Pineal Organ, its Hormone Melatonin, and the Photoneuroendocrine System. Adv Anat, Embryol Cell Biol. No. 146. Berlin: Springer; 1998.

196. McCord CP, Allen FP. Evidences associating pineal gland function with alterations in pigmentation. J Exp Zool A: Ecol Genet Physiol. 1917; 23(1):207–24 https://doi.org/10.1002/jez.1400230108

197. Charlton HM. The pineal gland and color change in *Xenopus laevis* Daudin. Gen Comp Endocrinol. 1966; 7(2):384–97 https://doi.org/10.1016/0016-6480(66)90058-X

198. Bors A, Ralston WC. A simple assay of mammalian pineal extracts. Proc Soc Exp Biol Med. 1951; 77 (4):807–8. PMID: 14891877

199. Lerner AB, Case JD, Takahashi Y, Lee TH, Mori W. Isolation of melatonin, the pineal gland factor that lightens melanocytes. J Am Chem Soc. 1958; 80(10):2587.

200. Lindgren J, Sjövall P, Carney RM, Uvdal P, Gren JA, Dyke G, et al. Skin pigmentation provides evidence of convergent melanism in extinct marine reptiles. Nature. 2014; 506:484–8 https://doi.org/10.1038/nature12899 PMID: 24402224

201. Shine R. All at sea: aquatic life modifies mate-recognition modalities in sea snakes (*Emydocephalus annulatus*, Hydrophiidae). Behav Ecol Sociobiol. 2005; 57:591–8 https://doi.org/10.1007/s00265-004-0897-z

202. Kröger RHH, Katzir G. Comparative anatomy and physiology of vision in aquatic tetrapods. In: Thewissen JGM, Nummela S, editors. Sensory Evolution on the Threshold Adaptations in Secondarily Aquatic Vertebrates [ISBN 978-0-520-25278-3]. Berkeley: University of California Press; 2008. p. 121–47.

203. Young BA. Evaluating hypotheses for the transfer of stimulus particles to Jacobson organ in snakes. Brain Behav Evol. 1993; 41:203–9. PMID: 8386589

204. Cooper WE. Chemical discrimination by tongue-flicking in lizards: A review with hypotheses on its origin and its ecological and phylogenetic relationships. J Chem Ecol. 1993; 20(2):439–87 https://doi.org/10.1007/BF02064449 PMID: 24242066

205. Brooks DR, McLennan DA. The Nature of Diversity: An Evolutionary Voyage of Discovery. Chicago: University of Chicago Press; 2002.

206. Negus V. The Comparative Anatomy and Physiology of the Nose and Paranasal Sinuses. Edinburgh: Harcourt Brace/Churchill Livingstone; 1958. 418 p.

207. Bertmar G. Evolution of vomeronasal organs in vertebrates. Evolution. 1981; 35(2):359–66. https://doi.org/10.1111/j.1558-5646.1981.tb04893.x PMID: 28563370

208. Schulp AS, Mulder EWA, Schwenk K. Did mosasaurs have forked tongues? Netherlands J Geosci / Geol Mijnbouw. 2005; 84(3):359–71.

209. Fd Castro. Wiring olfaction: the cellular and molecular mechanisms that guide the development of synaptic connections from the nose to the cortex. Front Neurosci. 2009; 3:52 https://doi.org/10.3389/neuro.22.004.2009 PMID: 20582279

210. Czech-Damal NU, Liebschner A, Miersch L, Klauer G, Hanke FD, Marshall C, et al. Electroreception in the Guiana dolphin (*Sotalia guianensis*Proc R Soc B. 2012; 279:663–8 https://doi.org/10.1098/rspb.2011.1127 PMID: 21795271

211. Shichida Y, Yamashita T, Imai H, Kishida T. Evolution and Senses: Opsins, Bitter Taste, and Olfaction. Springer Briefs in Biology. Tokyo: Springer; 2013. 46 https://doi.org/10.1007/978-4-431-54222-3] p.

212. Nummela S, Pihlström H, Puolamäki K, Fortelius M, Hemilä S, Reuter T. Exploring the mammalian sensory space: co-operations and trade-offs among senses. J Comp Physiol A Neuroethol Sens Neural Behav Physiol. 2013; 199(12):1077–92 https://doi.org/10.1007/s00359-013-0846-2 PMID: 24043357

213. Cruickshank ARI, Small PG, Taylor MA. Dorsal nostrils and hydrodynamically driven underwater olfaction in plesiosaurs. Nature. 1991; 352:62–4.

214. Sander PM. The pachypleurosaurids (Reptilia: Nothosauria) from the Middle Triassic of Monte San Giorgio (Switzerland) with the description of a new species. Phil Trans R Soc B. 1989; 325(1230):561–666 https://doi.org/10.1098/rstb.989.0103 PMID: 2575768

215. Hirayama R. Oldest known sea turtle. Nature. 1998; 392:705–8.

216. Lutz PL, Musick JA, Wyneken J, editors. The Biology of Sea Turtles, Volume II. Boca Raton: CRC Press; 2003.

217. Klein N, Sichelschmidt OJ. Remarkable dorsal ribs with distinct uncinate processes from the early Anisian of the Germanic Basin (Winterswijk, The Netherlands). N Jb Geol Palaeont Abh. 2014; 271 (3):307–14.

218. Storrs GW. Function and phylogeny in sauropterygian (Diapsida) evolution. Am J Sci. 1993; 293-A:63–90.

219. Araújo R, Polcyn MJ. A biomechanical analysis of the skull and adductor chamber muscles in the Late Cretaceous plesiosaur *Libonectes.* Palaeontologia Electronica. 2013; 16(2): 10A; 25p [palaeo-electronica.org/content/2013/418-plesiosaur-mastication].

220. Borkhataria R, Aigner T, Pipping KJCP. An unusual, muddy, epeiric carbonate reservoir: The Lower Muschelkalk (Middle Triassic) of the Netherlands. AAPG Bulletin. 2006; 90(1):61–89.

221. Bajpai S, Thewissen JGM, Conley RW. Cranial anatomy of middle Eocene *Remingtonocetus* (Cetacea, Mammalia) from Kutch, India. J Paleontol. 2011; 85(4):703–18 https://doi.org/10.1666/10-128.1

222. Motani R, Schmitz L. Phylogenetic versus functional signals in the evolution of form-function relationships in terrestrial vision. Evolution. 2011; 65(8):2245–57 https://doi.org/10.1111/j.1558-5646.2011.01271.x PMID: 21790572

223. Storrs GW, Taylor MA. Cranial anatomy of a new plesiosaur genus from the lowermost Lias (Rhaetian/Hettangian) of Street, Somerset, England. J Vertebr Paleontol. 1996; 16(3):403–20 https://doi.org/10.1080/02724634.1996.10011330

224. Taylor MA, Cruickshank ARI. Cranial anatomy and functional morphology of *Pliosaurus brachyspondylus* (Reptilia: Pleasiosauria) from the Upper Jurasic of Westbury, Wilshire. Philos Trans R Soc B. 1993; 335:247–80 https://doi.org/10.1098/rstb.993.0124

225. Serratos DJ, Druckenmiller PS, Benson RBJ. A new elasmosaurid (Sauropterygia, Plesiosauria) from the Bearpaw Shale (Late Cretaceous, Maastrichtian) of Montana demonstrates multiple evolutionary reductions of neck length within Elasmosauridae. J Vertebr Paleontol. 2017:e1278608 (25 pages) https://doi.org/10.1080/02724634.2017.1278608

226. Warrant EJ. Seeing in the dark: vision and visual behaviour in nocturnal bees and wasps. J Exp Biol. 2008; 211:1737–46 https://doi.org/10.1242/jeb.015396 PMID: 18490389

227. Grigg GC, Kirschner D. Biology and Evolution of Crocodylians. Clayton South, Melbourne: Csiro Publishing; 2015.

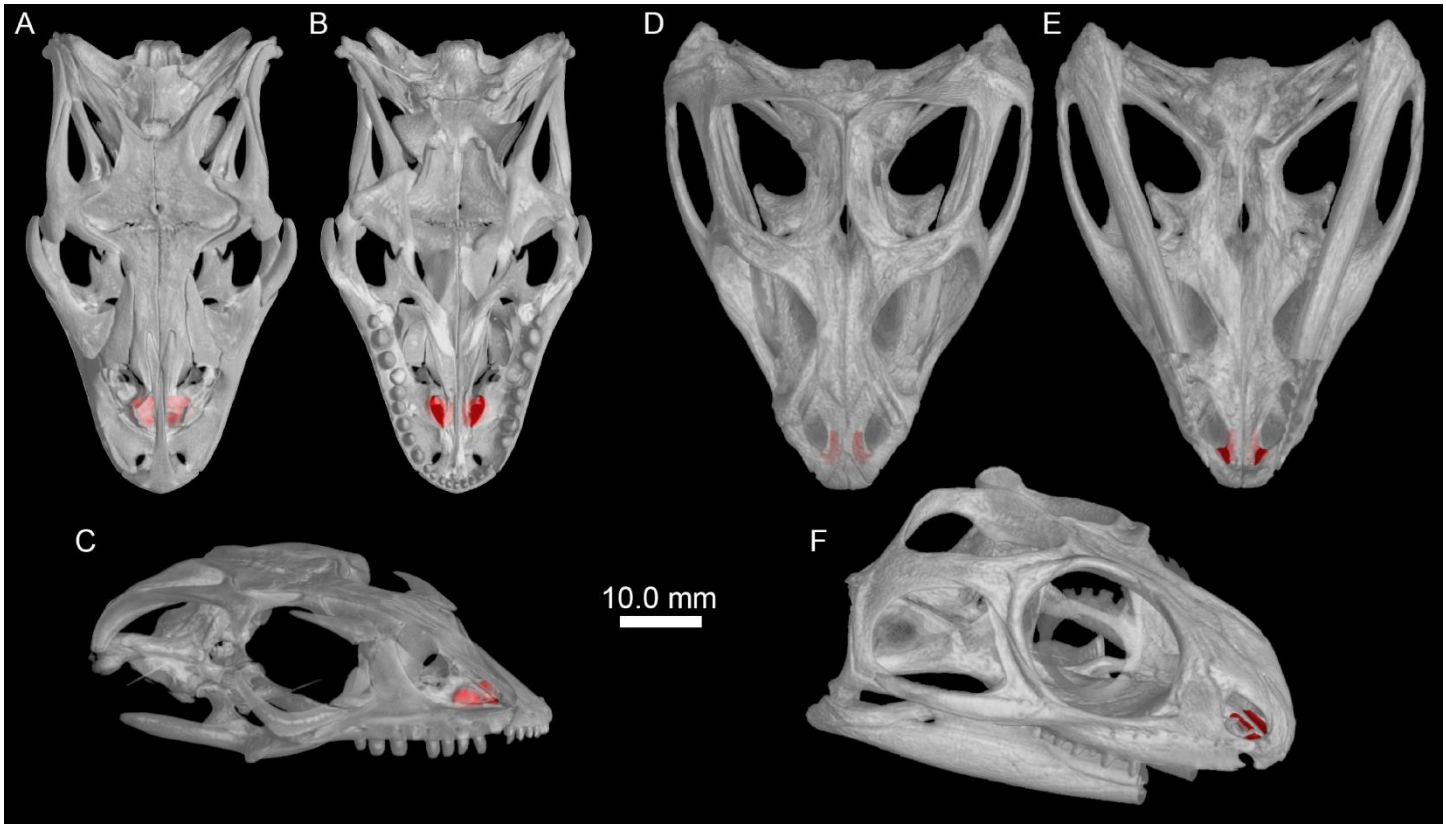

Supporting information

S1 Fig. Vomeronasal structure in extant squamates. A-C. Virtual surface model of *Varanus exanthematicus* cranium in dorsal (A), ventral (B), and angled lateral (C) view. D-F. Virtual surface model of *Sphenodon punctatus* skull in dorsal (D), ventral (E), and angled lateral (F) view; anterior mandible excluded to reveal anterior palate in ventral view. The paired vomeronasal organ is labeled in red in both partially transparent crania. CT data sets of *Varanus exanthematicus* and *Sphenodon punctatus* were consulted on December 12 2016 through DigiMorph.org (Digimorph, 2004; The University of Texas High-Resolution X-ray CT Facility UTCT, and NSF grants IIS-0208675 and EF-0334961).
(TIF)

Chapter 5: Wing bone geometry reveals active flight in *Archaeopteryx*

Reference: **Voeten, D. F. A. E.**, J. Cubo, E. de Margerie, M. Röper, V. Beyrand, S. Bureš, P. Tafforeau, and S. Sanchez. Wing bone geometry reveals active flight in Archaeopteryx. *Nature Communications* (in press).

Abstract *Archaeopteryx* is an iconic fossil taxon with feathered wings from the Late Jurassic of Germany that occupies a crucial position for understanding the early evolution of avian flight. After over 150 years of study, its mosaic anatomy unifying characters of both non-flying dinosaurs and flying birds has remained challenging to interpret in a locomotory context. Here, we compare new data from three *Archaeopteryx* specimens obtained through phase-contrast synchrotron microtomography to a representative sample of archosaurs employing a diverse array of locomotory strategies. Our analyses reveal that the architecture of *Archaeopteryx*'s wing bones consistently exhibits a combination of cross-sectional geometric properties uniquely shared with volant birds, particularly those occasionally utilizing short-distance flapping. We therefore interpret that *Archaeopteryx* actively employed wing flapping to take to the air through a more anterodorsally-posteroventrally oriented flight stroke than used by modern birds. This unexpected outcome implies that avian powered flight must have originated before the latest Jurassic.

Wing bone geometry reveals active flight in *Archaeopteryx*

Dennis F.A.E. Voeten[1,2], Jorge Cubo[3], Emmanuel de Margerie[4], Martin Röper[5,6], Vincent Beyrand[1,2], Stanislav Bureš[2], Paul Tafforeau[1] & Sophie Sanchez[7,1]

Correspondence and requests for materials should be addressed to D.F.A.E.V. (email: dennis.voeten1@upol.cz).

[1]European Synchrotron Radiation Facility, 71 Avenue des Martyrs, CS-40220, 38043 Grenoble Cedex, France

[2]Department of Zoology and Laboratory of Ornithology, Palacký University, 17. listopadu 50, 771 46 Olomouc, Czech Republic

[3]Sorbonne Université, CNRS-INSU, Institut des Sciences de la Terre Paris, ISTeP UMR 7193, F-75005 Paris, France

[4]CNRS, Université de Rennes 1, Université de Caen Normandie, Laboratoire d'éthologie animale et humaine, 263 Avenue du Général Leclerc, 35042 Rennes, France

[5]Bürgermeister-Müller-Museum, Bahnhofstrasse 8, 91807 Solnhofen, Germany

[6]Bayerische Staatssammlung für Paläontologie und Geologie, Richard-Wagner-Str. 10, D-80333 München, Germany

[7]Science for Life Laboratory and Uppsala University, Subdepartment of Evolution and Development, Department of Organismal Biology, Evolutionary Biology Centre, Norbyvägen 18A, 752 36 Uppsala, Sweden

ABSTRACT

Archaeopteryx is an iconic fossil taxon with feathered wings from the Late Jurassic of Germany that occupies a crucial position for understanding the early evolution of avian flight. After over 150 years of study, its mosaic anatomy unifying characters of both non-flying dinosaurs and flying birds has remained challenging to interpret in a locomotory context. Here, we compare new data from three *Archaeopteryx* specimens obtained through phase-contrast synchrotron microtomography to a representative sample of archosaurs employing a diverse array of locomotory strategies. Our analyses reveal that the architecture of *Archaeopteryx*'s wing bones consistently exhibits a combination of cross-sectional geometric properties uniquely shared with volant birds, particularly those occasionally utilising short-distance flapping. We therefore interpret that *Archaeopteryx* actively employed wing flapping to take to the air through a more anterodorsally-posteroventrally oriented flight stroke than used by modern birds. This unexpected outcome implies that avian powered flight must have originated before the latest Jurassic.

INTRODUCTION

The earliest phases of avian evolution and development of avian flight remain obscured by the rarity of representative fossil material and consequential limited phylogenetic resolution[1]. As the oldest potentially free-flying avialian known[1-3], *Archaeopteryx* represents the prime candidate to consider in resolving the initial chapter of bird flight. Although the traditional dichotomy between an arboreal and a cursorial origin of avian flight[4] has relaxed towards the consideration of intermediate perspectives[3,5], the question whether the first flying bird-line dinosaurs took flight under their own power remains unanswered.

Skeletal adaptations that structurally accompany known locomotor modes provide reliable proxies for inferring the habits of extinct tetrapods. The cross-sectional geometry of limb bones is largely determined by evolutionary selection on the interplay between strength and weight[6] and continuous morphological and structural adaptation to the biomechanical loading regimes experienced during life[7]. Therefore, the avian wing skeleton informs on this stress regime through the application of beam theory mechanics[8-10].

Although the value of exceptional and rare fossils discourages physical cross-sectioning, Propagation Phase-Contrast Synchrotron X-Ray Microtomography (PPC-SRμCT) now offers non-destructive alternatives[11]. Using PPC-SRμCT at the European Synchrotron Radiation Facility with a novel data acquisition protocol (Supplementary Note 1), we visualised complete circa mid-diaphyseal humeral and ulnar cross sections of three *Archaeopteryx* specimens (Fig. 1 c-h) because these elements exhibit the strongest flight-related biomechanical adaption in the modern avian brachium[10,12]. Their full transverse cross-sectional geometry was reconstructed (Fig. 1 i-n) and compared with an extensive set of archosaurian humeri and ulnae representing 69 species spanning a wide variety of locomotory behaviors (Supplementary Fig. 1 and Supplementary Data 1). Notably, we included the basal "long-tailed" pterosaur *Rhamphorhynchus* and the derived "short-tailed" pterosaur *Brasileodactylus* in our archosaurian reference set to contrast conditions associated with pterosaurian volancy against those of the independently arisen avian flight apparatus. Although the pterosaurian and avian flight apparatus differ in fundamental morphological aspects, comparing them may be expected to reveal underlying analogous adaptations in wing bone geometry.

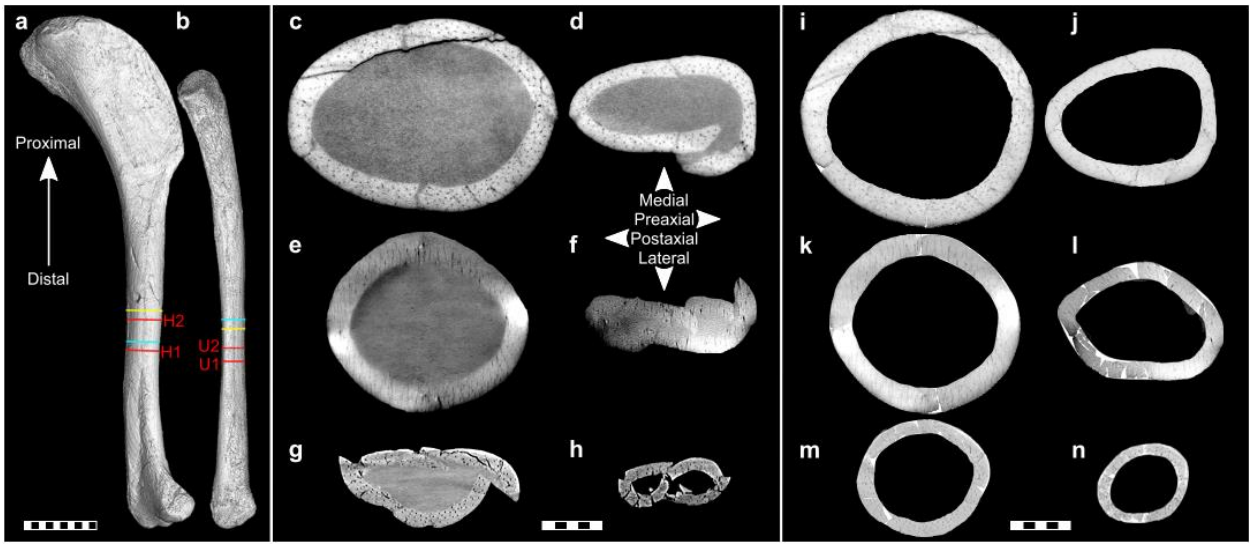

Figure 1. ***Archaeopteryx*** **humeral and ulnar virtual cross sections used in this study. a,** Right humerus and **b,** right ulna of the ninth (Bürgermeister-Müller) specimen in lateral respectively medial view, with virtual sampling locations (red) and relative sampling locations in seventh (Munich) specimen (light blue) and fifth (Eichstätt) specimen (yellow). **c-h,** Virtual cross sections, as preserved, with optimised intraosseous contrast, of **c,** right humerus (H2) and **d,** right ulna (U2) of ninth specimen, **e,** right humerus and **f,** right ulna of seventh specimen, and **g,** left humerus and **h,** left ulna of fifth specimen. **i-n,** Reconstructed cross-sectional geometry, with optimised contrast of bone margins, of **i,** humerus and **j,** ulna of ninth specimen, **k,** humerus and **l,** ulna of seventh specimen, and **m,** humerus and **n,** ulna of fifth specimen; pure white indicates supplemented fragments. Morphological orientation applies to all sections (c-h). Scale bar (a-b), 10mm; scale bars (c-n), 1 mm.

Raw virtual slice data revealed that the long-bone cortex of *Archaeopteryx* exhibits a vascular density in the range of modern birds, which proposes substantial metabolic performance. Cortical vascular density varies strongly among the three specimens of *Archaeopteryx* studied, which we interpret reflects ontogenetic disparity based on body size differences. Relative cortical thickness of archosaurian anterior limb bones successfully discriminates between known non-volant and volant forms, and confidently indicates that *Archaeopteryx* was volant. Mass-normalised torsional resistance in the same set of limb bones describes a gradient within modern volant birds that ranges from flight strategies relying on occasional or intermittent flapping to gain altitude to hyperaerial specialists employing prolonged gliding or soaring in their flight. The three specimens of *Archaeopteryx* were found to unanimously ally with birds that incidentally employ flapping flight to evade predators or cross physical barriers, through which we interpret that

Archaeopteryx actively flapped its wings to take to the air. Since the morphology of the flight apparatus in *Archaeopteryx* is known to be incompatible with the flight stroke executed by modern volant birds, we furthermore conclude that *Archaeopteryx* adopted a different flight stroke than used by modern birds today. Finally, we found that the evolution from primitive long-tailed pterosaurs to more derived short-tailed pterosaurs was accompanied by qualitatively comparable modifications to wing bone geometry as those that distinguish *Archaeopteryx* and principally flapping birds from hyperaerial birds, respectively.

RESULTS

Cortical vascularisation

Contrary to previously reported data[13], the bone cortex of *Archaeopteryx* is well vascularised (Fig. 1c-h, Supplementary Data 1). The ninth specimen exhibits a cortical vascular density (Supplementary Fig. 2) in the lower range of neognaths (circa 69 canals/mm^2), but higher than the hoatzin (*Opisthocomus hoazin*; circa 43 canals/mm^2), whereas cortical vascular density of the smaller fifth specimen is higher than in most neognaths assessed (circa 116 canals/mm^2; Supplementary Fig. 3). This is consistent with a higher bone growth rate[14] and associated higher resting metabolic rate[15] than inferred from nearly avascular bone chips of the seventh specimen[13]. Ontogenetic progression is accompanied by a reduction in the apposition rate and vascular density of forming bone[16]. Providing that the fifth and ninth specimen represent the same species or that we are observing the shared generic ontogenetic pattern, their marked differential vascular density scaling inversely with body size would indicate disparate ontogenetic stages for these individuals.

Relative cortical thickness

Average relative cortical thickness of anterior limb bones successfully separates volant from non-volant archosaurs in our data set, although individual element values may slightly cross the average relative cortical thickness value of 0.60 found to separate these groups (Supplementary Figs. 4 and 5). Within non-volant groups, aquatic and (facultatively) quadrupedal species have relatively thicker humeral bone cortices than terrestrial bipeds. The basal pterosaur

Rhamphorhynchus exhibits an average relative cortical thickness in the upper range of volant archosaurs, whereas the pterodactyloid pterosaur *Brasileodactylus* presents the lowest relative cortical thickness recorded. Only volant birds that engage in wing-propelled diving may exhibit an average relative cortical thickness in the range of non-volant archosaurs to counteract buoyancy and manage the demands of subaqueous locomotion[17]. Charadriiformes (Supplementary Fig. 1) share an elevated average relative cortical thickness with respect to other orders of flying birds (Supplementary Data 1, Supplementary Fig. 6), likely as an adaptation to negotiate "strong winds" in coastal and marine habitats[10]. The humeral and ulnar bone walls of *Archaeopteryx*, comparatively thinner than those of any element in the non-volant sample, reveal a strong affinity with volant birds but disqualify this taxon as a wing-propelled diver[18] or obligatory "wind-assisted" flyer[19].

Mass-normalised torsional resistance

Because a lower relative cortical thickness positions bone material further away from the bone section centroid (Supplementary Fig. 2) than a higher relative cortical thickness at the same amount of bone present, relative cortical thickness and mass-normalised torsional resistance are inherently not completely decoupled. Furthermore, mass-normalised torsional resistance retains a small yet significant allometric effect that reflects the inherent proportional relation between flight adaptations and body size, and should thus not be removed when investigating the locomotory affinities of extinct taxa[12,20]. Nevertheless, we focus on obvious signals and trends that exist relative to such relations, since those are particularly informative towards distinguishing the effects of related locomotory regimes.

Mass-normalised torsional resistance successfully separates non-avian theropods from flightless birds with comparable body mass values, but also exhibits subtle variation across avian flight modes (Supplementary Figs. 4 and 5). Burst-flying[20] birds (incidental explosive take off and brief horizontal flight followed by a running escape) exhibit humeral and ulnar relative torsional resistance values overlapping with those of intermittent bounding[20] flyers (flapping phases aimed at gaining altitude and speed, alternated with passive phases with folded wings). However, burst-flying[20] birds attain body mass values that are, on average, two orders of magnitude higher than those of intermittent bounding[20] flyers, which is informative when discriminating these two groups. Conversely, flap-gliding[20] birds have a similar to higher humeral and ulnar relative

torsional resistance compared to burst[20]-adapted and most continuously flapping[20] flyers at body masses that are, on average, one order of magnitude lower. Notably, the two large non-domesticated anatids in our data set share elevated relative torsional resistance values compared to other continuously flapping birds. Soaring birds[20] may attain comparatively high body mass values, yet exhibit distinctly elevated normalised torsional resistance values relative to their body mass throughout (Supplementary Figs. 4 and 5).

The fifth, seventh, and ninth specimens of *Archaeopteryx* have reconstructed body mass values of 158, 254, and 456 g[13], respectively. These inferred ontogenetic[13] mass differences do not scale linearly with humeral and ulnar torsional resistance: the seventh and ninth specimen exhibit comparable values that are elevated proportional to those of the fifth specimen and within the lower range of modern volant birds. This may reflect an ontogenetic ecomorphological shift between the ages associated with reconstructed body mass values of 158 and 254 g towards increased volant adaptation. The seventh and ninth specimens of *Archaeopteryx* exhibit relative humeral torsional resistance approaching those of modern short[21]/burst[20] flying birds of similar mass and higher than some heavier non-volant archosaurs. Ulnar torsional resistance values in these specimens are comparable to those of lighter volant birds and much heavier non-volant birds, and are higher than in the small non-avian coelurosaur *Compsognathus*. A shared proportional disparity between relative humeral and ulnar torsional resistance in the seventh and ninth specimen of *Archaeopteryx* with respect to flying birds indicates an underlying different employment of the epipodium, such as a possible larger contribution of the radius in wing load transfer to the humerus relative to the modern avian flight apparatus. Like *Archaeopteryx*, humeral and ulnar relative torsional resistance of *Rhamphorhynchus*, circa 40% lighter than the fifth specimen of *Archaeopteryx*, also scale with the lightest volant birds that have body masses up to one order of magnitude lower. The piscivorous diet of *Rhamphorhynchus*[22] strongly favours active flight, and specimens substantially smaller than the individual considered here have been concluded to have been volant[23]. This, in turn, demonstrates that comparatively low relative torsional resistance of the bones supporting the limb carrying the airfoil does not preclude the capacity of active flight.

Volancy

Phylogenetic Principal Component Analysis (pPCA) of the referred parameters places *Archaeopteryx* in a domain shared almost exclusively with modern volant birds (Supplementary Fig. 7). Partitioning Around Medoids (PAM) of the first three phylogenetic Principal Components resolves volancy with a 95.52% success rate and allies *Archaeopteryx* with volant archosaurs (Supplementary Data 2). Only three volant but (incidentally) wing-propelled diving birds were misclassified as flightless through their elevated relative cortical thickness. This outcome, including misclassification of the three wing-propelled divers and the assignment of *Archaeopteryx* to the volant group, is identically recapitulated by k-means clustering of the raw parameter values into two clusters (Supplementary Data 2). Additional discussion of volancy in *Archaeopteryx* through individual parameters is included in Supplementary Note 2.

Locomotor mode

Phylogenetic autocorrelation was found to be insignificant towards Phylogenetically Informed Discriminant Analysis (Supplementary Figure 8), thus rendering Linear Discriminant Analysis (LDA) appropriate for resolving the locomotory affinity of *Archaeopteryx*. Linear discriminant analysis (LDA) principally separates volant and non-volant archosaurs along discriminant axis (DA) 1 (Fig. 2 and Supplementary Fig. 9) through predominantly humeral and ulnar relative cortical thickness. DA 2 is loaded more equally on all parameters than DA 1, but slightly stronger on relative cortical thickness for the classification expanded from Viscor et al.[21], and slightly stronger on mass-normalised torsional resistance for the classification expanded from Close et al.[20]. Within modern volant birds, an overlapping succession of avian flight modes extends upwards along DA 2 (Fig. 2). This sequence starts at the bottom of DA 2 with short[21] or burst[20] flight and intermittent bounding[20]. These flight modes share a strong climbing component during powered flight phases, where intermittent bounding remains restricted to species with an adult body mass typically below 200 g[21]. Forward flapping[21], high-frequency flapping[21] or continuous flapping[20] flight is observed in birds that maintain level flapping flight after take-off. The avian sequence terminates in undulating[21] or flap-gliding[20] fliers that structurally alternate between flapping and gliding during flight, and aerial specialists in the gliding – soaring[21] and soaring[20] flight categories that harvest atmospheric movements to gain altitude and engage in sustained gliding.

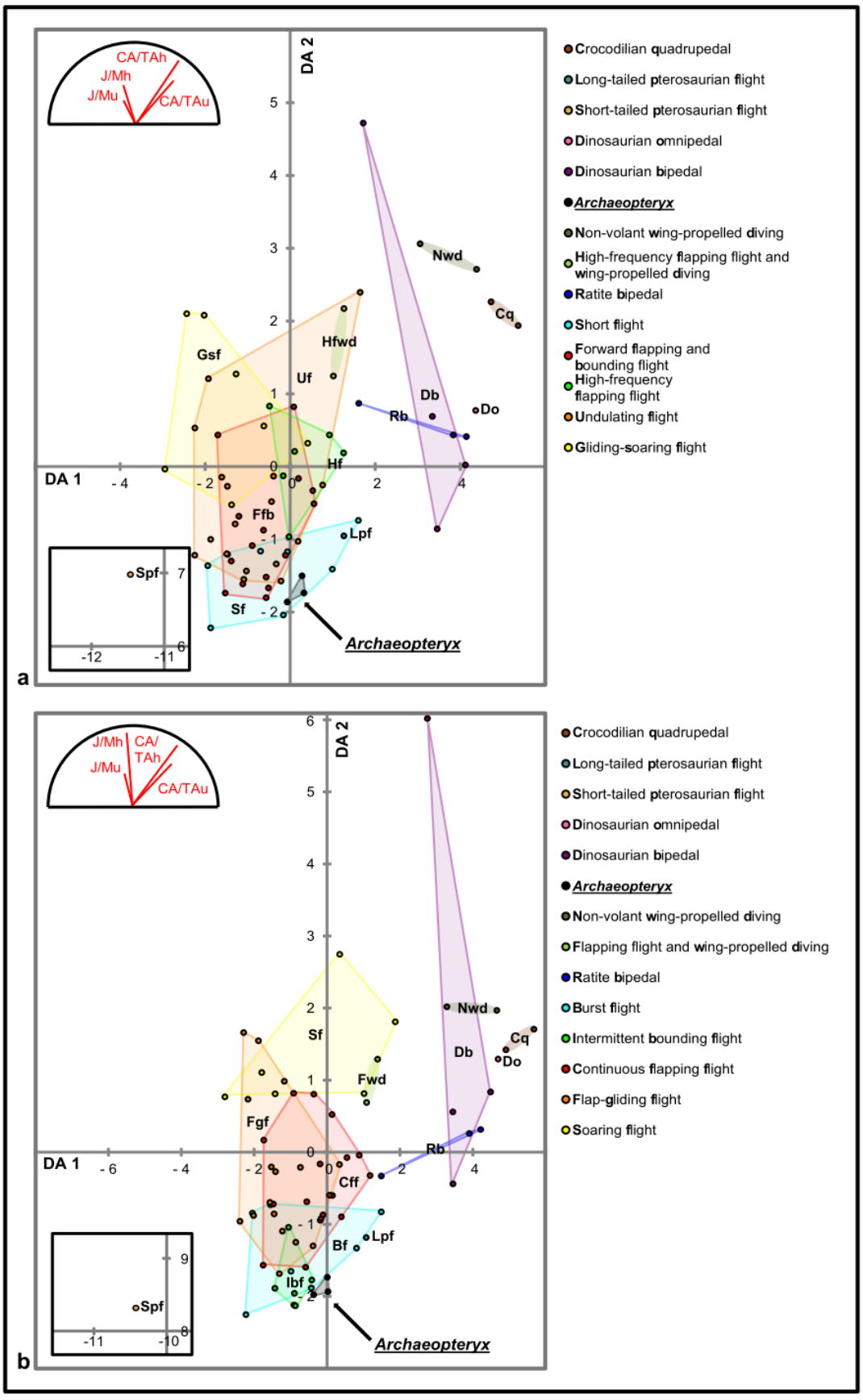
a
CA/TAh
J/Mh
J/Mu
CA/TAu
DA 2
DA 1
Nwd
Cq
Hfwd
Gsf
Uf
Db
Rb
Do
Hf
Ffb
Lpf
Spf
Sf
Archaeopteryx
Crocodilian quadrupedal
Long-tailed pterosaurian flight
Short-tailed pterosaurian flight
Dinosaurian omnipedal
Dinosaurian bipedal
Archaeopteryx
Non-volant wing-propelled diving
High-frequency flapping flight and wing-propelled diving
Ratite bipedal
Short flight
Forward flapping and bounding flight
High-frequency flapping flight
Undulating flight
Gliding-soaring flight
b
J/Mh
CA/TAh
J/Mu
CA/TAu
DA 2
DA 1
Nwd
Cq
Db
Do
Sf
Fwd
Fgf
Rb
Cff
Bf
Lpf
Ibf
Spf
Archaeopteryx
Crocodilian quadrupedal
Long-tailed pterosaurian flight
Short-tailed pterosaurian flight
Dinosaurian omnipedal
Dinosaurian bipedal
Archaeopteryx
Non-volant wing-propelled diving
Flapping flight and wing-propelled diving
Ratite bipedal
Burst flight
Intermittent bounding flight
Continuous flapping flight
Flap-gliding flight
Soaring flight

⬆**Figure 2. LDA plot for specific archosaurian humeral and ulnar CA/TA and J/M.** First and second linear discriminant axes are presented. Classification follows the locomotory divisions adapted from a, Viscor et al.[21] and b, Close et al.[20], non-pterosaurian flight strategies represent avian flight modes. Dots correspond to species, *Archaeopteryx* specimens plotted individually. Coloured hulls delimit groups with a minimum of three representatives; coloured ellipses link the members of groups with two representatives. Parameters labelled ¨_h¨ and ¨_u¨ in loading biplots designate humeral and ulnar affinity, respectively.

Across avian flight strategies and relative to mass-specific effects, relative torsional resistance of wing bones appears to scale inversely with a reliance on flapping during flight. This may reflect either a multidirectional stress regime or elevated torsional loading experienced during gliding and soaring as opposed to the directionally confined stresses associated with flapping[12]. A coupled decrease in relative cortical thickness and torsional resistance of anterior limb bones accompanied the transition from non-avian dinosaurs to birds (Fig. 2). A subsequent increase in relative torsional resistance at rather constant relative cortical thickness within volant birds accompanies the establishment of distinct avian flight modes (Fig. 2). Although basal and derived pterosaurs are represented by only one taxon each, their reciprocal relationship in pPCA and LDA morphospace qualitatively agrees with those between (occasionally) flapping birds and avian hyperaerial soarers, respectively. From a biomechanical point of view, this lends some support for an analogous evolutionary trajectory leading from flapping volancy in *Rhamphorhynchus* to an affinity with prolonged soaring in *Brasileodactylus*.

Discriminant classification unanimously groups the specimens of *Archaeopteryx* with short[21] or burst[20] flyers in our set (Supplementary Data 2). Substantial group overlap within the volant avian cluster in discriminant morphospace results in relatively low percentages of correctly classified training species (53.62% and 56.52% for the Viscor et al.[21] and Close et al.[20] divisions, respectively), and this uncertainty undoubtedly carries over to the characterisation of extinct taxa with unknown locomotory strategies. Nevertheless, the position of *Archaeopteryx* is chiefly shared with short[21]/burst[20] flyers (Fig. 2 and Supplementary Fig. 9), which supports the resolved affinity with these near-synonymous flight groups. Although *Archaeopteryx* plots close to intermittent bounding[20] birds as well, its reconstructed adult body mass[13] vastly exceeds the mass threshold that modern bounding birds adhere to[21]. Finally, short[21] and burst[20] flyers exhibit significantly deviating means from respectively gliding – soaring[21], and flap-gliding[20] and

soaring[20] birds (Supplementary Tables 1 and 2), thereby underlining an affinity to habitual flapping for *Archaeopteryx*.

DISCUSSION

Obligatory gliding (non-serpent) amniotes, such as the extant flying lizard *Draco* and flying squirrels in the family Pteromyini, converge on the employment of typically low-aspect-ratio limb-supported patagia along the lateral body wall that are occasionally supplemented with webbed digits[24]. The pterosaurian and chiropteran flight apparatus superficially resemble derived, powered modifications of this general configuration that achieved active flight. In contrast, even the oldest avian wings represent specialised anterior limbs that are inherently mobile and structurally connect to the body exclusively through articulation with the glenoid. Such a particular modification of the non-avian maniraptoran arm, which constitutes a highly dexterous limb in its own right[25], sharply disagrees with the conventional condition shared by limbed amniotes primarily adapted to passive gliding. This advocates the employment of an actively moved wing in *Archaeopteryx*.

Earlier conclusions that *Archaeopteryx* was capable of active flight[26] have not received universal support, largely because three skeletomorphological conditions considered essential for a functional avian flight stroke (ossified, keeled sternum; supracoracoideal "pully" arrangement; glenohumeral tolerance permitting supradorsal humeral abduction) were not yet present in *Archaeopteryx*[26-30]. Such challenges in reconciling *Archaeopteryx*'s dromaeosaurid-like pectoral morphology[30] with the modern avian dorsoventral flight stroke exemplify that avian powered flight may have worked through alternative configurations in the past. A putative aerodynamic control function for the long, stiff, frond-feathered tail[2] and hindlimb plumage[31] argue for an alternative aerial posture compared to modern birds. *Archaeopteryx*'s large coracoids[30] and robust, flattened and more dorsally positioned furcula lacking hypocleidial communication with the sternum[2] could have provided support for an anterodorsally-posteroventrally oriented flight stroke cycle that was morphologically closer to the "grabbing" motion of maniraptorans[25] and did not or hardly extend over the dorsum.

The avian nature of *Archaeopteryx*'s humeral and ulnar cross-sectional geometry shares more flight-related biomechanical and physiological adaptations with modern volant birds than previously known, which we argue to reflect the shared capability of powered flight. *Confuciusornis* from the Early Cretaceous of China also lacked the supracoracoideal pully[30] and sufficient dorsal humeral excursion[5] to permit a modern avian flight stroke. However, a variety of Early Cretaceous enantiornitine and euornithine birds (Supplementary Figure 1) was likely already capable of executing a dorsoventral wingbeat cycle[3,5,30], which suggests the development of dorsoventral flapping is primitive for Ornithothoraces and approximately coincided with the appearance of the avian alula[3]. The origin of the modern avian flight stroke was conceivably promoted by selective pressure towards vertical take-off[30], which contributed to the prosperous avian radiation that continued ever since.

METHODS

Materials

Specimens of *Archaeopteryx* in this study are designated through a commonly used numerical sequence that roughly corresponds to their succession of discovery[2]. The fifth specimen of *Archaeopteryx*[2] (JM 2257) is a nearly complete and largely articulated skeleton of the smallest *Archaeopteryx* specimen known to date. It is also known as the Eichstätt Specimen and housed at the Jura Museum in Eichstätt, Germany (JM). The seventh specimen of *Archaeopteryx*[2] (BSP 1999 I 50) is represented by a comparably complete skeleton exhibiting a substantial degree of articulation. It is formally named Solnhofen-Aktien-Verein Specimen but generally referred to as Munich Specimen, and is kept at the Paläontologisches Museum München in Munich, Germany (PMM). Skeletal elements of both the fifth and seventh specimen of *Archaeopteryx* have experienced brittle deformation during post-depositional compaction that resulted in splintering of the bone cortex. The ninth specimen of *Archaeopteryx*[2] (BMMS-BK1a) preserves a partially disarticulated right wing skeleton of comparably large size that is presently housed at the Bürgermeister-Müller-Museum in Solnhofen, Germany (BMM). It is officially named "Exemplar der Familien Ottman & Steil", also known as Bürgermeister-Müller Specimen, and colloquially referred to as "Chicken Wing". Although a certain degree of post-depositional

compaction is evidenced by the presence of several fractures that propagate through the long bone cortex, cortical splintering has not occurred. Its elements have therefore largely preserved their original three-dimensional geometry[2].

Comparative material (Supplementary Data 1) was sourced from the collections of the European Synchrotron Radiation Facility, Grenoble, France (ESRF), the Musée des Confluences, Lyon, France (MdC), the Muséum national d'Histoire naturelle, Paris, France (MNHM), the Museum of Evolution, Uppsala, Sweden (MoE), and the University of Manchester, Manchester, England (TUoM).

Data acquisition

The humeral and ulnar cross-sectional geometry of the three specimens of *Archaeopteryx*, 28 species of neornithine birds, the small coelurosaur *Compsognathus longipes*, the rhamphorhynchid pterosaur *Rhamphorhynchus* sp., the anhanguerid pterosaur *Brasileodactylus araripensis*, and the crocodile *Crocodylus niloticus* were visualised through propagation phase-contrast X-ray synchrotron radiation microtomography (PPC-SRμCT) at beamlines BM05 and ID19 of the European Synchrotron Radiation Facility. An ulnar cross section of aff. *Deinonychus antirrhopus* was imaged and subsequently paired with a humeral section of *D. antirrhopus* from literature[32] through morphological and dimensional comparison.

Synchrotron X-ray tomography was conducted by utilising an optimised polychromatic beam with sufficient coherence to permit the application of PPC-SRμCT. Propagation phase-contrast imaging relies on a certain propagation distance between the sample and the detector that allows for the exploitation of the phase-contrast effect towards emphasising low-contrast features[33]. The fifth and seventh specimen of *Archaeopteryx* were imaged in accumulation mode, a novel acquisition protocol developed for imaging fossils encased in lithic slabs. The motivation for and implementation of the accumulation mode are explained in Supplementary Note 1 Further details of the adopted data acquisition parameters for each sample are provided in Supplementary Data 3.

Data processing

Three-dimensional volume reconstruction was conducted through filtered back projection following a phase retrieval protocol that relies on a homogeneity assumption by using a modified[33] version of the algorithm developed by Paganin et al.[34]. Virtual two-dimensional cross-sectional slides were extracted directly from the reconstructed volumes at the developmental mid-diaphyseal plane oriented perpendicular to the local bone long axis in VGStudio MAX 2.2 (Volume Graphics, Heidelberg, Germany). Avian ulnae that carry a quill knob (ulnar papilla) at mid-diaphysis were virtually sampled at the level nearest to mid-diaphysis where no quill knob was present. The data set was supplemented with avian samples used in earlier studies[8,10,35]. Furthermore, scaled figures depicting complete perpendicular humeral and ulnar cross sections of non-avian archosaurs were sourced from literature[36-39] and processed in tandem with data obtained through PPC-SRμCT.

Cross-sectional geometry

Based on the characteristically unfolded nature of the Solnhofen Plattenkalk[40], the geometry of *Archaeopteryx* wing elements was assumed to have experienced only brittle deformation during unidirectional compaction with insignificant movement of bone fragments perpendicular to the visualised cross sections. Two-dimensional restoration was conducted with image editing software by virtual extraction of the bone fragments and visually applying optimal fit of local fracture geometry, periosteal and endosteal curvature across adjacent fragments, and internal structures (e.g. canalisation). For the ninth specimen of *Archaeopteryx*, humeral and ulnar parameters were obtained by averaging the values found for two reconstructed circa mid-diaphyseal cross sections each. As the humeral and ulnar geometry of the fifth and seventh specimen are distorted to a markedly larger degree than those of the ninth specimen, they are represented by the single best-preserved cross section present in the circa mid-diaphyseal domain.

The elements of *Compsognathus* and *Rhamphorhynchus* used in this study were recovered from the Solnhofen Plattenkalk as well, and were reconstructed following the same protocol as the *Archaeopteryx* material (Supplementary Fig. 10). One fragment of cortical bone is conspicuously absent at the optimal sample location for the *Compsognathus* ulna in the upper right quadrant of

the bone in the extracted slide, as also evidenced by an ulnar cross section extracted 3.58 mm proximal to the used sample location (Supplementary Fig. 10). The geometry of this cortical fragment at the sample location was reconstructed through close comparison with the bone and fracture geometry visible in the referred more proximal cross section.

All transverse cross sections were converted to binary cortical bone profiles by tracing the periosteal and endosteal surfaces and subsequently filling the area of the original cortical bone white[41]. Occasionally occurring spongy bone and obvious irregularities, such as cracks or protruding splints, were digitally removed. The area of the few small splints in fossil material that could not be accurately repositioned in their exact original orientation was taken into account during restoration of typically the periosteal margin. Cross-sectional geometric parameters were calculated with MomentMacro 1.4 (http://www.hopkinsmedicine.org/fae/mmacro.html) in the public-domain image analysis software ImageJ *(https://imagej.nih.gov/ij/).*

Most species in our data set are represented by the humerus and ulna of a single adult individual, although some were included as a composite of elements sourced from two individuals, or as average values derived from elements from two, three or four individuals (see Supplementary Data 1). Individuals sampled in this study are believed to represent adults based on element size and bone structure. *Archaeopteryx* specimens are often considered to be juveniles, which has been specifically concluded for the specimens of *Archaeopteryx* included in this study through relative size and bone surface texture[2,13]. The sampled *Compsognathus* specimen was also concluded to represent a juvenile individual[42]. The studied *Rhamphorhynchus* individual is of comparably small size, suggesting juvenility as well. Gender composition across the data set is generally unknown and was therefore not considered.

Locomotor modes and body mass

Avian flight mode categorisation notoriously suffers from the qualitative, non-discrete nature of faunal flight strategies[20]. To overcome classification-specific effects in discriminant analysis, we considered the classifications suggested by Viscor et al.[21] and Close et al.[20] independently. Both avian flight mode divisions were expanded with one group that encompasses volant wing-propelled diving auks, and supplemented with alternative archosaurian locomotory strategies

represented by exemplary taxa (Supplementary Data 1). The avian flight mode categories *sensu* Viscor et al.[21] encompass 1) short flight, 2) forward flapping/bounding flight, 3) high-frequency flapping flight, 4) undulating flight and 5) gliding – soaring flight, which were assigned following the proposed taxonomical designations[21]. Taxa not included in their work were assigned flight modes according to the provided description[21]. *Geococcyx californianus* was classified as 'short flight' rather than as 'forward flapping/bounding flight' proposed for Cuculidae. A second, more recent avian flight mode division by Close et al.[20] separates 1) burst flight, 2) intermittent bounding flight, 3) continuous flapping flight, 4) flap-gliding flight and 5) soaring flight, and was applied through description. We chose to score volant wing-propelled divers separately in both subdivisions as their aquatic locomotory strategy is known to profoundly influence wing bone morphology[8,43] and, consequently, the expression of flight-related adaptations recorded therein[43]. Both referred avian flight classifications were complemented with the following locomotor categories: 6) long-tailed pterosaurian flight, 7) short-tailed pterosaurian flight 8) (avian) non-volant wing-propelled diving, 9) ratite bipedal, 10) (non-avian) dinosaurian bipedal, 11) (non-avian) dinosaurian omnipedal, and 12) crocodilian quadrupedal.

Body mass values for extant taxa were either directly available for the referred individuals or sourced from online databases[44,45] and literature[46,47] as species averages (see Supplementary Data 1). For extinct forms, either specimen-specific body mass estimates[13,39,48] or average specific body mass estimates were available[49,50]. The Malagasy shelduck *Alopochen sirabensis*, reported to have been "slightly larger" than the Egyptian goose *Alopochen aegyptiaca*[51] (average body mass of 1900 g[44]), was assigned a reconstructed body mass of 2000 g. Body mass for the *Rhamphorhynchus* sp. MdC 20269891 was reconstructed through the relation between body mass and wing span for basal pterosaurs proposed by Witton[52]. Total wing length for MdC 20269891 was measured as the cumulative length of the humerus (19 mm), radius (34 mm), wing metacarpal (14 mm), phalange I (47 mm), phalange II (40 mm), phalange III (35 mm) and phalange IV (44 mm) taken from photographic and scan data, and amounts to 233 mm. In the Dark Wing specimen of *Rhamphorhynchus muensteri* (JME SOS 4785; Jura Museum Eichstätt), the distance between left and right glenoid measures 1.56 x humeral length, which proposes an original interglenoid distance of 30 mm for for McD 20269891. Its corresponding wingspan, calculated as twice the wing length plus the interglenoid distance, amounts to 0.496 m. From the

relation of Witton[52] follows a reconstructed body mass of 95 g. The body mass for the *Brasileodactylus araripensis* individual in our study was inferred through close morphological and dimensional agreement between its humerus (length 168 mm, maximum distal width of 47) and the humerus of AMNH 22552 (length 170 mm, maximum distal width of 46 mm)[53,54], for which a reconstructed wingspan of 3270 mm was reported[55]. From the described relation between wingspan and body mass in pterodactyloids[56] follows a reconstructed body mass of 6540 g.

Body mass values for the studied specimens of *Alligator mississippiensis* (141 cm[38]) and the domestically bred *Crocodylus niloticus* (200 cm; personal observation PT) were reconstructed through specific allometric scaling relations between body length and body mass offered in literature[57,58].

Cross-sectional parameters

Relative cortical thickness[12] (CA/TA) and mass-normalised resistance against torsional forces[12] (J/M) were quantified for archosaurian humeri and ulnae (Supplementary Data 1, Supplementary Figs. 4 and 5). CA/TA describes element hollowness as the ratio of cortical bone area to the total area delimited by the external surface of the bone in cross section (Supplementary Fig. 2). As such, CA/TA is proportionate to the corticodiaphysary index (CDI)[59] and inversely related to the K-parameter[6,10]. Polar moment of inertia of an area J quantifies the mechanical resistance against torsion around the longitudinal axis of the considered element. J mathematically equals the sum of the maximum second moment of area (Imax) and minimum second moment of area (Imin) that quantify resistance against deflection along the respective orthogonal major and minor principal axes (Supplementary Fig. 2) through the relative distribution of matter[12]. Values for J obtained from cross sections with an Imax/Imin > 1.50 are typically overestimated[12,60,61], but remain informative when considered proportionally rather than quantitatively (as is its derivative Zp[41,61]). J was normalised over body mass to permit comparison in a highly body mass-diversified comparative framework that spans well over five orders of magnitude (Supplementary Data 1).

Cortical vascular density, expressed as the amount of canals per mm^2 of bone area in cross-section[62-65], was considered qualitatively for a modest selection of archosaurs for which high-

resolution data was available, but not challenged statistically (Supplementary Data 1). Bone area in section was calculated as CA (see Cross-sectional geometry) with MomentMacro 1.4 in ImageJ 1.49. In the fifth and ninth specimen of *Archaeopteryx*, cortical canals were counted visually. Absolute canal abundance in the cross-sectional cortex of archosaurs other than *Archaeopteryx* was obtained through selection of the darkest gray levels in the grayscale histogram (including canals) by thresholding the cortical domain and subsequently counting the amount of elements within canal size range using the Analyze Particles function of ImageJ 1.49.

The ratio of Imax over Imin provides a reliable measure for the ellipticity of the transverse bone shaft and has been considered as such in biomechanical explorations[12,60,66,67]. These approaches traditionally assume that the degree and orientation of ellipticity reflect an adaptation that offers optimised resistance against bending, with the direction of Imax corresponding to the orientation of the maximum bending moment. However, an opposite functional interpretation of cross-sectional element ellipticity in which a preferred bending direction is achieved through orientation of Imin has also been proposed specifically for avian wing bones[68]. Such conflicting explanations of the same parameter illustrate the complexity of interpreting cross-sectional bone ellipticity in a functional context and thereby obscure the information offered by other characters when assessed in a multivariate context. We therefore chose not to include quantified bone ellipticity measures in our comparative study.

Tree inference and divergence chronogram

Mesozoic topology and timing used in this study (Supplementary Data 3 and Supplementary Figure 1) were derived from the Paleobiology Database[69] (PaleoDB). Divergence nodes were adopted as the older bound date for the oldest report of a taxon nested beyond the respective split. Mesozoic terminal nodes and the Tertiary terminal node for *Mancalla cedrosensis* were placed at the younger bound date of their occurrence. *Alopochen sirabensis* is placed at 656 AD, which represents the median calibrated radiocarbon age for the last-occurrence date for the species[70]. The 19th century terminal node for *Pinguinus impennis* was dated through its well-documented last observation in 1844 AD[71]. Topology and timing within the extant avian subset were largely adopted from the well-resolved phylogeny by Jarvis et al.[72] (Supplementary Data 3 and Supplementary Figure 1), since the more recent neoavian phylogeny proposed by Prum et al.[73] was found to conflict PaleoDB on numerous crucial accounts. Several higher-order

divergence times in Aves were obtained from PaleoDB following the procedure described above. Two specific inconsistencies in PaleoDB were negotiated through literature (see Supplementary Note 3). Insufficiently resolvable divergence nodes were placed at a standard + 4 MY with respect to their closest established crownward node. The three *Archaeopteryx* specimens were included as a polytomy at + 4 MY with respect to the older bound date for the genus in recognition of taxonomic and ontogenetic uncertainty[2]. The phylogenetic tree was constructed in Mesquite 3.04[74].

Statistical Analyses

The relations between individual geometric parameters and locomotor divisions in the training taxa were statistically assessed through phylogenetic analysis of covariance using the PDAP module of Garland et al.[75]. For each parameter, 10000 unbound simulations were performed along the constructed tree (Supplementary Figure 1) under a Brownian motion regime in PDSIMUL. ANCOVA was performed with a grouping of the training taxa according to their locomotor classes as response variable, parameter values as predictor variable, and body mass as covariate (Supplementary Data 5).

Phylogenetic PCA[76] scores for the studied taxa, founded on humeral and ulnar CA/TA and J/M (Supplementary Data 2), were obtained with the phyl.pca function (method: BM; mode: cor) of the phytools package[77] in the R-environment[78] through RStudio 0.99.484[79]. The phylogenetic PCA scores were subsequently subjected to Partitioning Around Medoids specified to two clusters with the pam function of the cluster package[80] in RStudio 0.99.484.

The archosaurian outgroups to *Archaeopteryx* serve as training taxa that represent known locomotor modes and thus form a morphological reference environment for discriminant analysis. The optimum value of Pagel's λ, the scaling factor of autocorrelation for a certain parameter on a given phylogenetic tree[81] to be applied in phylogenetically informed discriminant analysis, was found using the approach described by Schmitz et al.[82] in RStudio 0.99.484 (Supplementary Fig. 8). Linear discriminant analysis and classification of mystery taxa (Supplementary Data 2) was conducted in PAST 3.10[83], as was one-way MANOVA (Supplementary Tables 1-3) among individual locomotor strategies. Additional motivation for and information on the statistical approach used here is available as Supplementary Note 4.

Data Availability

All data underlying the study are available in Supplementary Data 1.

References

1. Ksepka, D. T. Evolution - A rapid flight towards birds. *Current Biology* **24,** 1052-1055 (2014).
2. Wellnhofer, P. *Archaeopteryx. Der Urvogel von Solnhofen* (Dr Friedrich Pfeil, 2008).
3. Chiappe, L. M., Qingjin, L. M. *Birds of Stone. Chinese Avian Fossils from the Age of Dinosaurs* (John Hopkins University Press, 2016).
4. Burgers, P. & Chiappe, L. M. The wing of Archaeopteryx as a primary thrust generator. *Nature* **399,** 60–62 (1999).
5. Mayr, G. Avian Evolution. *The Fossil Record of Birds and Its Paleobiological Significance* (Wiley Blackwell 2016).
6. Currey, J. D. & Alexander, R. The thickness of the walls of tubular bones. *Journal of Zoology* **206,** 453–468 (1985).
7. Frost, H. M. From Wolff's law to the Utah paradigm: Insights about bone physiology and its clinical applications. *The Anatomical Record* **262,** 398-419 (2001).
8. Cubo, J., & Casinos, A. Biomechanical significance of cross-sectional geometry of avian long bones. *European Journal of Morphology* **36**, 19-28 (1998).
9. Pennycuick, C. J. *Modelling the flying bird. Volume 5* (Elsevier, 2008).
10. De Margerie, E., Sanchez, S., Cubo, J. & Castanet, J. Torsional resistance as a principal component of the structural design of long bones: Comparative multivariate evidence in birds. *The Anatomical Record Part A: Discoveries in Molecular, Cellular, and Evolutionary Biology* (2005).
11. Tafforeau, P. *et al.* Applications of X-ray synchrotron microtomography for non-destructive 3D studies of paleontological specimens. *Applied Physics A* **83,** 195–202 (2006).

12. Simons, E. L. R., Hieronymus, T. L. & O'Connor, P. M. Cross sectional geometry of the forelimb skeleton and flight mode in pelecaniform birds. *Journal of Morphology* **272,** 958–971 (2011).
13. Erickson, G. M. *et al.* Was Dinosaurian Physiology Inherited by Birds? Reconciling Slow Growth in Archaeopteryx. *PLoS ONE* **4,** e7390 (2009).
14. Cubo, J., Le Roy, N., Martinez-Maza, C., & Montes, L. Paleohistological estimation of bone growth rate in extinct archosaurs. *Paleobiology* **38**, 335-349 (2012).
15. Montes, L., Le Roy, N., Perret, M., De Buffrenil, V., Castanet, J., & Cubo, J. Relationships between bone growth rate, body mass and resting metabolic rate in growing amniotes: a phylogenetic approach. *Biological Journal of the Linnean Society* **92**, 63-76 (2007).
16. Chinsamy-Turan, A. The microstructure of dinosaur bone: deciphering biology with fine-scale techniques (John Wiley & Sons, 2005).
17. Smith, N. A. & Clarke, J. A. Osteological Histology of the Pan-Alcidae (Aves, Charadriiformes): Correlates of Wing-Propelled Diving and Flightlessness: Osteological Histology of The Pan-Alcidae. *The Anatomical Record* **297,** 188–199 (2014).
18. Ebel, K. On the origin of flight in Archaeopteryx and in pterosaurs. *Neues Jahrbuch für Geologie und Palaöntologie – Abhandlungen* **202,** 269-285 (1996).
19. Thulborn, R. A. Wind-assisted flight of Archaeopteryx. *Neues Jahrbuch für Geologie und Palaöntologie – Abhandlungen* **229,** 61-74 (2003).
20. Close, R. A. & Rayfield, E. J. Functional morphometric analysis of the furcula in Mesozoic birds. *PloS one* **7,** e36664 (2012).
21. Viscor, G. & Fuster, J. F. Relationships between morphological parameters in birds with different flying habits. *Comp. Biochem. Physiol.* **87A,** 231-249 (1987).
22. Hone, D., Henderson, D. M., Therrien, F. & Habib, M. B. A specimen of Rhamphorhynchus with soft tissue preservation, stomach contents and a putative coprolite. *PeerJ* **3**, e1191 (2015).
23. Bennett, S. C. A statistical study of Rhamphorhynchus from the Solnhofen Limestone of Germany: year-classes of a single large species. *Journal of Paleontology* **69**, 569-580 (1995).

24. Socha, J. J., Jafari, F., Munk, Y. & Byrnes, G. How animals glide: from trajectory to morphology. *Canadian Journal of Zoology* **93**, 901-924 (2015).
25. Gishlick, A. D. in *New perspectives on the origin and early evolution of birds* (Gauthier, J., & Gall, L. F. eds.) 301-318 (Peabody Museum of Natural History, 2001).
26. Olson, S. L. & Feduccia, A. Flight capability and the pectoral girdle of Archaeopteryx. *Nature* **278,** 247–248 (1979).
27. Zheng, X. *et al.* On the absence of sternal elements in Anchiornis (Paraves) and Sapeornis (Aves) and the complex early evolution of the avian sternum. *Proceedings of the National Academy of Sciences* **111,** 13900–13905 (2014).
28. Poore, S. O., Sánchez-Haiman, A., & Goslow, G. E. Wing upstroke and the evolution of flapping flight. *Nature* **387**, 799-802 (1997).
29. Senter, P. Scapular orientation in theropods and basal birds, and the origin of flapping flight. *Acta Palaeontologica Polonica* **51,** 305-313 (2006).
30. Mayr, G. Pectoral girdle morphology of Mesozoic birds and the evolution of the avian supracoracoideus muscle. *Journal of Ornithology* (2017).
31. Longrich, N. Structure and function of hindlimb feathers in Archaeopteryx lithographica. *Paleobiology* **32,** 417–431 (2006).
32. Parsons, W. L. & Parsons, K. M. Further descriptions of the osteology of Deinonychus antirrhopus (Saurischia, Theropoda). *Bulletin of the Buffalo Society of Natural Sciences* **38,** 43-54 (2009).
33. Sanchez, S., Ahlberg, P. E., Trinajstic, K. M., Mirone, A. & Tafforeau, P. Three-Dimensional Synchrotron Virtual Paleohistology: A New Insight into the World of Fossil Bone Microstructures. *Microscopy and Microanalysis* **18,** 1095–1105 (2012).
34. Paganin, D., Mayo, S. C., Gureyev, T. E., Miller, P. R., & Wilkins, S. W. Simultaneous phase and amplitude extraction from a single defocused image of a homogeneous object. *Journal of Microscopy* **206**, 33-40 (2002).
35. Cubo, J. & Casinos, A. Incidence and mechanical significance of pneumatization in the long bones of birds. *Zoological Journal of the Linnean Society* **130,** 499–510 (2000).
36. Werning, S. The ontogenetic osteohistology of Tenontosaurus tilletti. *PLoS One* **7,** e33539 (2012).

37. White, M. A., Cook, A. G., Hocknull, S. A., Sloan, T., Sinapius, G. H., & Elliott, D. A. New forearm elements discovered of holotype specimen Australovenator wintonensis from Winton, Queensland, Australia. *PloS One* **7,** e39364 (2012).
38. Woodward, H. N., Horner, J. R. & Farlow, J. O. Quantification of intraskeletal histovariability in Alligator mississippiensis and implications for vertebrate osteohistology. *PeerJ* **2,** e422 (2014).
39. Bybee, P. J., Lee, A. H., & Lamm, E. T. Sizing the Jurassic theropod dinosaur Allosaurus: assessing growth strategy and evolution of ontogenetic scaling of limbs. *Journal of Morphology* **267,** 347-359 (2006).
40. Barthel, K. W., Swinburne, N. H. M., Conway Morris, S. *Solnhofen. A study in Mesozoic palaeontology* (Cambridge University Press, 1990).
41. Lee, A. H. & Simons, E. L. R. Wing bone laminarity is not an adaptation for torsional resistance in bats. *PeerJ* **3,** e823 (2015).
42. Callison, G., Quimby, H. M. Tiny dinosaurs: Are they fully grown? *Journal of Vertebrate Paleontology* **3**, 200-209 (1984).
43. Habib, M. B., & Ruff, C. B. The effects of locomotion on the structural characteristics of avian limb bones. *Zoological Journal of the Linnean Society* **153**, 601-624 (2008).
44. De Magalhaes, J. P., & Costa, J. A database of vertebrate longevity records and their relation to other life-history traits. *Journal of evolutionary biology* **22,** 1770-1774 (2009). Retrieved from on http://genomics.senescence.info/species/ on 18 January 2016.
45. del Hoyo, J., Elliott, A., Sargatal, J., Christie, D. A., & de Juana, E. *Handbook of the Birds of the World Alive* (Lynx Editions, 2015). Retrieved from http://www.hbw.com on 19 January 2016.
46. Batty, J. *Domesticated ducks and geese* (Nimrod Book Services, 1985).
47. Macky, R. & White, B. (eds.) *Gastrointestinal Microbiology: Volume 1 Gastrointestinal Ecosystems and Fermentations* (Nimrod Book Services, 1996).
48. Paul, G. S. *Predatory dinosaurs of the world: a complete illustrated guide* (Simon & Schuster, 1988).
49. Livezey, B. C. Morphometrics of flightlessness in the Alcidae. *The Auk* **105,** 681-698 (1988).
50. Paul, G. S. *The Princeton field guide to dinosaurs* (Princeton University Press, 2010).

51. Andrews, C. On some fossil remains of carinate birds from Central Madagascar. *Ibis* **39,** 343-359 (1897).
52. Witton, M. P. in *Special volume: Flugsaurier: pterosaur papers in honour of Peter Wellnhofer* (Buffetaut, E. & Hone, D. W. E. eds.) 143-158 (München, 2008).
53. Kellner, A. W. A., & Tomida, Y. Description of a new species of Anhangueridae (Pterodactyloidea) with comments on the pterosaur fauna from the Santana Formation (Aptian-Albian), northeastern Brazil. *National Science Museum Monographs* **17,** 1-135 (2000).
54. Veldmeijer, A. J. Pterosaurs from the Lower Cretaceous of Brazil in the Stuttgart Collection. *Stuttgarter Beitr. Naturk. Ser. B.* **327,** 1-27 (2002).
55. Wellnhofer, P. Weitere Pterosaurierfunde aus der Santana-Formation (Apt) der Chapada do Araripe, Brasilien. *Palaeontographica Abteilung A.* **187,** 43-101 (1991).
56. Henderson, D. M. Pterosaur body mass estimates from three-dimensional mathematical slicing. *Journal of Vertebrate Paleontology* **30,** 768-785 (2010).
57. Masser, M. P. Alligator Production: Grow-out and harvest. *SRAC Publication* **232**, 1-4 (1993).
58. Huchzermeyer, F. W. *Crocodiles: Biology, Husbandry, and Diseases* (CABI, 2003).
59. Castanet, J., Grandin, A., Abourachid, A., & de Ricqlès, A. (1996). Expression de la dynamique de croissance dans la structure de l'os périostique chez Anas platyrhynchos. *Comptes Rendus de l'Académie des Sciences – Series III* **319,** 301-308 (1996).
60. Daegling, D. J. Estimation of torsional rigidity in primate long bones. *Journal of Human Evolution* **43,** 229–239 (2002).
61. Ruff, C. B., Burgess, M. L., Bromage, T. G., Mudakikwa, A. & McFarlin, S. C. Ontogenetic changes in limb bone structural proportions in mountain gorillas (Gorilla beringei beringei). *Journal of Human Evolution* **65,** 693–703 (2013).
62. de Buffrénil, V., Houssaye, A. & Böhme, W. Bone vascular supply in monitor lizards (Squamata: Varanidae): Influence of size, growth, and phylogeny. *Journal of Morphology* **269,** 533–543 (2008).
63. Legendre, L. *et al.* Phylogenetic signal in bone histology of amniotes revisited. *Zoologica Scripta* **42,** 44–53 (2013).

64. Cubo, J., Baudin, J., Legendre, L., Quilhac, A., & De Buffrénil, V. Geometric and metabolic constraints on bone vascular supply in diapsids. *Biological Journal of the Linnean Society* **112,** 668-677 (2014).
65. Wilson, L. E. & Chin, K. Comparative osteohistology of Hesperornis with reference to pygoscelid penguins: the effects of climate and behaviour on avian bone microstructure. *Royal Society Open Science* **1,** 140245–140245 (2014).
66. Carlson, K. J. Investigating the form-function interface in African apes: Relationships between principal moments of area and positional behaviors in femoral and humeral diaphyses. *American Journal of Physical Anthropology* **127,** 312–334 (2005).
67. Patel, B. A., Ruff, C. B., Simons, E. L. R. & Organ, J. M. Humeral Cross-Sectional Shape in Suspensory Primates and Sloths: Long Bone Cross-Sectional Shape. *The Anatomical Record* **296,** 545–556 (2013).
68. Bertram, J. E., & Biewener, A. A. Bone curvature: sacrificing strength for load predictability? *Journal of Theoretical Biology* **131,** 75-92 (1988).
69. Paleobiology Database (2016). Retrieved from http://paleobiodb.org on 29 January 2016.
70. Turvey, S. T. (ed.) *Holocene extinctions*. (OUP Oxford, 2009).
71. Bengtson, S.-A. Breeding ecology and extinction of the great auk (Pinguinus impennis): anecdotal evidence and conjectures. *The Auk* **101,** 1-12 (1984).
72. Jarvis, E. D. *et al.* Whole-genome analyses resolve early branches in the tree of life of modern birds. *Science* **346**, 1320-1331 (2014).
73. Prum, R. O. *et al.* A comprehensive phylogeny of birds (Aves) using targeted next-generation DNA sequencing. *Nature* **526,** 569–573 (2015).
74. Madison, W. P. & Madison, D. R. Mesquite: A Modular System for Evolutionary Analysis - Version 3.04 (2015). Retrieved from http://mesquiteproject.org on 29 September 2015.
75. Garland, T., Dickerman, A. W., Janis, C. M., & Jones, J. A. Phylogenetic analysis of covariance by computer simulation. *Systematic Biology* **42,** 265-292 (1993).
76. Revell, L. J. Size-correction and principal components for interspecific comparative studies. *Evolution* **63,** 3258-3268 (2009).

77. Revell, L. J. phytools: an R package for phylogenetic comparative biology (and other things). *Methods Ecol. Evol.* **3,** 217-223 (2012).
78. R Core Team. A language and environment for statistical computing. Vienna: R Foundation for Statistical Computing. (2015).
79. RStudio Team RStudio: Integrated Development for R. RStudio, Inc. (2015).
80. Maechler, M., Rousseeuw, P., Struyf, A., Hubert, M. & Hornik, K. *cluster: Cluster analysis basics and extensions.* R package version 2.0.4. *CRAN* (2016).
81. Pagel, M. Inferring the historical patterns of biological evolution. *Nature* **401,** 877–884 (1999).
82. Schmitz, L. & Motani, R. Nocturnality in dinosaurs inferred from scleral ring and orbit morphology. *Science* **332,** 705–708 (2011).
83. Hammer, Ø., Harper, D. A. T., & Ryan, P. D. Past: paleontological statistics software package for education and data analysis. *Palaeontologia Electronica* **4,** art. 4 (2004).

Acknowledgements The authors thank P.E. Ahlberg, V. Fernandez, D.J. Field, D. Hanley, A. Houssaye, G. Oatley, O.W.M. Rauhut, F.J. Serrano, and E.L.R. Simons for discussions or providing advice. D. Berthet (Musee des Confluences, Lyon, France), M. Eriksson (Museum of Evolution, Uppsala, Sweden), C.K. Lefèvre (MNHN, Paris, France), and J. R. Nudds (School of Earth and Environmental Sciences, University of Manchester, UK) are acknowledged for providing access to the material kept in their care. Beamtime was available as inhouse beamtime at the ESRF.

Author Contributions D.F.A.E.V., P.T. and S.S. conceived the study and designed the experiments, D.F.A.E.V., M.R., V.B., P.T. and S.S. performed the experiments, D.F.A.E.V., J.C., E.d.M. and S.S. analysed the data, D.F.A.E.V. wrote the manuscript, J.C., E.d.M., M.R., V.B., S.B., P.T. and S.S. helped with and edited the manuscript.

Competing interests The authors declare no competing financial interests.

Chapter 6: Future perspective - The vascular network in cortical bone of *Archaeopteryx* and its implications for reconstructing phylogeny, ontogeny, physiology, and locomotory aspects

Abstract The Bavarian Urvogel *Archaeopteryx* arguably represents the oldest fossil bird described to date and, as such, plays an important role in our understanding of early avian evolution. Despite extensive study, its mosaic morphology has complicated reliable reconstructions of its locomotory habits, including the performance and mode of its volancy. I propose the study of vascular patterns in the long bones of its wings and hind limbs that, in a comparative framework, will inform on the stress regime experienced by these elements *in vivo*. Such parameters will furthermore provide insight into the metabolic regime, crucially linked with activity patterns, and ontogenetic and phylogenetic disparity in *Archaeopteryx* towards answering long-standing questions on the nature of variations observed within this iconic taxon. High-resolution tomographic data obtained non-destructively at the European Synchrotron Radiation Facility will be made available for the proposed study. These data encompass scans of various elements of different specimens of *Archaeopteryx* and a comprehensive sample of other fossil archosaurian taxa from equivalent deposits, additional Mesozoic dinosaurs spanning a broad size range, a Mesozoic bird, extant crocodiles, and a large diversity of modern birds spanning all their locomotory strategies from obligate non-volant to hyperaerial flight. With state-of-the-art visualization and analytical software, I aim to disentangle the various physiological parameters influencing intracortical vascular morphology and orientation in archosaurs to contextualize the conditions encountered in *Archaeopteryx* and interpret the findings in a locomotory context.

6.1 Challenges

Archaeopteryx fossils are exclusively preserved on slabs of strongly compacted limestone that expose up to an estimated circa 60% of its skeletal elements (Wellnhofer 2008), which hampers insight in the true, three-dimensional morphology of the skeleton. Furthermore, these fossils represent valuable museum pieces that are typically not available for further preparation or for invasive sampling techniques that may offer improved insight into its bone structure (Witmer et al. 2002). Analysis of minute bone chips extracted from the seventh (Munich) specimen has provided sparse information on osteohistological microstructure (Erickson et al. 2009), but these findings are challenging to reconcile with other lines of evidence and have raised new questions that can only be answered with robust sampling and rigorous comparison with an extensive set of representative reference taxa.

Synchrotron tomography has enabled the reliable visualization of bone microstructures in both modern and fossil vertebrates (e.g. Sanchez et al. 2012, 2014, 2016). Particular properties of the vascular network, such as orientation, volume, and differential distribution, are known to be influenced by the biomechanical regime imposed on the considered bones (De Margerie et al. 2005, 2006), but also relate to the phylogenetic relations, metabolic regime, and ontogenetic stage of the studied animal (Montes et al. 2007; Cubo et al. 2012; Sanchez et al. 2014, 2016). Such properties can be studied in extant animals with observable habits and known life strategies, which in turn informs on equivalent conditions in the extinct vertebrates they are compared to. Although the relation between physiological conditions and bone microanatomy is complex, reflection of particular characters encountered in fossil life forms on their broad phylogenetic bracket (Witmer 1995) allows for the recognition of the factors involved towards disentangling these individual influences and adopting them as informative proxies.

6.2 Key research objectives

We propose the investigation of the intracortical vascular mesh in long bones of the fourth (but consider Foth et al. 2017), fifth, seventh, eighth, and ninth specimen of *Archaeopteryx* (following Wellnhofer 2008 but consider Rauhut et al. 2018; Fig. 6.1-a) towards answering outstanding questions on their locomotory affinity. To achieve this, we will test the hypothesis that intracortical vascular orientation in the humerus and ulna of *Archaeopteryx* recorded flight-related biomechanical adaptations that can be contextualized and interpreted through comparison with a diverse reference set of archosaurs employing well-understood locomotory strategies. In addition, we expect to retrieve additional insights into ontogenetic variation and metabolic strategy. This study will offer a valuable reference for future studies and will promote the adoption of high-resolution non-destructive imaging techniques through demonstration of its superior applications towards understanding the true, three-dimensional nature of the microstructure of fossil bone.

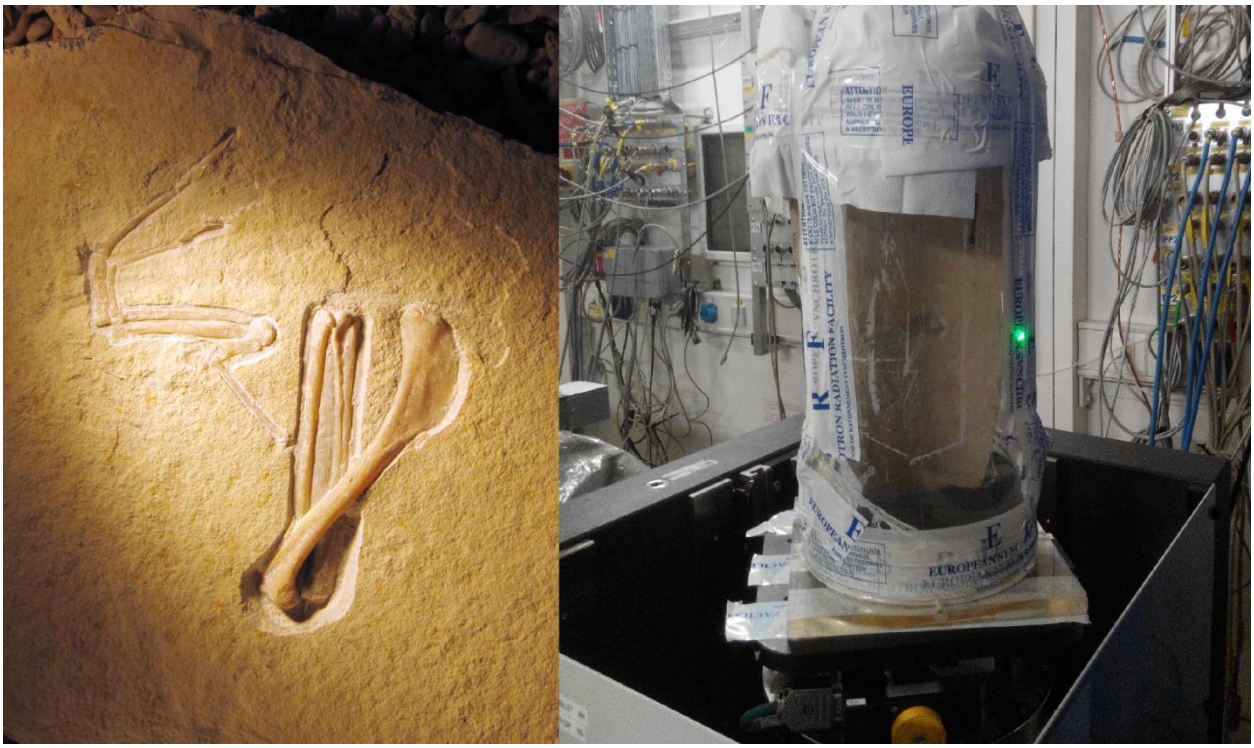

Figure 6.1 The ninth (Bürgermeister-Müller) specimen of *Archaeopteryx* represents a well-preserved right wing skeleton **(a)** that was visualized at beamline BM05 of the European Synchrotron Radiation Facility **(b)**.

6.3 Proposed methodology

Two-dimensional virtual cross sections revealed the presence of moderately abundant vascular canals inside the humerus and ulna of *Archaeopteryx* (Chapter 5). We propose this indicates a higher metabolic rate and growth rate than was originally suggested based on earlier analysis of minute bone chips extracted from the femur and fibula of the seventh (Munich) specimen (Erickson et al. 2009). In addition, the scant information on vascularization that could be extracted from these cross sections suggests that cortical canals are oriented longitudinally or obliquely, as radial or circumferential patterns seem absent, although this cannot be ascertained without additional confirmation. Furthermore, since intra-elemental and intraskeletal histovariability is common in archosaurs (Woodward 2012; Woodward et al. 2014), it remains unclear whether these preliminary observations are representative for the vascular record throughout the fossil skeletons of *Archaeopteryx*. Because a recent study has demonstrated that two-dimensional histological analysis by transverse sectioning often results in a distorted representation that is uncharacteristic for the true distribution of microstructural phenomena inside bone (Stein et al. 2014), resolving such issues requires three-dimensional data from a variety of skeletal elements.

Since long bones represent the standard elements traditionally used in comparative osteohistological study (Francillon-Vieillot et al. 1990; Chinsamy-Turan 2005) and because the expression of avian skeletal adaptations to flight mode is strongest in the humerus and ulna (De Margerie et al. 2005), we will focus on these elements in various *Archaeopteryx* specimens to obtain information on the morphology and geometry of their vascular pattern in three dimensions. To investigate the condition in elements subjected to different locomotory demands, the data sample extracted from the winged anterior limb will be expanded to include additional long bones from the posterior limb. Furthermore, three-dimensional visualization will permit a contrast of the archaeopterygian vascular mesh against those of modern archosaurs that represent end-members of a well-understood coupled life-strategic and metabolic continuum: exothermic crocodiles exhibiting protracted growth, and endothermic birds that adhere to a particularly determinate growth pattern (Chinsamy-Turan 2005) and often reach adult size within the first year of life. Extensive comparison with wing elements and posterior limb bones of modern birds has the potential to inform on wing employment in *Archaeopteryx*, but may also provide insight

in the habitual position of the femur that was positioned upright in non-avian dinosaurs but is held nearly horizontal in modern birds (Wellnhofer 2008). Beside such qualitative investigations, the availability of digital models of the vascular mesh permits quantification of the dominant vascular orientation relative to the bone long axis (Jia et al. 2010; Pratt et al. 2017), which will allow for rigorous statistical assessment of this parameter across archosaurs and contextualization of the condition that will be encountered in the elements of *Archaeopteryx*.

We will also investigate the intracortical vascular mesh of selected extinct archosaurs recovered from the same Jurassic deposits as *Archaeopteryx*. The basal pterosaur *Rhamphorhynchus* and the small coelurosaurian dinosaur *Compsognathus* were preserved under the same conditions as *Archaeopteryx* and arguably inhabited the same or nearby environments. This offers a unique opportunity to prevent uncertainty regarding the particular external influence of climate and seasonal variability, taphonomical and post-depositional processes, and preservational bias when interpreting the osteohistology of *Archaeopteryx*. In addition, the study is expected to offer new insights into the physiology and life history of these taxa that appear to have lived alongside *Archaeopteryx*.

Obtained comparative data furthermore covers the iconic large theropod *Tyrannosaurus*, its moderately large relative *Nanotyrannus*, and the smaller maniraptoran *Deinonychus*; all from the Cretaceous of the United States, the Cretaceous enantiornithine bird *Martinavis* from southern France, and several size classes of the extant crocodile *Crocodylus niloticus*. A diversity of non-volant paleognaths (the ostrich, rhea, and kiwi) is represented in addition to the tinamou; the only volant extant paleognath, which will offer phylogenetic control on volancy among Neornithes. The wide selection of modern volant neognaths includes a well-sampled diversity of ecological specialties, body sizes, and associated locomotory strategies, ranging from taxa that hardly fly, such as the enigmatic hoatzin, the turaco, and the Californian roadrunner, to hyperaerial specialists, such as the albatross, the petrel, and the harrier.

Tomographic data has been collected at the beamlines BM05, ID17 and ID19 of the European Synchrotron Radiation Facility in Grenoble, France (Fig. 6.1-b), which arguably present the most advanced microtomographic instruments in the world. To ensure sufficient image contrast and spatial resolution towards the reliable visualization of the often minute intracortical canals, propagation phase-contrast imaging using appropriate energy levels, propagation distances, and

filters, combined with state-of-the-art detector setups and innovative reconstruction and post-processing algorithms, has been conducted. The quality of the resulting image stacks that reliably describe the contained data in three dimensions, even those of fossil taxa, often exceeds those of data obtained by alternative approaches for visualizing osteohistological features in modern material (Fig. 6.2).

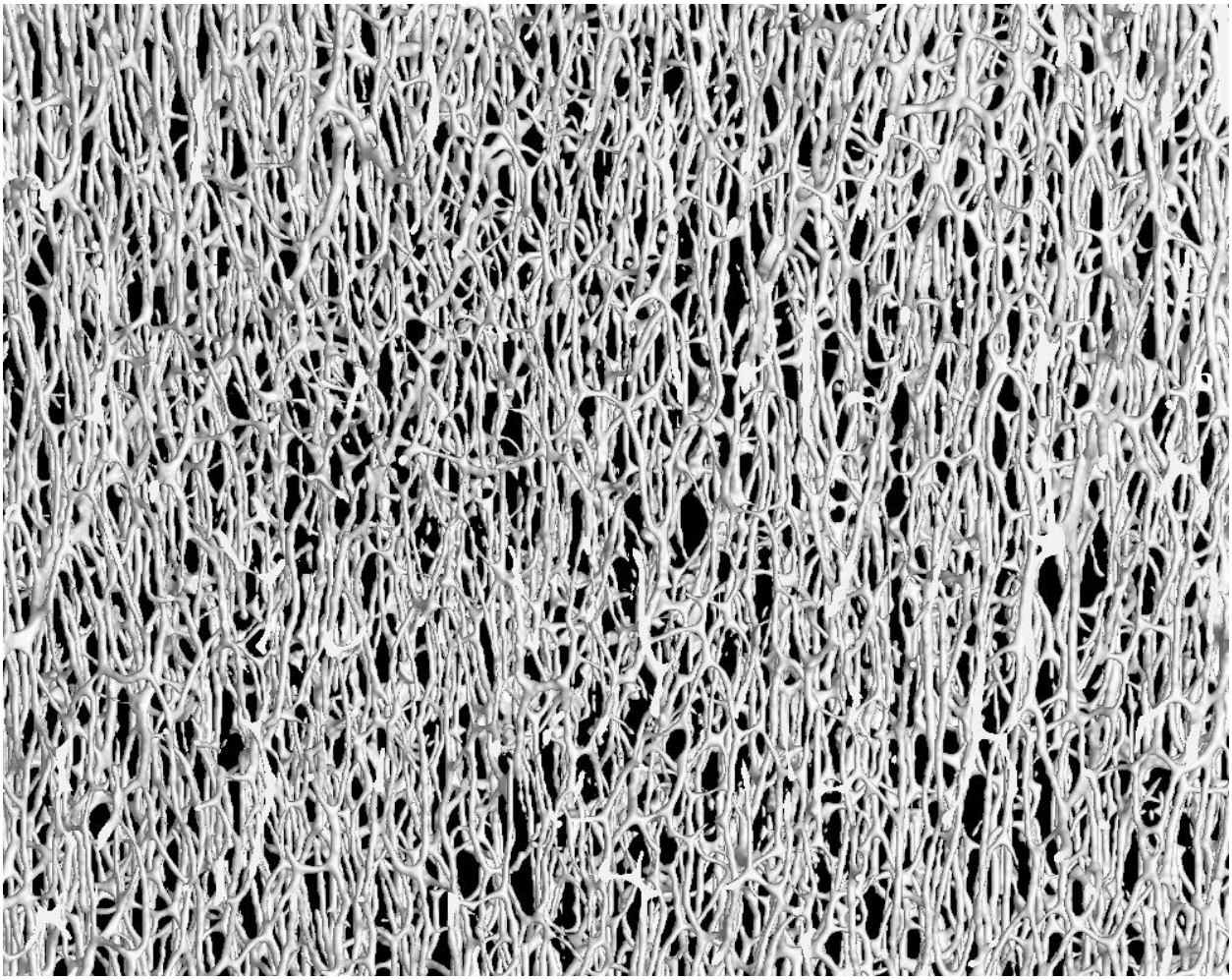

Figure 6.2 Segmented vascular mesh inside the mid-diaphyseal ulnar cortex of *Deinonychus*.

The cortical mesh will be extracted from the sample using VGStudio MAX (Volume Graphics, Heidelberg, Germany), and representatively visualized in various standard orientations.

VGStudio MAX offers complete freedom in data representation in three dimensions towards optimal presentation of the vascular mesh and allows for objective comparison throughout the sample. An additional analytic algorithm implemented in VGStudio MAX, the Fiber Composite Material Analysis Module, available at the ESRF and Uppsala University, is capable of quantifying true fiber orientation relative to a predetermined reference environment (such as the bone long axis) based on element integration size (such as the diameter of the considered canals). Fiber orientation is presented as a mean orientation tensor that, when the z-direction of the reference environment is aligned with the local long axis of the bone, provides the directional affinity of the vascular mesh as its "ZZ statistic" (Fig 6.3). This parameter will be obtained for a selected interval around the mid-diaphyseal point of the element. This location often corresponds to the ontogenetic origin of the bone, since this location is typically positioned furthest away from muscle insertions, and represents the most constrained domain of the element during locomotion (Simons et al. 2011) because of the elongated hourglass-shaped morphology of long bones.

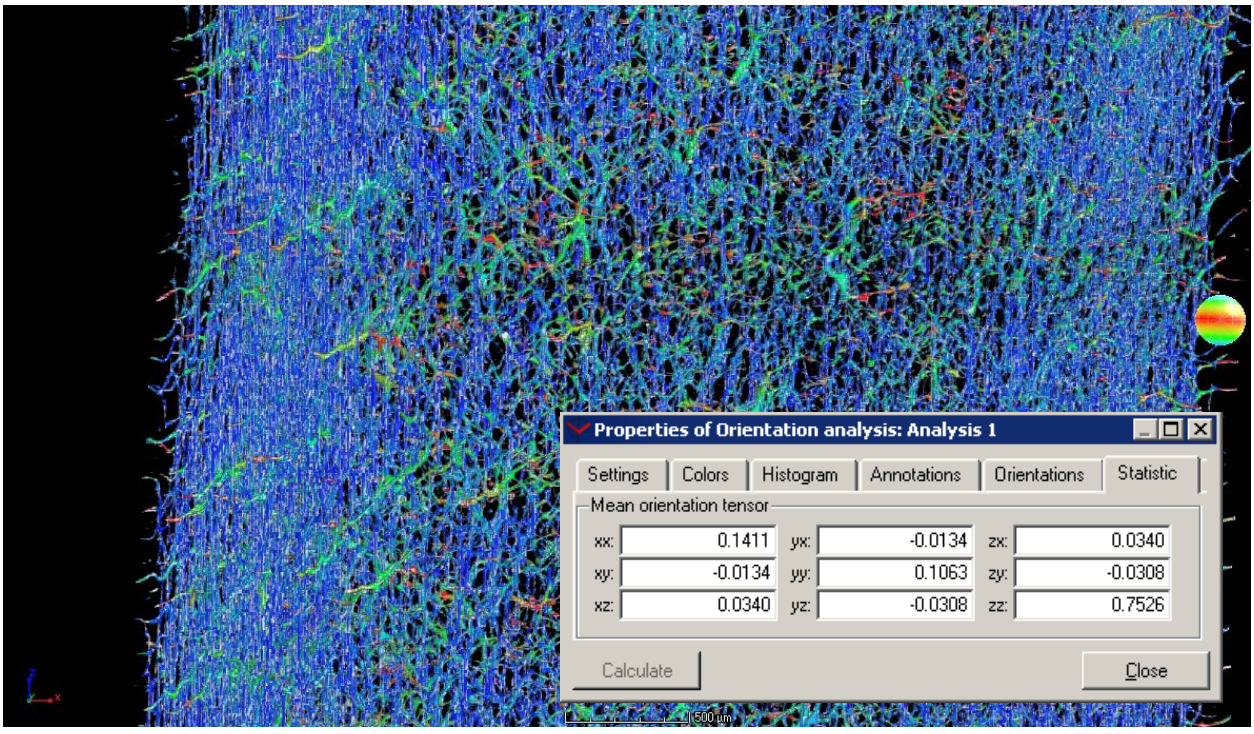

Figure 6.3 Humeral cortical vascularization of the Eurasian collared dove (*Streptopelia decaocto*) with ZZ tensor indicating percentage or vascular orientation along the bone long axis.

Preliminary tests of this method have offered promising results; a brief overview of the approach and a proof-of-concept that included four elements (humeri of two volant birds and a crocodile, as well as the ulna of *Deinonychus*) was presented at the International Symposium of Palaeohistology in Bonn, Germany (August 2015), where it was awarded "best student presentation". I therefore feel encouraged to implement this method in an applied study towards uncovering long-awaited fresh insights into the biology and life history of the Bavarian icon of evolution: *Archaeopteryx*.

References

Aigner, T. *An Ancient Storm Depositional system: Dynamic Stratigraphy of Intracratonic Carbonates, Upper Muschelkalk (Middle Triassic), South-German Basin*. Springer Berlin Heidelberg, 1985.

Alibardi, L., L. W. Knapp, and R. H. Sawyer. "Beta-keratin localization in developing alligator scales and feathers in relation to the development and evolution of feathers." *Journal of Submicroscopic Cytology and Pathology* 38, no. 2-3 (2006): 175-192.

Albers, P. C. H., and O. Rieppel. "A new species of the sauropterygian genus Nothosaurus from the Lower Muschelkalk of Winterswijk, the Netherlands." *Journal of Paleontology* 77, no. 4 (2003): 738-744.

Albers, P. C. H. "New Nothosaurus skulls from the Lower Muschelkalk of the western Lower Saxony Basin (Winterswijk, The Netherlands) shed new light on the status of Nothosaurus winterswijkensis." *Netherlands Journal of Geosciences* 90, no. 1 (2011): 15-22.

Alexander, D. E., E. Gong, L. D. Martin, D. A. Burnham, and A. R. Falk. "Model tests of gliding with different hindwing configurations in the four-winged dromaeosaurid Microraptor gui." *Proceedings of the National Academy of Sciences* 107, no. 7 (2010): 2972-2976.

Allen, V., K. T. Bates, Z. Li, and J. R. Hutchinson. "Linking the evolution of body shape and locomotor biomechanics in bird-line archosaurs." *Nature* 497, no. 7447 (2013): 104-107.

Alonso, P. D., A. C. Milner, R. A. Ketcham, M. J. Cookson, and T. B. Rowe. "The avian nature of the brain and inner ear of Archaeopteryx." *Nature* 430, no. 7000 (2004): 666-669.

Askew, G. N., R. L. Marsh, and C. P. Ellington. "The mechanical power output of the flight muscles of blue-breasted quail (Coturnix chinensis) during take-off." *Journal of Experimental Biology* 204, no. 21 (2001): 3601-3619.

Askew, G. N., and R. L. Marsh. "Muscle designed for maximum short-term power output: quail flight muscle." *Journal of Experimental Biology* 205, no. 15 (2002): 2153-2160.

Bachmann, G. H., G. Beutler, H. Hagdorn, and N. Hauschke. "Stratigraphie der germanischen Trias." *Trias-Eine ganz andere Welt.* Pfeil Verlag (1999): 81-104.

Baier, D. B., S. M. Gatesy, and F. A. Jenkins. "A critical ligamentous mechanism in the evolution of avian flight." *Nature* 445, no. 7125 (2007): 307-310.

Balanoff, A. M., G. S. Bever, T. B. Rowe, and M. A. Norell. "Evolutionary origins of the avian brain." *Nature* 501, no. 7465 (2013): 93-96.

Balda, R. P., G. Caple, and W. R. Willis. “Comparison of the gliding to flapping sequence with the flapping to gliding sequence.” *The Beginnings of Birds* (1985): 267–277

Barker, C. T., D. Naish, E. Newham, O. L. Katsamenis, and G. Dyke. “Complex neuroanatomy in the rostrum of the Isle of Wight theropod Neovenator salerii.” *Scientific Reports* 7 (2017): srep03749.

Barthel, K. W., N. H. M. Swinburne, and S. C. Morris. *Solnhofen – A Study in Mesozoic Palaeontology*. CUP Archive, 1990.

Benson, R.B.J. and S. Brussatte. *Prehistoric Life*. London: Dorling Kindersley, 2012.

Benson, R. B. J., M. Evans, and P. S. Druckenmiller. “High diversity, low disparity and small body size in plesiosaurs (Reptilia, Sauropterygia) from the Triassic–Jurassic boundary.” *PLoS One* 7, no. 3 (2012): e31838.

Benson, R. B. J., E. Starmer-Jones, R. A. Close, and S. A. Walsh. “Comparative analysis of vestibular ecomorphology in birds.” *Journal of Anatomy* 231, no. 6 (2017): 990-1018.

Beyrand, V., D. F. A. E. Voeten, S. Bureš, V. Fernandez, J. Janáček, D. Jirák, O. Rauhut, and P. Tafforeau. “Developmental evolution of the brain enabled archosaurian flight.” *Nature* (submitted).

Biewener, A. A., and J. E. A. Bertram. “Mechanical loading and bone growth in vivo.” *Bone* 7 (1993): 1-36.

Bonnin, A., M. Renier, J.-P. Valade, V. Beyrand, D. F. A. E. Voeten, M. Röper, and P. Tafforeau. “3D scattering imaging: large fossils on rock slabs.” *XTOP 2014 Abstract Book* (2014): 81.

Bordas, J., M. H. J. Koch, P. N. Clout, E. Dorrington, C. Boulin, and A. Gabriel. “A synchrotron radiation camera and data acquisition system for time resolved X-ray scattering studies.” *Journal of Physics E: Scientific Instruments* 13, no. 9 (1980): 938.

Bracewell, R. N., and A. Riddle. “Inversion of fan-beam scans in radio astronomy.” *The Astrophysical Journal* 150 (1967): 427-434.

Brooks, R. A., and G. Di Chiro. “Theory of image reconstruction in computed tomography.” *Radiology* 117, no. 3 (1975): 561-572.

Brooks, R. A. “A quantitative theory of the Hounsfield unit and its application to dual energy scanning.” *Journal of Computer Assisted Tomography* 1, no. 4 (1977): 487-493.

Brusatte, S. L., J. K. O’Connor, and E. D. Jarvis. “The origin and diversification of birds.” *Current Biology* 25, no. 19 (2015): 888-898.

Burgers, P., and L. M. Chiappe. “The wing of Archaeopteryx as a primary thrust generator.” *Nature* 399, no. 6731 (1999): 60-62.

Callaway, J. M., and E. L. Nicholls. *Ancient Marine Reptiles*. Academic Press, 1997.

Caple, G., R. P. Balda, and W. R. Willis. “The physics of leaping animals and the evolution of preflight.” *The American Naturalist* 121, no. 4 (1983): 455-476.

Carlson, W. D., T. B. Rowe, R. A. Ketcham, and M. W. Colbert. “Applications of high-resolution X-ray computed tomography in petrology, meteoritics and palaeontology.” *Geological Society, London, Special Publications* 215, no. 1 (2003): 7-22.

Carlson, K. J., D. Stout, T. Jashashvili, D. J. De Ruiter, P. Tafforeau, K. Carlson, and L. R. Berger. “The endocast of MH1, Australopithecus sediba.” *Science* 333, no. 6048 (2011): 1402-1407.

Carney, R. M., J. Vinther, M. D. Shawkey, L. D'alba, and J. Ackermann. “New evidence on the colour and nature of the isolated Archaeopteryx feather.” *Nature Communications* 3 (2012): 637.

Carney, R. M. “Evolution of the archosaurian shoulder joint and the flight stroke of Archaeopteryx.” *SVP 2016 Abstract Book* (2016): 110.

Carpenter, K. *The Carnivorous Dinosaurs.* Indiana University Press, 2005.

Casinos, A., and J. Cubo. “Avian long bones, flight and bipedalism.” *Comparative Biochemistry and Physiology Part A: Molecular & Integrative Physiology* 131, no. 1 (2001): 159-167.

Cau, A., T. Brougham, and D. Naish. “The phylogenetic affinities of the bizarre Late Cretaceous Romanian theropod Balaur bondoc (Dinosauria, Maniraptora): dromaeosaurid or flightless bird?” *PeerJ* 3 (2015): e1032.

Cau, A., V. Beyrand, Dennis F. A. E. Voeten, V. Fernandez, P. Tafforeau, K. Stein, R. Barsbold, K. Tsogtbaatar, P. J. Currie, and P. Godefroit. “Synchrotron scanning reveals amphibious ecomorphology in a new clade of bird-like dinosaurs.” *Nature* 552, no. 7685 (2017): 395-400.

Chatterjee, S., and R. J. Templin. “The flight of Archaeopteryx.” *Naturwissenschaften* 90, no. 1 (2003): 27-32.

Chatterjee, S. *The Rise of Birds: 225 Million Years of Evolution*. JHU Press, 2015.

Chen, Z.-Q., and M. J. Benton. “The timing and pattern of biotic recovery following the end-Permian mass extinction.” *Nature Geoscience* 5, no. 6 (2012): 375-383.

Chenevier, D, and A. Joly. “ESRF: Inside the Extremely Brilliant Source Upgrade.” *Synchrotron Radiation News* 31, no. 1 (2018): 32-35.

Chiappe, L. M. *Glorified Dinosaurs*. John Wiley, 2007.

Chiappe, L. M., and M. Qingjin. *Birds of Stone: Chinese Avian Fossils from the Age of Dinosaurs*. JHU Press, 2016.

Chinsamy-Turan, A. *The Microstructure of Dinosaur Bone: Deciphering Biology with Fine-Scale Techniques*. John Wiley & Sons, 2005.

Christiansen, P., and N. Bonde. “Axial and appendicular pneumaticity in Archaeopteryx.” *Proceedings of the Royal Society of London B: Biological Sciences* 267 (2000): 2501-2505.

Clarke, J. “Feathers before flight.” *Science* 340, no. 6133 (2013): 690-692.

Cloetens, P., R. Barrett, J. Baruchel, J.-P. Guigay, and M. Schlenker. “Phase objects in synchrotron radiation hard x-ray imaging.” *Journal of Physics D: Applied Physics* 29, no. 1 (1996): 133.

Close, R. A., and E. J. Rayfield. “Functional morphometric analysis of the furcula in Mesozoic birds.” *PLoS One* 7, no. 5 (2012): e36664.

Corbacho, J., and C. Sendino. “Fossil fakes and their recognition.” *Deposits Magazine* 30 (2012): 35-40.

Cubo, J., and A. Casinos. “The variation of the cross-sectional shape in the long bones of birds and mammals.” *Annales des Sciences Naturelles-Zoologie et Biologie Animale* 19, no. 1 (1998): 51-62).

Cubo, J., and A. Casinos. “Incidence and mechanical significance of pneumatization in the long bones of birds.” *Zoological Journal of the Linnean Society* 130, no. 4 (2000): 499-510.

Cubo, J., P. Legendre, A. De Ricqlès, L. Montes, E. De Margerie, J. Castanet, and Y. Desdevises. “Phylogenetic, functional, and structural components of variation in bone growth rate of amniotes.” *Evolution & Development* 10 (2008): 217-227.

Cubo, J., N. Le Roy, C. Martinez-Maza, and L. Montes. “Paleohistological estimation of bone growth rate in extinct archosaurs.” *Paleobiology* 38, no. 2 (2012): 335-349.

Cunningham, J. A., I. A. Rahman, S. Lautenschlager, E. J. Rayfield, and P. C. J. Donoghue. “A virtual world of paleontology.” *Trends in Ecology & Evolution* 29, no. 6 (2014): 347-357.

Currey, J. D., and R. Alexander. “The thickness of the walls of tubular bones.” *Journal of Zoology* 206, no. 4 (1985): 453-468.

Currey, J. D. “The structure and mechanics of bone.” *Journal of Materials Science* 47, no. 1 (2012): 41-54.

Czerkas, S. A., D. Zhang, J. Li, and Y. Li. “Flying dromaeosaurs.” *Dinosaur Museum Journal* 1 (2002): 97-126.

Dalla Vecchia, F. M. “Triassic pterosaurs.” *Geological Society, London, Special Publications* 379, no. 1 (2013): 119-155.

Deans, S. R. *The Radon Transform and Some of Its Applications*. Courier Corporation, 2007.

Dececchi, T. A., and H. C. Larsson. “Assessing arboreal adaptations of bird antecedents: testing the ecological setting of the origin of the avian flight stroke.” *PLoS One* 6, no. 8 (2011): e22292.

Dececchi, T. A., H. C. Larsson, and M. B. Habib. “The wings before the bird: an evaluation of flapping-based locomotory hypotheses in bird antecedents.” *PeerJ* 4 (2016): e2159.

De Margerie, E., S. Sanchez, J. Cubo, and J. Castanet. “Torsional resistance as a principal component of the structural design of long bones: comparative multivariate evidence in birds.” *The Anatomical Record* 282, no. 1 (2005): 49-66.

De Margerie, E., P. Tafforeau, and L. Rakotomanana. “In silico evolution of functional morphology: a test on bone tissue biomechanics.” *Journal of The Royal Society Interface* 3, no. 10 (2006): 679-687.

Dial, K. P. “Evolution of avian locomotion: correlates of flight style, locomotor modules, nesting biology, body size, development, and the origin of flapping flight.” *The Auk* 120, no. 4 (2003): 941-952.

Donovan, S. K. *The Processes of Fossilization*. Columbia University Press, 1991.

Dyke, G., R. De Kat, C. Palmer, J. Van Der Kindere, D. Naish, and B. Ganapathisubramani. “Aerodynamic performance of the feathered dinosaur Microraptor and the evolution of feathered flight.” *Nature Communications* 4 (2013): 2489.

Easley, R. R. “Ground effect and the beginnings of avian flight.” *Journal of Vertebrate Paleontology* 19:34 (1999).

Ebel, K. “On the origin of flight in Archaeopteryx and in pterosaurs.” *Neues Jahrbuch für Geologie und Palaöntologie-Abhandlungen* 202, no. 3 (1996): 269-286.

Eisenberg, R. L. *Radiology: An Illustrated History*. Mosby Incorporated, 1992.

Elzanowski, A. “Biology of basal birds and the origin of avian flight.” *Proceedings of the 5th Symposium of the Society of Avian Paleontology and Evolution, Beijing* (2000): 1-4.

Elzanowski, A. “Archaeopterygidae (Upper Jurassic of Germany).” *Mesozoic Birds: Above the Heads of Dinosaurs*. (2002): 129-159.

Erickson, G. M., O. W. M. Rauhut, Z. Zhou, A. H. Turner, B. D. Inouye, D. Hu, and M. A. Norell. “Was dinosaurian physiology inherited by birds? Reconciling slow growth in Archaeopteryx.” *PLoS One* 4, no. 10 (2009): e7390.

Eriksson, M. E., F. Terfelt, R. Elofsson, and F. Marone. “Internal soft-tissue anatomy of Cambrian ‘Orsten’arthropods as revealed by synchrotron X-ray tomographic microscopy.” *PLoS One* 7, no. 8 (2012): e42582.

Erwin, D. H. B. “The Permo–Triassic extinction.” *Nature* 367, no. 6460 (1994): 231-236.

Erwin, D. H. B. “Increasing returns, ecological feedback and the Early Triassic recovery.” *Palaeoworld* 16, no. 1 (2007): 9-15.

Evangelista, D., G. Cardona, E. Guenther-Gleason, T. Huynh, A. Kwong, D. Marks, N. Ray, A. Tisbe, K. Tse, and M. Koehl. “Aerodynamic characteristics of a feathered dinosaur measured using physical models. Effects of form on static stability and control effectiveness.” *PLoS One* 9, no. 1 (2014a): e85203.

Evangelista, D., S. Cam, T. Huynh, A. Kwong, H. Mehrabani, K. Tse, and R. Dudley. “Shifts in stability and control effectiveness during evolution of Paraves support aerial maneuvering hypotheses for flight origins.” *PeerJ* 2 (2014b): e632.

Feduccia, A., and S. A. Czerkas. “Testing the neoflightless hypothesis: propatagium reveals flying ancestry of oviraptorosaurs.” *Journal of Ornithology* 156, no. 4 (2015): 1067-1074.

Feo, T. J., D. J. Field, and R. O. Prum. “Barb geometry of asymmetrical feathers reveals a transitional morphology in the evolution of avian flight.” *Proceedings of the Royal Society of London B: Biological Sciences* 282, no. 1803 (2015): 20142864.

Fernandez, V., E. Buffetaut, E. Maire, J. Adrien, V. Suteethorn, and P. Tafforeau. “Phase contrast synchrotron microtomography: improving noninvasive investigations of fossil embryos in ovo.” *Microscopy and Microanalysis* 18, no. 1 (2012): 179-185.

Fernandez, V., E. Buffetaut, V. Suteethorn, J.-C. Rage, P. Tafforeau, and M. Kundrát. “Evidence of egg diversity in squamate evolution from Cretaceous anguimorph embryos.” *PloS One* 10, no. 7 (2015): e0128610.

Forster, C. A., S. D. Sampson, L. M. Chiappe, and D. W. Krause. “The theropod ancestry of birds: new evidence from the Late Cretaceous of Madagascar.” *Science* 279, no. 5358 (1998): 1915-1919.

Foth, C., H. Tischlinger, and O. W. M. Rauhut. “New specimen of Archaeopteryx provides insights into the evolution of pennaceous feathers.” *Nature* 511, no. 7507 (2014): 79-82.

Foth, C., and O. W. M. Rauhut. “Re-evaluation of the Haarlem Archaeopteryx and the radiation of maniraptoran theropod dinosaurs.” *BMC Evolutionary Biology* 17, no. 1 (2017): 236.

Fowler, D. W., Freedman, E. A., Scannella, J. B., & Kambic, R. E. “The predatory ecology of Deinonychus and the origin of flapping in birds.” *PLoS One* 6, no. 12 (2011): e28964.

Francillon-Vieillot, H., V. De Buffrénil, J. D. Castanet, J. Géraudie, F. J. Meunier, J. Y. Sire, L. Zylberberg, and A. De Ricqlès. “Microstructure and mineralization of vertebrate skeletal tissues.” *Skeletal Biomineralization: Patterns, Processes and Evolutionary Trends* (1990): 175-234.

Frankel, R. I. “Centennial of Röntgen's discovery of x-rays.” *Western Journal of Medicine* 164, no. 6 (1996): 497.

Fraser, G. ““Bizarre structures” point to dromaeosaurs as parasites and a new theory for the origin of avian flight.” *The Journal of Paleontological Sciences* 1 (2014): 2-4.

Garner, J. P., G. K. Taylor, and A. L. R. Thomas. “On the origins of birds: the sequence of character acquisition in the evolution of avian flight.” *Proceedings of the Royal Society of London B: Biological Sciences* 266, no. 1425 (1999): 1259-1266.

Gatesy, S. M., and K. P. Dial. “From frond to fan: Archaeopteryx and the evolution of short-tailed birds.” *Evolution* 50, no. 5 (1996): 2037-2048.

Gatesy, S. M., and K. M. Middleton. “Bipedalism, flight, and the evolution of theropod locomotor diversity.” *Journal of Vertebrate Paleontology* 17, no. 2 (1997): 308-329.

Gatesy, S. M. “Locomotor evolution on the line to modern birds.” *Mesozoic Birds: Above the Heads of Dinosaurs* (2002): 432-447.

Gauthier, J. A., and K. Padian. “The origin of birds and the evolution of flight.” *Short Courses in Paleontology* 2 (1989): 121-133.

Gauthier, J. A., and K. De Queiroz. “Feathered dinosaurs, flying dinosaurs, crown dinosaurs, and the name “Aves”.” *New Perspectives on the Origin and Early Evolution of Birds: Proceedings of the International Symposium in Honor of John H. Ostrom*, Peabody Museum of Natural History (2001): pp. 7-41.

Gishlick, A. D. “The function of the manus and forelimb of Deinonychus antirrhopus and its importance for the origin of avian flight. *New Perspectives on the Origin and Early Evolution of Birds: Proceedings of the International Symposium in Honor of John H. Ostrom*, Peabody Museum of Natural History (2001): 301-318.

Godefroit, P., A. Cau, H. Dong-Yu, F. Escuillié, W. Wenhao, and G. Dyke. "A Jurassic avialan dinosaur from China resolves the early phylogenetic history of birds." *Nature* 498, no. 7454 (2013): 359-362.

Gould, S. J. *Ontogeny and Phylogeny*. Harvard University Press, 1977.

Gould, S. J., and E. S. Vrba. "Exaptation - A missing term in the science of form." *Paleobiology* 8, no. 1 (1982): 4-15.

Habib, M. B., and C. B. Ruff. "The effects of locomotion on the structural characteristics of avian limb bones." *Zoological Journal of the Linnean Society* 153, no. 3 (2008): 601-624.

Häggmark, I., W. Vågberg, H. M. Hertz, and A. Burvall. "Comparison of quantitative multi-material phase-retrieval algorithms in propagation-based phase-contrast X-ray tomography." *Optics Express* 25, no. 26 (2017): 33543-33558.

Heptonstall, W. B. "Quantitative assessment of the flight of Archaeopteryx." *Nature* 228, no. 5267 (1970): 185-186.

Herman, G. T. *Fundamentals of Computerized Tomography: Image Reconstruction from Projections*. Springer Science & Business Media, 2009.

Hesse, B., M. Langer, P. Varga, A. Pacureanu, P. Dong, S. Schrof, N. Männicke, H. Suhonen, C. Olivier, P. Mauer, G. J. Kazakia, K. Raum, and F. Peyrin. "Alterations of mass density and 3D osteocyte lacunar properties in bisphosphonate-related osteonecrotic human jaw bone, a synchrotron μCT study." *PloS One* 9, no. 2 (2014): e88481.

Horowitz, P., and J. A. Howell. "A scanning x-ray microscope using synchrotron radiation." *Science* 178, no. 4061 (1972): 608-611.

Houssaye, A., F. Xu, L. Helfen, V. De Buffrénil, T. Baumbach, and P. Tafforeau. "Three-dimensional pelvis and limb anatomy of the Cenomanian hind-limbed snake Eupodophis descouensi (Squamata, Ophidia) revealed by synchrotron-radiation computed laminography." *Journal of Vertebrate Paleontology* 31, no. 1 (2011): 2-7.

Hsieh, J. *Computed Tomography: Principles, Design, Artifacts, and Recent Advances.* Bellingham, SPIE, 2015.

Hu, D., J. A. Clarke, D. M. Eliason, R. Qiu, Q. Li, M. D. Shawkey, C. Zhao, L. D'Alba, J. Jiang, and X. Xu. "A bony-crested Jurassic dinosaur with evidence of iridescent plumage highlights complexity in early paravian evolution." *Nature Communications* 9 (2018): 217.

Hunter, J. P. "Key innovations and the ecology of macroevolution." *Trends in Ecology & Evolution* 13, no. 1 (1998): 31-36.

Jäger, K. “Über die Federbildung und den Erwerb der Flugfähigkeit bei Vögeln.” *Jahreshefte der Gesellschaft für Naturkunde in Württemberg* 133 (1978): 133-143.

Jakubek, J. “Data processing and image reconstruction methods for pixel detectors.” *Nuclear Instruments and Methods in Physics Research Section A: Accelerators, Spectrometers, Detectors and Associated Equipment* 576, no. 1 (2007): 223-234.

Ji, C., D. Y. Jiang, and W. L. Fu, W.L. “Highly diversified Chaohu Fauna (Olenekian, Early Triassic) and sequence of Triassic marine reptile faunas from South China.” *Palaeobiology and Geobiology of Fossil Lagerstatten Through Earth History, Abstract.* (1978): pp.80-81.

Jia, F., F. Peyrin, L. Malaval, L. Vico, and M.-H. Lafage-Proust. “Imaging and quantitative assessment of long bone vascularization in the adult rat using microcomputed tomography.” *The Anatomical Record* 293, no. 2 (2010): 215-224.

Jenkins, F. A. “The evolution of the avian shoulder joint.” *American Journal of Science* 293 (1993) 253-253.

Kak, A. C., and M. Slaney. *Principles of Computerized Tomographic Imaging*. Society for Industrial and Applied Mathematics, 2001.

Klein, N., and P. C. H. Albers. “A new species of the sauropsid reptile Nothosaurus from the Lower Muschelkalk of the western Germanic Basin, Winterswijk, The Netherlands.” *Acta Palaeontologica Polonica* 54, no. 4 (2009): 589-598.

Klein, N., D. F. A. E. Voeten, J. Lankamp, R. Bleeker, O. J. Sichelschmidt, M. Liebrand, D. C. Nieweg, and P. M. Sander. “Postcranial material of Nothosaurus marchicus from the Lower Muschelkalk (Anisian) of Winterswijk, The Netherlands, with remarks on swimming styles and taphonomy.” *Paläontologische Zeitschrift* 89, no. 4 (2015): 961-981.

Klein, N., D. F. A. E. Voeten, A. Haarhuis, and R. Bleeker. “The earliest record of the genus Lariosaurus from the early middle Anisian (Middle Triassic) of the Germanic Basin.” *Journal of Vertebrate Paleontology* 36, no. 4 (2016): e1163712.

Korte, C., H. W. Kozur, and J. Veizer. “δ 13 C and δ 18 O values of Triassic brachiopods and carbonate rocks as proxies for coeval seawater and palaeotemperature.” *Palaeogeography, Palaeoclimatology, Palaeoecology* 226, no. 3 (2005): 287-306.

Koschowitz, M.-C., C. Fischer, and P. M. Sander. “Beyond the rainbow.” *Science* 346, no. 6208 (2014): 416-418.

Kozur, H. *Biostratigraphie der Germanischen Mitteltrias*. Deutscher Verlag für Grundstoffindustrie, 1974.

Krahl, A., N. Klein, and P. M. Sander. “Evolutionary implications of the divergent long bone histologies of Nothosaurus and Pistosaurus (Sauropterygia, Triassic).” *BMC Evolutionary Biology* 13, no. 1 (2013): 123.

Ksepka, D. T. “Evolution: a rapid flight towards birds.” *Current Biology* 24, no. 21 (2014): 1052-1055.

Kunz, C. “Synchrotron radiation: third generation sources.” *Journal of Physics: Condensed Matter* 13, no. 34 (2001): 7499.

Lak, M., D, Néraudeau, A. Nel, P. Cloetens, V. Perrichot, and P. Tafforeau. “Phase contrast X-ray synchrotron imaging: opening access to fossil inclusions in opaque amber.” *Microscopy and Microanalysis* 14, no. 3 (2008): 251-259.

Lautenschlager, S. “Digital reconstruction of soft-tissue structures in fossils.” *The Paleontological Society Papers* 22 (2016): 101-117.

Lee, M. S. Y., and P. Doughty. “The relationship between evolutionary theory and phylogenetic analysis.” *Biological Reviews* 72, no. 4 (1997): 471-495.

Lee, M. S. Y., and T. H. Worthy. “Likelihood reinstates Archaeopteryx as a primitive bird.” *Biology Letters* 8, no. 2 (2012): 299-303.

Lee, M. S. Y. “Turtle origins: insights from phylogenetic retrofitting and molecular scaffolds.” *Journal of Evolutionary Biology* 26, no 12 (2013): 2729-2738.

Lefèvre, U., D. Hu, F. Escuillié, G. Dyke, and P. Godefroit. “A new long-tailed basal bird from the Lower Cretaceous of north-eastern China.” *Biological Journal of the Linnean Society* 113, no. 3 (2014): 790-804.

Lefèvre, U., A. Cau, A. Cincotta, D. Hu, A. Chinsamy-Turan, F. Escuillié, and P. Godefroit. “A new Jurassic theropod from China documents a transitional step in the macrostructure of feathers.” *The Science of Nature* 104, no. 9-10 (2017): 74.

Lehman, J. P. *L’Évolution des Vertébrés Inférieurs: Quelques Problèmes.* (Vol. 5). Dunod, 1959.

Li, Q., K.-Q. Gao, J. Vinther, M. D. Shawkey, J. A. Clarke, L. D’Alba, Q. Meng, D. E. G. Briggs, and R. O. Prum. “Plumage color patterns of an extinct dinosaur.” *Science* 327, no. 5971 (2010): 1369-1372.

Li, Q., J. A. Clarke, K.-Q. Gao, C.-F. Zhou, Q. Meng, D. Li, L. D’Alba, and M. D. Shawkey. “Melanosome evolution indicates a key physiological shift within feathered dinosaurs.” *Nature* 507, no. 7492 (2014): 350-353.

Lingham-Soliar, T. “Dinosaur protofeathers: Pushing back the origin of feathers into the Middle Triassic?” *Journal of Ornithology* 151, no. 1 (2010): 193.

Liu, Y.-Q., H.-W. Kuang, X.-J. Jiang, N. Peng, H. Xu, and H.-Y. Sun. "Timing of the earliest known feathered dinosaurs and transitional pterosaurs older than the Jehol Biota." *Palaeogeography, Palaeoclimatology, Palaeoecology* 323 (2012): 1-12.

Liu, J., S.-X. Hu, O. Rieppel, D.-Y. Jiang, M. J. Benton, N. P. Kelley, J. C. Aitchison, C.-Y Zhou, W. Wen, J-Y. Huang, T. Xie, and T. Lv. "A gigantic nothosaur (Reptilia: Sauropterygia) from the Middle Triassic of SW China and its implication for the Triassic biotic recovery." *Scientific Reports* 4 (2014): srep07142.

Long, C. A., G. P. Zhang, T. F. George, and C. F. Long. "Physical theory, origin of flight, and a synthesis proposed for birds." *Journal of Theoretical Biology* 224, no. 1 (2003): 9-26.

Longrich, N. R. "Structure and function of hindlimb feathers in Archaeopteryx lithographica." *Paleobiology* 32, no. 3 (2006): 417-431.

Longrich, N. R., J. Vinther, Q. Meng, Q. Li, and A. P. Russell. "Primitive wing feather arrangement in Archaeopteryx lithographica and Anchiornis huxleyi." *Current Biology* 22, no. 23 (2012): 2262-2267.

Lowe, C. B., J. A. Clarke, A. J. Baker, D. Haussler, and S. V. Edwards. "Feather development genes and associated regulatory innovation predate the origin of Dinosauria." *Molecular Biology and Evolution* 32, no. 1 (2014): 23-28.

Ma, W. J., M. S. Ma, I. Nieuwland, and R. R. Easley. "Why Archaeopteryx did not run over water." *Archaeopteryx* 20 (2002): 51-56.

Mabee, P. "Heterochrony: The Evolution of Ontogeny." *Science* 254, no. 5033(1991): 874-876.

Maldanis, L., M. Carvalho, M. R. Almeida, F. I. Freitas, J. A. F. G. de Andrade, R. S. Nunes, C. E. Rochitte, R. J. Poppie, R. O. Freitas, F. Rodrigues, S. Siljeström, F. A. Lima, D. Galante, I. S. Carvalho, C. A. Perez, M. R. de Carvalho, J. Bettini, V. Fernandez, J. Xavier-Neto. "Heart fossilization is possible and informs the evolution of cardiac outflow tract in vertebrates." *Elife* 5 (2016): e14698.

Manning, P. L., N. P. Edwards, R. A. Wogelius, U. Bergmann, H. E. Barden, P. L. Larson, D. Schwarz-Wings, V. M. Egerton, D. Sokaras, R. A. Mori, and W. I. Sellers. "Synchrotron-based chemical imaging reveals plumage patterns in a 150 million year old early bird." *Journal of Analytical Atomic Spectrometry* 28, no. 7 (2013): 1024-1030.

Marden, J. H. "From damselflies to pterosaurs: how burst and sustainable flight performance scale with size." *American Journal of Physiology-Regulatory, Integrative and Comparative Physiology* 266, no. 4 (1994): 1077-1084.

Mateus, O., M. Overbeeke, and F. Rita. “Dinosaur frauds, hoaxes and “Frankensteins”: how to distinguish fake and genuine vertebrate fossils.” *Journal of Paleontological Techniques* 2 (2008): 1-5.

Mayr, G. *Avian Evolution: The Fossil Record of Birds and its Paleobiological Significance*. John Wiley & Sons, 2016.

Mayr, G. “Pectoral girdle morphology of Mesozoic birds and the evolution of the avian supracoracoideus muscle.” *Journal of Ornithology* 158, no. 3 (2017): 859-867.

McCann, Tom. *The Geology of Central Europe*. Geological Society of London, 2008.

Meers, M. B. “Cross-sectional geometric properties of the crocodylian humerus: an exception to Wolff's Law?” *Journal of Zoology* 258, no. 3 (2002): 405-418.

Meseguer, J., L. M. Chiappe, J. L. Sanz, F. Ortega, A. Sanz-Andres, I. P. Grande, and S. Franchini. “Lift devices in the flight of Archaeopteryx.” *Revista Española de Paleontología* 27, no. 2 (2012): 125-130.

Milner, A. C., P. L. Forey, T. Greenwood, and C. T. Williams. “Caveat emptor–fake fossils from the Far East.” *Geology Today* 17, no. 2 (2001): 52-58.

Monte-Luna, D., B. W. Brook, M. J. Zetina-Rejón, and V. H. Cruz-Escalona. “The carrying capacity of ecosystems.” *Global Ecology and Biogeography* 13, no. 6 (2004): 485-495.

Montes, L., N. Le Roy, M. Perret, V. De Buffrénil, J. Castanet, and J. Cubo. “Relationships between bone growth rate, body mass and resting metabolic rate in growing amniotes: a phylogenetic approach.” *Biological Journal of the Linnean Society* 92, no. 1 (2007): 63-76.

Neenan, J. M., N. Klein, and T. M. Scheyer. “European origin of placodont marine reptiles and the evolution of crushing dentition in Placodontia.” *Nature Communications* 4 (2013): 1621.

Neenan, J. M., T. Reich, S. W. Evers, P. S. Druckenmiller, D. F. A. E. Voeten, J. N. Choiniere, P. M. Barrett, S. E. Pierce, and R. B. J. Benson. “Evolution of the sauropterygian labyrinth with increasingly pelagic lifestyles.” *Current Biology* 27, no. 24 (2017): 3852-3858.

Norberg, U. M. *Vertebrate Flight: Mechanics, Physiology, Morphology, Ecology and Evolution.* Springer, 1990.

Nudds, R. L., and G. J. Dyke. “Narrow primary feather rachises in Confuciusornis and Archaeopteryx suggest poor flight ability.” *Science* 328, no. 5980 (2010): 887-889.

Nudds, R. L. “Reassessment of the wing feathers of Archaeopteryx lithographica suggests no robust evidence for the presence of elongated dorsal wing coverts.” *PloS One* 9, no. 4 (2014): e93963.

O'Farrel, B., J. Davenport, and T. Kelly. "Was Archaeopteryx a wing-in-ground effect flier?" *Ibis* 144 (2002): 686-688.

Olshevsky, G. "The birds first? A theory to fit the facts." *Omni* 16, no. 9 (1994): 34-45.

Olson, S. L., and A. Feduccia. "Flight capability and the pectoral girdle of Archaeopteryx." *Nature* 278, no. 5701 (1979): 247-248.

Oosterink, H., W. Berkelder, C. de Jong, J. Lankamp, and H. Winkelhorst. "Sauriers uit de Onder-Muschelkalk van Winterswijk." *Staringia* 11 (2002).

Ostrom, J. H. "A new theropod dinosaur from the Lower Cretaceous of Montana." *Postilla* 128 (1969a.): 1-17.

Ostrom, J. H. *Osteology of Deinonychus antirrhopus, an Unusual Theropod from the Lower Cretaceous of Montana*. Peabody Museum of Natural History, 1969b.

Ostrom, J. H. "Archaeopteryx: Notice of a" new" specimen." *Science* 170, no. 3957 (1970): 537-538.

Ostrom, J. H. "Archaeopteryx and the origin of flight." *The Quarterly Review of Biology* 49, no. 1 (1974): 27-47.

Ostrom, J. H. "Some hypothetical anatomical stages in the evolution of avian flight." *Smithsonian Contributions to Paleobiology* 27 (1976): 1-21.

Ostrom, J. H. "Bird Flight: How Did It Begin? Did birds begin to fly" from the trees down" or" from the ground up"? Reexamination of Archaeopteryx adds plausibility to an" up from the ground" origin of avian flight." *American Scientist* 67, no. 1 (1979): 46-56.

Padian, K. "Pterosaurs: were they functional birds or functional bats?" *Biomechanics in Evolution* 146 (1991): 160.

Padian, K., and L. M. Chiappe. "Bird origins." *Encyclopedia of Dinosaurs* (1997): 71-79.

Padian, K., and L. M. Chiappe. "The origin of birds and their flight." *Scientific American* 278, no. 2 (1998): 38-47.

Padian, K., and K. P. Dial. "Origin of flight: Could 'four-winged' dinosaurs fly?" *Nature* 438, no. 7066 (2005): 3.

Paganin, D., S. C. Mayo, T. E. Gureyev, P. R. Miller, and S. W. Wilkins. "Simultaneous phase and amplitude extraction from a single defocused image of a homogeneous object." *Journal of Microscopy* 206, no. 1 (2002): 33-40.

Palermo, D., T. Aigner, B. Seyfang, and S. Nardon. “Reservoir properties and petrophysical modelling of carbonate sand bodies: outcrop analogue study in an epicontinental basin (Triassic, Germany).” *Geological Society, London, Special Publications* 370 (2012): 111-138.

Paul, G. S. *Predatory Dinosaurs of the World: a Complete Illustrated Guide*. Simon & Schuster, 1988.

Paul, G. S. *Dinosaurs of the Air: The Evolution and Loss of Flight in Dinosaurs and Birds*. JHU Press, 2002.

Pennycuick, C. J. *Modelling the Flying Bird* (Vol. 5). Elsevier, 2008.

Perreau, M., and P. Tafforeau, “Three new species of Leiodidae (Coleptera) from Baltic amber: pushing further the paleoentomological descriptions by virtual dissection of fossils using phase-contrast X-ray synchrotron microtomography.” *Systematic Entomology* 36 (2011): 573-580.

Persons, W. S., and P. J. Currie. “Bristles before down: a new perspective on the functional origin of feathers.” *Evolution* 69, no. 4 (2015): 857-862.

Peters, D. S., and W. F. Gutmann. “Constructional and functional preconditions for the transition to powered flight in vertebrates”. *The Beginnings of Birds* (1985): 233-242.

Peters, T. “CT image reconstruction.” *SLIDES REVL* (2002): 05697-05745.

Peterson, A. “The locomotor adaptations of Archaeopteryx: glider or cursor.” *The Beginnings of Birds.* (1985): 99-103.

Peteya, J. A., J. A. Clarke, Q. Li, K.-Q. Gao, and M. D. Shawkey. “The plumage and colouration of an enantiornithine bird from the Early Cretaceous of China.” *Palaeontology* 60, no. 1 (2017): 55-71.

Poore, S. O., A. Sanchez-Haiman, and G. E. Goslow Jr. “Wing upstroke and the evolution of flapping flight.” *Nature* 387, no. 6635 (1997): 799.

Pouech, J. *Position des Mammifères dans les Écosystèmes Mésozoïques d'Europe Occidentale: Le site de Cherves-de-Cognac (Berriasien, Charente, France)*. Unpublished Ph.D. thesis, Université Lyon.

Pradel, A., M. Langer, J. G. Maisey, D. Geffard-Kuriyama, P. Cloetens, P. Janvier, and P. Tafforeau. “Skull and brain of a 300-million-year-old chimaeroid fish revealed by synchrotron holotomography.” *Proceedings of the National Academy of Sciences* 106, no. 13 (2009): 5224-5228.

Pratt, I. V., and D. M. L. Cooper. “A method for measuring the three-dimensional orientation of cortical canals with implications for comparative analysis of bone microstructure in vertebrates.” *Micron* 92 (2017): 32-38.

Prum, R. O., J. S. Berv, A. Dornburg, D. J. Field, J. P. Townsend, E. M. Lemmon, and A. R. Lemmon. “A comprehensive phylogeny of birds (Aves) using targeted next-generation DNA sequencing.” *Nature* 526, no. 7574 (2015): 569-573.

Qiang, J., P. J. Currie, M. A. Norell, and J. Shu-An. “Two feathered dinosaurs from northeastern China.” *Nature* 393, no. 6687 (1998): 753-761.

Qing-Hua, S. “A new species of Nothosaurus from the early Middle Triassic of Guizhou, China.” *Vertebrata PalAsiatica* 44, no. 3 (2006): 237-249.

Qvarnström, M., G. Niedźwiedzki, P. Tafforeau, Ž. Žigaitė, and P. E. Ahlberg. “Synchrotron phase-contrast microtomography of coprolites generates novel palaeobiological data.” *Scientific Reports* 7 (2017): srep02723.

Radon, J. “Über die Bestimmung von Funktionen durch ihre Integralwerte längs gewisser Mannigfaltigkeiten.” *Berichte der Königlichen Sächsischen Gesellschaft der Wissenschaft. Math. Phys., Klass* 69 (1917): 262.

Rahman, I. A., K. Adcock, and R. J. Garwood. “Virtual fossils: a new resource for science communication in paleontology.” *Evolution: Education and Outreach* 5, no. 4 (2012): 635-641.

Rauhut, O. W. M., C. Foth, and H. Tischlinger. “The oldest Archaeopteryx (Theropoda: Avialiae): a new specimen form the Kimmeridgian/Tithonian boundary of Schamhaupten, Bavaria. *PeerJ* 6 (2018): e4191

Raven, C., A. Snigirev, I. Snigireva, P. Spanne, A. Souvorov, and V. Kohn. “Phase-contrast microtomography with coherent high-energy synchrotron x rays.” *Applied Physics Letters* 69, no. 13 (1996): 1826-1828.

Rayner, J. M. “Estimating power curves of flying vertebrates.” *Journal of Experimental Biology* 202, no. 23 (1999): 3449-3461.

Remsen Jr, J. V., and S. K. Robinson. “A classification scheme for foraging behavior of birds in terrestrial habitats.” *Studies in Avian Biology* 13 (1990): 144-160.

Rieppel, O., & Wild, R. “A revision of the genus Nothosaurus (Reptilia: Sauropterygia) from the Germanic Triassic”. *Fieldiana New Series* 34 (1996).

Rieppel, O. “Phylogeny and paleobiogeography of Triassic Sauropterygia: problems solved and unresolved.” *Palaeogeography, Palaeoclimatology, Palaeoecology* 153, no. 1 (1999): 1-15.

Rieppel, O. *Sauropterygia: Handbuch Der Paläoherpetologie: Placodontia, Pachypleurosauria, Nothosauroidea, Pistosauroidea*. Pfeil Verlag, 2000.

Rieppel. O. “Feeding mechanics in Triassic stem-group sauropterygians: the anatomy of a successful invasion of Mesozoic seas.” *Zoological Journal of the Linnean Society* 135, no. 1 (2002): 33-63.

Röntgen, W. K. “A new form of radiation.” *Science* 3, no. 72 (1896): 726-729.

Rowe, T. B., R. A. Ketcham, C. Denison, M. Colbert, X. Xu, and P. J. Currie. “Forensic palaeontology: the Archaeoraptor forgery.” *Nature* 410, no. 6828 (2001): 539-540.

Rowe, T. B., Zhe-Xi Luo, Richard A. Ketcham, Jessica A. Maisano, and Matthew W. Colbert. “X-ray computed tomography datasets for forensic analysis of vertebrate fossils.” *Scientific Data* 3 (2016): 160040.

Ruben, J. “Reptilian physiology and the flight capacity of Archaeopteryx.” *Evolution* 45, no. 1 (1991): 1-17.

Ruben, J. A., and T. D. Jones. “Selective factors associated with the origin of fur and feathers.” *American Zoologist* 40, no. 4 (2000): 585-596.

Ruxton, G. D., W. S. Persons IV, and P. J. Currie. “A continued role for signaling functions in the early evolution of feathers.” *Evolution* 71, no. 3 (2017): 797-799.

Sander, P. M., N. Klein, P. C. H. Albers, C. Bickelmann, and H. Winkelhorst. “Postcranial morphology of a basal Pistosauroidea (Sauropterygia) from the Lower Muschelkalk of Winterswijk, The Netherlands.” *Paläontologische Zeitschrift* 88, no. 1 (2014): 55-71.

Sanchez, S., P. E. Ahlberg, K. M. Trinajstic, A. Mirone, and P. Tafforeau. “Three-dimensional synchrotron virtual paleohistology: a new insight into the world of fossil bone microstructures.” *Microscopy and Microanalysis* 18, no. 5 (2012): 1095-1105.

Sanchez, S., V. Fernandez, S. E. Pierce, and P. Tafforeau. “Homogenization of sample absorption for the imaging of large and dense fossils with synchrotron microtomography.” *Nature Protocols* 8, no. 9 (2013a): 1708-1717.

Sanchez, S., V. Dupret, P. Tafforeau, K. M. Trinajstic, B. Ryll, P.-J. Gouttenoire, L. Wretman, L. Zylberberg, F. Peyrin, and P. E. Ahlberg. “3D microstructural architecture of muscle attachments in extant and fossil vertebrates revealed by synchrotron microtomography.” *PloS One* 8, no. 2 (2013b): e56992.

Sanchez, S., P. Tafforeau, and P. E. Ahlberg. “The humerus of Eusthenopteron: a puzzling organization presaging the establishment of tetrapod limb bone marrow.” *Proceedings of the Royal Society of London B: Biological Sciences* 281, no. 1782 (2014): 20140299.

Sanchez, S., P. Tafforeau, J. A. Clack, and P. E. Ahlberg. “Life history of the stem tetrapod Acanthostega revealed by synchrotron microtomography.” *Nature* 537 (2016): 408-411.

Sanz, J. L., and F. Ortega. “The birds from Las Hoyas.” *Science Progress* 85, no. 2 (2002): 113-130.

Scheyer, T. M., C. Romano, J. Jenks, and H. Bucher. “Early Triassic marine biotic recovery: the predators' perspective.” *PLoS One* 9, no. 3 (2014): e88987.

Schwenk, K. “Comparative anatomy and physiology of chemical senses in nonavian aquatic reptiles.” *Sensory Evolution on the Threshold.* University of California Press, Berkley (2008): 65-81.

Senter, P. “Comparison of forelimb function between Deinonychus and Bambiraptor (Theropoda: Dromaeosauridae).” *Journal of Vertebrate Paleontology* 26, no. 4 (2006): 897-906.

Senter, P. “Scapular orientation in theropods and basal birds, and the origin of flapping flight.” *Acta Palaeontologica Polonica* 51, no. 2 (2006).

Senter, P. “A new look at the phylogeny of Coelurosauria (Dinosauria: Theropoda).” *Journal of Systematic Palaeontology* 5, no. 4 (2007): 429-463.

Senter, P., J. I. Kirkland, D. D. DeBlieux, S. Madsen, S., and N. Toth. “New dromaeosaurids (Dinosauria: Theropoda) from the Lower Cretaceous of Utah, and the evolution of the dromaeosaurid tail.” *PLoS One* 7, no. 5 (2012): e36790.

Shang, Q.-H. “New information on the dentition and tooth replacement of Nothosaurus (Reptilia: Sauropterygia).” *Palaeoworld* 16, no. 1 (2007): 254-263.

Shipman, P. *Taking Wing: Archaeopteryx and the Evolution of Bird Flight*. Simon and Schuster, 1999.

Simons, E. L., T. L. Hieronymus, and P. M. O'Connor. “Cross sectional geometry of the forelimb skeleton and flight mode in pelecaniform birds.” *Journal of Morphology* 272, no. 8 (2011): 958-971.

Speakman, J. R. “Flight capabilities in Archaeopteryx.” *Evolution* 47, no. 1 (1993): 336-340.

Stein, K., and E. Prondvai. “Rethinking the nature of fibrolamellar bone: an integrative biological revision of sauropod plexiform bone formation.” *Biological Reviews* 89, no. 1 (2014): 24-47.

Stollhofen, H., G. H. Bachmann, J. Barnasch, U. Bayer, G. Beutler, M. Franz, M. Kästner, B. Legler, J. Mutterlose, and D. Radies. "Upper Rotliegend to Early Cretaceous basin development." *Dynamics of Complex Intracontinental Basins. The Central European Basin System* (2008): 181-210.

Stone, R. "Altering the past: China's faked fossils problem." *Science* 330, no. 6012 (2010): 1740-1741.

Storrs, G. W. "Function and phylogeny in sauropterygian (Diapsida) evolution." *American Journal of Science* 293, no. A (1993): 63.

Stürmer, W. "Das Röntgen-Schichtaufnahme-Verfahren als Hilfsmittel der Stereologie." *First International Congress on Stereology, Abstracts* 33 (1963): 1-5.

Sullivan, C., D. W. E. Hone, X. Xu, and F. Zhang. "The asymmetry of the carpal joint and the evolution of wing folding in maniraptoran theropod dinosaurs." *Proceedings of the Royal Society of London B: Biological Sciences* (2010): rspb20092281.

Sumida, S. S., and C. A. Brochu. "Phylogenetic context for the origin of feathers." *American Zoologist* 40, no. 4 (2000): 486-503.

Switek, B. "Thomas Henry Huxley and the reptile to bird transition." *Geological Society, London, Special Publications* 343, no. 1 (2010): 251-263.

Szulc, J. "Anisian-Carnian evolution of the Germanic basin and its eustatic, tectonic and climatic controls." *Epicontinental Triassic* 1, no. 7–8 (1999): 813-852.

Tafforeau, P., R. Boistel, E. Boller, A. Bravin, M. Brunet, Y. Chaimanee, P. Cloetens, M. Feist, J. Hoszowska, J.-J. Jaeger, R. F. Kay, V. Lazzari, L. Marivaux, A. Nel, C. Nemoz, X. Thibault, P. Vignaud, S. Zabler. "Applications of X-ray synchrotron microtomography for non-destructive 3D studies of paleontological specimens." *Applied Physics A* 83, no. 2 (2006): 195-202.

Tafforeau, P., and T. M. Smith. "Nondestructive imaging of hominoid dental microstructure using phase contrast X-ray synchrotron microtomography." *Journal of Human Evolution* 54, no. 2 (2008): 272-278.

Thulborn, R. A. "The avian relationships of Archaeopteryx, and the origin of birds." *Zoological Journal of the Linnean Society* 82, no. 1-2 (1984): 119-158.

Thulborn, R. A., and T. L. Hamley. "A new palaeoecological role for Archaeopteryx." *The Beginnings of Birds* (1985): 81-89.

Thulborn, R. A. "Wind-assisted flight of Archaeopteryx." *Neues Jahrbuch für Geologie und Paläontologie-Abhandlungen* (2003): 61-74.

Tong, J., S. Zhang, J. Zuo, and X. Xiong. “Events during Early Triassic recovery from the end-Permian extinction.” *Global and Planetary Change* 55, no. 1 (2007): 66-80.

Trinajstic, K., S. Sanchez, V. Dupret, P. Tafforeau, J. Long, G. Young, T. Senden, C. Boisvert, N. Power, and P. E. Ahlberg. “Fossil musculature of the most primitive jawed vertebrates.” *Science* 341, no. 6142 (2013): 160-164.

Urf, A. J. *Birds: Beyond Watching*. Universities Press, 2004.

Van den Hout, P. J., K. J. Mathot, L. R. Maas, T. Piersma. “Predator escape tactics in birds: linking ecology and aerodynamics.” *Behavioral Ecology* 21, no. 1 (2009): 16-25.

Van der Reest, A. J., A. P. Wolfe, and P. J. Currie. “A densely feathered ornithomimid (Dinosauria: Theropoda) from the Upper Cretaceous Dinosaur Park Formation, Alberta, Canada.” *Cretaceous Research* 58 (2016): 108-117.

Vazquez, R. J. “Functional osteology of the avian wrist and the evolution of flapping flight.” *Journal of Morphology* 211, no. 3 (1992): 259-268.

Vidal, F. P., J. M. Létang, G. Peix, and P. Cloetens. “Investigation of artifact sources in synchrotron microtomography via virtual X-ray imaging.” *Nuclear Instruments and Methods in Physics Research Section B: Beam Interactions with Materials and Atoms* 234, no. 3 (2005): 333-348.

Videler, J. J. “Archaeopteryx: a dinosaur running over water.” *Archaeopteryx* 18 (2000): 27-34.

Videler, J. J. *Avian Flight*. Oxford University Press, 2006.

Viscor, G., & J. F. Fuster. “Relationships between morphological parameters in birds with different flying habits.” *Comparative Biochemistry and Physiology Part A: Physiology* 87, no. 2 (1987): 231-249.

Voeten, D. F. A. E., P. M. Sander, and N. Klein. “Skeletal material from larger Eusauropterygia (Reptilia: Eosauropterygia) with nothosaurian and cymatosaurian affinities from the Lower Muschelkalk of Winterswijk, The Netherlands.” *Paläontologische Zeitschrift* 89, no. 4 (2015): 943-960.

Von Alberti, F. *Beitrag zu einer Monographie des bunten Sandsteins, Muschelkalks und Keupers: und die Verbindung dieser Gebilde zu einer Formation*. JG Cotta'schen Buchhandlung, 1834.

Wang, X., A. J. McGowan, and G. J. Dyke. “Avian wing proportions and flight styles: first step towards predicting the flight modes of Mesozoic birds.” *PLoS One* 6, no. 12 (2011): e28672.

Wang, X., and J. A. Clarke. “The evolution of avian wing shape and previously unrecognized trends in covert feathering.” In *Proc. R. Soc. B*, vol. 282, no. 1816, p. 20151935. The Royal Society, 2015.

Weitkamp, T., P. Tafforeau, E. Boller, P. Cloetens, J-P. Valade, P. Bernard, F. Peyrin, W. Ludwig, L. Helfen, and J. Baruchel. “Parallel-beam imaging at the ESRF beamline ID19: current status and plans for the future.” *AIP Conference Proceedings*, vol. 1221, no. 1 (2010): 83-86.

Weitkamp, T., P. Tafforeau, E. Boller, P. Cloetens, J.-P. Valade, P. Bernard, F. Peyrin, W. Ludwig, L. Helfen, and J. Baruchel. “Status and evolution of the ESRF beamline ID19.” *AIP Conference Proceedings*, vol. 1221, no. 1 (2010): 33-38.

Wellnhofer, Peter. *Archaeopteryx: The Icon of Evolution*. Pfeil Verlag, 2009.

Wintrich, T., S. Hayashi, A. Houssaye, Y. Nakajima, and P. M. Sander. “A Triassic plesiosaurian skeleton and bone histology inform on evolution of a unique body plan.” *Science Advances* 3, no. 12 (2017): e1701144.

Witmer, L. M. “The extant phylogenetic bracket and the importance of reconstructing soft tissues in fossils.” *Functional Morphology in Vertebrate Paleontology* 1 (1995): 19-33.

Witmer, L. M., and L. M. Chiappe. *Mesozoic Birds: Above the Heads of Dinosaurs*. University of California Press, 2002.

Witmer, L. M., R. C. Ridgely, D. L. Dufeau, and M. C. Semones. “Using CT to peer into the past: 3D visualization of the brain and ear regions of birds, crocodiles, and nonavian dinosaurs.” *Anatomical Imaging* (2008): 67-87.

Woodward, H. N. *Comparative Population Histovariability within the Archosauria*. Montana State University, 2012.

Woodward, H. N., J. R. Horner, and J. O. Farlow. “Quantification of intraskeletal histovariability in Alligator mississippiensis and implications for vertebrate osteohistology.” *PeerJ* 2 (2014): e422.

Wu, P., J. Yan, Y.-C. Lai, C. S. Ng, A. Li, X. Jiang, R. Elsey, R. Widelitz, R. Baipai, W. H. Li, C. M. Chuong. “Multiple regulatory modules are required for scale-to-feather conversion.” *Molecular Biology and Evolution* (2017): 1-14.

Xu, X., Z. Zhou, X. Wang, X. Kuang, F. Zhang, and X. Du. “Four-winged dinosaurs from China.” *Nature* 421, no. 6921 (2003): 335-340.

Xu, X., X. Zheng, and H. You. “A new feather type in a nonavian theropod and the early evolution of feathers.” *Proceedings of the National Academy of Sciences* 106, no. 3 (2009): 832-834.

Xu, X., and Y. Guo. “The origin and early evolution of feathers: insights from recent paleontological and neontological data.” *Vertebrata PalAsiatica* 47, no. 4 (2009): 311-329.

Xu, X., X. Zheng, C. Sullivan, X. Wang, L. Xing, Y. Wang, X. Zhang, J. K. O’Connor, F. Zhang, and Y. Pan. “A bizarre Jurassic maniraptoran theropod with preserved evidence of membranous wings.” *Nature* 521, no. 7550 (2015): 70-73.

Yalden, D. W. “The flying ability of Archaeopteryx.” *Ibis* 113, no. 3 (1971): 349-356.

Zhang, F., Z. Zhou, X. Xu, and X. Wang. “A juvenile coelurosaurian theropod from China indicates arboreal habits.” *Naturwissenschaften* 89, no. 9 (2002): 394-398.

Zhang, Q., W. Wen, S. Hu, M. J. Benton, C. Zhou, T. Xie, T. Lü, J. Huang, B. Choo, Z.-Q. Chen, J. Liu, and Q. Zhang. “Nothosaur foraging tracks from the Middle Triassic of southwestern China.” *Nature Communications* 5 (2014): 3973.

Zhang, H., M. Wang, and X. Liu. “Constraints on the upper boundary age of the Tiaojishan Formation volcanic rocks in West Liaoning-North Hebei by LA-ICP-MS dating.” *Chinese Science Bulletin* 53, no. 22 (2008): 3574-3584.

Zheng, X., H.-L. You, X. Xu, and Z.-M. Dong. “An Early Cretaceous heterodontosaurid dinosaur with filamentous integumentary structures.” *Nature* 458, no. 7236 (2009): 333-336.

Zheng, X., J. O’Connor, X. Wang, M. Wang, X. Zhang, and Z. Zhou. “On the absence of sternal elements in Anchiornis (Paraves) and Sapeornis (Aves) and the complex early evolution of the avian sternum.” *Proceedings of the National Academy of Sciences* 111, no. 38 (2014): 13900-13905.

Zhou, Z-H., and J. O. Farlow. “Flight capability and habits of Confuciusornis.” *New Perspectives on the Origin and Early Evolution of Birds: Proceedings of the International Symposium in Honor of John H. Ostrom*, Peabody Museum of Natural History (2001): 237-254.

Ziegler, P. A. “Triassic rifts and facies patterns in Western and Central Europe.” *Geologische Rundschau* 71, no. 3 (1982): 747-772.

Publication record

Voeten, D. F. A. E., J. Cubo, E. de Margerie, M. Röper, V. Beyrand, S. Bureš, P. Tafforeau, and S. Sanchez. "Wing bone geometry reveals active flight in Archaeopteryx." *Nature Communications* (in press).

Voeten, D. F. A. E., T. Reich, R. Araújo, and T. M. Scheyer. "Synchrotron microtomography of a Nothosaurus marchicus skull informs on nothosaurian physiology and neurosensory adaptations in early Sauropterygia." *PloS One* 13, no. 1 (2018): e0188509.

Neenan, J. M., T. Reich, S. W. Evers, P. S. Druckenmiller, **D. F. A. E. Voeten**, J. N. Choiniere, P. M. Barrett, S. E. Pierce, and R. B. Benson. "Evolution of the sauropterygian labyrinth with increasingly pelagic lifestyles." *Current Biology* 27, no. 24 (2017): 3852-3858.

Cau, A., V. Beyrand, **D. F. A. E Voeten**, V. Fernandez, P. Tafforeau, K. Stein, R. Barsbold, K. Tsogtbaatar, P. J. Currie, and P. Godefroit. "Synchrotron scanning reveals amphibious ecomorphology in a new clade of bird-like dinosaurs." *Nature* 552, no. 7685 (2017): 395-400.

Sardar Abadi, M., E. I. Kulagina, and **D. F. A. E. Voeten**. "Foraminiferal proliferations in the Alborz Basin (northern Iran): global responses to Early Carboniferous glaciations." *Palaeobiodiversity and Palaeoenvironments* 97, no. 3 (2017): 669-686.

Sardar Abadi, M., E. I. Kulagina, **D. F. A. E. Voeten**, F. Boulvain, and A. C. Da Silva. "Sedimentologic and paleoclimatic reconstructions of carbonate factory evolution in the Alborz Basin (northern Iran) indicate a global response to Early Carboniferous (Tournaisian) glaciations." *Sedimentary Geology* 348 (2017): 19-36.

During, M. A. D., **D. F. A. E.** Voeten, A. S. Schulp, and J. W. F. Reumer. "A possible Pararcus diepenbroeki vertebra from the Vossenveld Formation (Triassic, Anisian), Winterswijk, the Netherlands." *Netherlands Journal of Geosciences* 96, no. 1 (2017), 63-68.

Klein, N., **D. F. A. E.** Voeten, A. Haarhuis, and R. Bleeker. "The earliest record of the genus Lariosaurus from the early middle Anisian (Middle Triassic) of the Germanic Basin." *Journal of Vertebrate Paleontology* 36, no. 4 (2016): e1163712.

Klein, N., **Voeten, D. F. A. E.**, J. Lankamp, R. Bleeker, O. J. Sichelschmidt, M. Liebrand, D. C. Nieweg, and P. M. Sander. "Postcranial material of Nothosaurus marchicus from the Lower Muschelkalk (Anisian) of Winterswijk, The Netherlands, with remarks on swimming styles and taphonomy." *Paläontologische Zeitschrift* 89, no. 4 (2015): 961-981.

Voeten, D. F. A. E., P. M. Sander, and N. Klein. "Skeletal material from larger Eusauropterygia (Reptilia: Eosauropterygia) with nothosaurian and cymatosaurian affinities from the Lower Muschelkalk of Winterswijk, The Netherlands." *Paläontologische Zeitschrift* 89, no. 4 (2015): 943-960.

Acknowledgements

The thesis in front of you represents the destination of an adventurous academic voyage that I would never have been able to undertake alone. Late 2013 and only three weeks after learning about the existence of Olomouc, a picturesque town in the eastern Czech Republic, I was accepted into a PhD program with its Faculty of Zoology and Laboratory of Ornithology. After having emigrated there and less than two months later, everything had changed. Unbeknownst to me, the apparent premature termination of my academic journey would ultimately represent the beginning of an experience far more exotic than I could ever have hoped for, for which I owe numerous special people my deep gratitude.

Stanislav Bureš shared in the initial shock of unexpected developments but nevertheless decided to support my improvised plan of attack. He expressed great faith in my initially unconventional approach within only four weeks after having personally met for the first time and has relentlessly done so until this very day. I am tremendously grateful for him warmly welcoming me into his department, kindly allowing me to drive his rally-inspired Subaru, and assisting me in uncountable formal and practical matters that I would never have been able to resolve without him over the last years.

Paul Tafforeau is undoubtedly the foremost authority in synchrotron tomography of paleontological, paleoanthropological, and archaeological material, and among the most inspiring scientists I have ever met. Paul unifies a unique combination of deep academic rigor, ready knowledge far exceeding his original specialty, and understanding for and patience with those of us attempting to acquire a fraction of the skills he possesses. In the face of his unbelievably dense schedule, he took me under his wing and trusted me with manipulating priceless fossils and controlling an unbelievably powerful radiation source. Nothing has boosted my academic confidence more than having received his respect and the opportunity to work under his expert supervision. Thank you for sharing your experience and making me feel like a capable scientist.

Throughout my project, Sophie Sanchez has always offered kind reflection and perspective. Her capability of unifying the execution of top-notch research with a rare degree of approachability,

an honest desire to help out, and a sincere sympathy made her a warm beacon of peace and understanding in the at times sobering reality of scientific turmoil. I thank her for demonstrating to me that great academic success does not necessarily require a hard-hearted attitude.

Vincent Beyrand came into the PhD with more knowledge on dinosaurs than I feature while finishing up and we spent many, many hours together in both the Czech Republic and in France. I owe him thanks for having put up with me for all this time and for lending a hand when his outstanding memory and detailed documentation saved the day at those times when I was less organized than I had realized.

Vincent Fernandez is capable of achieving the most outstanding academic and technological objectives. He has offered crucial assistance and guidance on numerous accounts, often without being requested to do so or even without realizing this himself. His modest and calm conduct has set an important example for me and I am grateful for the selfless and unconditional help he has provided.

Although I met Benoit Cordonnier only towards the end of my PhD trajectory and he has not had a direct involvement in my professional research, his innate enthusiasm, diligence, sharp perception, and extraordinary hospitality quickly made him a close friend whom I have greatly enjoyed learning from and spending time with.

The sterile presentation of the author list on academic publications obscures the true involvement that typically remains below the surface. Tobias Reich shares an incredible amount of interests with me that I enjoyed exploring together and he kept me sharp while working on our beloved nothosaurs. Ricardo Araújo deserves deep credit for his upbeat, original, and productive involvement in the same study. Torsten Scheyer offered crucial assistance and warmly welcomed apt advice, and kindly negotiated the means to have our shared labor come to publication. Jorge Cubo invested valuable time and exhibited great patience in illuminating important biostatistical aspects for me. Emmanuel de Margerie has a keen eye for detail that allowed me to optimize our report. Martin Röper not only made the valuable material kept in his care available for this project and personally transported priceless fossils to Grenoble on numerous occasions, but his amical enthusiasm also made our scientific discussions always feel like joyful conversations. Oliver Rauhut, Raymund Albersdörfer, and Alexandra Houssaye, all went out of their way to

enable the research as presented. A special word of thanks goes out to Richard de Haan who selflessly donated one of his prized finds to a public repository to make it available for research.

I have never experienced office life becoming truly isolating, which is why I am particularly thankful for the inspiring and supportive colleagues that I had the pleasure of working alongside at my everyday whereabouts. In Olomouc, I enjoyed good times with Zdeněk, Robin, Graeme, Tim, Milan, Matěj, Martin, Jana, Eva, Markéta, Kateřina, Lenka, Jakub, "the Michals", Tomáš, Daniel, and Beata. I also warmly thank the faculty professors that educated and subsequently tested me on the fascinating aspects of biology, and occasionally shared a drink with me. At ID19 and around Grenoble, I laughed with Pierre-Jean, Benedikt, Chris, Camille, Felix, Jean-David, Yin, Craig, Margie, Maxim, Emilio, Bastian, Michaela, Yannick, Eva, Shanna, Adam, Alexander, Lukas, Elodie, Jean-Paul, and many more. In both Olomouc and Grenoble, I was very fortunate to have met and spent time with numerous friends that I would never have known if it were not for The Project. Thank you all very much for your support, for the leisure, and for making me feel at home wherever I was!

A few well-deserved and deeply felt words of thanks go out to a very special person and good friend, Mehrdad Sardar Abadi. We met early 2014 and together we explored our new home away from home in Olomouc. His vibrant personality, contagious humor, and all-round benevolent and compassionate spirit gave me strength to negotiate a particularly uncertain period with a persistent smile on my face. He has the ability to efficiently translate a deeply rooted passion for geology into strong research regardless of the conditions he is working in, and I am very grateful he invited me into his research endeavors on numerous occasions.

Nicole Klein, Martin Sander, and the members of the Werkgroep Muschelkalk Winterswijk have kindly shared their expertise with me and opened doors towards gaining valuable research experience outside the scope of my PhD on fossils for which we all share a special place in our hearts.

Andrea Cau efficiently and successfully fronted an international team of scientists during the study and description of a spectacular new Mongolian species of dinosaur, and I am very proud to have received the opportunity to work in this team. Another international collaboration led by James Neenan that I was also allowed to take part in revealed particularly interesting patterns in

the organ of balance preserved within the fossilized skulls of a wide variety of sauropterygian marine reptiles. I thank all workers involved for granting me the experience of contributing to these prestigious studies.

I thank Anneke van Heteren for drawing my attention to the advertisement for the original vacancy, for urging me to apply, and for supporting me during the first phase of my postgraduate studies. Martin Kundrát, Daniel Jirák, and Jiří Janáček exhibited confidence in my ability to conduct sound research and I will never forget the excitement I felt when they collectively selected me for fulfilling the referred position.

The projects presented in this thesis would not have been possible without the means, infrastructure, and logistic guidance provided to me by Palacký University (partially through internal grant IGA_PrF_2017_023) and by the European Synchrotron Radiation Facility. These institutes offered ample support in maintaining accommodation in both Olomouc and Grenoble, as well as towards the other general costs of living. Furthermore, Paul and the ESRF in particular kindly allowed me to make the transit between Olomouc and Grenoble multiple times a year and enabled me to attend various international conferences, notably including the intercontinental meeting of the Society of Avian Paleontology and Evolution in Diamante, Argentina. Without their trust instilled in me towards attending such meetings, where I was proud to represent my hosting facilities, I would not have been able to enjoy the freedom I experienced when deciding on and engaging in the events I took part in.

Melanie During bravely entered into an international long-distance relationship with me and went to great lengths to be able to spend valuable time together, which meant a great deal to me. She has supported me, believed in me, and demonstrated great understanding in those cases where my academic responsibilities proved incompatible with our personal plans. Furthermore, her enthusiasm for our shared interests made working together on a study of a fossil from Winterswijk a real pleasure. Nevertheless, in light of all these qualities, I am most grateful for her sheer endless and unconditional love.

Although my research prevented me from spending as much time with my brother Stefan as I would have wanted, I now realize that we have never let such practicalities drive us apart either. Wherever I was, our contact was always warm, his advice was always encouraging, and his

words and acts of support always fell in fertile soil. I feel privileged to have one of my best friends in my brother.

My parents Ludo and Marja, to whom I proudly dedicate this work, never chose to see their son emigrate but nevertheless supported my academic adventures in any way they could. All pages in this thesis would have been blank if it were not for you and I thank you both wholeheartedly for your endless efforts in laying the foundations that I was allowed to build my dreams on.

Appendix I: Maniraptoran phylogeny (modified after Cau et al. 2017)

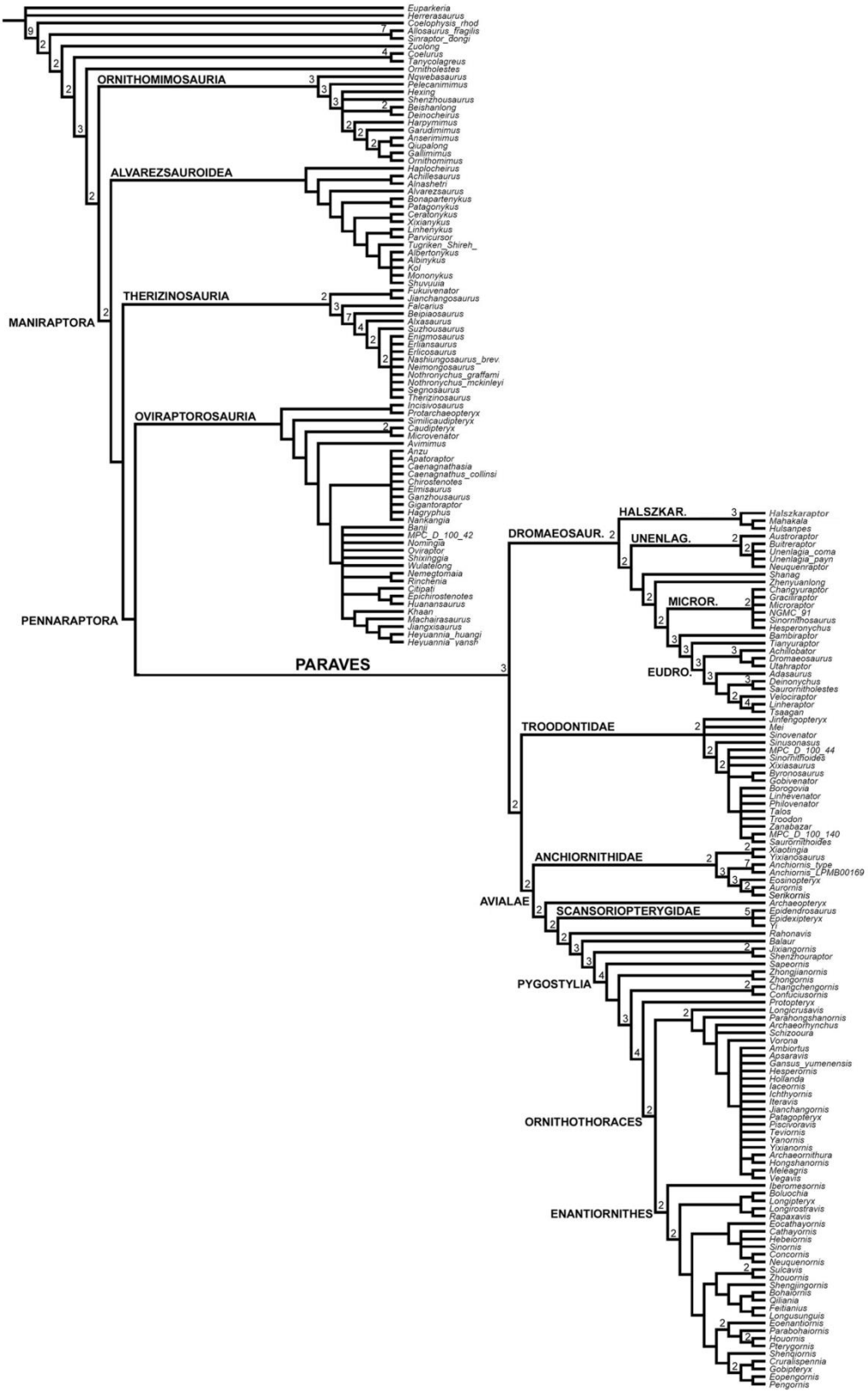

Appendix II: Supplementary information for "Wing bone geometry reveals active flight in *Archaeopteryx*" by Voeten et al.

Includes:

- 10 Supplementary Figures
- 3 Supplementary Tables
- 4 Supplementary Notes
- 35 Supplementary References

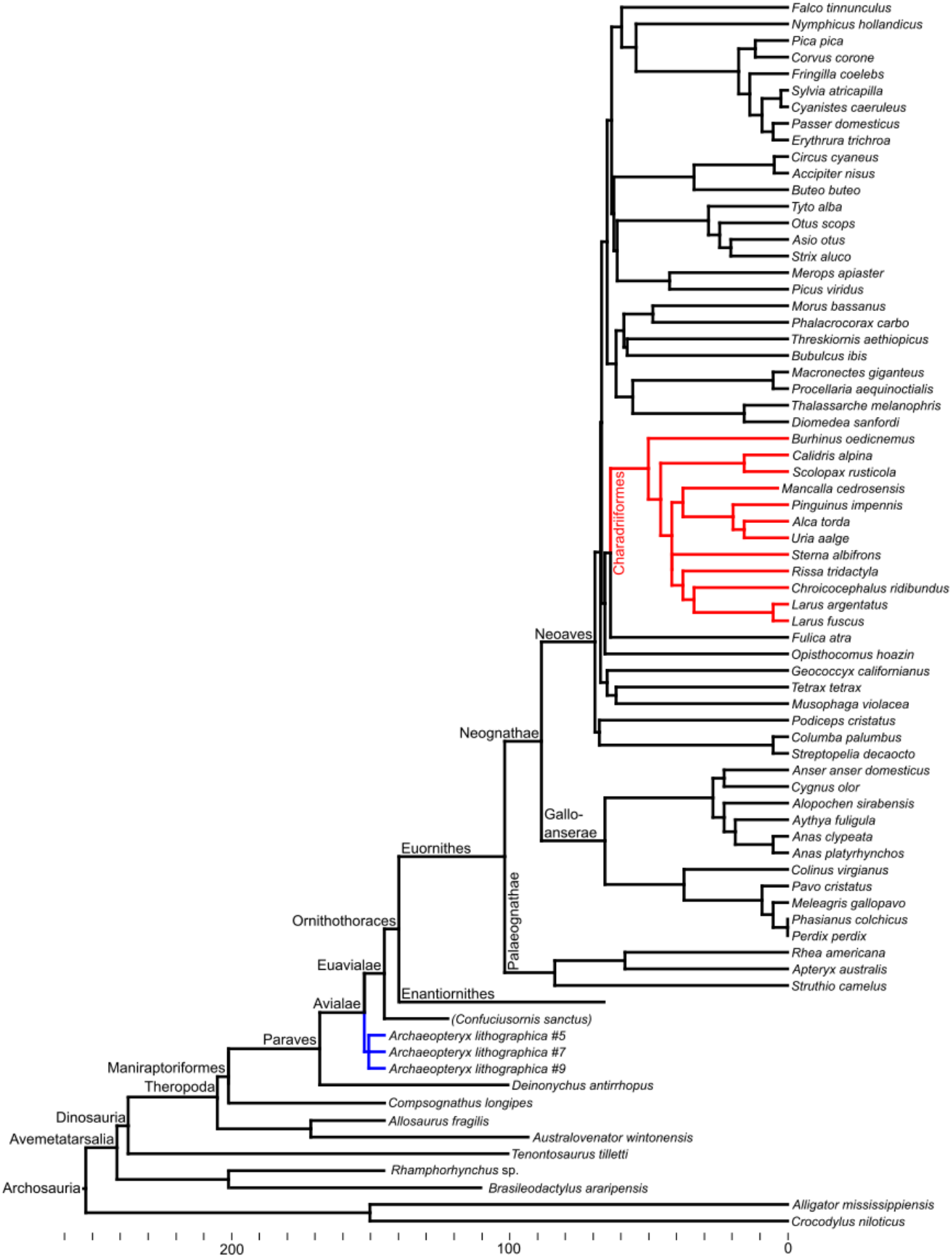

Supplementary Figure 1. Phylogenetic tree used in this study. X-axis in million years before present. Selected ranks specified. *Archaeopteryx* (blue) and Charadriiformes (red) indicated, *Confuciusornis sanctus* (between parentheses) not included in analysis. For sources see Supplementary Data 4.

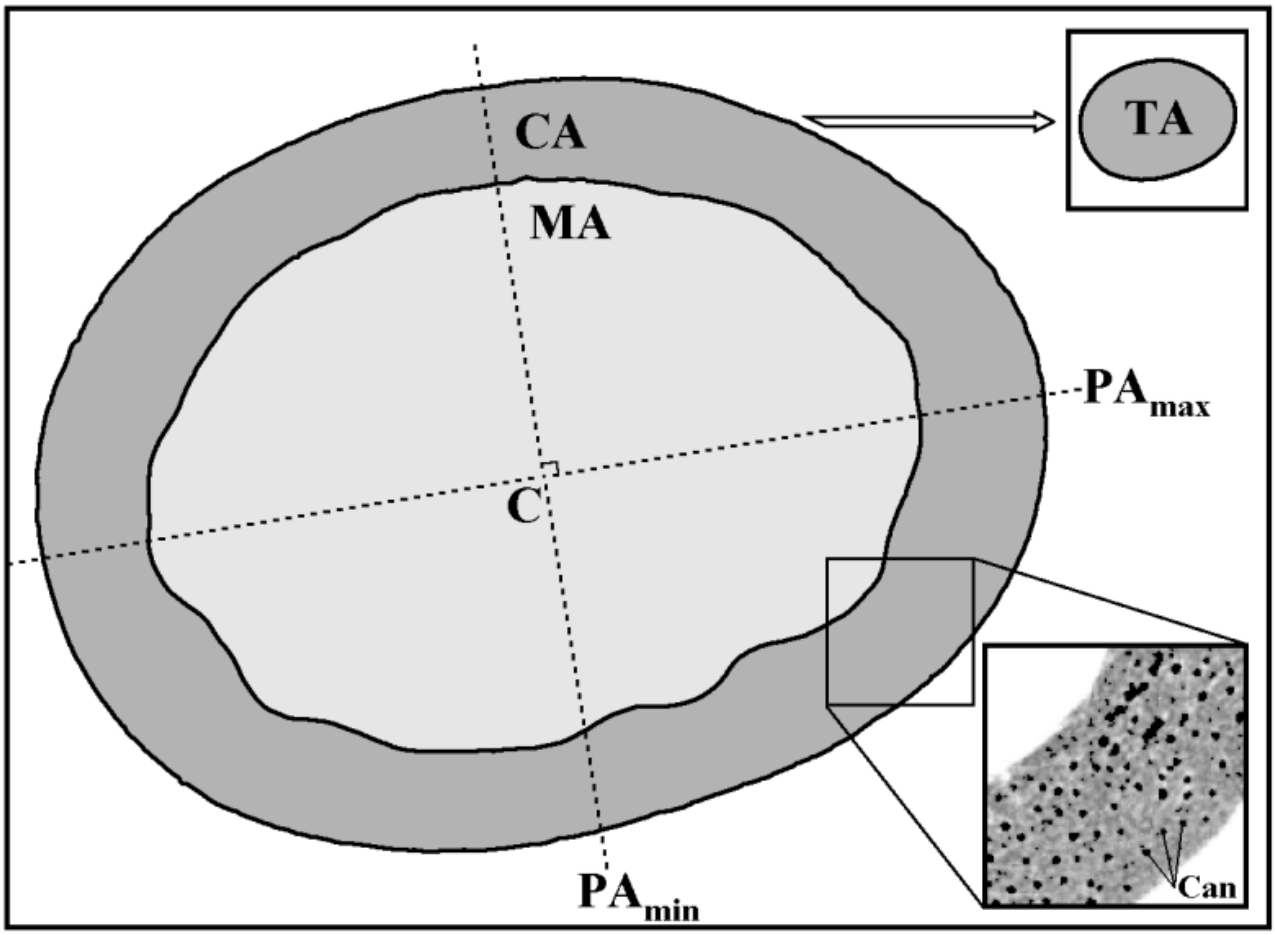

Supplementary Figure 2. Bone cross-sectional parameters. Schematic cross section of the common pheasant humerus illustrating parameters and orientations obtained with ImageJ and MomentMacro for ImageJ: Cortical area (CA), Medullary area (MA), Total area contained within periosteal margin (TA), Longest principal axis (PA_{max}), Shortest principal axis (PA_{min}), Section centroid (C), Cortical canals (Can indicates selected canals; accentuated here through ImageJ threshold selection). CA/TA, our index of relative cortical thickness, equals CA/(CA+MA). Polar moment of area J quantifies the resistance against torsion around the longitudinal bone axis (perpendicular to this section) and equals Imax+Imin; the second moments of area in the directions of PA_{max} and PA_{min}, respectively. In this study, J is normalised through division by body mass M. Cortical vascular density it defined as CAN/CA and quantifies the average amount of canals present per mm^2 of cortical bone in cross section.

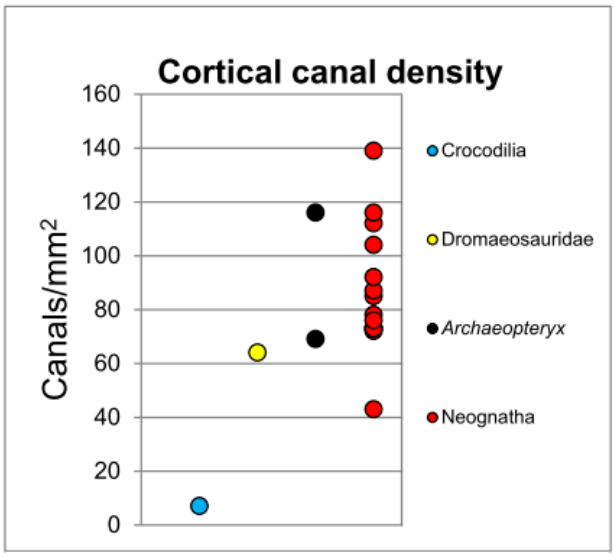

Supplementary Figure 3. Average cortical canal density across selected archosaurs. Cortical canal density of species expressed as Can/mm^2. Values averaged over humerus and ulna, cortical canal density of Dromaeosauridae represents ulnar value exclusively. *Archaeopteryx* specimens plotted individually.

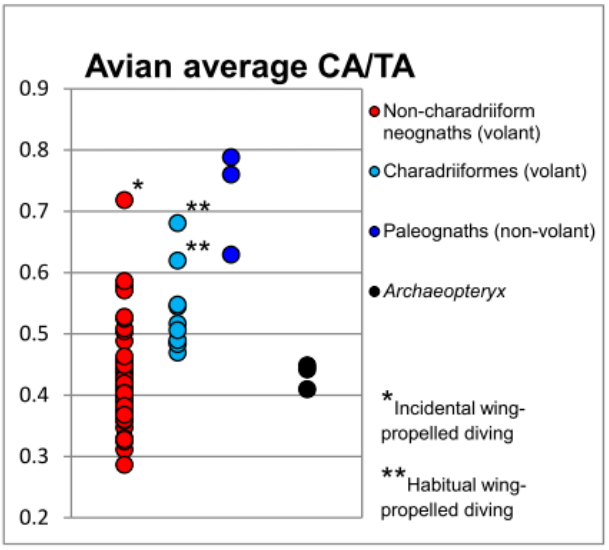

Supplementary Figure 6. Average relative cortical thickness across birds. Note the elevated relative cortical thickness of Charadriiformes with respect to non-charadriiform neognaths.

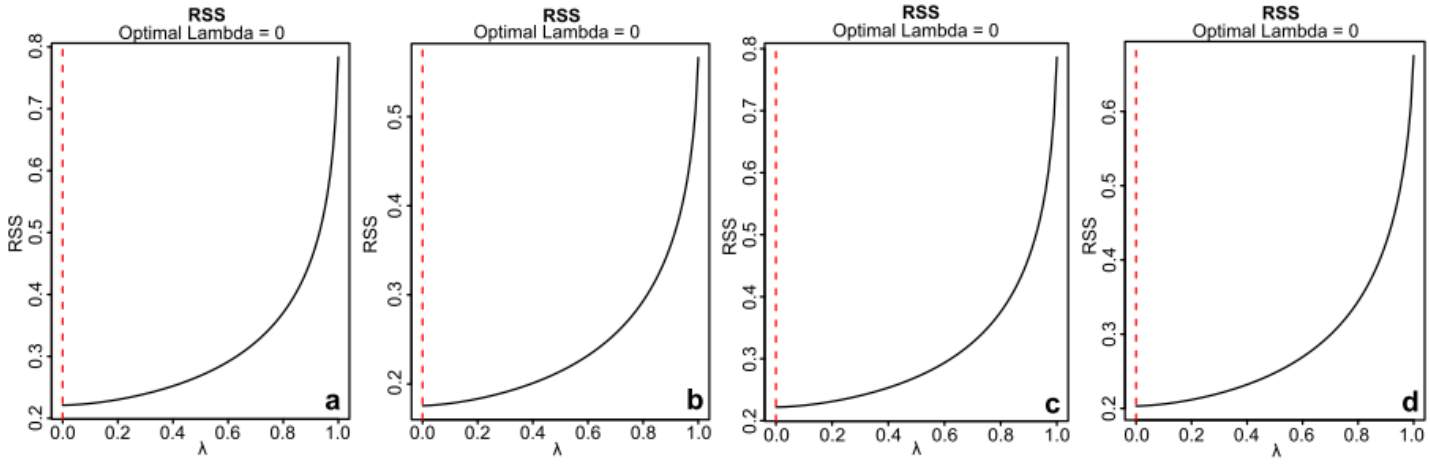

Supplementary Figure 8. Log-likelihood plots showing optimum value of Pagel's λ required to control for phylogenetic non-independence in phylogenetic Flexible Discriminant Analysis (pFDA). Phylogenetic independence is revealed for the data sets categorised following the locomotory divisions adapted from **a,** Viscor et al.[1], training taxa only, **b,** Viscor et al.[1], all taxa, **c,** Close et al.[2], training taxa only, and **d,** Close et al.[2], all taxa.

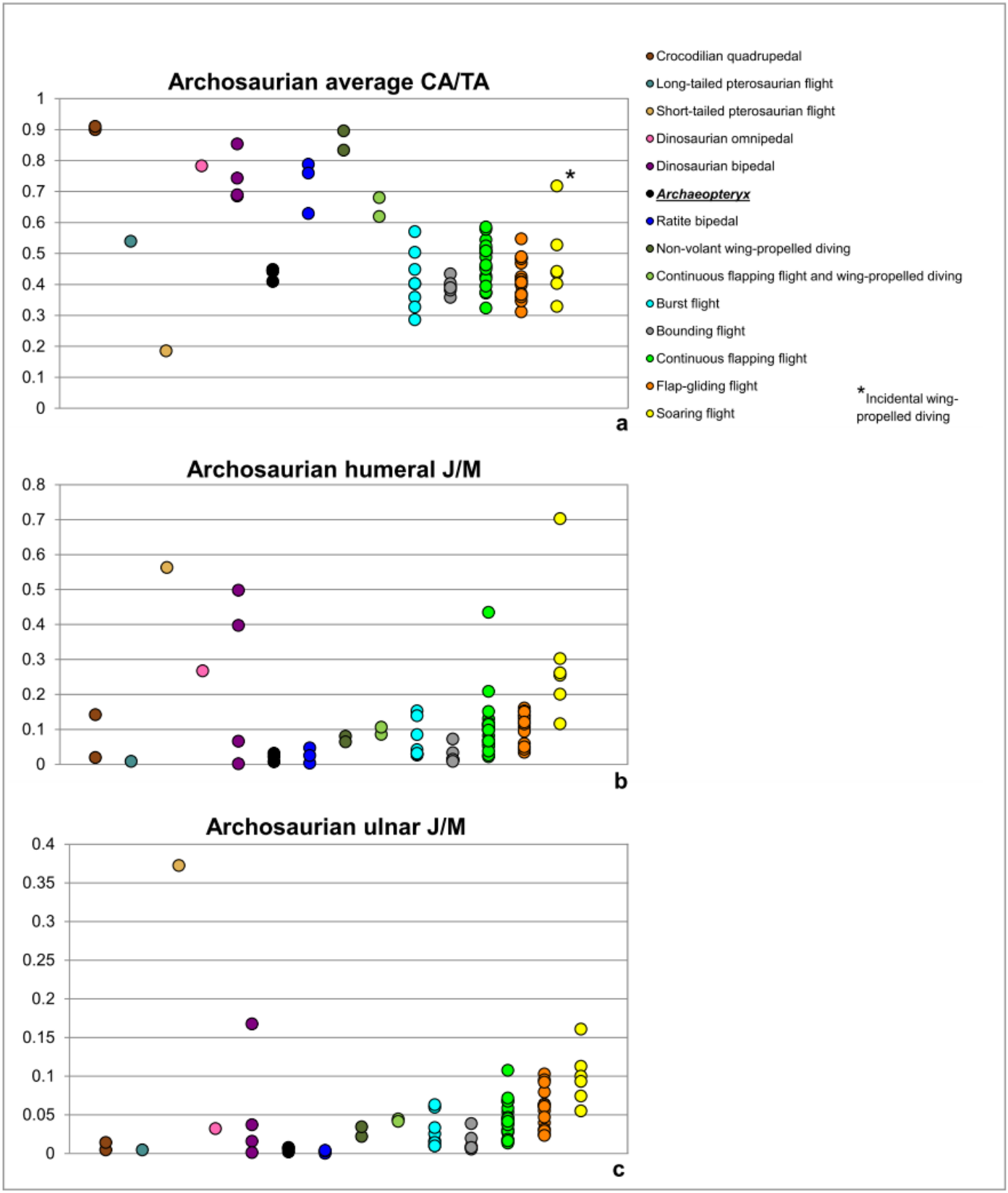

Supplementary Figure 4. Univariate plots of cross-sectional parameters of archosaurian anterior limb bones according to the locomotor classification modified after Close et al.[2]. a, Average humeroulnar relative cortical thickness. **b,** Mass-normalised humeral torsional resistance. **c,** Mass-normalised ulnar torsional resistance.

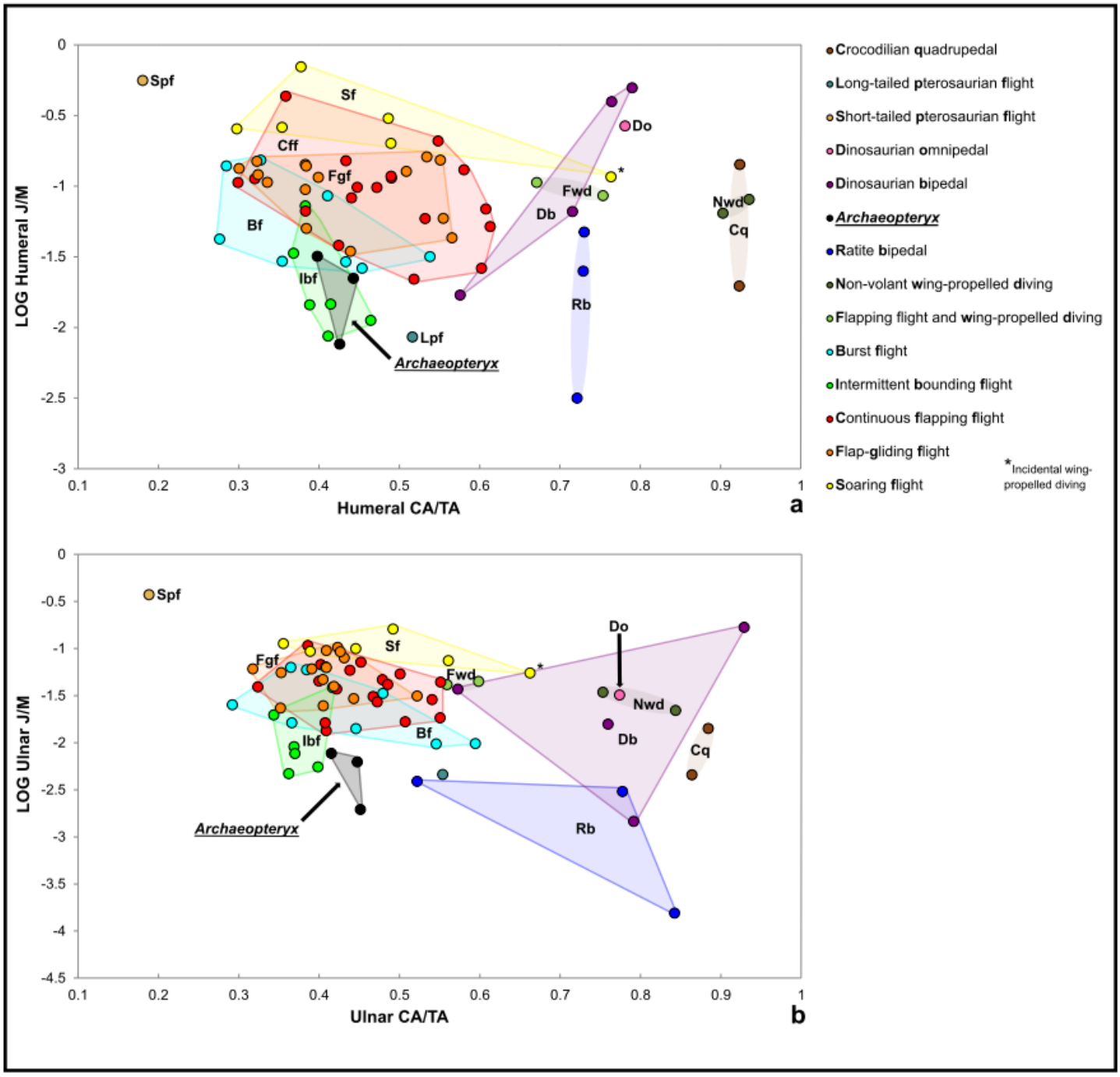

Supplementary Figure 5. Bivariate plots of cross-sectional parameters from archosaurian anterior limb bones according to the locomotor classification modified after Close et al.[2]. a, Humeral relative cortical thickness versus mass-normalised torsional resistance. **b,** Ulnar relative cortical thickness versus mass-normalised torsional resistance.

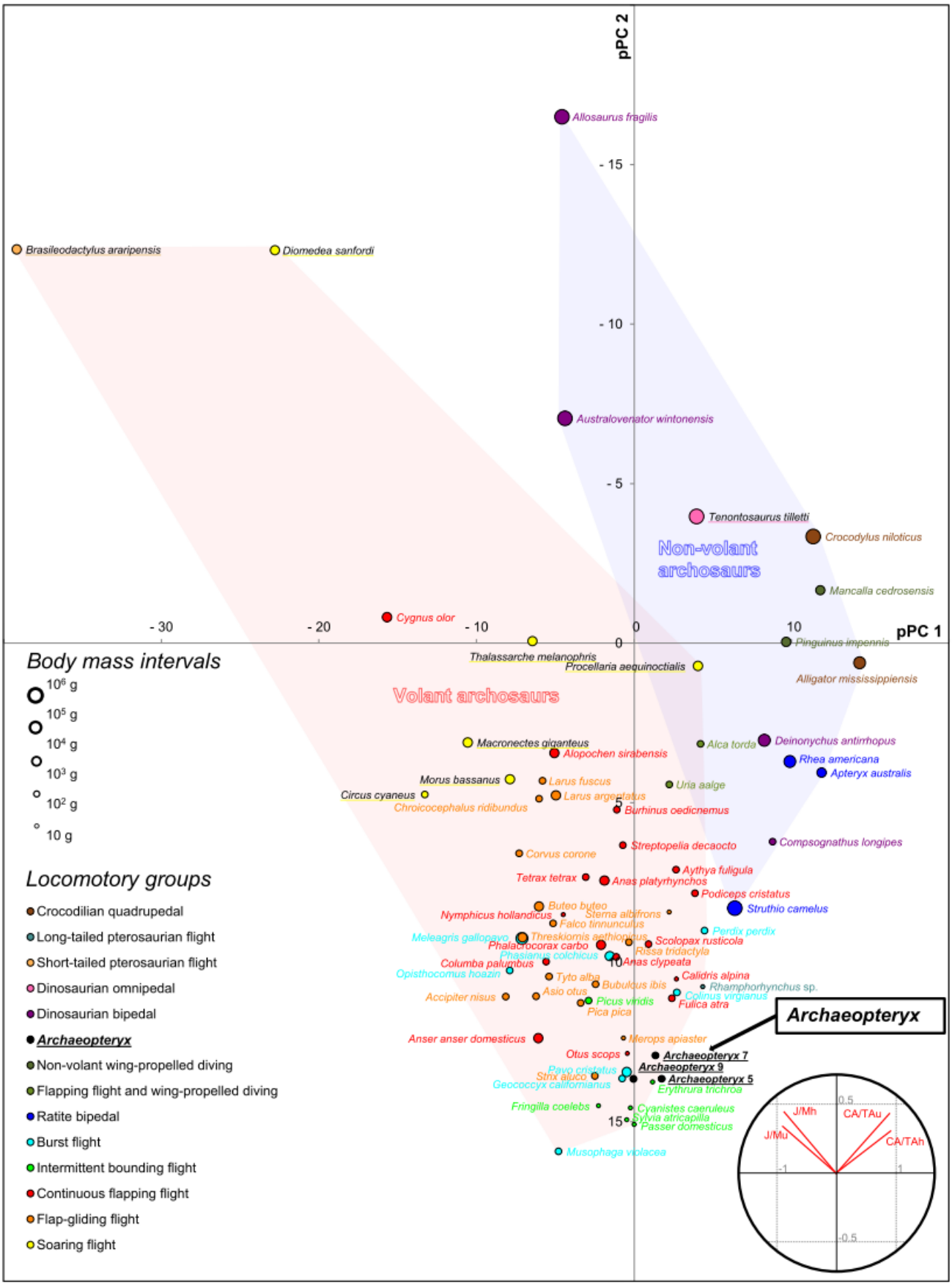

Supplementary Figure 7. First and second phylogenetic principal component plot for specific archosaurian humeral and ulnar relative cortical thickness (CA/TA) and mass-corrected polar moment of inertia of an area (J/M). Circles represent species, *Archaeopteryx* specimens plotted individually. Circle diameter reflects body mass class, circle color indicates locomotory strategy (adapted from the division by Close et al.[2]). Parameters labeled "_h" and "_u" in the loading biplot indicate humeral and ulnar affinity, respectively.

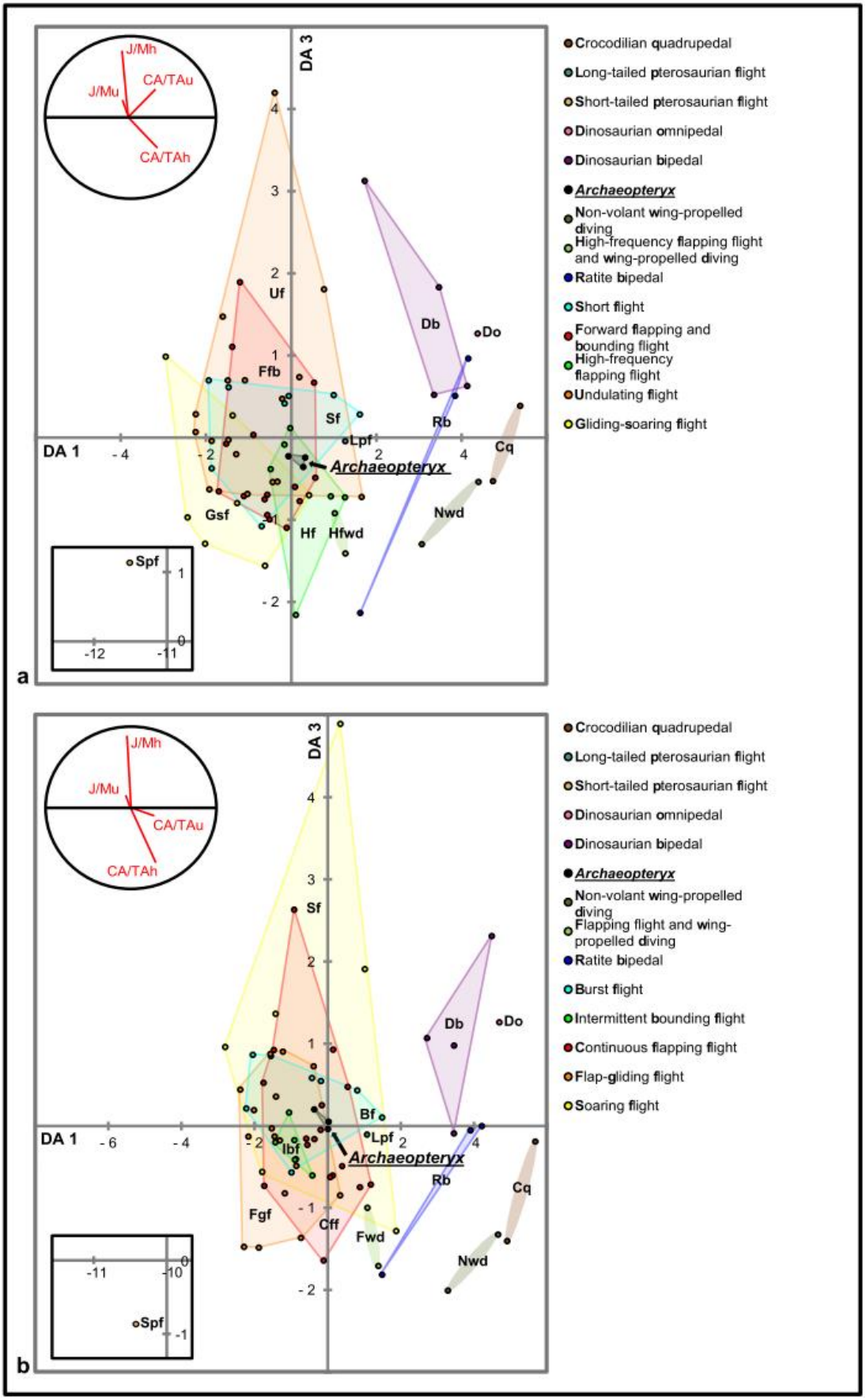

Supplementary Figure 9. LDA plot for specific archosaurian humeral and ulnar CA/TA and J/M. First and third linear discriminant axes are presented. Classification follows the locomotory divisions adapted from **a,** Viscor et al.[1] and **b,** Close et al.[2], non-pterosaurian flight strategies represent avian flight modes. Dots correspond to species, Archaeopteryx specimens plotted individually. Colored hulls delimit groups with a minimum of three representatives. Parameters labeled "_h" and "_u" in loading biplots designate humeral and ulnar affinity, respectively.

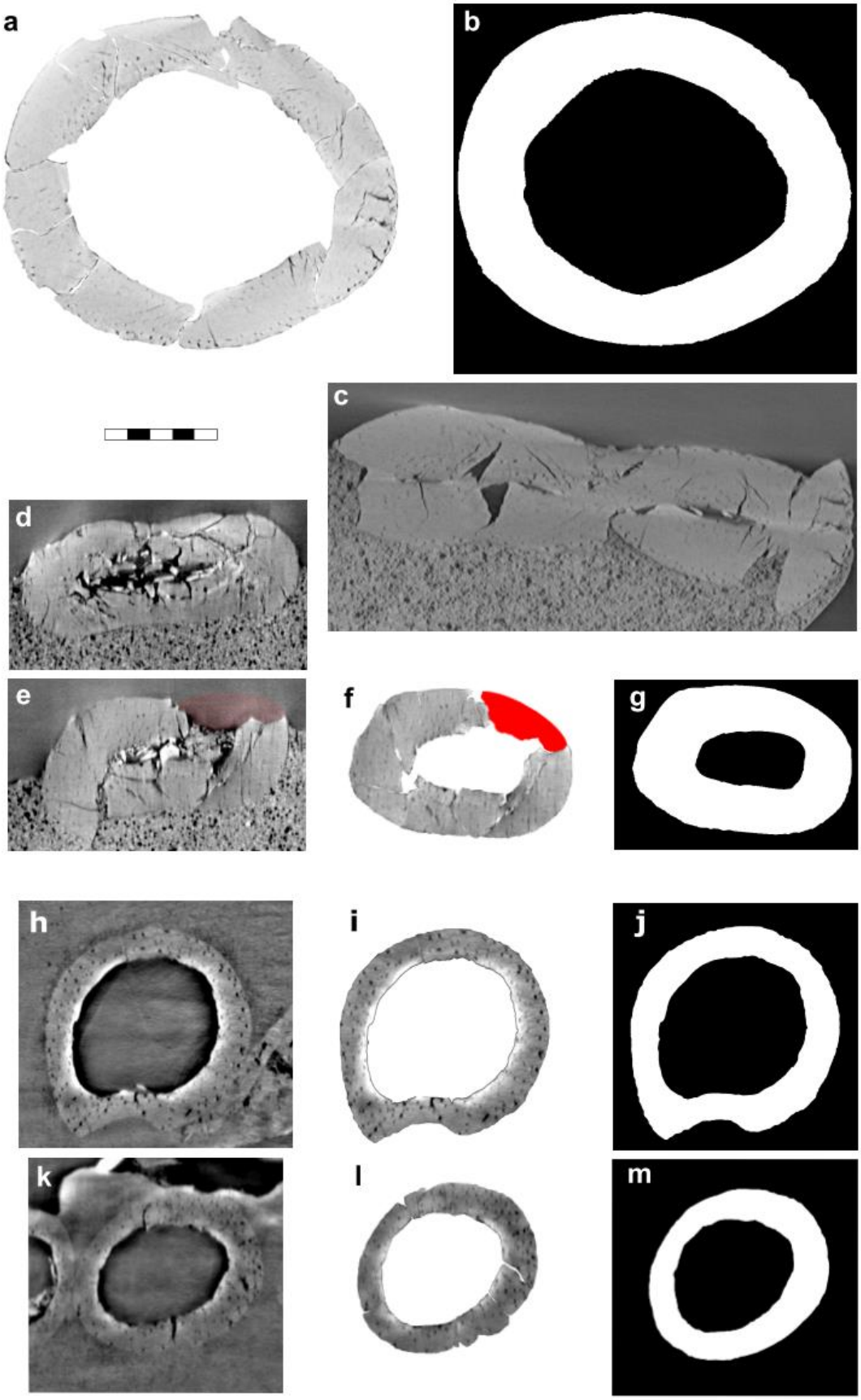

Supplementary Figure 10. ***Compsognathus*** **and** ***Rhamphorhynchus*** **sectional data used in this study. a-c,** *Compsognathus* left humerus **a,** restored section, **b,** binary section, and **c,** sampled virtual cross section. **d-g,** *Compsognathus* right ulnar **d,** virtual cross section 3.58 mm proximal to sampled location (e); note fractured cortex top right in image, **e,** sampled virtual cross section with supplemented cortical fragment top right in image, **f,** restored section, and **g,** binary section. **h-j,** *Rhamphorhynchus* right humeral **h,** sampled virtual cross section, **i,** restored section, and **j,** binary section. **k-m,** *Rhamphorhynchus* left ulnar **k,** sampled virtual cross section, **l,** restored section, and **m,** binary section. Scale bar measures 1 mm.

Supplementary Table 1. P-values with uncorrected significance of pairwise MANOVA including CA/TA_h, CATA_u, J/M_h, and J/M_u for the classification adapted from Viscor et al.[1]. WPD designates wing-propelled diving. Mystery taxa and groups represented by a single specimen are not included. Red indicates failed tests, light red indicates insignificant difference in means, yellow indicates marginally significant difference in means (significant at CI=90%, insignificant at CI=95%), blue indicates significant difference in means (CI=95%).

Locomotor mode (1)	Crocodilian quadrupedal	Dinosaurian bipedal	Ratite bipedal	Non-volant (WPD)	Short Flight	Forward flapping/ bounding flight	High-frequency flapping flight	High-frequency flapping (WPD)	Undulating flight	Gliding/ Soaring flight
Crocodilian quadrupedal		0.73287	fail	fail	0.011561	0.00015631	0.10411	fail	4.66E-05	0.023769
Dinosaurian bipedal	0.73287		0.66948	0.67827	0.0049269	8.72E-05	0.047207	0.63156	4.66E-05	0.0062851
Ratite bipedal	fail	0.66948		fail	0.023877	0.0012843	0.16997	fail	0.0003783	0.025003
Non-volant (WPD)	fail	0.67827	fail		0.015474	0.00041253	0.15331	fail	0.00014284	0.043361
Short Flight	0.011561	0.0049269	0.023877	0.015474		0.52778	0.10757	0.092063	0.18763	0.017928
Forward flapping/ bounding flight	0.00015631	8.72E-05	0.0012843	0.00041253	0.52778		0.19453	0.033387	0.29029	0.021149
High-frequency flapping flight	0.10411	0.047207	0.16997	0.15331	0.10757	0.19453		0.65051	0.064075	0.17321
High-frequency flapping (WPD)	fail	0.63156	fail	fail	0.092063	0.033387	0.65051		0.018948	0.29628
Undulating flight	4.66E-05	4.66E-05	0.0003783	0.00014284	0.18763	0.29029	0.064075	0.018948		0.033829
Gliding/ Soaring flight	0.023769	0.0062851	0.025003	0.043361	0.017928	0.021149	0.17321	0.29628	0.033829	

Supplementary Table 2. P-values with uncorrected significance of pairwise MANOVA including CA/TA_h, CATA_u, J/M_h, and J/M_u for the classification adapted from Close et al.[2]. WPD designates wing-propelled diving. Mystery taxa and groups represented by a single specimen are not included. Red indicates failed tests, light red indicates insignificant difference in means, yellow indicates marginally significant difference in means (significant at CI=90%, insignificant at CI=95%), blue indicates significant difference in means (CI=95%).

Locomotor mode (2)	Crocodilian quadrupedal	Dinosaurian bipedal	Ratite bipedal	Non-volant (WPD)	Burst flight	Bounding flight	Continuous flapping flight	Continuous flapping (WPD)	Flap-gliding flight	Soaring flight
Crocodilian quadrupedal		0.75026	fail	fail	0.01033	0.04736	0.00012138	fail	3.85E-05	0.070081
Dinosaurian bipedal	0.75026		0.55749	0.71276	0.0025153	0.0074973	4.44E-05	0.61262	7.19E-06	0.035217
Ratite bipedal	fail	0.55749		fail	0.023133	0.054083	0.0022136	fail	0.00027326	0.063626
Non-volant (WPD)	fail	0.71276	fail		0.015813	0.063726	0.00056317	fail	0.00017818	0.10014
Burst flight	0.01033	0.0025153	0.023133	0.015813		0.56165	0.1463	0.10972	0.076519	0.016082
Bounding flight	0.04736	0.0074973	0.054083	0.063726	0.56165		0.08788	0.22614	0.091914	0.016204
Continuous flapping flight	0.00012138	4.44E-05	0.0022136	0.00056317	0.1463	0.08788		0.11103	0.067407	0.01168
Continuous flapping (WPD)	fail	0.61262	fail	fail	0.10972	0.22614	0.11103		0.031402	0.32431
Flap-gliding flight	3.85E-05	7.19E-06	0.00027326	0.00017818	0.076519	0.091914	0.067407	0.031402		0.0059127
Soaring flight	0.070081	0.035217	0.063626	0.10014	0.016082	0.016204	0.01168	0.32431	0.0059127	

Supplementary Table 3. Statistics of one-way MANOVA of parameter set including CA/TA_h, CA/TA_u, J/M_h, and J/M_u for the classifications adapted from Viscor et al.[1] and Close et al.[2]. Mystery taxa and groups represented by a single specimen not included.

Viscor et al.[1]			
Wilks´ lambda:	0.08448	Pillai trace:	1.492
df1:	36	df1:	36
df2:	200.4	df2:	224
F:	5.196	F:	3.701
p (same):	1.29E-14	p (same):	9.72E-10

Close et al.[2]			
Wilks´ lambda:	0.06962	Pillai trace:	1.59
df1:	36	df1:	36
df2:	200.4	df2:	224
F:	5.766	F:	4.105
p (same):	1.75E-16	p (same):	3.19-11

Supplementary Notes

Supplementary Note 1: Accumulation mode for tomographic acquisition

X-ray tomography relies on the image contrast present in an X-ray beam after transmission through an object. It therefore requires the detection of a signal that is significantly different from both the incoming beam and the electronic noise of the detector. However, an object absorbing most of the incoming signal during imaging may result in recorded data statistically indiscriminable from the electronic noise of the detector. To negotiate this effect, two solutions are available: 1) increasing the energy (and thus the penetration) of the incoming beam, or 2) extended sampling of the incoming signal by prolonging the exposure time. The energy range available in an X-ray tomographic setup depends on inherent properties of the source (e.g., the maximum voltage for laboratory X-ray tomographs, or electron beam energy in the storage ring and the magnetic field in insertion devices or bending magnets for synchrotron radiation). Such a setup has a maximum operational energy level threshold that often cannot be exceeded. Furthermore, since transmission increases with energy, raising the operational energy level may adversely affect the relative contrast of interest in the tomographic reconstruction. It is therefore often preferable to amplify the recorded signal by prolonging the exposure time. Most X-ray tomographic setups record data in 16 bit, which corresponds to a dynamic range of 65535 grey levels. The exposure time is ideally set to approach the saturation limit in the flat-field image as closely as possible without actually achieving saturation. However, the exposure time can only be prolonged to a certain maximum. In specific cases, traditional setups do not allow for a sufficiently long exposure time without saturation of the detector.

A designated setup was developed at the ESRF to circumvent this problem[33,34]. Implementation of the so-called attenuation protocol involves the application of three physical components in the tomographic setup. Firstly, a cylinder with a diameter equal to or slightly larger than the observed horizontal field of view is filled with a material that has a density close to that of the sample medium of interest (e.g. small glass or aluminium micro balls when associated with fossilised remains). Secondly, a solid U-shaped block, the profiler, is installed to neutralise the laterally variable absorption of the cylinder. The specific geometry of the profiler induces a stronger absorption laterally than centrally, which normalises the signal. Thirdly, a solid and semicircular block composed of the same material as the profiler, the attenuator, is applied to

achieve homogenised absorption during flat-field correction. When the sample is placed in the cylinder filled with micro balls during tomographic acquisition, the exposure time can be sufficiently prolonged to obtain and record an adequately detectable signal while preventing saturation of the object edges. During recording of the flat-field images (incoming beam without interference), the profiler and attenuator are placed in the beam to emulate the acquisition configuration of profiler plus cylinder with micro balls. The subsequent flat-field correction thus acts principally on the contrast induced by the sample.

Although the attenuation protocol enabled experiments that were previously impossible[33,35], the associated setup does introduce two new problems. Firstly, perfect alignment of all the components in the optic path is crucial but proved challenging and tedious. Secondly, and more importantly, containing a fossil in a cylinder filled with glass or aluminium micro balls is often impractical and may damage delicate structures. Imaging a fossil preserved on a lithic slab was particularly challenging, since immersing it completely in micro balls would result in an exceedingly heavy setup. The alternative of placing the fossil in a smaller cylinder with vertical slots that allow the slab to extend beyond the cylinder itself is problematic in that achieving a sufficiently good seal between the sample and the cylinder to prevent micro balls from escaping without risking damage to the fossil itself poses a substantial challenge.

The PCO.edge 4.2 and PCO.edge 5.5 (PCO AG, Kelheim, Germany) have gradually replaced the ESRF proprietary FReLoN-2K as the preferred detectors, largely because of their higher recording frame rate achieved through a lower full-well capacity (each pixel of the PCO.edge detectors is saturated at an approximately ten-fold lower electron count than the FReLoN-2k). Although both detector families share a dynamical range of 14 bit, the signal-to-noise ratio of the PCO.edge detectors is inherently inferior to that of the FReLoN-2k, which was initially overcome by increasing the amount of projections per scan. Although this does increase overall X-ray sampling per rotation of the object, it also increases tomographic reconstruction times significantly.

To overcome particular shortcomings of the attenuation protocol, we developed the accumulation mode that exploits the high recording frame rate of the PCO.edge detectors by essentially summing multiple images to produce a single image. As in traditional acquisition, a projection is generated over a given angular range during the rotation of the object. However, in accumulation

mode and with the accumulation count set to 10, the camera records images every 10^{th} of that angular range and transmits the frames to a device server where those 10 images are progressively summed to generate a single image. Because the dynamic range of the resulting images can exceed the 65535 grey values of 16-bit images, the projection is recorded as a 32-bit image. Doubling the bit depth also doubles the file size of the final image, but the amount of accumulated images prior recording does not further impact data size. Consequently, where doubling the number of projections has the same effect as applying an accumulation count of 2, an accumulation count of 10 is equivalent to a ten-fold increase in the amount of projections being recorded for only twice the occupied disk space. This approach is similar to the "average mode" available on selected laboratory tomographs. Compared to the attenuation protocol used before, the accumulation mode is vastly simpler to implement. While the attenuation protocol increases image dynamic in the most strongly absorbing parts of the sample, accumulation mode only offers improved sampling of the X-ray signal itself. As such, the accumulation mode does not solve the challenge of complete attenuations, but does provide a broader dynamic range for specifically fossils on lithic slabs oriented perpendicularly to the X-ray beam. Conversely, the differential transmission within the slab and at its surface reinforces the diffusion in the scintillator when the width of the slab is oriented parallel to the X-ray beam, which results in an artificial lightening of grey levels at the surface of the slab. Although this effect does cause artefacts along the surface of the slab (e.g. Fig. 1 e and 1 f) that may interfere with subsequent analyses, the accumulation mode is to be preferred over the attenuation protocol when imaging potentially fragile specimens, as it prevents physical contact with the fossil itself.

Supplementary Note 2: Functional interpretation

Although CA/TA values for *Archaeopteryx* were found to exclusively fall within the range occupied by modern volant birds, J/M values of particularly the smallest (fifth) specimen of *Archaeopteryx* plot within those of small (body mass < 26g) extant volant birds and flightless archosaurs. There are three reasons why we believe this transitional signal is more consistent with early avian volancy than with (retained) non-volancy. Firstly, high CA/TA values account for the generalised non-volant archosaurian condition, including the ancestral pre-avian condition (>95%). The departure of *Archaeopteryx* from this condition into the range of exclusively volant birds represents a functional adaptation that is most parsimoniously explained

by selective pressures relating specifically to volancy. Secondly, the secondarily flightless paleognaths record a return to CA/TA values in the range of non-volant archosaurs and few wing-propelled diving birds, which indicates the presence of sufficient selective pressure to induce cortical thickening when the demands of volancy are relinquished. Thirdly, a decrease in CA/TA implies less bone mass is present within a given periosteal margin. All other factors being equal, this will inherently result in an absolute decrease in J, which we observe is compensated for particularly in modern highly aerial flap-gliding and soaring birds, but also in the trajectory from long- to short-tailed pterosaurs, by a redistribution of bone mass.

Additionally, the reconstructed ulnar geometry of the seventh specimen (Fig. 1 l) of *Archaeopteryx* suffers from a poorly resolved cortical interval in the original data (most left in Fig. 1 f) that describes a suspicious cortical curvature. We choose not to correct for this structural artefact as to not introduce irreproducible manipulation. Since this artefact results in a reconstructed bone geometry presumably less circular than the original *in vivo* condition, the recovered value for J likely represents an underestimation.

Supplementary Note 3: Phylogenetic considerations towards tree topology and timing

Two particular inconsistencies emerged during creation of the chronogram (see Supplementary Figure 1 and Supplementary Data 3) through PaleoDB[27]. Firstly, *Chroicocephalus ridibundus* is lacking from PaleoDB, yet *Larus ridibundus* is present, albeit without associated specimens. Here, we followed Pons et al.[31] in recognition of the genus *Chroicocephalus*. Secondly, the oldest record of the genus *Phasianius* in PaleoDB was recognised as an erroneous entry; this in fact considers the grouse *Archaeophasianus mioceanus*[8].

Supplementary Note 4: Statistical analyses

Phylogenetic univariate analysis revealed that both humeral and ulnar CA/TA offer statistically significant discrimination between several archosaurian locomotor modes in our data set (Supplementary Table 1) for both locomotor classifications tested (Supplementary Data 4). Specific average CA/TA values below 0.60 are only present in volant forms, whereas non-volant archosaurs exclusively exhibit specific average CA/TA values over 0.60. Wing-propelled diving in volant birds is occasionally associated with average CA/TA values in the range of non-volant archosaurs. *Archaeopteryx* exhibits low average CA/TA values that range between 0.40 and 0.46.

Humeral J/M alone does not contribute significantly to locomotor discrimination (Supplementary Data 4) and lacks a significant size effect (Supplementary Data 4). As such, humeral J/M supplements the functional distinction of ulnar J/M, which does provide significant separation but also retains a small yet significant residual size effect (Supplementary Data 4). Multivariate analyses thus involved humeral and ulnar CA/TA and J/M to elucidate on wing function in *Archaeopteryx.*

The first three phylogenetic principal components extracted through phylogenetic PCA of the entire data set (Supplementary Data 5) explain 79.99%, 16.07% and 2.67% of total variance. Partitioning Around Medoids of these three phylogenetic principal components set to two clusters (Supplementary Data 5) explains 78.27% of total point variability. The two recovered clusters were found to primarily recapitulate the separation between known volant and non-volant archosaurian taxa. Only the (incidental) wing-propelled diving birds *Alca torda, Procellaria aequinoctialis* and *Uria aalge* (4.54% of training taxa set) incorrectly group with non-volant archosaurs.

Contrasting pPCA scores with (non-phylogenetic) LDA results revealed identical group assignments that underline the phylogenetic independence of the traits considered. Post-hoc pairwise MANOVA confirmed a significant relation between locomotory strategy and the parameter set used (Supplementary Table 3). The resolved affinity of *Archaeopteryx* with the short[1] and burst[2] flight categories (Supplementary Data 5) is reinforced by the observation that volant birds employing other flight strategies yet recovered close to both *Archaeopteryx* and the short[1]/burst[2] flyers in discriminant morphospace typically exhibit a markedly lower body mass (Supplementary Data 1 and Supplementary Fig. 9).

Supplementary References

1. Viscor, G. & Fuster, J. F. Relationships between morphological parameters in birds with different flying habits. *Comp. Biochem. Physiol.* **87A,** 231-249 (1987).
2. Close, R. A. & Rayfield, E. J. Functional morphometric analysis of the furcula in Mesozoic birds. *PloS one* **7,** e36664 (2012).
3. De Margerie, E., Sanchez, S., Cubo, J. & Castanet, J. Torsional resistance as a principal component of the structural design of long bones: Comparative multivariate evidence in birds. *The Anatomical Record Part A: Discoveries in Molecular, Cellular, and Evolutionary Biology* (2005).
4. Cubo, J., & Casinos, A. Biomechanical significance of cross-sectional geometry of avian long bones. *European Journal of Morphology* **36**, 19-28 (1998).
5. Smith, N. A. & Clarke, J. A. Osteological Histology of the Pan-Alcidae (Aves, Charadriiformes): Correlates of Wing-Propelled Diving and Flightlessness: Osteological Histology of The Pan-Alcidae. *The Anatomical Record* **297,** 188–199 (2014).
6. Bybee, P. J., Lee, A. H., & Lamm, E. T. Sizing the Jurassic theropod dinosaur Allosaurus: assessing growth strategy and evolution of ontogenetic scaling of limbs. *Journal of Morphology* **267,** 347-359 (2006).
7. Parsons, W. L. & Parsons, K. M. Further descriptions of the osteology of Deinonychus antirrhopus (Saurischia, Theropoda). *Bulletin of the Buffalo Society of Natural Sciences* **38,** 43-54 (2009).
8. White, M. A., Cook, A. G., Hocknull, S. A., Sloan, T., Sinapius, G. H., & Elliott, D. A. New forearm elements discovered of holotype specimen Australovenator wintonensis from Winton, Queensland, Australia. *PloS One* **7,** e39364 (2012).
9. Werning, S. The ontogenetic osteohistology of Tenontosaurus tilletti. *PLoS One* **7,** e33539 (2012).
10. Woodward, H. N., Horner, J. R. & Farlow, J. O. Quantification of intraskeletal histovariability in Alligator mississippiensis and implications for vertebrate osteohistology. *PeerJ* **2,** e422 (2014).
11. De Magalhaes, J. P., & Costa, J. A database of vertebrate longevity records and their relation to other life-history traits. *Journal of evolutionary biology* **22,** 1770-1774 (2009). Retrieved from on http://genomics.senescence.info/species/ on 18 January 2016.

12. Cubo, J. & Casinos, A. Incidence and mechanical significance of pneumatization in the long bones of birds. *Zoological Journal of the Linnean Society* **130,** 499–510 (2000).
13. Andrews, C. On some fossil remains of carinate birds from Central Madagascar. *Ibis* **39,** 343-359 (1897).
14. Livezey, B. C. Morphometrics of flightlessness in the Alcidae. *The Auk* **105,** 681-698 (1988).
15. del Hoyo, J., Elliott, A., Sargatal, J., Christie, D. A., & de Juana, E. *Handbook of the Birds of the World Alive* (Lynx Editions, 2015). Retrieved from http://www.hbw.com on 19 January 2016.
16. Macky, R. & White, B. (eds.) *Gastrointestinal Microbiology: Volume 1 Gastrointestinal Ecosystems and Fermentations* (Nimrod Book Services, 1996).
17. Erickson, G. M. *et al.* Was Dinosaurian Physiology Inherited by Birds? Reconciling Slow Growth in Archaeopteryx. *PLoS ONE* **4,** e7390 (2009).
18. Paul, G. S. *Predatory dinosaurs of the world: a complete illustrated guide* (Simon & Schuster, 1988).
19. Paul, G. S. *The Princeton field guide to dinosaurs* (Princeton University Press, 2010).
20. Kellner, A. W. A., & Tomida, Y. Description of a new species of Anhangueridae (Pterodactyloidea) with comments on the pterosaur fauna from the Santana Formation (Aptian-Albian), northeastern Brazil. *National Science Museum Monographs* **17,** 1-135 (2000).
21. Veldmeijer, A. J. Pterosaurs from the Lower Cretaceous of Brazil in the Stuttgart Collection. *Stuttgarter Beitr. Naturk. Ser. B.* **327,** 1-27 (2002).
22. Wellnhofer, P. Weitere Pterosaurierfunde aus der Santana-Formation (Apt) der Chapada do Araripe, Brasilien. *Palaeontographica Abteilung A.* **187,** 43-101 (1991).
23. Henderson, D. M. Pterosaur body mass estimates from three-dimensional mathematical slicing. *Journal of Vertebrate Paleontology* **30,** 768-785 (2010).
24. Witton, M. P. in *Special volume: Flugsaurier: pterosaur papers in honour of Peter Wellnhofer* (Buffetaut, E. & Hone, D. W. E. eds.) 143-158 (München, 2008).
25. Masser, M. P. Alligator Production: Grow-out and harvest. *SRAC Publication* **232**, 1-4 (1993).
26. Huchzermeyer, F. W. *Crocodiles: Biology, Husbandry, and Diseases* (CABI, 2003).

27. Paleobiology Database (2016). Retrieved from http://paleobiodb.org on 29 January 2016.
28. Jarvis, E. D. *et al.* Whole-genome analyses resolve early branches in the tree of life of modern birds. *Science* **346**, 1320-1331 (2014).
29. Bengtson, S.-A. Breeding ecology and extinction of the great auk (Pinguinus impennis): anecdotal evidence and conjectures. *The Auk* **101,** 1-12 (1984).
30. Turvey, S. T. (ed.) *Holocene extinctions*. (OUP Oxford, 2009).
31. Pons, J.-M., Hassanin, A., Crochet, P.-A. Phylogenetic relationships within the Laridae (Charadriiformes: Aves) inferred from mitochondrial markers. *Molecular Phylogenetics and Evolution* **37,** 686-699 (2005).
32. Johnsgard, P.A. *Grouse and quails of North America* (University of Nebraska Press, 1973).
33. Carlson, K. J., Stout, D., Jashashvili, T., de Ruiter, D. J., Tafforeau, P., Carlson, K. & Berger. L. R. The endocast of MH1, *Australopithecus sediba*. *Science* **333**, 1402-1407 (2011).
34. Sanchez, S., Fernandez, V., Pierce, S. E. & Tafforeau, P. Homogenization of sample absorption for the imaging of large and dense fossils with synchrotron microtomography. *Nature Protocols* **8**, 1708–1717 (2013).
35. Fernandez, V., Abdala, F., Carlson, K. J., Collins Cook, D., Rubidge, B. S., Yates, A. & Tafforeau, P. Synchrotron reveals Early Triassic odd couple: injured amphibian and aestivating therapsid share burrow. *PLoS One* **8**, e64978 (2013).

Appendix III: Supplementary Data 1 for "Wing bone geometry reveals active flight in *Archaeopteryx*" by Voeten et al.

Raw data and declaration of external data sources. Organised by taxon, includes raw data values, locomotor mode, and body mass.

Latin name	"Order"	"Family"	Vernacular name
Buteo buteo	Accipitriformes	Accipitridae	Common buzzard
Accipiter nisus			Eurasian sparrowhawk
Circus cyaneus			Hen harrier
Anser anser domesticus	Anseriformes	Anatidae	Domestic goose
† *Alopochen sirabensis*			Malagasy shelduck
Anas platyrhynchos			Mallard
Cygnus olor			Mute swan
Anas clypeata			Northern shoveler
Aythya fuligula			Tufted duck
Apteryx australis	Apterygiformes	Apterygidae	Southern brown kiwi
Uria aalge	Charadriiformes	Alcidae	Common murre
† *Pinguinus impennis*			Great Auk
† *Mancalla cedrosensis*			Mancalla
Alca torda			Razorbill
Burhinus oedicnemus		Burhinidae	Eurasian stone-curlew
Chroicocephalus ridibundus		Laridae	Black-headed gull
Rissa tridactyla			Black-legged kittiwake
Larus argentatus			European herring gull
Larus fuscus			Lesser black-backed gull
Calidris alpina		Scolopacidae	Dunlin
Scolopax rusticola			Eurasian woodcock
Sterna albifrons		Sternidae	Little tern
Columba palumbus	Columbiformes	Columbidae	Common wood pigeon
Streptopelia decaocto			Eurasian collared dove
Merops apiaster	Coraciiformes	Meropidae	European bee-eater
Geococcyx californianus	Cuculiformes	Cuculidae	Greater roadrunner
Falco tinnunculus	Falconiformes	Falconidae	Common kestrel
Colinus virgianus	Galliformes	Odontophoridae	Northern bobwhite
Phasianus colchicus		Phasianidae	Common pheasant
Perdix perdix			Grey partridge
Pavo cristatus			Indian peafowl
Meleagris gallopavo			Domesticated turkey
Tetrax tetrax	Gruiformes	Otidae	Little bustard
Fulica atra		Rallidae	Eurasian coot
Musophaga violacea	Musophagiformes	Musophagidae	Violet turaco
Opisthocomus hoazin	Opisthocomiformes	Opisthocomidae	Hoatzin
Corvus corone	Passeriformes	Corvidae	Carrion crow
Pica pica			Eurasian magpie
Erythrura trichroa		Estrildidae	Blue-faced parrotfinch
Fringilla coelebs		Fringillidae	Common chaffinch
Cyanistes caeruleus		Paridae	Eurasian blue tit
Passer domesticus		Passeridae	House sparrow
Sylvia atricapilla		Sylviidae	Eurasian blackcap
Bubulcus ibis	Pelicaniformes	Ardeidae	Cattle egret
Threskiornis aethiopicus		Threskiornithidae	African sacred ibis
Picus viridis	Piciformes	Picidae	European green woodpecker
Podiceps cristatus	Podicipediformes	Podicipedidae	Great crested grebe
Diomedea sanfordi	Procellariiformes	Diomedeidae	Northern royal albatross
Thalassarche melanophris			Black-browed albatross
Procellaria aequinoctialis		Procellaridae	White-chinned petrel
Macronectes giganteus			Southern giant petrel
Nymphicus hollandicus	Psittaciformes	Cacatuidae	Cockatiel
Rhea americana	Rheiformes	Rheidae	Greater rhea
Otus scops	Strigiformes	Strigidae	Eurasian scops owl
Asio otus			Long-eared owl
Strix aluco			Tawny owl
Tyto alba		Tytonidae	Barn owl
Struthio camelus	Struthioniformes	Struthionidae	Common ostrich
Phalacrocorax carbo	Suliformes	Phalacrocoracidae	Great cormorant
Morus bassanus		Sulidae	Northern gannet
† *Allosaurus fragilis*	Saurischia	† Allosauridae	Allosaurus
† *Archaeopteryx* cf. *lithographica* 5		† Archaeopterygidae	Archaeopteryx #5 (Eichstätt Specimen)
† *Archaeopteryx* cf. *lithographica* 7		† Archaeopterygidae	Archaeopteryx #7 (Munich Specimen)
† *Archaeopteryx* cf. *lithographica* 9		† Archaeopterygidae	Archaeopteryx #9 (Bürgermeister-Müller)
† *Compsognathus longipes*		† Compsognathidae	Compsognathus
† aff. *Deinonychus antirrhopus*		† Dromaeosauridae	Deinonychus
† *Australovenator wintonensis*		† Neovenatoridae	Australovenator
† *Tenontosaurus tiletti*	† Ornithischia	† Tenontosauridae	Tenontosaurus
† *Brasileodactylus araripensis*	Pterosauria	† ?Anhangueridae	Brasileodactylus
† *Rhamphorhynchus* sp.		† Rhamphorhynchidae	Rhamphorhynchus
Alligator missisipiensis	Crocodilia	Alligatoridae	American alligator
Crocodylus niloticus		Crocodylidae	Nile crocodile

Latin name	Data source (for humerus / ulna where relevant)	Amount of humerus/ulna sets
Buteo buteo	3	1
Accipiter nisus	3 + 4	2
Circus cyaneus	4	1
Anser anser domesticus	ESRF (Collection and data acquisition)	1
† *Alopochen sirabensis*	MdC (Collection) - ESRF (Data acquisition)	1
Anas platyrhynchos	3	1
Cygnus olor	3	1
Anas clypeata	3	1
Aythya fuligula	3	1
Apteryx australis	MdC (Collection) - ESRF (Data acquisition)	1
Uria aalge	ESRF (Collection and data acquisition) + 3	2
† *Pinguinus impennis*	5	1
† *Mancalla cedrosensis*	5	1
Alca torda	3 + 4	2
Burhinus oedicnemus	4	1
Chroicocephalus ridibundus	4	2
Rissa tridactyla	ESRF (Collection and data acquisition)	1
Larus argentatus	ESRF (Collection and data acquisition)	1
Larus fuscus	3	1
Calidris alpina	4	1
Scolopax rusticola	3	1
Sterna albifrons	4	1
Columba palumbus	4	1
Streptopelia decaocto	ESRF (Collection and data acquisition)	1
Merops apiaster	4	1
Geococcyx californianus	MNHM (Collection) - ESRF (Data acquisition)	1
Falco tinnunculus	3 + 4	2
Colinus virgianus	ESRF (Collection and data acquisition)	1
Phasianus colchicus	ESRF (Collection and data acquisition) + 3 + 4	3
Perdix perdix	3	1
Pavo cristatus	4	1
Meleagris gallopavo	ESRF (Collection and data acquisition)	1
Tetrax tetrax	4	1
Fulica atra	3	1
Musophaga violacea	ESRF (Collection and data acquisition)	1
Opisthocomus hoazin	MNHM (Collection) - ESRF (Data acquisition)	1
Corvus corone	3	1
Pica pica	ESRF (Collection and data acquisition)	1
Erythrura trichroa	ESRF (Collection and data acquisition)	1
Fringilla coelebs	ESRF (Collection and data acquisition)	1
Cyanistes caeruleus	ESRF (Collection and data acquisition)	1
Passer domesticus	ESRF (Collection and data acquisition)	1
Sylvia atricapilla	ESRF (Collection and data acquisition)	1
Bubulcus ibis	ESRF (Collection and data acquisition)	1
Threskiornis aethiopicus	ESRF (Collection and data acquisition)	1
Picus viridis	ESRF (Collection and data acquisition) + 4	3 (1 composite of 2 individuals)
Podiceps cristatus	3	1
Diomedea sanfordi	MoE (Collection) - ESRF (Data acquisition)	1
Thalassarche melanophris	3	1
Procellaria aequinoctialis	3	1
Macronectes giganteus	MoE (Collection) - ESRF (Data acquisition)	1
Nymphicus hollandicus	4	1
Rhea americana	MdC (Collection) - ESRF (Data acquisition)	1
Otus scops	4	2
Asio otus	3 + 4	2 (1 composite of 2 individuals)
Strix aluco	ESRF (Collection and data acquisition)	1
Tyto alba	3 + 4	3
Struthio camelus	MdC (Collection) - ESRF (Data acquisition)	1
Phalacrocorax carbo	3	1
Morus bassanus	ESRF (Collection and data acquisition)	1
† *Allosaurus fragilis*	6	1 (composite of 2 individuals)
† *Archaeopteryx* cf. *lithographica* 5	JM (Collection) - ESRF (Data acquisition)	1 (reconstructed)
† *Archaeopteryx* cf. *lithographica* 7	PMM (Collection) - ESRF (Data acquisition)	1 (reconstructed)
† *Archaeopteryx* cf. *lithographica* 9	BMM (Collection) - ESRF (Data acquisition)	1 (reconstructed, average of 2 sections)
† *Compsognathus longipes*	PMM (Collection) - ESRF (Data acquisition)	1 (reconstructed)
† aff. *Deinonychus antirrhopus*	7 / TUoM (Collection) - ESRF (Data acquisition)	1 (composite of 2 individuals)
† *Australovenator wintonensis*	8	1
† *Tenontosaurus tiletti*	9	1
† *Brasileodactylus araripensis*	MdC (Collection) - ESRF (Data acquisition)	1
† *Rhamphorhynchus* sp.	MdC (Collection) - ESRF (Data acquisition)	1 (reconstructed)
Alligator missisipiensis	10	1
Crocodylus niloticus	ESRF (Collection and data acquisition)	1

Latin name	Canal density (Can/mm^2) hum.	Canal density (Can/mm^2) ulna	Avg. canal density (Can/mm2)
Buteo buteo	N.A.	N.A.	N.A.
Accipiter nisus	N.A.	N.A.	N.A.
Circus cyaneus	N.A.	N.A.	N.A.
Anser anser domesticus	**85**	**85**	**85**
† *Alopochen sirabensis*	N.A.	N.A.	N.A.
Anas platyrhynchos	N.A.	N.A.	N.A.
Cygnus olor	N.A.	N.A.	N.A.
Anas clypeata	N.A.	N.A.	N.A.
Aythya fuligula	N.A.	N.A.	N.A.
Apteryx australis	N.A.	N.A.	N.A.
Uria aalge	**72**	**80**	**76**
† *Pinguinus impennis*	N.A.	N.A.	N.A.
† *Mancalla cedrosensis*	N.A.	N.A.	N.A.
Alca torda	N.A.	N.A.	N.A.
Burhinus oedicnemus	N.A.	N.A.	N.A.
Chroicocephalus ridibundus	N.A.	N.A.	N.A.
Rissa tridactyla	**115**	**110**	**112**
Larus argentatus	**74**	**72**	**73**
Larus fuscus	N.A.	N.A.	N.A.
Calidris alpina	N.A.	N.A.	N.A.
Scolopax rusticola	N.A.	N.A.	N.A.
Sterna albifrons	N.A.	N.A.	N.A.
Columba palumbus	N.A.	N.A.	N.A.
Streptopelia decaocto	**104**	**105**	**104**
Merops apiaster	N.A.	N.A.	N.A.
Geococcyx californianus	**86**	**59**	**72**
Falco tinnunculus	N.A.	N.A.	N.A.
Colinus virgianus	N.A.	N.A.	N.A.
Phasianus colchicus	**154**	**124**	**139**
Perdix perdix	N.A.	N.A.	N.A.
Pavo cristatus	N.A.	N.A.	N.A.
Meleagris gallopavo	**94**	**81**	**87**
Tetrax tetrax	N.A.	N.A.	N.A.
Fulica atra	N.A.	N.A.	N.A.
Musophaga violacea	N.A.	N.A.	N.A.
Opisthocomus hoazin	**43**	**43**	**43**
Corvus corone	N.A.	N.A.	N.A.
Pica pica	**93**	**91**	**92**
Erythrura trichroa	N.A.	N.A.	N.A.
Fringilla coelebs	N.A.	N.A.	N.A.
Cyanistes caeruleus	N.A.	N.A.	N.A.
Passer domesticus	N.A.	N.A.	N.A.
Sylvia atricapilla	N.A.	N.A.	N.A.
Bubulcus ibis	N.A.	N.A.	N.A.
Threskiornis aethiopicus	N.A.	N.A.	N.A.
Picus viridis	**82**	**65**	**73**
Podiceps cristatus	N.A.	N.A.	N.A.
Diomedea sanfordi	N.A.	N.A.	N.A.
Thalassarche melanophris	N.A.	N.A.	N.A.
Procellaria aequinoctialis	N.A.	N.A.	N.A.
Macronectes giganteus	**76**	**81**	**78**
Nymphicus hollandicus	N.A.	N.A.	N.A.
Rhea americana	N.A.	N.A.	N.A.
Otus scops	N.A.	N.A.	N.A.
Asio otus	N.A.	N.A.	N.A.
Strix aluco	**122**	**110**	**116**
Tyto alba	N.A.	N.A.	N.A.
Struthio camelus	N.A.	N.A.	N.A.
Phalacrocorax carbo	N.A.	N.A.	N.A.
Morus bassanus	**76**	**70**	**73**
† *Allosaurus fragilis*	N.A.	N.A.	N.A.
† *Archaeopteryx* cf. *lithographica* 5	**119**	**112**	**116**
† *Archaeopteryx* cf. *lithographica* 7	N.A.	N.A.	N.A.
† *Archaeopteryx* cf. *lithographica* 9	**67**	**70**	**69**
† *Compsognathus longipes*	N.A.	N.A.	N.A.
† aff. *Deinonychus antirrhopus*	N.A.	**64**	**(64)**
† *Australovenator wintonensis*	N.A.	N.A.	N.A.
† *Tenontosaurus tiletti*	N.A.	N.A.	N.A.
† *Brasileodactylus araripensis*	N.A.	N.A.	N.A.
† *Rhamphorhynchus* sp.	N.A.	N.A.	N.A.
Alligator missisipiensis	N.A.	N.A.	N.A.
Crocodylus niloticus	**6**	**8**	**7**

Latin name	CA/TA humerus	J/M humerus	CA/TA ulna	J/M ulna
Buteo buteo	0.383035066	0.142470356	0.413583006	0.063794466
Accipiter nisus	0.300655437	0.133276952	0.321731984	0.06081476
Circus cyaneus	0.297806989	0.254718644	0.360453964	0.112715254
Anser anser domesticus	0.320338225	0.112677878	0.327976462	0.039011067
† *Alopochen sirabensis*	0.548408306	0.20882475	0.458341555	0.07155945
Anas platyrhynchos	0.490271193	0.113751718	0.485536957	0.046529294
Cygnus olor	0.358655851	0.434599096	0.391145028	0.107586506
Anas clypeata	0.440643446	0.082220217	0.473704525	0.030855776
Aythya fuligula	0.607600488	0.068718318	0.548408398	0.028613542
Apteryx australis	0.72124376	0.003105654	0.854876835	0.000155038
Uria aalge	0.670926142	0.106026183	0.567259963	0.041303126
† *Pinguinus impennis*	0.902703267	0.06394892	0.764363579	0.0342886
† *Mancalla cedrosensis*	0.935270271	0.080194042	0.856210475	0.022028958
Alca torda	0.753547232	0.085292064	0.607273269	0.044660654
Burhinus oedicnemus	0.580563558	0.130077295	0.507866583	0.053463768
Chroicocephalus ridibundus	0.508791209	0.126940701	0.429133557	0.10287062
Rissa tridactyla	0.554714648	0.058847634	0.424184669	0.039560252
Larus argentatus	0.534196309	0.160967185	0.437226693	0.079385009
Larus fuscus	0.551064842	0.152655573	0.414624219	0.095358392
Calidris alpina	0.518215867	0.021755102	0.514529252	0.016673469
Scolopax rusticola	0.532178156	0.058641583	0.479027786	0.027088874
Sterna albifrons	0.565656566	0.042820513	0.529373997	0.031333333
Columba palumbus	0.299424269	0.105967581	0.444505495	0.058715711
Streptopelia decaocto	0.489701572	0.117526115	0.559247124	0.043961146
Merops apiaster	0.439232409	0.034263158	0.410895155	0.024649123
Geococcyx californianus	0.433332002	0.028949734	0.370949491	0.016216489
Falco tinnunculus	0.399314864	0.115288846	0.414768911	0.062782337
Colinus virgianus	0.453819909	0.026035567	0.553519278	0.009712371
Phasianus colchicus	0.410823191	0.085017843	0.486188793	0.033276177
Perdix perdix	0.538094287	0.031415041	0.603000943	0.009773577
Pavo cristatus	0.354360528	0.0291584	0.452007693	0.0140868
Meleagris gallopavo	0.327658596	0.152917609	0.38961981	0.05951776
Tetrax tetrax	0.433741912	0.150852399	0.492226912	0.041439114
Fulica atra	0.602213904	0.025979572	0.414468297	0.01337723
Musophaga violacea	0.276482635	0.041950556	0.295961883	0.025294722
Opisthocomus hoazin	0.284945867	0.139051867	0.369740441	0.0630188
Corvus corone	0.384128129	0.138617093	0.432241279	0.092254072
Pica pica	0.383406853	0.066341011	0.405470745	0.045110674
Erythrura trichroa	0.464590701	0.011071429	0.404057805	0.005528571
Fringilla coelebs	0.368339971	0.033294686	0.348201575	0.019710145
Cyanistes caeruleus	0.414559647	0.014446602	0.37389358	0.009075728
Passer domesticus	0.411440914	0.008565217	0.367062421	0.0046917
Sylvia atricapilla	0.388594944	0.014299401	0.375	0.007676647
Bubulcus ibis	0.383023174	0.094286667	0.449303139	0.029329231
Threskiornis aethiopicus	0.322832595	0.149934052	0.396315102	0.060651373
Picus viridis	0.383044873	0.072234125	0.422579761	0.038489389
Podiceps cristatus	0.613110355	0.05148274	0.558503079	0.018346826
Diomedea sanfordi	0.377697765	0.7030357	0.498913633	0.160659047
Thalassarche melanophris	0.486403138	0.302450557	0.568863158	0.074272803
Procellaria aequinoctialis	0.76333944	0.11603035	0.672179059	0.0548407
Macronectes giganteus	0.354124218	0.26160119	0.451796696	0.099828989
Nymphicus hollandicus	0.447616369	0.098017241	0.407613135	0.0675
Rhea americana	0.730117368	0.047033748	0.789066788	0.003034757
Otus scops	0.424514512	0.037833333	0.413183028	0.016227273
Asio otus	0.335796545	0.106071854	0.357657727	0.055272209
Strix aluco	0.384493681	0.049850864	0.356673461	0.023331862
Tyto alba	0.32446869	0.120400213	0.410410381	0.046808765
Struthio camelus	0.72891093	0.024803952	0.529364799	0.003883958
Phalacrocorax carbo	0.472168456	0.097557922	0.427702297	0.03712863
Morus bassanus	0.489486786	0.200836949	0.394367176	0.093050441
† *Allosaurus fragilis*	0.764206637	0.397614807	0.942806396	0.167617125
† *Archaeopteryx* cf. *lithographica* 5	0.425933179	0.00750443	0.457776149	0.001947468
† *Archaeopteryx* cf. *lithographica* 7	0.442851336	0.022033858	0.453850325	0.006232677
† *Archaeopteryx* cf. *lithographica* 9	0.398101885	0.031617983	0.421016577	0.00770625
† *Compsognathus longipes*	0.575785507	0.016787931	0.803182837	0.00145931
† aff. *Deinonychus antirrhopus*	0.715489824	0.06575101	0.770907115	0.015714318
† *Australovenator wintonensis*	0.789803407	0.498072284	0.580916146	0.037041202
† *Tenontosaurus tiletti*	0.780816679	0.267233485	0.785390822	0.032071554
† *Brasileodactylus araripensis*	0.180680481	0.562860153	0.190413939	0.372418639
† *Rhamphorhynchus* sp.	0.51645331	0.008438947	0.561901654	0.004596842
Alligator missisipiensis	0.922903195	0.0194388	0.876883655	0.004561075
Crocodylus niloticus	0.923589302	0.142029759	0.897568437	0.014148504

Latin name	Locomotor mode (1)	Locomotor mode (2)
Buteo buteo	Gliding/Soaring flight	Flap-gliding flight
Accipiter nisus	Undulating flight	Flap-gliding flight
Circus cyaneus	Gliding/Soaring flight	Soaring flight
Anser anser domesticus	Forward flapping/bounding flight	Continuous flapping flight
† *Alopochen sirabensis*	High frequency flapping flight	Continuous flapping flight
Anas platyrhynchos	High frequency flapping flight	Continuous flapping flight
Cygnus olor	Forward flapping/bounding flight	Continuous flapping flight
Anas clypeata	High frequency flapping flight	Continuous flapping flight
Aythya fuligula	High frequency flapping flight	Continuous flapping flight
Apteryx australis	Non-volant ("Ratite bipedal")	Non-volant ("Ratite bipedal")
Uria aalge	High frequency flapping ("Wing-propelled dive")	Continuous flap ("Wing-propelled diving")
† *Pinguinus impennis*	Non-volant ("Wing-propelled dive")	Non-volant ("Wing-propelled diving")
† *Mancalla cedrosensis*	Non-volant ("Wing-propelled dive")	Non-volant ("Wing-propelled diving")
Alca torda	High frequency flapping ("Wing-propelled dive")	Continuous flap ("Wing-propelled diving")
Burhinus oedicnemus	Forward flapping/bounding flight	Continuous flapping flight
Chroicocephalus ridibundus	Gliding/Soaring flight	Flap-gliding flight
Rissa tridactyla	Gliding/Soaring flight	Flap-gliding flight
Larus argentatus	Gliding/Soaring flight	Flap-gliding flight
Larus fuscus	Gliding/Soaring flight	Flap-gliding flight
Calidris alpina	Forward flapping/bounding flight	Continuous flapping flight
Scolopax rusticola	Forward flapping/bounding flight	Continuous flapping flight
Sterna albifrons	Gliding/Soaring flight	Flap-gliding flight
Columba palumbus	Forward flapping/bounding flight	Continuous flapping flight
Streptopelia decaocto	Forward flapping/bounding flight	Continuous flapping flight
Merops apiaster	Forward flapping/bounding flight	Flap-gliding flight
Geococcyx californianus	Short flight	Burst flight
Falco tinnunculus	Undulating flight	Flap-gliding flight
Colinus virgianus	Short flight	Burst flight
Phasianus colchicus	Short flight	Burst flight
Perdix perdix	Short flight	Burst flight
Pavo cristatus	Short flight	Burst flight
Meleagris gallopavo	Short flight	Burst flight
Tetrax tetrax	Undulating flight	Continuous flapping flight
Fulica atra	High frequency flapping flight	Continuous flapping flight
Musophaga violacea	Short flight	Burst flight
Opisthocomus hoazin	Short flight	Burst flight
Corvus corone	Undulating flight	Flap-gliding flight
Pica pica	Undulating flight	Continuous flapping flight
Erythrura trichroa	Forward flapping/bounding flight	Bounding flight
Fringilla coelebs	Forward flapping/bounding flight	Bounding flight
Cyanistes caeruleus	Forward flapping/bounding flight	Bounding flight
Passer domesticus	Forward flapping/bounding flight	Bounding flight
Sylvia atricapilla	Forward flapping/bounding flight	Bounding flight
Bubulcus ibis	Undulating flight	Flap-gliding flight
Threskiornis aethiopicus	Undulating flight	Flap-gliding flight
Picus viridis	Forward flapping/bounding flight	Bounding flight
Podiceps cristatus	High frequency flapping flight	Continuous flapping flight
Diomedea sanfordi	Undulating flight	Soaring flight
Thalassarche melanophris	Undulating flight	Soaring flight
Procellaria aequinoctialis	Undulating flight	Soaring flight
Macronectes giganteus	Undulating flight	Soaring flight
Nymphicus hollandicus	Forward flapping/bounding flight	Continuous flapping flight
Rhea americana	Non-volant ("Ratite bipedal")	Non-volant ("Ratite bipedal")
Otus scops	Undulating flight	Continuous flapping flight
Asio otus	Undulating flight	Flap-gliding flight
Strix aluco	Undulating flight	Flap-gliding flight
Tyto alba	Undulating flight	Flap-gliding flight
Struthio camelus	Non-volant ("Ratite bipedal")	Non-volant ("Ratite bipedal")
Phalacrocorax carbo	Undulating flight	Continuous flapping flight
Morus bassanus	Undulating flight	Soaring flight
† *Allosaurus fragilis*	Non-volant ("Dinosaurian bipedal")	Non-volant ("Dinosaurian bipedal")
† *Archaeopteryx* cf. *lithographica* 5	Archaeopteryx (unknown)	Archaeopteryx (unknown)
† *Archaeopteryx* cf. *lithographica* 7	Archaeopteryx (unknown)	Archaeopteryx (unknown)
† *Archaeopteryx* cf. *lithographica* 9	Archaeopteryx (unknown)	Archaeopteryx (unknown)
† *Compsognathus longipes*	Non-volant ("Dinosaurian bipedal")	Non-volant ("Dinosaurian bipedal")
† aff. *Deinonychus antirrhopus*	Non-volant ("Dinosaurian bipedal")	Non-volant ("Dinosaurian bipedal")
† *Australovenator wintonensis*	Non-volant ("Dinosaurian bipedal")	Non-volant ("Dinosaurian bipedal")
† *Tenontosaurus tiletti*	Non-volant ("Dinosaurian omnipedal")	Non-volant ("Dinosaurian omnipedal")
† *Brasileodactylus araripensis*	Volant ("Short-tailed pterosaurian flight")	Volant ("Short-tailed pterosaurian flight")
† *Rhamphorhynchus* sp.	Volant ("Long-tailed pterosaurian flight")	Volant ("Long-tailed pterosaurian flight")
Alligator missisipiensis	Non-volant ("Crocodilian quadrupedal")	Non-volant ("Crocodilian quadrupedal")
Crocodylus niloticus	Non-volant ("Crocodilian quadrupedal")	Non-volant ("Crocodilian quadrupedal")

Latin name	Body mass humerus (/ulna if divergent)	Source body mass
Buteo buteo	1012	Species average (11)
Accipiter nisus	148	Weighed (12) / Species average (11)
Circus cyaneus	295	Weighed (12)
Anser anser domesticus	9000	Species average (Embden goose; 11)
† *Alopochen sirabensis*	2000	Reconstructed through species average *Alopochen aegyptiacus* (13, 11)
Anas platyrhynchos	1048	Species average (11)
Cygnus olor	8300	Species average (11)
Anas clypeata	554	Species average (11)
Aythya fuligula	701.5	Species average (11)
Apteryx australis	2600	Species average (11)
Uria aalge	992	Species average (11)
† *Pinguinus impennis*	5000	Species average (14)
† *Mancalla cedrosensis*	2400	Species average (14)
Alca torda	607.5	Weighed (12) / Species average (11)
Burhinus oedicnemus	207	Weighed (12)
Chroicocephalus ridibundus	185.5	Weighed (12)
Rissa tridactyla	317	Species average (11)
Larus argentatus	1094	Species average (11)
Larus fuscus	766.2	Species average (11)
Calidris alpina	49	Weighed (12)
Scolopax rusticola	308.3	Species average (11)
Sterna albifrons	39	Weighed (12)
Columba palumbus	401	Weighed (12)
Streptopelia decaocto	157	Species average (11)
Merops apiaster	57	Weighed (12)
Geococcyx californianus	376	Species average (11)
Falco tinnunculus	176	Weighed (12)
Colinus virgianus	194	Species average (11)
Phasianus colchicus	1005.33	Weighed (12) / Species average (11)
Perdix perdix	492	Species average (11)
Pavo cristatus	4200	Species average (11)
Meleagris gallopavo	35000	Weighed (P. Tafforeau)
Tetrax tetrax	271	Weighed (12)
Fulica atra	734.3	Species average (11)
Musophaga violacea	360	Species average (15)
Opisthocomus hoazin	750	Species average (16)
Corvus corone	472.7	Species average (11)
Pica pica	178	Species average (11)
Erythrura trichroa	14	Species average (15)
Fringilla coelebs	20.7	Species average (11)
Cyanistes caeruleus	10.3	Species average (11)
Passer domesticus	25.3	Species average (11)
Sylvia atricapilla	16.7	Species average (11)
Bubulcus ibis	390	Species average (11)
Threskiornis aethiopicus	1530	Species average (11)
Picus viridis	154.67 / 164	Weighed (12) / Species average (11)
Podiceps cristatus	738.7	Species average (11)
Diomedea sanfordi	7577	Species average (15)
Thalassarche melanophris	3232	Species average (11)
Procellaria aequinoctialis	1285	Species average (15)
Macronectes giganteus	3698	Species average (11)
Nymphicus hollandicus	58	Weighed (12)
Rhea americana	23000	Species average (11)
Otus scops	66	Weighed (12)
Asio otus	257 / 227.5	Weighed (12) / Species average (11)
Strix aluco	520	Species average (11)
Tyto alba	359.33	Weighed (12) / Species average (11)
Struthio camelus	111000	Species average (11)
Phalacrocorax carbo	3629	Species average (11)
Morus bassanus	2950	Species average (11)
† *Allosaurus fragilis*	789000 / 984000	Reconstructed (6)
† *Archaeopteryx* cf. *lithographica* 5	158	Reconstructed (17)
† *Archaeopteryx* cf. *lithographica* 7	254	Reconstructed (17)
† *Archaeopteryx* cf. *lithographica* 9	456	Reconstructed (17)
† *Compsognathus longipes*	580	Reconstructed (18)
† aff. *Deinonychus antirrhopus*	60000	Reconstructed (19)
† *Australovenator wintonensis*	500000	Reconstructed (19)
† *Tenontosaurus tiletti*	600000	Reconstructed (19)
† *Brasileodactylus araripensis*	6540	Reconstructed through comparative material (20-23)
† *Rhamphorhynchus* sp.	95	Reconstructed (24)
Alligator missisipiensis	14469	Reconstructed through body length - body mass relationship (25)
Crocodylus niloticus	149227	Reconstructed through body length - body mass relationship (26)

Appendix IV: Supplementary Data 2 for "Wing bone geometry reveals active flight in *Archaeopteryx*" by Voeten et al.

Multivariate statistics underlying this study. Includes raw pPCA scores, the results of k-means clustering, PAM of pPCA scores, and LDA classification.

Taxon (specimen)	K-means clustering of parameters set to two clusters (K=2)	
	Volant (1) / Non-volant (2)	K-means clusters (1 / 2)
Accipiter nisus	1	1
Alca torda	1	2
Alligator mississippiensis	2	2
Allosaurus fragilis	2	2
Alopochen sirabensis	1	1
Anas clypeata	1	1
Anas platyrhynchos	1	1
Anser anser domesticus	1	1
Apteryx australis	2	2
Asio otus	1	1
Australovenator wintonensis	2	2
Aythya fuligula	1	1
Brasileodactylus araripensis	1	1
Bubulcus ibis	1	1
Burhinus oedicnemus	1	1
Buteo buteo	1	1
Calidris alpina	1	1
Chroicocephalus ridibundus	1	1
Circus cyaneus	1	1
Colinus virgianus	1	1
Columba palumbus	1	1
Compsognathus longipes	2	2
Corvus corone	1	1
Crocodylus niloticus	2	2
Cyanistes caeruleus	1	1
Cygnus olor	1	1
Deinonychus antirrhopus	2	2
Diomedea sanfordi	1	1
Erythrura trichroa	1	1
Falco tinnunculus	1	1
Fringilla coelebs	1	1
Fulica atra	1	1
Geococcyx californianus	1	1
Larus argentatus	1	1
Larus fuscus	1	1
Macronectes giganteus	1	1
Mancalla cedrosensis	2	2
Meleagris gallopavo	1	1
Merops apiaster	1	1
Morus bassanus	1	1
Musophaga violacea	1	1
Nymphicus hollandicus	1	1
Opisthocomus hoazin	1	1
Otus scops	1	1
Passer domesticus	1	1
Pavo cristatus	1	1
Perdix perdix	1	1
Phalacrocorax carbo	1	1
Phasianus colchicus	1	1
Pica pica	1	1
Picus viridis	1	1
Pinguinus impennis	2	2
Podiceps cristatus	1	1
Procellaria aequinoctialis	1	2
Rhamphorhynchus sp.	1	1
Rhea americana	2	2
Rissa tridactyla	1	1
Scolopax rusticola	1	1
Sterna albifrons	1	1
Streptopelia decaocto	1	1
Strix aluco	1	1
Struthio camelus	2	2
Sylvia atricapilla	1	1
Tenontosaurus tilletti	2	2
Tetrax tetrax	1	1
Thalassarche melanophris	1	1
Threskiornis aethiopicus	1	1
Tyto alba	1	1
Uria aalge	1	2

Archaeopteryx (#5)	?	1
Archaeopteryx (#7)	?	1
Archaeopteryx (#9)	?	1

Correctly grouped as Volant (1) or Non-Volant (2)
Incorrectly grouped as Non-Volant (2)
Grouping of *Archaeopteryx* specimens (with 1; Volant)

Taxon (specimen)	pPC scores		
	pPC1	pPC2	pPC3
Accipiter nisus	-8.143251606	10.94049717	-0.086793012
Alca torda	4.208419633	3.069670796	0.866415095
Alligator mississippiensis	14.29189979	0.465597628	0.197489669
Allosaurus fragilis	-4.594206526	-16.70314377	2.406447571
Alopochen sirabensis	-5.056440212	3.352664908	-1.082836116
Anas clypeata	-1.130497027	9.680378675	-0.636747349
Anas platyrhynchos	-1.886601299	7.302048515	-0.236878807
Anser anser domesticus	-6.074099022	12.2468877	-1.267049152
Apteryx australis	11.87087968	3.831753105	0.19251194
Asio otus	-6.212556288	10.92633107	0.377464867
Australovenator wintonensis	-4.374999649	-7.080080595	-12.47076576
Aythya fuligula	2.657786191	6.974484995	-0.17104097
Brasileodactylus araripensis	-39.16648017	-12.3991948	12.60890774
Bubulcus ibis	-2.448138169	10.52031718	-1.214840298
Burhinus oedicnemus	-1.100270425	5.110805378	-0.065056981
Buteo buteo	-6.034220862	8.106852256	0.12612713
Calidris alpina	2.675183008	10.37844791	0.149138823
Chroicocephalus ridibundus	-6.023001699	4.781182911	3.977475173
Circus cyaneus	-13.27260681	4.602639629	0.644034804
Colinus virgianus	2.703207306	10.75349718	-0.505793265
Columba palumbus	-5.59312544	9.78261939	0.853040191
Compsognathus longipes	8.76640187	7.357749977	-0.283589902
Corvus corone	-7.294636171	6.439951427	2.681227983
Crocodylus niloticus	11.35246827	-3.493910352	-2.705890478
Cyanistes caeruleus	-0.226957543	14.43505255	-0.630185869
Cygnus olor	-15.67147511	-0.93661669	-5.20503459
Deinonychus antirrhopus	8.253573171	2.858276753	-0.612543278
Diomedea sanfordi	-22.78372344	-12.45536412	-8.714271695
Erythrura trichroa	1.175895247	13.62854395	-0.735321628
Falco tinnunculus	-5.139586832	8.641900326	0.883626388
Fringilla coelebs	-2.26162198	14.36820465	-0.391308666
Fulica atra	2.396876255	11.06243924	-0.450434321
Geococcyx californianus	-0.751054498	13.52727801	-0.472840407
Larus argentatus	-4.958422408	4.681987068	0.988127304
Larus fuscus	-5.808460111	4.244797592	2.542101501
Macronectes giganteus	-10.55541667	2.951975587	-0.418968389
Mancalla cedrosensis	11.79944967	-1.78900886	-0.237157815
Meleagris gallopavo	-7.120937675	9.095011683	-0.631738184
Merops apiaster	-0.675650111	12.24896798	0.167207107
Morus bassanus	-7.869298703	4.182524174	0.799168296
Musophaga violacea	-4.790915261	15.78295478	-0.344547536
Nymphicus hollandicus	-4.489597891	8.38958446	1.813823665
Opisthocomus hoazin	-7.887946875	10.09237697	0.024463361
Otus scops	-0.432200574	12.72367383	-0.651627021
Passer domesticus	0.011185389	14.95548913	-0.835592895
Pavo cristatus	-0.475698163	13.25381032	-0.506776122
Perdix perdix	4.454128638	8.825951962	-0.517282672
Phalacrocorax carbo	-2.098193326	9.338896193	-0.670795982
Phasianus colchicus	-1.544413809	9.634972626	-0.502962282
Pica pica	-3.393423212	11.12963578	0.869424365
Picus viridis	-2.889992782	11.04584423	0.170681628
Pinguinus impennis	9.636119862	-0.138407631	1.068924017
Podiceps cristatus	3.855435408	7.710985065	-0.481082488
Procellaria aequinoctialis	4.04862917	0.605629372	0.932744283
Rhamphorhynchus sp.	4.352559846	10.59257838	-0.351346148
Rhea americana	9.866355306	3.518702557	-1.057919217
Rissa tridactyla	-0.329137268	9.289408107	0.746869409
Scolopax rusticola	0.914995225	9.31291626	-0.180336143
Sterna albifrons	2.224440793	8.296203636	0.790465248
Streptopelia decaocto	-0.72323234	6.156756602	-0.400779965
Strix aluco	-2.49201875	13.43455817	-0.567980612
Struthio camelus	6.394091134	8.237973607	-0.897759817
Sylvia atricapilla	-0.474783339	14.79754802	-0.751756037
Tenontosaurus tilletti	3.956299709	-4.120334443	-5.351379683
Tetrax tetrax	-3.070272204	7.171411865	-1.810678092
Thalassarche melanophris	-6.452830077	-0.226224838	-3.49823434
Threskiornis aethiopicus	-7.084649212	9.062265231	-0.431699852
Tyto alba	-5.401313282	10.27626073	-0.658118487
Uria aalge	2.235231558	4.32695281	-0.177458998

Archaeopteryx (#5)	1.748717628	13.49183709	-0.821013807
Archaeopteryx (#7)	1.349003557	12.7666816	-0.907699104
Archaeopteryx (#9)	-0.040639275	13.50139651	-1.171157361

Taxon (specimen)	Partitioning Around Medoids of pPC scores	
	Volant (1) / Non-volant (2)	PAM grouping (1 / 2)
Accipiter nisus	1	1
Alca torda	1	2
Alligator mississippiensis	2	2
Allosaurus fragilis	2	2
Alopochen sirabensis	1	1
Anas clypeata	1	1
Anas platyrhynchos	1	1
Anser anser domesticus	1	1
Apteryx australis	2	2
Asio otus	1	1
Australovenator wintonensis	2	2
Aythya fuligula	1	1
Brasileodactylus araripensis	1	1
Bubulcus ibis	1	1
Burhinus oedicnemus	1	1
Buteo buteo	1	1
Calidris alpina	1	1
Chroicocephalus ridibundus	1	1
Circus cyaneus	1	1
Colinus virgianus	1	1
Columba palumbus	1	1
Compsognathus longipes	2	2
Corvus corone	1	1
Crocodylus niloticus	2	2
Cyanistes caeruleus	1	1
Cygnus olor	1	1
Deinonychus antirrhopus	2	2
Diomedea sanfordi	1	1
Erythrura trichroa	1	1
Falco tinnunculus	1	1
Fringilla coelebs	1	1
Fulica atra	1	1
Geococcyx californianus	1	1
Larus argentatus	1	1
Larus fuscus	1	1
Macronectes giganteus	1	1
Mancalla cedrosensis	2	2
Meleagris gallopavo	1	1
Merops apiaster	1	1
Morus bassanus	1	1
Musophaga violacea	1	1
Nymphicus hollandicus	1	1
Opisthocomus hoazin	1	1
Otus scops	1	1
Passer domesticus	1	1
Pavo cristatus	1	1
Perdix perdix	1	1
Phalacrocorax carbo	1	1
Phasianus colchicus	1	1
Pica pica	1	1
Picus viridis	1	1
Pinguinus impennis	2	2
Podiceps cristatus	1	1
Procellaria aequinoctialis	2	2
Rhamphorhynchus sp.	1	1
Rhea americana	2	2
Rissa tridactyla	1	1
Scolopax rusticola	1	1
Sterna albifrons	1	1
Streptopelia decaocto	1	1
Strix aluco	1	1
Struthio camelus	2	2
Sylvia atricapilla	1	1
Tenontosaurus tilletti	2	2
Tetrax tetrax	1	1
Thalassarche melanophris	1	1
Threskiornis aethiopicus	1	1
Tyto alba	1	1
Uria aalge	1	2

Archaeopteryx (#5)	?	1
Archaeopteryx (#7)	?	1
Archaeopteryx (#9)	?	1

Correctly grouped as Volant (1) or Non-Volant (2)
Incorrectly grouped as Non-Volant (2)
Grouping of *Archaeopteryx* specimens (with 1; Volant)

Taxon (specimen)	Linear Discriminant Analysis - Classification	
	Given group Viscor et al. (1)	Classification Viscor et al. (1)
Accipiter nisus	Undulating flight	Undulating flight
Alca torda	High frequency flapping ("Wing-propelled dive")	High frequency flapping ("Wing-propelled dive")
Alligator mississippiensis	Non-volant ("Crocodilian quadrupedal")	Non-volant ("Crocodilian quadrupedal")
Allosaurus fragilis	Non-volant ("Dinosaurian bipedal")	Non-volant ("Dinosaurian bipedal")
Alopochen sirabensis	High frequency flapping flight	Gliding/Soaring flight
Anas clypeata	High frequency flapping flight	Short flight
Anas platyrhynchos	High frequency flapping flight	High frequency flapping flight
Anser anser domesticus	Forward flapping/bounding flight	Forward flapping/bounding flight
Apteryx australis	Non-volant ("Ratite bipedal")	Non-volant ("Ratite bipedal")
Asio otus	Undulating flight	Undulating flight
Australovenator wintonensis	Non-volant ("Dinosaurian bipedal")	Non-volant ("Dinosaurian omnipedal")
Aythya fuligula	High frequency flapping flight	High frequency flapping flight
Brasileodactylus araripensis	Short-tailed pterosaurian flight	Short-tailed pterosaurian flight
Bubulcus ibis	Undulating flight	Short flight
Burhinus oedicnemus	Forward flapping/bounding flight	High frequency flapping flight
Buteo buteo	Gliding/Soaring flight	Undulating flight
Calidris alpina	Forward flapping/bounding flight	Long-tailed pterosaurian flight
Chroicocephalus ridibundus	Gliding/Soaring flight	Gliding/Soaring flight
Circus cyaneus	Gliding/Soaring flight	Undulating flight
Colinus virgianus	Short flight	Long-tailed pterosaurian flight
Columba palumbus	Forward flapping/bounding flight	Short flight
Compsognathus longipes	Non-volant ("Dinosaurian bipedal")	High frequency flapping ("Wing-propelled dive")
Corvus corone	Undulating flight	Gliding/Soaring flight
Crocodylus niloticus	Non-volant ("Crocodilian quadrupedal")	Non-volant ("Crocodilian quadrupedal")
Cyanistes caeruleus	Forward flapping/bounding flight	Forward flapping/bounding flight
Cygnus olor	Forward flapping/bounding flight	Undulating flight
Deinonychus antirrhopus	Non-volant ("Dinosaurian bipedal")	Non-volant ("Ratite bipedal")
Diomedea sanfordi	Undulating flight	Undulating flight
Erythrura trichroa	Forward flapping/bounding flight	Forward flapping/bounding flight
Falco tinnunculus	Undulating flight	Undulating flight
Fringilla coelebs	Forward flapping/bounding flight	Forward flapping/bounding flight
Fulica atra	High frequency flapping flight	High frequency flapping flight
Geococcyx californianus	Short flight	Forward flapping/bounding flight
Larus argentatus	Gliding/Soaring flight	Gliding/Soaring flight
Larus fuscus	Gliding/Soaring flight	Gliding/Soaring flight
Macronectes giganteus	Undulating flight	Undulating flight
Mancalla cedrosensis	Non-volant ("Wing-propelled dive")	Non-volant ("Wing-propelled dive")
Meleagris gallopavo	Short flight	Undulating flight
Merops apiaster	Forward flapping/bounding flight	Forward flapping/bounding flight
Morus bassanus	Undulating flight	Gliding/Soaring flight
Musophaga violacea	Short flight	Short flight
Nymphicus hollandicus	Forward flapping/bounding flight	Gliding/Soaring flight
Opisthocomus hoazin	Short flight	Undulating flight
Otus scops	Undulating flight	Forward flapping/bounding flight
Passer domesticus	Forward flapping/bounding flight	Forward flapping/bounding flight
Pavo cristatus	Short flight	Short flight
Perdix perdix	Short flight	Long-tailed pterosaurian flight
Phalacrocorax carbo	Undulating flight	Forward flapping/bounding flight
Phasianus colchicus	Short flight	Short flight
Pica pica	Undulating flight	Forward flapping/bounding flight
Picus viridis	Forward flapping/bounding flight	Short flight
Pinguinus impennis	Non-volant ("Wing-propelled dive")	Non-volant ("Wing-propelled dive")
Podiceps cristatus	High frequency flapping flight	High frequency flapping flight
Procellaria aequinoctialis	Undulating flight	High frequency flapping ("Wing-propelled dive")
Rhamphorhynchus sp.	Long-tailed pterosaurian flight	Long-tailed pterosaurian flight
Rhea americana	Non-volant ("Ratite bipedal")	Non-volant ("Ratite bipedal")
Rissa tridactyla	Gliding/Soaring flight	High frequency flapping flight
Scolopax rusticola	Forward flapping/bounding flight	High frequency flapping flight
Sterna albifrons	Gliding/Soaring flight	High frequency flapping flight
Streptopelia decaocto	Forward flapping/bounding flight	Long-tailed pterosaurian flight
Strix aluco	Undulating flight	Forward flapping/bounding flight
Struthio camelus	Non-volant ("Ratite bipedal")	High frequency flapping ("Wing-propelled dive")
Sylvia atricapilla	Forward flapping/bounding flight	Short flight
Tenontosaurus tilletti	Non-volant ("Dinosaurian omnipedal")	Non-volant ("Dinosaurian omnipedal")
Tetrax tetrax	Undulating flight	Short flight
Thalassarche melanophris	Undulating flight	Undulating flight
Threskiornis aethiopicus	Undulating flight	Undulating flight
Tyto alba	Undulating flight	Short flight
Uria aalge	High frequency flapping ("Wing-propelled dive")	High frequency flapping ("Wing-propelled dive")
Archaeopteryx (#5)	?	Short flight
Archaeopteryx (#7)	?	Short flight
Archaeopteryx (#9)	?	Short flight

Correctly classified locomotor mode
Misclassified locomotor mode
Retrodicted locomotor mode

Taxon (specimen)	Linear Discriminant Analysis - Classification	
	Given group Close et al. (2)	Classification Close et al. (2)
Accipiter nisus	Flap-gliding flight	Flap-gliding flight
Alca torda	Continuous flap ("Wing-propelled diving")	Continuous flap ("Wing-propelled diving")
Alligator mississippiensis	Non-volant ("Crocodilian quadrupedal")	Non-volant ("Crocodilian quadrupedal")
Allosaurus fragilis	Non-volant ("Dinosaurian bipedal")	Non-volant ("Dinosaurian bipedal")
Alopochen sirabensis	Continuous flapping flight	Soaring flight
Anas clypeata	Continuous flapping flight	Burst flight
Anas platyrhynchos	Continuous flapping flight	Continuous flapping flight
Anser anser domesticus	Continuous flapping flight	Bounding flight
Apteryx australis	Non-volant ("Ratite bipedal")	Non-volant ("Ratite bipedal")
Asio otus	Flap-gliding flight	Flap-gliding flight
Australovenator wintonensis	Non-volant ("Dinosaurian bipedal")	Non-volant ("Dinosaurian omnipedal")
Aythya fuligula	Continuous flapping flight	Continuous flapping flight
Brasileodactylus araripensis	Short-tailed pterosaurian flight	Short-tailed pterosaurian flight
Bubulcus ibis	Flap-gliding flight	Burst flight
Burhinus oedicnemus	Continuous flapping flight	Continuous flapping flight
Buteo buteo	Flap-gliding flight	Flap-gliding flight
Calidris alpina	Continuous flapping flight	Long-tailed pterosaurian flight
Chroicocephalus ridibundus	Flap-gliding flight	Flap-gliding flight
Circus cyaneus	Soaring flight	Flap-gliding flight
Colinus virgianus	Burst flight	Long-tailed pterosaurian flight
Columba palumbus	Continuous flapping flight	Burst flight
Compsognathus longipes	Non-volant ("Dinosaurian bipedal")	Continuous flap ("Wing-propelled diving")
Corvus corone	Flap-gliding flight	Flap-gliding flight
Crocodylus niloticus	Non-volant ("Crocodilian quadrupedal")	Non-volant ("Crocodilian quadrupedal")
Cyanistes caeruleus	Bounding flight	Bounding flight
Cygnus olor	Continuous flapping flight	Soaring flight
Deinonychus antirrhopus	Non-volant ("Dinosaurian bipedal")	Non-volant ("Ratite bipedal")
Diomedea sanfordi	Soaring flight	Soaring flight
Erythrura trichroa	Bounding flight	Bounding flight
Falco tinnunculus	Flap-gliding flight	Flap-gliding flight
Fringilla coelebs	Bounding flight	Bounding flight
Fulica atra	Continuous flapping flight	Continuous flapping flight
Geococcyx californianus	Burst flight	Bounding flight
Larus argentatus	Flap-gliding flight	Flap-gliding flight
Larus fuscus	Flap-gliding flight	Flap-gliding flight
Macronectes giganteus	Soaring flight	Soaring flight
Mancalla cedrosensis	Non-volant ("Wing-propelled diving")	Non-volant ("Wing-propelled diving")
Meleagris gallopavo	Burst flight	Flap-gliding flight
Merops apiaster	Flap-gliding flight	Bounding flight
Morus bassanus	Soaring flight	Flap-gliding flight
Musophaga violacea	Burst flight	Bounding flight
Nymphicus hollandicus	Continuous flapping flight	Flap-gliding flight
Opisthocomus hoazin	Burst flight	Flap-gliding flight
Otus scops	Continuous flapping flight	Bounding flight
Passer domesticus	Bounding flight	Bounding flight
Pavo cristatus	Burst flight	Burst flight
Perdix perdix	Burst flight	Long-tailed pterosaurian flight
Phalacrocorax carbo	Continuous flapping flight	Continuous flapping flight
Phasianus colchicus	Burst flight	Burst flight
Pica pica	Flap-gliding flight	Flap-gliding flight
Picus viridis	Bounding flight	Burst flight
Pinguinus impennis	Non-volant ("Wing-propelled diving")	Non-volant ("Wing-propelled diving")
Podiceps cristatus	Continuous flapping flight	Continuous flapping flight
Procellaria aequinoctialis	Soaring flight	Continuous flap ("Wing-propelled diving")
Rhamphorhynchus sp.	Long-tailed pterosaurian flight	Long-tailed pterosaurian flight
Rhea americana	Non-volant ("Ratite bipedal")	Non-volant ("Ratite bipedal")
Rissa tridactyla	Flap-gliding flight	Continuous flapping flight
Scolopax rusticola	Continuous flapping flight	Continuous flapping flight
Sterna albifrons	Flap-gliding flight	Continuous flapping flight
Streptopelia decaocto	Continuous flapping flight	Continuous flapping flight
Strix aluco	Flap-gliding flight	Bounding flight
Struthio camelus	Non-volant ("Ratite bipedal")	Continuous flap ("Wing-propelled diving")
Sylvia atricapilla	Bounding flight	Bounding flight
Tenontosaurus tilletti	Non-volant ("Dinosaurian omnipedal")	Non-volant ("Dinosaurian omnipedal")
Tetrax tetrax	Continuous flapping flight	Continuous flapping flight
Thalassarche melanophris	Soaring flight	Soaring flight
Threskiornis aethiopicus	Flap-gliding flight	Burst flight
Tyto alba	Flap-gliding flight	Burst flight
Uria aalge	Continuous flap ("Wing-propelled diving")	Continuous flap ("Wing-propelled diving")
Archaeopteryx (#5)	?	Burst flight
Archaeopteryx (#7)	?	Burst flight
Archaeopteryx (#9)	?	Burst flight

Correctly classified locomotor mode
Misclassified locomotor mode
Retrodicted locomotor mode

Appendix V: Supplementary Data 3 for "Wing bone geometry reveals active flight in *Archaeopteryx*" by Voeten et al.

Data acquisition parameters for synchrotron µCT. Scanning parameters as used on beamlines BM05 and ID19 of the European Synchrotron Radiation Facility.

Species	Element	Voxel size (µm)	Energy (keV)	Filter, mm
† *Alopochen sirabensis*	Humerus	25.37	142	Al, 2.8; Cu, 6.5
† *Alopochen sirabensis*	Ulna	25.37	142	Al, 2.8; Cu, 6.5
Anser anser domesticus	Humerus	6.24	74	Al, 6; W, 0.3
Anser anser domesticus	Ulna	6.24	74	Al, 6; W, 0.3
Apteryx australis	Humerus	25.37	77	Al, 2.8; Au, 0.28
Apteryx australis	Ulna	25.37	77	Al, 2.8; Au, 0.28
Bubulcus ibis	Humerus	4.66	72	Al, 2.8; Cu, 1.4
Bubulcus ibis	Ulna	4.66	72	Al, 2.8; Cu, 1.4
Colinus virgianus	Humerus	4.66	72	Al, 2.8; Cu, 1.4
Colinus virgianus	Ulna	4.66	72	Al, 2.8; Cu, 1.4
Cyanistes caeruleus	Humerus	4.66	72	Al, 2.8; Cu, 1.4
Cyanistes caeruleus	Ulna	4.66	72	Al, 2.8; Cu, 1.4
Erythrura trichroa	Humerus	4.66	72	Al, 2.8; Cu, 1.4
Erythrura trichroa	Ulna	4.66	72	Al, 2.8; Cu, 1.4
Fringilla coelebs	Humerus	4.66	72	Al, 2.8; Cu, 1.4
Fringilla coelebs	Ulna	4.66	72	Al, 2.8; Cu, 1.4
Geococcyx californianus	Humerus	6.26	77	Al, 2; Au, 0.35
Geococcyx californianus	Ulna	6.26	77	Al, 2; Au, 0.35
Larus argentatus	Humerus	6.24	74	Al, 6; W, 0.3
Larus argentatus	Ulna	6.24	74	Al, 6; W, 0.3
Macronectes giganteus	Humerus	6.26	77	Al, 2; Au, 0.35
Macronectes giganteus	Ulna	6.26	77	Al, 2; Au, 0.35
Meleagris gallopavo	Humerus	6.24	74	Al, 6; W, 0.3
Meleagris gallopavo	Ulna	6.24	74	Al, 6; W, 0.3
Morus bassanus	Humerus	6.24	74	Al, 6; W, 0.3
Morus bassanus	Ulna	6.24	74	Al, 6; W, 0.3
Musophaga violacea	Humerus	4.66	72	Al, 2.8; Cu, 1.4
Musophaga violacea	Ulna	4.66	72	Al, 2.8; Cu, 1.4
Opisthocomus hoazin	Humerus	6.31	136	Al, 40; Cu, 3.1; Mo, 0.1
Opisthocomus hoazin	Ulna	6.31	136	Al, 40; Cu, 3.1; Mo, 0.1
Passer domesticus	Humerus	4.66	72	Al, 2.8; Cu, 1.4
Passer domesticus	Ulna	4.66	72	Al, 2.8; Cu, 1.4
Phasianus colchicus	Humerus	6.24	74	Al, 6; W, 0.3
Phasianus colchicus	Ulna	6.24	74	Al, 6; W, 0.3
Pica pica	Humerus	6.24	71	Al, 12; W, 0.15
Pica pica	Ulna	6.24	71	Al, 12; W, 0.15
Picus viridis	Humerus	6.24	81	Alprof, 17; W, 0.3
Picus viridis	Ulna	6.24	81	Alprof, 17; W, 0.3
Rhea americana	Humerus	25.37	142	Al, 2.8; Cu, 6.5
Rhea americana	Ulna	25.37	142	Al, 2.8; Cu, 6.5
Rissa tridactyla	Humerus	6.24	81	Alprof, 17; W, 0.3
Rissa tridactyla	Ulna	6.24	81	Alprof, 17; W, 0.3
Streptopelia decaocto	Humerus	6.24	71	Al, 12; W, 0.15
Streptopelia decaocto	Ulna	6.24	71	Al, 12; W, 0.15
Strix aluco	Humerus	6.24	74	Al, 6; W, 0.3
Strix aluco	Ulna	6.24	74	Al, 6; W, 0.3
Struthio camelus	Humerus	25.37	142	Al, 2.8; Cu, 6.5
Struthio camelus	Ulna	25.37	142	Al, 2.8; Cu, 6.5
Sylvia atricapilla	Humerus	6.26	81	Al, 12; Au, 0.35
Sylvia atricapilla	Ulna	6.26	81	Al, 12; Au, 0.35
Threskiornis aethiopicus	Humerus	4.66	72	Al, 2.8; Cu, 1.4
Threskiornis aethiopicus	Ulna	4.66	72	Al, 2.8; Cu, 1.4
Uria aalge	Humerus	6.25	71	Al, 12; W, 0.15
Uria aalge	Ulna	6.24	71	Al, 12; W, 0.15
† *Archaeopteryx* cf. *lithographica* #5	Humerus	3.11	184	Al, 2.8; Cu, 6; W, 0.5
† *Archaeopteryx* cf. *lithographica* #5	Ulna	3.11	184	Al, 2.8; Cu, 6; W, 0.5
† *Archaeopteryx* cf. *lithographica* #7	Humerus	6.3	137	Al, 5.6; Cu, 6
† *Archaeopteryx* cf. *lithographica* #7	Ulna	6.3	137	Al, 5.6; Cu, 6
† *Archaeopteryx* cf. *lithographica* #9	Humerus	6.56	129	Al, 2.8; Cu, 4
† *Archaeopteryx* cf. *lithographica* #9	Ulna	6.56	129	Al, 2.8; Cu, 4
† *Brasileodactylus araripensis*	Humerus	25.37	103	Al, 2.8; Cu, 6.5
† *Brasileodactylus araripensis*	Ulna	25.37	103	Al, 2.8; Cu, 6.5
† *Compsognathus longipes*	Humerus	6.43	160	Al, 3; Cu, 6
† *Compsognathus longipes*	Ulna	6.43	160	Al, 3; Cu, 6
Crocodylus niloticus	Humerus	12.56	90	Mo 0.3, Au, 0.1
Crocodylus niloticus	Ulna	12.56	90	Mo 0.3, Au, 0.1
† aff. *Deinonychus antirrhopus*	Ulna	6.46	88	Al, 65
† *Rhamphorhynchus* sp.	Humerus	4.24	105	Al, 65 ; Mo, 0.3
† *Rhamphorhynchus* sp.	Ulna	4.24	105	Al, 65 ; Mo, 0.3

Species	Propagation distance (cm)	Camera	Scintillator	Insertion device
† *Alopochen sirabensis*	640	PCO EDGE 5.5	LuAG_2000	W150
† *Alopochen sirabensis*	640	PCO EDGE 5.5	LuAG_2000	W150
Anser anser domesticus	225	PCO EDGE 5.5	LuAG_200	BM
Anser anser domesticus	225	PCO EDGE 5.5	LuAG_200	BM
Apteryx australis	640	PCO EDGE 5.5	LuAG_2000	W150
Apteryx australis	640	PCO EDGE 5.5	LuAG_2000	W150
Bubulcus ibis	130	PCO EDGE 5.5	GGG_100	W150
Bubulcus ibis	130	PCO EDGE 5.5	GGG_100	W150
Colinus virgianus	130	PCO EDGE 5.5	GGG_100	W150
Colinus virgianus	130	PCO EDGE 5.5	GGG_100	W150
Cyanistes caeruleus	130	PCO EDGE 5.5	GGG_100	W150
Cyanistes caeruleus	130	PCO EDGE 5.5	GGG_100	W150
Erythrura trichroa	130	PCO EDGE 5.5	GGG_100	W150
Erythrura trichroa	130	PCO EDGE 5.5	GGG_100	W150
Fringilla coelebs	130	PCO EDGE 5.5	GGG_100	W150
Fringilla coelebs	130	PCO EDGE 5.5	GGG_100	W150
Geococcyx californianus	225	PCO EDGE 5.5	GGG_100	BM
Geococcyx californianus	225	PCO EDGE 5.5	GGG_100	BM
Larus argentatus	225	PCO EDGE 5.5	LuAG_200	BM
Larus argentatus	225	PCO EDGE 5.5	LuAG_200	BM
Macronectes giganteus	225	PCO EDGE 5.5	GGG_100	BM
Macronectes giganteus	225	PCO EDGE 5.5	GGG_100	BM
Meleagris gallopavo	225	PCO EDGE 5.5	LuAG_200	BM
Meleagris gallopavo	225	PCO EDGE 5.5	LuAG_200	BM
Morus bassanus	225	PCO EDGE 5.5	LuAG_200	BM
Morus bassanus	225	PCO EDGE 5.5	LuAG_200	BM
Musophaga violacea	130	PCO EDGE 5.5	GGG_100	W150
Musophaga violacea	130	PCO EDGE 5.5	GGG_100	W150
Opisthocomus hoazin	225	PCO EDGE 5.5	GGG_500	BM
Opisthocomus hoazin	225	PCO EDGE 5.5	GGG_500	BM
Passer domesticus	130	PCO EDGE 5.5	GGG_100	W150
Passer domesticus	130	PCO EDGE 5.5	GGG_100	W150
Phasianus colchicus	225	PCO EDGE 5.5	LuAG_200	BM
Phasianus colchicus	225	PCO EDGE 5.5	LuAG_200	BM
Pica pica	225	PCO EDGE 5.5	LuAG_200	BM
Pica pica	225	PCO EDGE 5.5	LuAG_200	BM
Picus viridis	225	PCO EDGE 5.5	GGG_100	BM
Picus viridis	225	PCO EDGE 5.5	GGG_100	BM
Rhea americana	640	PCO EDGE 5.5	LuAG_2000	W150
Rhea americana	640	PCO EDGE 5.5	LuAG_2000	W150
Rissa tridactyla	225	PCO EDGE 5.5	GGG_100	BM
Rissa tridactyla	225	PCO EDGE 5.5	GGG_100	BM
Streptopelia decaocto	225	PCO EDGE 5.5	LuAG_200	BM
Streptopelia decaocto	225	PCO EDGE 5.5	LuAG_200	BM
Strix aluco	225	PCO EDGE 5.5	LuAG_200	BM
Strix aluco	225	PCO EDGE 5.5	LuAG_200	BM
Struthio camelus	640	PCO EDGE 5.5	LuAG_2000	W150
Struthio camelus	640	PCO EDGE 5.5	LuAG_2000	W150
Sylvia atricapilla	225	PCO EDGE 5.5	GGG_100	BM
Sylvia atricapilla	225	PCO EDGE 5.5	GGG_100	BM
Threskiornis aethiopicus	130	PCO EDGE 5.5	GGG_100	W150
Threskiornis aethiopicus	130	PCO EDGE 5.5	GGG_100	W150
Uria aalge	225	PCO EDGE 5.5	LuAG_200	BM
Uria aalge	225	PCO EDGE 5.5	LuAG_200	BM
† *Archaeopteryx* cf. *lithographica* #5	380	PCO EDGE 5.5	GGG_500	W150
† *Archaeopteryx* cf. *lithographica* #5	380	PCO EDGE 5.5	GGG_500	W150
† *Archaeopteryx* cf. *lithographica* #7	900	PCO EDGE 5.5	LuAG_500	W150
† *Archaeopteryx* cf. *lithographica* #7	900	PCO EDGE 5.5	LuAG_500	W150
† *Archaeopteryx* cf. *lithographica* #9	160	FReLoN 2K14	GGG_500	W150
† *Archaeopteryx* cf. *lithographica* #9	160	FReLoN 2K14	GGG_500	W150
† *Brasileodactylus araripensis*	640	PCO EDGE	LuAG_2000	W150
† *Brasileodactylus araripensis*	640	PCO EDGE	LuAG_2000	W150
† *Compsognathus longipes*	2100	PCO EDGE 5.5	LuAG_500	BM
† *Compsognathus longipes*	2100	PCO EDGE 5.5	LuAG_500	BM
Crocodylus niloticus	200	PCO EDGE	LuAG_500	BM
Crocodylus niloticus	200	PCO EDGE	LuAG_500	BM
† aff. *Deinonychus antirrhopus*	225	PCO EDGE	GGG_100	BM
† *Rhamphorhynchus* sp.	250	PCO EDGE 4.2	LuAG_500	BM
† *Rhamphorhynchus* sp.	250	PCO EDGE 4.2	LuAG_500	BM

Species	Gap (mm)	Number of projections	Accumulation mode, factor	Half-acquisition mode
† *Alopochen sirabensis*	35	6000	NO	YES
† *Alopochen sirabensis*	35	6000	NO	YES
Anser anser domesticus	N.A.	8000	NO	YES
Anser anser domesticus	N.A.	8000	NO	YES
Apteryx australis	56	6000	NO	YES
Apteryx australis	56	6000	NO	YES
Bubulcus ibis	60	6000	NO	NO
Bubulcus ibis	60	6000	NO	NO
Colinus virgianus	60	6000	NO	YES
Colinus virgianus	60	6000	NO	YES
Cyanistes caeruleus	60	6000	NO	YES
Cyanistes caeruleus	60	6000	NO	YES
Erythrura trichroa	60	6000	NO	NO
Erythrura trichroa	60	6000	NO	NO
Fringilla coelebs	60	6000	NO	YES
Fringilla coelebs	60	6000	NO	YES
Geococcyx californianus	N.A.	6000	NO	YES
Geococcyx californianus	N.A.	6000	NO	YES
Larus argentatus	N.A.	3471	NO	YES
Larus argentatus	N.A.	3471	NO	YES
Macronectes giganteus	N.A.	5969	NO	NO
Macronectes giganteus	N.A.	5969	NO	NO
Meleagris gallopavo	N.A.	8000	NO	NO
Meleagris gallopavo	N.A.	8000	NO	NO
Morus bassanus	N.A.	8000	NO	YES
Morus bassanus	N.A.	3471	NO	YES
Musophaga violacea	60	6000	NO	YES
Musophaga violacea	60	6000	NO	YES
Opisthocomus hoazin	N.A.	3471	NO	NO
Opisthocomus hoazin	N.A.	3471	NO	NO
Passer domesticus	60	6000	NO	YES
Passer domesticus	60	6000	NO	YES
Phasianus colchicus	N.A.	3471	NO	YES
Phasianus colchicus	N.A.	3471	NO	YES
Pica pica	N.A.	3471	NO	NO
Pica pica	N.A.	3471	NO	NO
Picus viridis	N.A.	3471	NO	NO
Picus viridis	N.A.	3471	NO	NO
Rhea americana	35	6000	NO	YES
Rhea americana	35	6000	NO	YES
Rissa tridactyla	N.A.	3471	NO	NO
Rissa tridactyla	N.A.	3471	NO	NO
Streptopelia decaocto	N.A.	3471	NO	NO
Streptopelia decaocto	N.A.	3471	NO	NO
Strix aluco	N.A.	3471	NO	YES
Strix aluco	N.A.	3471	NO	YES
Struthio camelus	35	6000	NO	YES
Struthio camelus	35	6000	NO	YES
Sylvia atricapilla	N.A.	5969	NO	NO
Sylvia atricapilla	N.A.	5969	NO	NO
Threskiornis aethiopicus	60	6000	NO	NO
Threskiornis aethiopicus	60	6000	NO	NO
Uria aalge	N.A.	3471	NO	NO
Uria aalge	N.A.	3471	NO	NO
† *Archaeopteryx* cf. *lithographica* #5	26.5	6000	x5	YES
† *Archaeopteryx* cf. *lithographica* #5	26.5	6000	x5	YES
† *Archaeopteryx* cf. *lithographica* #7	26.5	6000	x21	YES
† *Archaeopteryx* cf. *lithographica* #7	26.5	6000	x21	YES
† *Archaeopteryx* cf. *lithographica* #9	26.5	4998	NO	YES
† *Archaeopteryx* cf. *lithographica* #9	26.5	4998	NO	YES
† *Brasileodactylus araripensis*	66	6000	NO	YES
† *Brasileodactylus araripensis*	66	6000	NO	YES
† *Compsognathus longipes*	N.A.	6000	x17	YES
† *Compsognathus longipes*	N.A.	6000	x17	YES
Crocodylus niloticus	N.A.	8000	NO	YES
Crocodylus niloticus	N.A.	8000	NO	YES
† aff. *Deinonychus antirrhopus*	N.A.	6000	NO	YES
† *Rhamphorhynchus* sp.	N.A.	4000	x10	YES
† *Rhamphorhynchus* sp.	N.A.	4000	x10	YES

Species	Exposure time (s)	Beamline
† *Alopochen sirabensis*	0.02	ID19
† *Alopochen sirabensis*	0.02	ID19
Anser anser domesticus	0.045	BM05
Anser anser domesticus	0.045	BM05
Apteryx australis	0.02	ID19
Apteryx australis	0.02	ID19
Bubulcus ibis	0.05	ID19
Bubulcus ibis	0.05	ID19
Colinus virgianus	0.05	ID19
Colinus virgianus	0.05	ID19
Cyanistes caeruleus	0.05	ID19
Cyanistes caeruleus	0.05	ID19
Erythrura trichroa	0.05	ID19
Erythrura trichroa	0.05	ID19
Fringilla coelebs	0.05	ID19
Fringilla coelebs	0.05	ID19
Geococcyx californianus	0.06	BM05
Geococcyx californianus	0.06	BM05
Larus argentatus	0.045	BM05
Larus argentatus	0.045	BM05
Macronectes giganteus	0.06	BM05
Macronectes giganteus	0.06	BM05
Meleagris gallopavo	0.045	BM05
Meleagris gallopavo	0.045	BM05
Morus bassanus	0.045	BM05
Morus bassanus	0.045	BM05
Musophaga violacea	0.05	ID19
Musophaga violacea	0.05	ID19
Opisthocomus hoazin	0.1	BM05
Opisthocomus hoazin	0.1	BM05
Passer domesticus	0.05	ID19
Passer domesticus	0.05	ID19
Phasianus colchicus	0.045	BM05
Phasianus colchicus	0.045	BM05
Pica pica	0.045	BM05
Pica pica	0.045	BM05
Picus viridis	0.045	BM05
Picus viridis	0.045	BM05
Rhea americana	0.02	ID19
Rhea americana	0.02	ID19
Rissa tridactyla	0.045	BM05
Rissa tridactyla	0.045	BM05
Streptopelia decaocto	0.045	BM05
Streptopelia decaocto	0.045	BM05
Strix aluco	0.045	BM05
Strix aluco	0.045	BM05
Struthio camelus	0.02	ID19
Struthio camelus	0.02	ID19
Sylvia atricapilla	0.06	BM05
Sylvia atricapilla	0.06	BM05
Threskiornis aethiopicus	0.05	ID19
Threskiornis aethiopicus	0.05	ID19
Uria aalge	0.045	BM05
Uria aalge	0.045	BM05
† *Archaeopteryx* cf. *lithographica* #5	0.15	ID19
† *Archaeopteryx* cf. *lithographica* #5	0.15	ID19
† *Archaeopteryx* cf. *lithographica* #7	0.25	ID19
† *Archaeopteryx* cf. *lithographica* #7	0.25	ID19
† *Archaeopteryx* cf. *lithographica* #9	0.32	ID19
† *Archaeopteryx* cf. *lithographica* #9	0.32	ID19
† *Brasileodactylus araripensis*	0.02	ID19
† *Brasileodactylus araripensis*	0.02	ID19
† *Compsognathus longipes*	0.25	BM05
† *Compsognathus longipes*	0.25	BM05
Crocodylus niloticus	0.04	BM05
Crocodylus niloticus	0.04	BM05
† aff. *Deinonychus antirrhopus*	0.04	BM05
† *Rhamphorhynchus* sp.	0.08	BM05
† *Rhamphorhynchus* sp.	0.08	BM05

Appendix VI: Supplementary Data 4 for "Wing bone geometry reveals active flight in *Archaeopteryx*" by Voeten et al.

Motivation for topography and timing of chronogram. Organised by node, includes timing for both extinct and extant taxa and declares corresponding sources. Remarks provided where relevant.

Node or Terminal #	Split or Node	Taxon
2	Pseudosuchia - Ornithosuchia	Oldest Pseudosuchia
3	Pterosauramorpha - Dinosauromorpha	
4	Saurischia - Ornithischia	Oldest Ornitischia
5	Coelurosauria - Allosauroidea	Oldest Coelurosauria
6	Compsognathidae - Maniraptoriformes	
7	Dromaeosauridae - Averaptora	Oldest Dromaeosauridae
8	*Archaeopteryx* - Euavialae	Oldest unequivocal "Aves" (= *Archaeopteryx*)
9	Confuciusornithidae - Ornithothoraces	Oldest Confuciusornithidae
10	Paleognathae - Neognathae	
11	Galloanserae - Neoaves	
12	Columbea - Passerea	
13	Otidimorphae - other Passerea	
14	(Cursorimorphae+Opisthocomus) - (Aequornithia+Telluraves)	
15	Aequornithia - Telluraves	
16	Australaves - Afroaves	
17	Falconiformes - Psittacopasserae	
18	*Falco tinnunculus*	
19	Psittaciformes - Passeriformes	
20	*Nymphicus hollandicus*	
21	Corvidae - other Passeridae	
22	*Pica - Corvus*	Oldest *Corvus*
23	*Pica pica*	
24	*Corvus corone*	
25	Fringilidae - ((Sylviidae+Paridae)+(Estrildidae+Passeridae))	Oldest Fringillidae
26	*Fringilla coelebs*	
27	((Sylviidae+Paridae)-(Estrildidae+Passeridae))	
28	Sylviidae - Paridae	Oldest Paridae
29	*Sylvia atricapilla*	
30	*Cyanistes caeruleus*	
31	Estrildidae - Passeridae	Oldest Passeridae
32	*Passer domesticus*	
33	*Erythrura trichroa*	
34	Accipitrimorphae - (Coraciimorphae+Strigiformes)	
35	*Buteo* - (Circinae+*Accipiter*)	Oldest *Buteo*
36	Circinae - *Accipiter*	Oldest *Accipiter*
37	*Circus cyaneus*	
38	*Accipiter nisus*	
39	*Buteo buteo*	
40	Coraciimorphae - Strigiformes	
41	Tytonidae - Strigidae	
42	*Tyto alba*	
43	*Otus* - (*Asio* +*Strix)*	
44	*Otus scops*	
45	*Asio - Strix*	Oldest *Strix*
46	*Asio otus*	
47	*Strix aluco*	
48	Coraciiformes - Piciformes	
49	*Merops apiaster*	
50	*Picus viridis*	
51	Procellariiformes - (Suliformes+Pelecaniformes)	
52	Suliformes - Pelecaniformes	
53	Sulidae - Phalacrocoracidae	Oldest Sulidae
54	*Morus bassanus*	
55	*Phalacrocorax carbo*	
56	Threskiornithidae - Ardeidae	
57	*Threskiornis aethiopicus*	
58	*Bubulcus ibis*	
59	Procellariidae - Diomedeidae	Oldest Diomedeidae
60	*Macronectes - Procellaria*	Oldest *Procellaria*
61	*Macronectes giganteus*	
62	*Procellaria aequinoctialis*	
63	*Thalassarche - Diomedea*	Oldest *Diomedea*
64	*Thalassarche melanophris*	
65	*Diomedea sanfordi*	
66	Gruimorphae - Opisthocomiformes	
67	Charadriiformes - Gruiformes	
68	Burhinidae - other Charadriiformes	Oldest Burhinidae
69	*Burhinus oedicnemus*	
70	Scolopaci - Lari	
71	*Calidris - Scolopax*	Oldest *Calidris*
72	*Calidris alpina*	
73	*Scolopax rusticola*	
74	Lari - Panalcidae	

Node or Terminal #	Split or Node	Taxon
75	Mancallinae - Alcidae	Oldest Alcidae
76	*Mancalla cedrosensis*	Youngest *Mancalla cedrosensis*
77	*Pinguinus* - Alcini	
78	*Pinguinus impennis*	Youngest *Pinguinus impennus*
79	*Alca - Uria*	Oldest *Alca*
80	*Alca torda*	
81	*Uria aalge*	
82	Sterninae - Larinae	
83	*Sterna albifrons*	
84	*Rissa - (Chroicocephalus +Larus)*	
85	*Rissa tridactyla*	
86	*Chroicocephalus - Larus*	Oldest *Larus*
87	*Chroicocephalus ridibundus*	
88	*Larus argentatus - Larus fuscus*	Oldest *Larus argentatus*
89	*Largus argentatus*	
90	*Larus fuscus*	
91	*Fulica atra*	
92	*Opisthocomus hoazin*	
93	Cuculiformes - Otidimorphae	
94	*Geococcyx californianus*	
95	Otidiformes - Musophagiformes	
96	*Tetrax tetrax*	
97	*Musophaga violacea*	
98	Phoenicopterimorphae - Columbimorphae	
99	*Podiceps cristatus*	
100	*Columba palumbus - Streptopelia decaocto*	Oldest *Columba*
101	*Columba palumbus*	
102	*Streptopelia decaocto*	
103	Anseriformes - Galliformes	
104	Anserinae - (Tadorninae+(Aythyini+Anatini))	
105	Anserini - Cygninae	Oldest Cygninae
106	*Anser anser domesticus*	
107	*Cygnus olor*	
108	Tadorninae - (Aythyini+Anatini)	
109	*Alopochen sirabensis*	Youngest *Alopochen sirabensis*
110	Aythyini - Anatini	Oldest Anatini
111	*Aythya fuligula*	
112	*Anas clypeata - Anas platyrhynchos*	Oldest *Anas clypeata*
113	*Anas clypeata*	
114	*Anas platyrhynchos*	
115	Odontophoridae - Phasianidae	Oldest Odontophoridae
116	*Colinus virgianus*	
117	Pavoninae - (Meleagridinae+(Phasianinae+Perdicinae))	
118	*Pavo cristatus*	
119	Meleagridinae - (Phasianinae+Perdicinae)	Oldest Meleagridinae
120	*Meleagris gallopavo*	
121	Phasianinae - Perdicinae	Oldest Phasianinae
122	*Phasianus colchicus*	
123	*Perdix perdix*	
124	Struthioniformes - Notopalaeognathae	
125	Rheidae - Apterygidae	Oldest Rheidae
126	*Rhea americana*	
127	*Apteryx australis*	
128	*Struthio camelus*	
129	Enantiornithes - Euornithes	Oldest Enantiornithes
130	Enantiornithes	Youngest Enantiornithes
131	*Confuciusornis sanctus*	Youngest *Confuciusornis sanctus*
132	*Archaeopteryx* 5 - *Archaeopteryx* 7 - *Archaeopteryx* 9	
133	*Archaeopteryx* 5	Youngest unequivocal *Archaeopteryx* sp.
134	*Archaeopteryx* 7	Youngest unequivocal *Archaeopteryx* sp.
135	*Archaeopteryx* 9	Youngest unequivocal *Archaeopteryx* sp.
136	*Deinonychus antirrhopus*	Youngest *Deinonychus antirrhopus*
137	*Compsognathus longipes*	Youngest *Compsognathus longipes*
138	Allosauria - Neovenatoridae	Oldest Allosauria
139	*Allosaurus fragilis*	Youngest *Allosaurus fragilis*
140	*Australovenator wintonensis*	Youngest *Australovenator wintonensis*
141	*Tenontosaurus tilletti*	Youngest *Tenontosaurus tilletti*
142	Rhamphorhynchidae - Pterodactylomorpha	Oldest Rhamphorhynchidae
143	*Rhamphorhynchus* sp.	Youngest *Rhamphorhynchus*
144	*Brasileodactylus araripensis*	Youngest *Brasileodactylus araripensis*
145	Alligatoridae - Crocodylidae	Oldest Crocodylidae
146	*Alligator mississippiensis*	
147	*Crocodylus niloticus*	

Node or Terminal #	First appearance (older bound, Ma)	Last appearance (younger bound, Ma)	Source
2	252.17		27
3			
4	237		27
5	201.3		27
6			
7	168.3		27
8	152.1		27
9	145		27
10			28
11			28
12			28
13			28
14			28
15			28
16			28
17			28
18			Extant
19			28
20			Extant
21			
22	11.1		27
23			Extant
24			Extant
25	13.6		27
26			Extant
27			
28	2.588		27
29			Extant
30			Extant
31	5.333		27
32			Extant
33			Extant
34			28
35	33.9		27
36	4.9		27
37			Extant
38			Extant
39			Extant
40			28
41			
42			Extant
43			
44			Extant
45	20.4		27
46			Extant
47			Extant
48			28
49			Extant
50			Extant
51			28
52			28
53	48.6		27
54			Extant
55			Extant
56	58		28
57			Extant
58			Extant
59	56		27
60	5.333		27
61			Extant
62			Extant
63	15.97		27
64			Extant
65			Extant
66	66		28
67	64		28
68	50.3		27
69			Extant
70			
71	16		27
72			Extant
73			Extant
74			

Node or Terminal #	First appearance (older bound, Ma)	Last appearance (younger bound, Ma)	Source
75	38		27
76		3.6	27
77			
78		0.000171	29
79	16		27
80			Extant
81			Extant
82			
83			Extant
84			
85			Extant
86	33.9		27
87			Extant
88	5.333		27
89			Extant
90			Extant
91			Extant
92			Extant
93	65		28
94			Extant
95	62		28
96			Extant
97			Extant
98	68		28
99			Extant
100	5.333		27
101			Extant
102			Extant
103	66		28
104			
105	23.03		27
106			Extant
107			Extant
108			
109		0.001359	30
110	19		27
111			Extant
112	5.333		27
113			Extant
114			Extant
115	37.2		27
116			Extant
117			
118			Extant
119	5.333		27
120			Extant
121	0.126		27
122			Extant
123			Extant
124	84		28
125	58.7		27
126			Extant
127			Extant
128			Extant
129	139.8		27
130		66	27
131		122.46	27
132			
133		145	27
134		145	27
135		145	27
136		100.5	27
137		145	27
138		171.6	27
139		145	27
140		93.5	27
141		100.5	27
142	201.3		27
143		145	27
144		109	27
145	150.3		27
146			Extant
147			Extant

Node or Terminal #	Standardised (Daughter node + 4MY)	Date (Ma)
2	no	**252.17**
3	yes: Node 4 + 4 MY	**241**
4	no	**237**
5	no	**201.3**
6	yes: Node 6 + 4 MY	**205.3**
7	no	**168.3**
8	no	**152.1**
9	no	**145**
10	no	**100**
11	no	**88.5**
12	no	**69.5**
13	no	**67.5**
14	no	**67**
15	no	**65**
16	no	**63.5**
17	no	**60**
18	no	**0**
19	no	**54.5**
20	no	**0**
21	yes: Node 24 + 4 MY	**17.6**
22	no	**11.1**
23	no	**0**
24	no	**0**
25	no	**13.6**
26	no	**0**
27	yes: Node 30 + 4 MY	**9.333**
28	no	**2.588**
29	no	**0**
30	no	**0**
31	no	**5.333**
32	no	**0**
33	no	**0**
34	no	**62.5**
35	no	**33.9**
36	no	**4.9**
37	no	**0**
38	no	**0**
39	no	**0**
40	no	**61.5**
41	yes: Node 42 + 4 MY	**28.4**
42	no	**0**
43	yes: Node 44 + 4 MY	**24.4**
44	no	**0**
45	no	**20.4**
46	no	**0**
47	no	**0**
48	no	**42.5**
49	no	**0**
50	no	**0**
51	no	**62**
52	no	**59**
53	no	**48.6**
54	no	**0**
55	no	**0**
56	no	**58**
57	no	**0**
58	no	**0**
59	no	**56**
60	no	**5.333**
61	no	**0**
62	no	**0**
63	no	**15.97**
64	no	**0**
65	no	**0**
66	no	**66**
67	no	**64**
68	no	**50.3**
69	no	**0**
70	yes: Node 73 + 4 MY	**46.03**
71	no	**16**
72	no	**0**
73	no	**0**
74	yes: Node 74 + 4 MY	**42**

Node or Terminal #	Standardised (Daughter node + 4MY)	Date (Ma)
75	no	**38**
76	no	**3.6**
77	yes: Node 78 + 4 MY	**20**
78	no	**0.00171**
79	no	**16**
80	no	**0**
81	no	**0**
82	yes: Node 83 + 4 MY	**41.9**
83	no	**0**
84	yes: Node 85 + 4 MY	**37.9**
85	no	**0**
86	no	**33.9**
87	no	**0**
88	no	**0**
89	no	**0**
90	no	**0**
91	no	**0**
92	no	**0**
93	no	**65**
94	no	**0**
95	no	**62**
96	no	**0**
97	no	**0**
98	no	**68**
99	no	**0**
100	no	**5.3**
101	no	**0**
102	no	**0**
103	no	**66**
104	yes: Node 104 + 4 MY	**27.03**
105	no	**23.03**
106	no	**0**
107	no	**0**
108	yes: Node 109 + 4 MY	**23**
109	no	**0.001359**
110	no	**19**
111	no	**0**
112	no	**5.333**
113	no	**0**
114	no	**0**
115	no	**37.2**
116	no	**0**
117	yes: Node 118 + 4 MY	**9.333**
118	no	**0**
119	no	**5.333**
120	no	**0**
121	no	**0.126**
122	no	**0**
123	no	**0**
124	no	**84**
125	no	**58.7**
126	no	**0**
127	no	**0**
128	no	**0**
129	no	**139.8**
130	no	**113**
131	no	**122.46**
132	yes: Node 130 + 4 MY	**149**
133	no	**145**
134	no	**145**
135	no	**145**
136	no	**100.5**
137	no	145
138	no	**171.6**
139	no	**145**
140	no	**93.5**
141	no	**100.5**
142	no	**201.3**
143	no	145
144	no	**109**
145	no	**150.3**
146	no	**0**
147	no	**0**

Node or Terminal #	Remarks (references between parentheses)
2	Trace fossils excluded; Aetosauria indet. (Antofagasta, Chile).
3	
4	
5	Trace fossils excluded; *Eshanosaurus deguchiianus* (Eshan, China).
6	
7	
8	Reports for earlier "Aves" are equivocal.
9	
10	
11	
12	
13	
14	
15	
16	
17	
18	*Falco tinnunculus* is not in PaleoDB: *Falco* is.
19	
20	*Nymphicus hollandicus* is not in PaleoDB: Cacatuidae is.
21	
22	
23	
24	*Corvus corone* is not in PaleoDB (lacks formal opinion data): *Corvus* is.
25	
26	*Fringilla coelebs* is not in PaleoDB: *Fringilla* is.
27	
28	
29	*Sylvia atricapilla* is not in PaleoDB: Sylviidae is.
30	*Cyanistes cyaneus* is not in PaleoDB: Paridae is.
31	
32	*Passer domesticus* is not in PaleoDB: *Passer* is.
33	*Erythrura trichroa* is not in PaleoDB: Passeriformes is (and *Estrilda*).
34	
35	
36	
37	*Circus cyaneus* is not in PaleoDB (lacks formal opinion data): *Circus* is.
38	
39	
40	
41	
42	
43	
44	*Otus scops* is not in PaleoDB: *Otus* is.
45	
46	*Asio otus* is not in PaleoDB: *Asio* is.
47	*Strix aluco* is not in PaleoDB: *Strix* is.
48	
49	*Merops apiaster* is not in PaleoDB: *Merops* is, but without taxonomy.
50	*Picus viridis* is not in PaleoDB (lacks formal opinion data): *Picus* is, but without taxonomy.
51	
52	
53	
54	*Morus bassanus* is not in PaleoDB: *Morus* is.
55	
56	
57	*Threskiornis aethiopicus* is not in PaleoDB: Threskiorninae is.
58	*Bubulcus ibis* is not in PaleoDB: Adeinae is.
59	
60	
61	*Macronectes giganteus* is not in PaleoDB: *Macronectes* is, but without taxonomy.
62	
63	
64	*Thalassarche melanophris* is not in PaleoDB: *Thalassarche* is.
65	*Diomedea sanfordi* is not in PaleoDB: *Diomedea* is.
66	
67	
68	
69	*Burhinus oedicnemus* is not in PaleoDB: *Burhinus* is.
70	
71	
72	*Calidris alpina* is not in PaleoDB: *Calidris* is.
73	*Scolopax rusticola* is not in PaleoDB: *Scolopax* is.
74	

Node or Terminal #	Remarks (references between parentheses)
75	
76	
77	
78	Extinct "1844 or shortly thereafter" (29).
79	
80	
81	
82	
83	*Sterna albifrons* is not in PaleoDB: *Sterna* is.
84	
85	
86	
87	*Chroicocephalus ridibundus* is not in PaleoDB: *Larus ridibundus* is without specimens. We recognise the genus *Chroicocephalus* (31).
88	
89	
90	*Larus fuscus* is not in PaleoDB: *Larus* is.
91	*Fulica atra* is not in PaleoDB: *Fulica* is.
92	
93	
94	*Geococcyx californianus* is not in PaleoDB: *Geococcyx* is, but without taxonomy.
95	
96	*Tetrax tetrax* is not in PaleoDB, *Otis* is.
97	*Musophaga violacea* is not in PaleoDB: *Musophaga* is (but erroneously recorded as "cuckoo").
98	
99	*Podiceps cristatus* is not in PaleoDB: *Podiceps* is.
100	
101	*Columba palumbus* is not in PaleoDB: *Columba* is.
102	*Streptopelia decaocto* is not in PaleoDB: *Streptopelia* is.
103	
104	
105	Cygninae is recorded as the daughter taxon of the subfamily Anserinae. Anserinae has *Cygnus* as a sister taxon.
106	*Anser anser domesticus* is not in PaleoDB: *Anser* is.
107	
108	
109	*Alopochen sirabensis* is not in PaleoDB: Tadorninae is. Last-occurrence date (median of calibrated radiocarbon range; 30).
110	
111	*Aythya fuligula* is not in PaleoDB: *Aythya* is.
112	
113	
114	
115	
116	
117	
118	*Pavo cristatus* is not in PaleoDB: *Pavo* is.
119	
120	
121	*Phasianus colchicus* is not in PaleoDB: *Phasianus* is. Oldest record *"Phasianus" mioceanus* considers *Archaeophasianus mioceanus* (32).
122	
123	*Perdix perdix* is not in PaleoDB: Perdicinae is.
124	PaleoDB conflicts with Jarvis et al. (28) with respect to "Struthioniformes".
125	
126	
127	*Apteryx australis* is not in PaleoDB: *Apteryx* is.
128	
129	Reports for earlier Enantiornithes are equivocal or too broadly constrained temporally.
130	
131	
132	
133	Reports for later *Archaeopteryx* sp. are equivocal.
134	Reports for later *Archaeopteryx* sp. are equivocal.
135	Reports for later *Archaeopteryx* sp. are equivocal.
136	
137	
138	
139	Material not referred further than generic level (6).
140	
141	
142	
143	
144	
145	
146	
147	

Appendix VII: Supplementary Data 5 for "Wing bone geometry reveals active flight in *Archaeopteryx*" by Voeten et al.

P-values for phylogenetic ANCOVA. Conducted using locomotory division as response variable, individual parameters as variates, and body mass as covariates. Non-phylogenetic p-values and f-values provided for reference.

Phylogenetic ANCOVA of Training Taxa

Locomotor group ~ Parameters, body mass as covariate

Locomotor division	Variate	Covariate	Element	F-Value Variate (non-phyl. Ancova)	F-Value Covariate (non-phyl. Ancova)
Viscor et al. (1)	CA/TA_h	Body mass	Humerus	17.35	1.77
Viscor et al. (1)	J/M_h	Body mass	Humerus	2.965	12.895
Viscor et al. (1)	CA/TA_u	Body mass	Ulna	15.305	0.489
Viscor et al. (1)	J/M_u	Body mass	Ulna	13.97	20.55
Close et al. (2)	CA/TA_h	Body mass	Humerus	14.746	1.497
Close et al. (2)	J/M_h	Body mass	Humerus	6.435	18.371
Close et al. (2)	CA/TA_u	Body mass	Ulna	17.349	0.505
Close et al. (2)	J/M_u	Body mass	Ulna	21.25	28.18

Locomotor division	Variate	Covariate	Element	Pr (>F) Variate (Group)	Pr (>F) Covariate (Body mass)
Viscor et al. (1)	CA/TA_h	Body mass	Humerus	1.42E-14	0.189
Viscor et al. (1)	J/M_h	Body mass	Humerus	0.00301	0.000703
Viscor et al. (1)	CA/TA_u	Body mass	Ulna	1.84E-13	0.487
Viscor et al. (1)	J/M_u	Body mass	Ulna	1.13E-12	3.18E-05
Close et al. (2)	CA/TA_h	Body mass	Humerus	3.87E-13	0.226
Close et al. (2)	J/M_h	Body mass	Humerus	5.65E-07	7.38E-05
Close et al. (2)	CA/TA_u	Body mass	Ulna	1.43E-14	0.48
Close et al. (2)	J/M_u	Body mass	Ulna	< 2e-16	2.05E-06

Locomotor division	Variate	Covariate	Element	F_Variate (Group)	F_Covariate (Body mass)
Viscor et al. (1)	CA/TA_h	Body mass	Humerus	9960	1096
Viscor et al. (1)	J/M_h	Body mass	Humerus	3893	5564
Viscor et al. (1)	CA/TA_u	Body mass	Ulna	9907	263
Viscor et al. (1)	J/M_u	Body mass	Ulna	9983	9784
Close et al. (2)	CA/TA_h	Body mass	Humerus	9920	978
Close et al. (2)	J/M_h	Body mass	Humerus	8539	7185
Close et al. (2)	CA/TA_u	Body mass	Ulna	9951	275
Close et al. (2)	J/M_u	Body mass	Ulna	9987	9925

Locomotor division	Variate	Covariate	Element	Phylogenetic pVariate (Group)	Phylogenetic pCovariate (Body mass)
Viscor et al. (1)	CA/TA_h	Body mass	Humerus	0.004	0.8904
Viscor et al. (1)	J/M_h	Body mass	Humerus	0.6107	0.4436
Viscor et al. (1)	CA/TA_u	Body mass	Ulna	0.0093	0.9737
Viscor et al. (1)	J/M_u	Body mass	Ulna	0.0017	0.0216
Close et al. (2)	CA/TA_h	Body mass	Humerus	0.008	0.9022
Close et al. (2)	J/M_h	Body mass	Humerus	0.1461	0.2815
Close et al. (2)	CA/TA_u	Body mass	Ulna	0.0049	0.9725
Close et al. (2)	J/M_u	Body mass	Ulna	0.0013	0.0075

Significant (95% CI)	Significant (95% CI)
Non-significant (95% CI)	Non-significant (95% CI)